Flow Direction Effects On Tidal Stream Turbines

A Thesis submitted to Cardiff University, for the Degree of Doctor of Philosophy

By

Carwyn Frost

School of Engineering

2016

Annex:

Declaration

This work has not been submitted in substance for any other degree or award at this or any other university or place of learning, nor is being submitted currently in candidature for any degree or otherward.

Signed: ………………………………………………………….. Date: …………………………………………

Statement 1

This thesis is being submitted in partial fulfilment of the requirements for the degree of PhD.

Signed: ………………………………………………………….. Date: …………………………………………

Statement 2

This thesis is the result of my own independent work/investigation, except where otherwise stated, and the thesis has not been edited by a third party beyond what is permitted by Cardiff University's Policy on the Use of Third Party Editors by Research Degree Students. Other sources are acknowledged by explicit references. The views expressed are my own.

Signed: ………………………………………………………….. Date: …………………………………………

Statement 3

I hereby give consent for my thesis, if accepted, to be available in the University's Open Access repository and for inter-library loan, and for the title and summary to be made available to outside organisations.

Signed: ………………………………………………………….. Date: …………………………………………

Acknowledgments

I would like to thank my PhD supervisors Prof. Tim O’Doherty and Dr. Daphne O’Doherty for their support and guidance throughout my studies at Cardiff University. I would also like to thank my family and friends for their encouragement, support and great patience, diolch yn fawr. Ecclesiastes 1:18.

The author wishes to acknowledge the financial support of EPSRC SuperGen Marine Grand Challenge and HPCW for use of their high performance computing facilities.

Abstract

This thesis investigated the non-dimensional performance characteristics of a tidal stream turbine and how they varied in response to changes in flow direction. The problem was considered from an industrial perspective and used the commercial software package ANSYS CFX and a 1:20th scale experimental turbine.

Initial considerations analysed the performance of the turbine in an ‘upstream’ or ‘downstream’ configuration relative to the turbines support structure. The conclusions resulting from this were that up to a point by increasing separation between an upstream turbine and its support structure the greater average non-dimensional performance characteristics became. Also, more significantly, it was identified that this orientation and clearance reduced the blade stanchion interaction considerably relative to the downstream orientation.

The study made justification for the inclusion of a yaw mechanism to rotate the turbine to face the flow for flood and ebb phases of the tide. In an operational environment this would be expected to enhance the life of the turbine’s blades, thrust bearings, and gearbox - which are known to be prone to fatigue failure, due to highly dynamic loads.

The thesis continued to expand into the potential uses of a yaw mechanism to address flow misalignment experienced throughout the tidal cycle. In order to justify this, the non-dimensional performance characteristics of the same turbine were compared for a series of flow misalignment cases. The CFD analysis showed that increased flow misalignment in either the positive and negative direction had the effect of reducing turbine torque and power performance characteristics, and also significantly increases the out-of-plane bending moments. A distinction between the positive yaw angles and negative yaw angles was identified in the turbine’s performance. The negative flow misalignment showed more favourable performance changes than the positive flow misalignment, this was due to the turbines rotational direction.

The subsequent recommendations to industry were included making use of the turbines rotational direction and yaw mechanism, to experience lower performance reductions in the case of flow misalignment.

Experimental results from tow tank testing at CNR-INSEAN using the 0.5 m diameter turbine validated the non-dimensional performance characteristics of the CFD results. It was identified that steady state CFD results did not capture the performance characteristics of flow misalignment cases as well as the transient CFD results. The experimental turbine captured temporal features identified in the CFD analysis. Recommendations to industry include the careful consideration of steady state CFD analysis in non-idealised flow conditions.

Table of Contents

List of Figures

List of Tables

Nomenclature

List of symbols and definitions…

Symbol	Definition	Units
A	Area	m^2
C_θ	Coefficient of Torque	-
C_P	Coefficient of Power	-
C_T	Coefficient of Thrust	-
L	Characteristic Geometric Length	m
P	Power	W
Q	Torque	Nm
t	Time	s
T	Thrust Force	N
V	Free Stream Velocity	$m.s^{-1}$
U_T	Tangential Velocity	$m.s^{-1}$
u	Velocity in the x-direction	$m.s^{-1}$
v	Velocity in the y-direction	$m.s^{-1}$
w	Velocity in the z-direction	$m.s^{-1}$
x	Cartesian Co-ordinate Reference	m
y	Cartesian Co-ordinate Reference	m
z	Cartesian Co-ordinate Reference	m
α	Angle of Attack/ Yaw Angle	°
β	Blade Pitch Angle	°
φ	Azimuth – Rotational Position	°
λ	Tip Speed Ratio	-

ω	Rotational Velocity	rad.s^{-1}
ρ	Density	kg.m^{-3}
μ	Kinematic Viscosity	kg.m^{-1}.s^{-1}
μ	Mean or Average Value	-
σ	Standard Deviation	-
θ	Resultant Fluid Direction	°
Φ	Phase Shift	°

1. Introduction

The drivers for renewable energy, marine energy and specifically tidal energy from a UK perspective are presented in this chapter. Specific attention is made to the science of tides, the present status of the offshore renewables sector and a broad review of the approaches to tidal energy, with examples given of current technology.

1.1. Energy Market and Mix

The UK economy is at a crucial decision making point when considering the way it produces and consumes electricity (DECC, 2015). With targets set by past governments (UK Gov., 2008) for reducing 'the net UK Carbon account for the year 2050' by at least 80% of 1990 baseline, the pending closure of many of the UK's power stations (DECC, 2015) and renewables target of 15% of our energy demand from renewable sources by 2020. The UK must decisively pursue alternative sources of energy through innovation and investment into clean and efficient power production. The goal of a low-carbon, secure and affordable energy future is central to the growth of the UK's economy and position on a global level. This objective is possible through growing support of renewable technologies and with improvements in energy efficiency. The current state of the UK's electricity mix shows a trend of growing contribution from renewables.

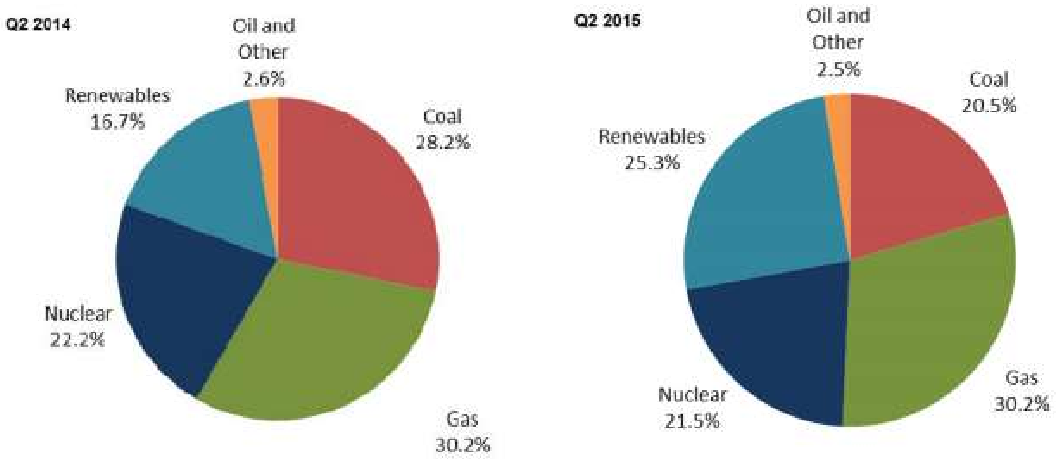

Figure 1.1 Electricity generation from resources in Quarter 2 2014/15 (DECC, 2012)

Figure 1.1 shows the same quarter for 2014 and 2015, the contribution from various resources with renewables being the second highest contributor, exceeding both coal and nuclear contributions for the first time in UK history. The contribution by the various renewable sectors to the UK electricity grid for the past three and a half years are shown in Figure 1.2.

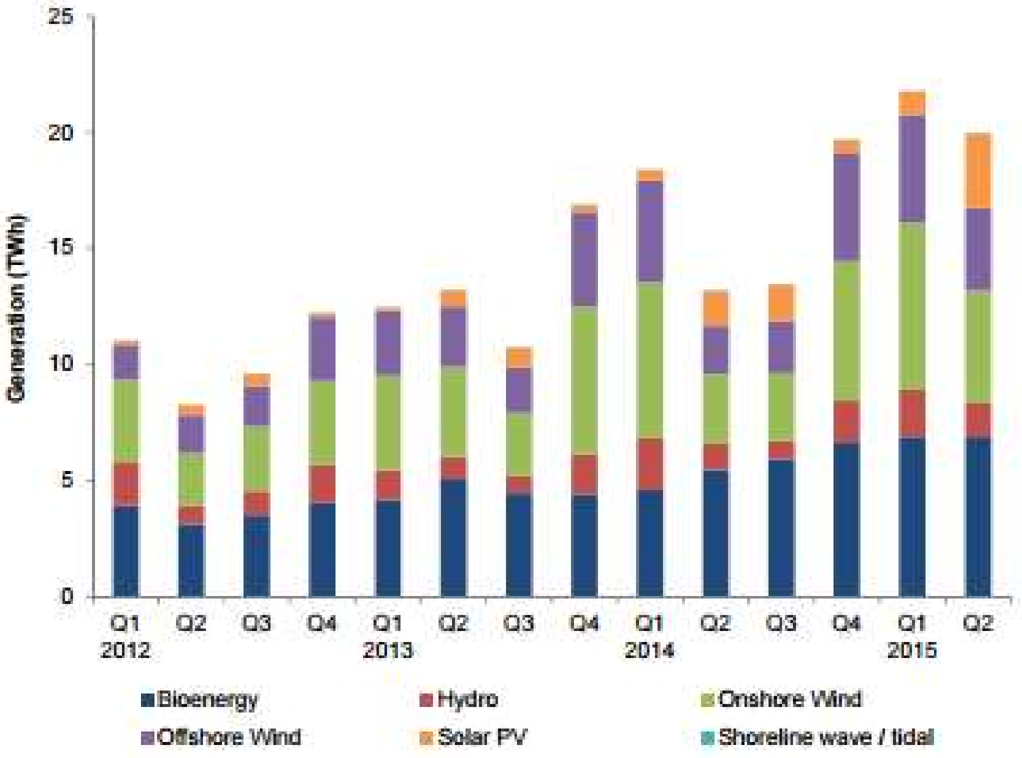

Figure 1.2 Renewable electricity generation by group 2012-2015 (GOV.UK, September 2015)

Whilst the contribution from renewables is clearly expanding, the contribution of each renewable resource fluctuates in each quarter. This problem is seen most significantly from the onshore wind and solar PV technologies. The onshore wind sector has high seasonal dependency with consistently higher contributions in Q1 and Q4 each year. However offshore wind, whilst showing less generating capacity than onshore wind, has less fluctuations in power generation because of its greater exposure to consistent prevailing winds. Nevertheless the intermittency and reduced flexibility of renewable energy sources overall has been highlighted as a challenge of the future (OfGEM, 2014). The necessity of a 'base-load' to the national grid presently requires Governments to continue to use conventional fossil fuel and nuclear power stations. Having established the clear growth in renewable energy generation, it is important to recognise the energy trilemma and resulting drivers for increasing the contribution of renewable energy, which are as follows:-

1.1.1. Environmental Drivers

The occurrence of climate change and extreme weather events has been linked to a rise in ocean temperatures. A 1°C rise in global ocean temperatures has occurred in the last 140 years (European Environment Agency, 2015). With the temperature rise continuing to accelerate, in order to remain under the 2°C limit significant changes to energy generation must be undertaken (United Nations, 2012). The consequences of increasing ocean temperatures is not limited to increasing extreme weather events, the thermal expansion of sea water and glacial melt from polar ice caps has elevated ocean levels by 0.2 m (Church, 2013) threatening the coastal areas of many nations.

1.1.2. Economic Drivers

The global economies are related to the response to climate change in a very clear way. With the depletion of fossil fuel reserves and increasing cost of extracting these from new areas, the decarbonisation of economies has been identified as a key to strengthening national security. Dependency on import fuels such as coal, gas and oil increases the vulnerability of any country to global price fluctuations. Therefore it is imperative that the cost of generation from renewable technologies compete with established technologies.

Figure 1.3 demonstrates the challenges facing the renewable sector, as it shows that the lowest cost for projects started in 2012 was from nuclear power generation at ~£80/MWh whilst the closest renewable technology in 2012 came from onshore wind that produced greater than 5 MW at ~£92/MWh. Solar power generation showed the highest cost at ~£167/MWh.

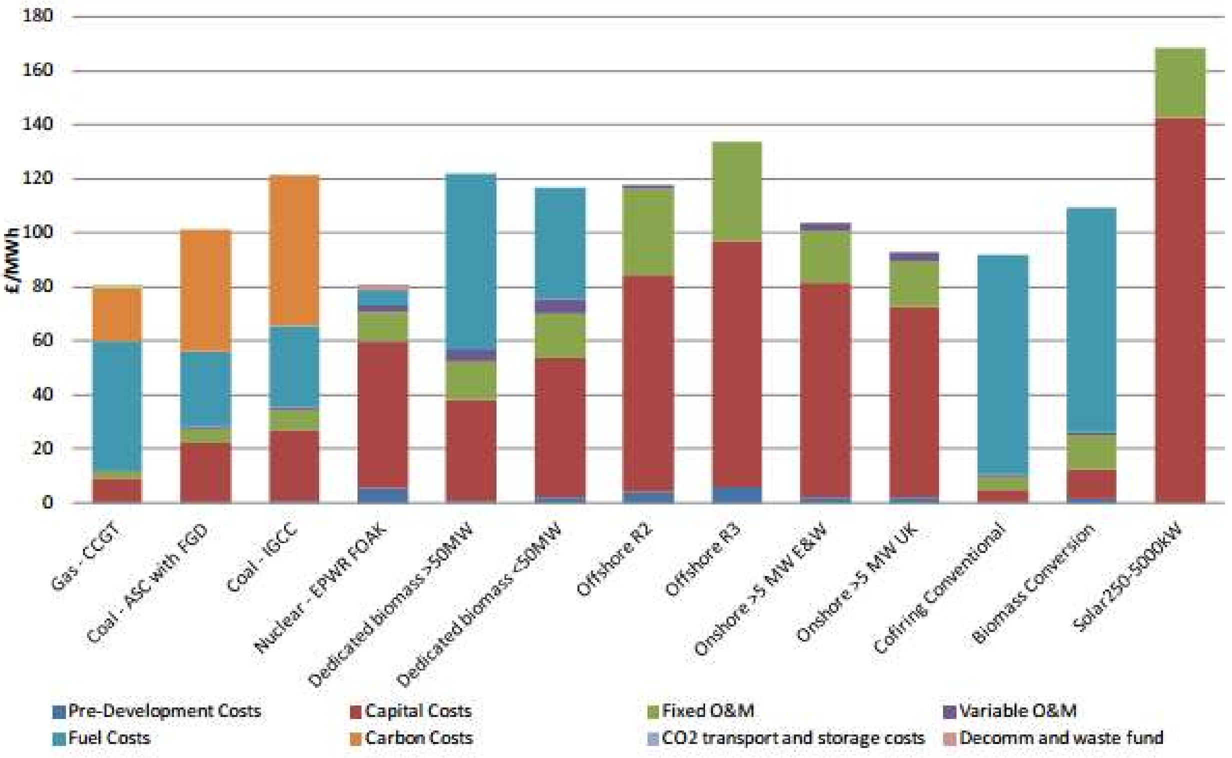

Figure 1.3 DECC - Electricity Generation Costs for Projects Started in 2012 (DECC, 2012)

In ‘developing’ nations, renewable energy whilst potentially more costly per unit of energy has a competitive advantage over conventional fossil fuels or nuclear generation. Due to the rapid growth in energy demand in these countries, there has been rapid response by Governments to develop power generation capacity quickly. This has drawn investment to renewable energy technologies being established because they are swift to install and commission in comparison to a conventional power stations. For example a wind turbine array will take between two and six months depending on capacity in comparison to a natural gas fired power station which is the quickest conventional fossil fuel, taking up to 3 year to install and commission (Nuclear Energy Agency, 2014; European Wind Energy Associsation, 2014).

As highlighted in section 1.1.1 rising global ocean temperatures has increased ocean levels by 0.2 m (Church, 2013) threatening many nations' coastal areas. This increases the requirement for significant coastal engineering defences, at significant central costs to nations. As well as disaster response funding required to respond to increasingly frequent severe weather conditions.

1.1.3. Security Drivers

Energy security is the 'uninterrupted availability of energy sources at an affordable price' as defined by the International Energy Agency (IEA, 2016). It is important for countries to be able to continue supply of energy to their domestic markets regardless of geo-politics, or natural disasters. Dependency on supply from other countries leaves vulnerability to market fluctuations. Renewable energy sources can reduce this need for external supply and can also provide a source of net energy export during favourable periods. Naturally, this is dependent upon the infrastructure in place between nations, an example of such infrastructure can be seen in Figure 1.4. The interconnections with continental Europe and Ireland enables the UK to both buy and sell electricity as required, in turn this enhances security for all nations connected. The planned expansion of interconnectivity with continental Europe and Iceland as shown in Figure 1.4 could offer economic benefits of reduced 'wholesale prices up to 1-2%' (UK Science and Technology Committee, 2015).

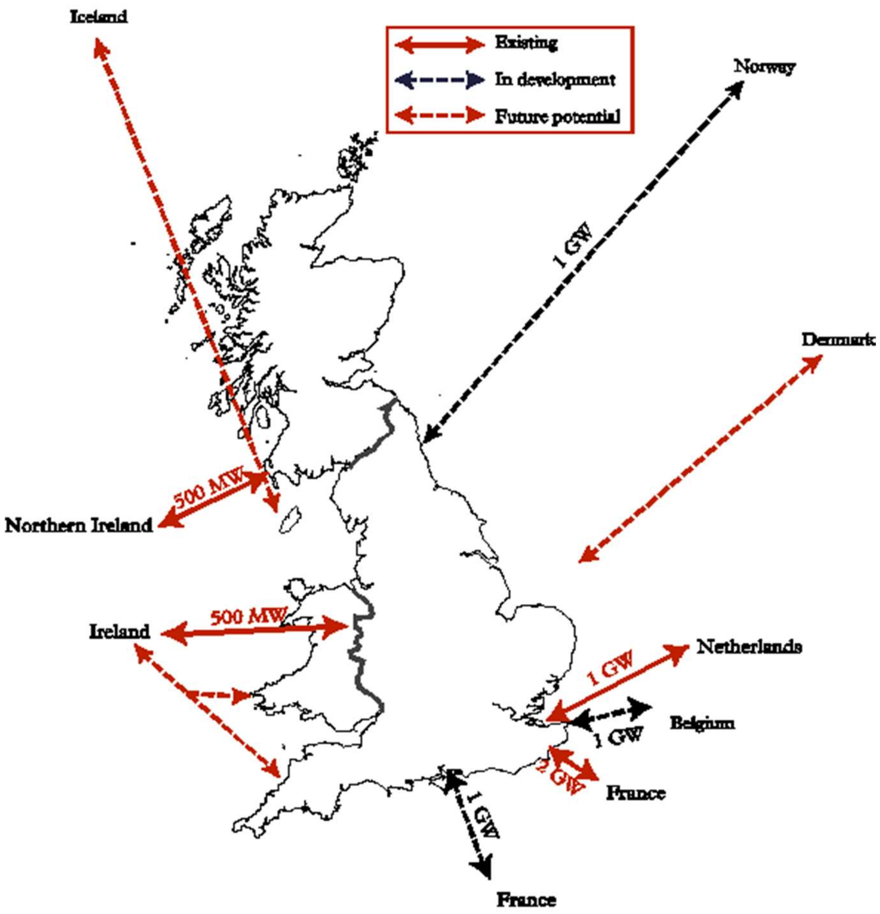

Figure 1.4 UK Interconnection Map (UK Science and Technology Committee, 2015)

1.2. Offshore Renewable Energy

Offshore renewables describe those technologies located under or above the ocean's surface. The oceans cover 70% of the earth's surface. It is an essential part of life on planet earth and plays an important role in civilisation. The ocean has been used as a source of renewable energy since the Victorian age with, tidal mills being the most common around the UK shores powering local machinery used in the production of grain (Eling Experience, 2015). Whilst this is a source that until lately has been neglected, it is important that there is a return to the ocean, as a source of renewable energy. Modern technology solutions enable renewable energy to venture further offshore in recent years.

1.2.1. Offshore Wind

The offshore wind industry has developed rapidly in the last decade as shown previously in Figure 1.2. With deployments reaching further offshore, and turbines increasing in diameter and height. The latest generation of Horizontal Axis Wind Turbines, HAWTs are commonly rated at 6 MW and feature in arrays of over 100 strong (Haddon, et al., 2011). The consistency of prevailing winds offshore makes it attractive to produce wind energy. However there are problems with the installation of offshore wind turbine foundations and bringing the power to shore through sub-sea cables, which requires specialist vessels. These were previously used by the petrochemical industry and competition for these vessels made initial deployments very expensive (Offshore-Technology, 2012). However with declining North Sea oil industry, vessels have adapted to support the wind sector offshore and this has driven down the capital expenditure (CapEx) of offshore wind. Still to be improved however is the operational expenditure (OpEx).

Some of the lessons learnt from the wind industry and specifically offshore wind can be directly applied to other technologies. An example of one such transferable knowledge is the development of sub-sea cabling techniques from the offshore wind, this can be applied to many of the marine energy sectors.

The term ‘marine energy’ is specific to the energy which can be extracted from the water of the oceans. Off-shore wind does not count technically as a source of marine energy for the purpose of this thesis, although it is acknowledged that the oceans currents and reactions with the atmosphere is a primary drive of off-shore wind. The main sources of marine energy are divided into three areas - Wave Energy, Tidal Range and Tidal Stream - each of which are now considered in Sections 1.2.2 and 1.2.3 respectively.

1.2.2. Wave

The source of wave energy comes from the large scale interaction of atmospheric pressure and the surface of the oceans. This makes wave energy essentially a concentrated form of wind energy and is determined by the wind speed and the fetch. The energy stored in a wave is dependent on the wave height and wave period, as a wave approaches the shore this energy is dissipated along the shoreline (Lynn, 2014). The UK and Ireland has the most favourable wave climate in Europe, as can be seen by Figure 1.5 which shows the resource on the west coast of Europe in kW m^{-1}.

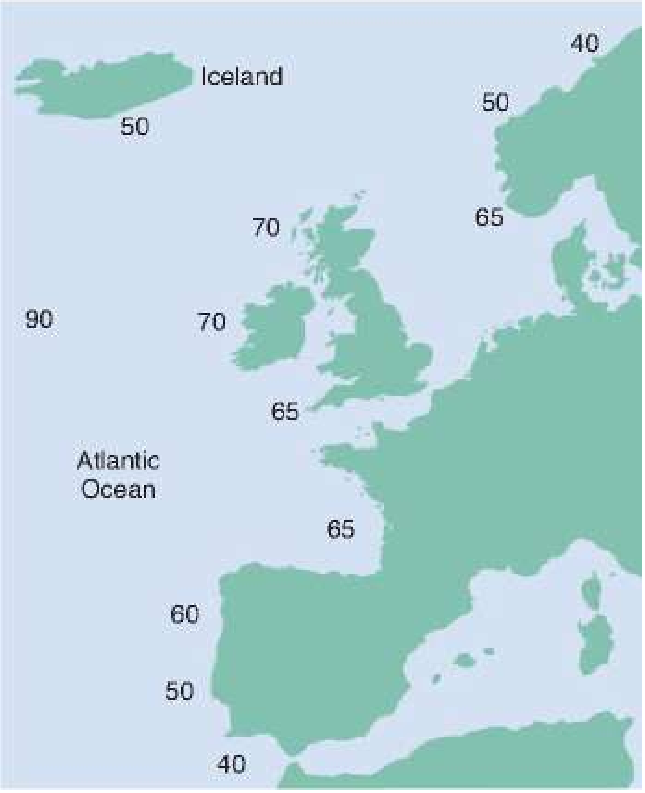

Figure 1.5 Wave Energy in kW m^{-1} along west coast Europe (Lynn, 2014)

There have been numerous proposed methods of harnessing wave power. Some typical technologies associated with wave power are described here:

i) Attenuator devices – float on the surface and have independent arms which ride the waves, the differential motion between the arms is used to generate electricity. An example of this device is Pelamis (European Marine Energy Centre, 2016).
ii) Point Absorber – the technology uses the linear motion caused by the rise and fall of sea level as a wave passes. A linear generator or 'linear to rotary' motion converter would be used as the power take off. An example of this device would be CorPower (CorPower Ocean, 2012).
iii) Oscillating wave surge converter – This would typical be a flap or hinged device that sits perpendicular to the wave motion and oscillates with the surge of the wave. A number of different power take off methods could be employed to this type of device. An example of a commercial surge device would be Aquamarine Power Ltds Oyster which was demonstrated at EMEC (European Marine Energy Centre, 2016).
iv) Oscillating water column – A chamber is created with one entrance for the waves and is usually submerged whilst the other entrance is open to the atmosphere and would host a Wells turbine. Electricity would be generated as the air rushes in and out of the chamber in response to the changing

volume due to the changing surface level as wave's peak and trough. The Limpet demonstration device in Scotland is an example of this technology (Whittaker, et al., 2002).

i) Rotating mass – The heaving and swaying of waves as they pass the device cause an eccentric mass to rotate about the axis of the device. This rotates the driveshaft which is connected to a variable speed generator housed inside the body of the device. An example of such a device as this was developed by Wello and is named the Penguine (Wello, 2012).

Wave energy by its nature being driven from atmospheric conditions has the same weaknesses as the wind industry in its unpredictability. Whilst forecasting provides a level of short-term predictability, the long-term certainty of expected capacity is essential for the national grid to regulate loads. This is one of the challenges recognised by the UK grid and this must be addressed by the sectors involved if more reliance on unpredictable renewable resources is to arise (E.ON Energy, 2011).

1.2.3. Tidal

The centripetal forces of the rotation of the earth causes the oceans to bulge around the equator. This bulging, combined with the moon and sun's gravitational effects bring about changes in ocean levels along the coasts of landmasses. There are three types of tidal coastlines; semidiurnal, diurnal and mixed. Semidiurnal systems experience two tides a day, whilst diurnal systems only experience one tide a day. Mixed coastlines experience one or two tides a day depending on the period in the solar and lunar cycle. Figure 1.6 shows the combined solar and lunar influences on tidal range. When the moon is in-line with the earth and sun, as in Figure 1.6 a), the tides are known as spring tides. As the gravitational forces are compounded the tidal amplitude increases, however the tidal period remains at approximately 12 hours 45 minutes and so the tidal flow can be said to be much greater during spring tides. When the moon is perpendicular relative to the earth and sun, as in Figure 1.6 (b). These tides are known as neap tides and these experience much shallower tidal amplitude.

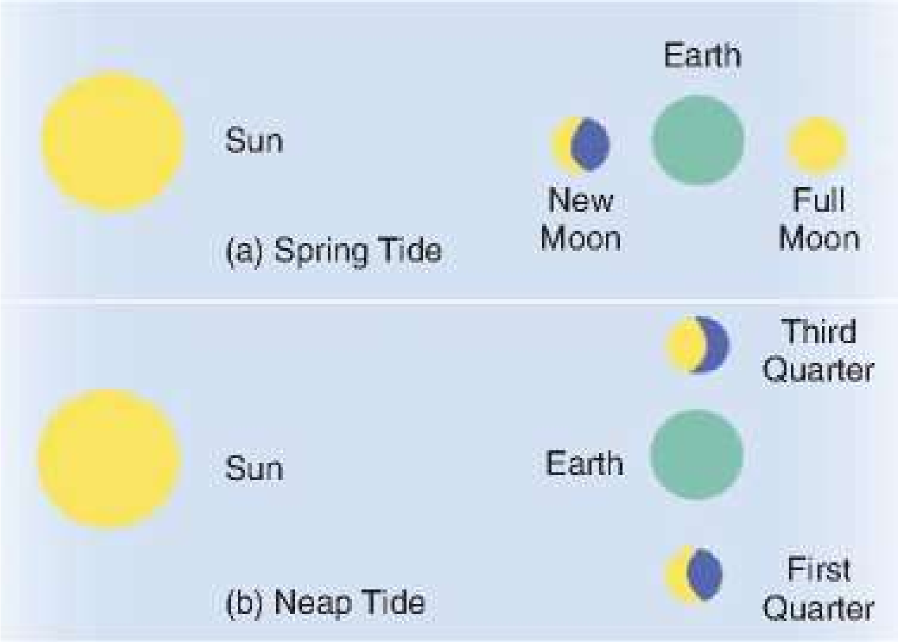

Figure 1.6 Solar and Lunar influence on tides (Lynn, 2014)

Tidal Energy as a renewable is in a unique position, compared to other renewable technologies. This is due to the resource being predictable over a hundred or more years in advance. The implications of this are significant in addressing the concerns of Ofgem regarding intermittency of renewable energy, as highlighted in the previous subsection (E.ON Energy, 2011). The potential to supply a base load of predictable and reliable renewable energy to the national electricity grid, sets tidal energy in an advantageous position in relation to any other renewable resource. Due to tidal phasing around the UK coastline, when considering all forms of tidal sites, it is possible to supply electricity from tidal sources for large periods of the tidal cycle (S P Neill, 2016). There are two primary forms of tidal energy extraction, those technologies dependent on the tidal range, and those technologies dependent on the tidal stream. The former uses the head difference between high and low tide while the latter uses the flow of the water toward the shore (flood tides) and away from the shore (ebb tides). Both technologies are described in summary in the following sub-sections.

1.2.3.1. *Tidal Range*

Tidal Range technologies operates through impoundment, whether by a tidal barrage or lagoon the principle of operation remains the same. A head difference is created by the amplitude of tidal elevation and this gravitational potential energy is captured through low-head bulb turbines in the wall of the structure. The technology is similar to hydroelectric schemes, however due to the low-head nature of these schemes some adaptations have been made. Schemes have been proposed for both two way and one way operation. An example of a tidal impoundment schemes in operation can be found at La Rance tidal barrage in France. This

750 m long structure spans the mouth of the Rance estuary and houses 24 turbines rated to 10 MW capacity each (Boyle, 2012). The barrage has been in operation since 1966 and has been studied carefully through the decades to determine the lasting impact to local fauna and flora (Retiere, 1994). Some of the conclusions and lessons to be learnt include; expected ecosystem recovery time of approximately 10 years. Ecosystem is dependent on the barrage operating on a regular pattern. Careful planning of Operation and maintenance regimes must be considered in order not to upset a highly dependent ecosystem.

At the time of writing the UK has plans for its first commercial tidal range project in Swansea bay, South Wales. The tidal lagoon scheme features a 9.5 km sea wall housing 26 Kaplan bulb turbines with a capacity for generating 320 MW from the 8.5 m tidal range (DECC, 2015; Tidal Lagoon Swansea Bay , 2015). Whilst still being in concept phase the potential from tidal lagoons is significant and as such a review of the role of this technology in the UK energy mix is underway (DECC, 2016). An existing tidal lagoon can be found in South Korea, the Sihwa tidal lagoon was commissioned in August 2011 and features 254 MW generating capacity through 10 bi-directional turbines (International Renewable energy Agency, 2014). Both concept and constructed scheme can be seen in Figure 1.7.

Figure 1.7 a) Proposed Swansea Bay Tidal Lagoon b) Shiwa Tidal Lagoon **(SubSea World News, 2015)**

1.2.3.2. *Tidal Stream*

The second form of tidal energy generation is by extracting energy through tidal stream turbines (TSTs). These operate on the principle of capturing the kinetic energy of the free stream flow as the tide floods and ebbs. There are a variety of devices with various benefits and drawback, these are discussed further in Section 1.3, below. These schemes by nature are less intrusive on the environment, with a significantly lower seabed foot print than an impoundment scheme. Also the potential for arrays of these devices across multiple sites makes it an attractive commercial opportunity for large scale supply chain and potential revenue. The technology has primary potential in regions such as tidal straits and channels where the bathymetric and coastline restrictions lead to increases in velocity. Examples of this technology is expanded in the next section.

1.3. Introduction to Tidal Stream Turbine Devices

With such an abundant resource on the shores of the UK, the technology to unlock this potential renewable energy source has led to a number of approaches by international and local companies. Many designs are taking inspiration from existing technology in the wind industry and applying it to the coastal and marine environment. A brief description of tidal turbine technology is follows in this section, together with examples of demonstration devices in operation and planned commercial devices. The details of the project type, capacity, date installed/planned, connection type and location are also provided. EMECs website (European Marine Energy Centre, 2016) contains a host of device developers, including their currently installed devices and their planned devices.

1.3.1. Vertical Axis Tidal Turbines (VATT)

The vertical axis technology has the advantage of being able to operate in flow regimes that come from any direction. The two design options for VATTs are with lift optimised blades or drag optimised blades. Examples of the former, lift optimised devises, would be variations of the Darrieus or Gorlov turbines, where the rotational motion of the turbine is driven by the lift forces on the hydrofoil. The latter, drag optimised devises, would be a variation of the Savonius rotor. These rotate by the differential drag characteristics of the two (or more) blades, the advancing blade experience less drag than the receding blade causing rotation (Ali, 2013). Their dependency on drag makes them less efficient than lift devices, however they are simpler to manufacture. The technology for VATTs has been demonstrated at full scale by commercial developers, some examples are shown here.

1.3.1.1. Blue Energy

The Canadian based commercial company has a modular design that can be incorporated into a tidal fence or bridge arrangement. The turbine is specified to full-scale of 10 m diameter with a power output up to 0.62 MW in 3 ms^{-1} flow. As can be seen in Figure 1.8 the turbine housing offers ducting to improve the performance of the turbine and the housing also forms the structural component of the bridge configuration. The turbine is mounted top and bottom with vertical bearings, having both the top and bottom bearings rigidly connected will help isolate the gearbox from undesirable loading as they are a common failure mode for vertical axis turbines (Shafiee & Dinmohammadi, 1996). Deployment at 5 kW sacle was completed in Nova Scotia, Canada in 1987, as a surface mounted structure.

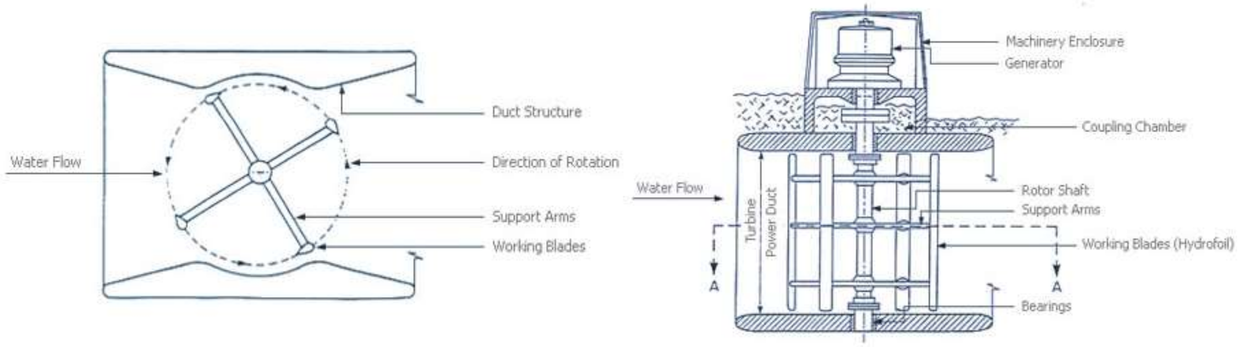

Figure 1.8 Blue Energy Technology Overview (Blue Energy, 2016)

1.3.1.2. *New Energy Corporation*

Another Canadian based company has designed a 7.4 m diameter turbine with 0.25 MW power output in 3 ms^{-1} flow. The turbine is supported at one end through conventional bearings, leading to a high speed generator after passing through the gearbox. In 2011 two medium size turbine (25 kW) systems were installed in India. The significant cantilever loading that the bearings and potentially gearbox will experience is a concern for this drive-train. However its modular nature and surface mounted design make access to these components simpler for maintenance. The project provides power to the local grid, Figure 1.9 shows the device installed in plane.

Figure 1.9 New Energy Cooperation Chilla Canal, India (New Energy Cooperation, 2011)

1.3.2. Transverse Horizontal Axis Tidal Turbines (THATT)

This technology is similar to that of the vertical axis turbine with the same rotor design options. The Gorlov style rotor has been developed primarily by Oxford University as a competitive second generation tidal stream turbine. The technology makes use of the greater cross-sectional area being rectangular to occupy the tidal site. The design can also increase power extraction through optimising the blockage ratio to its advantage (McAdams, 2012).

1.3.2.1. Kepler Energy

The technology has been commercially undertaken by developer; Kepler Energy based in the UK. Current plans are to deploy a 30 MW tidal fence by 2025 in the Bristol Channel, UK (Kepler Energy - Press Release, 2016). A single rotor of diameter 10 m and length 120 m is expected to produce 5.2 MW of power at 2.5 ms^{-1} flow. Development has consisted of numerical modelling and validation using a 1:20th scale model in a flume in Newcastle University (McAdams, et al., 2013). An artistic impression of the device can be found in Figure 1.10.

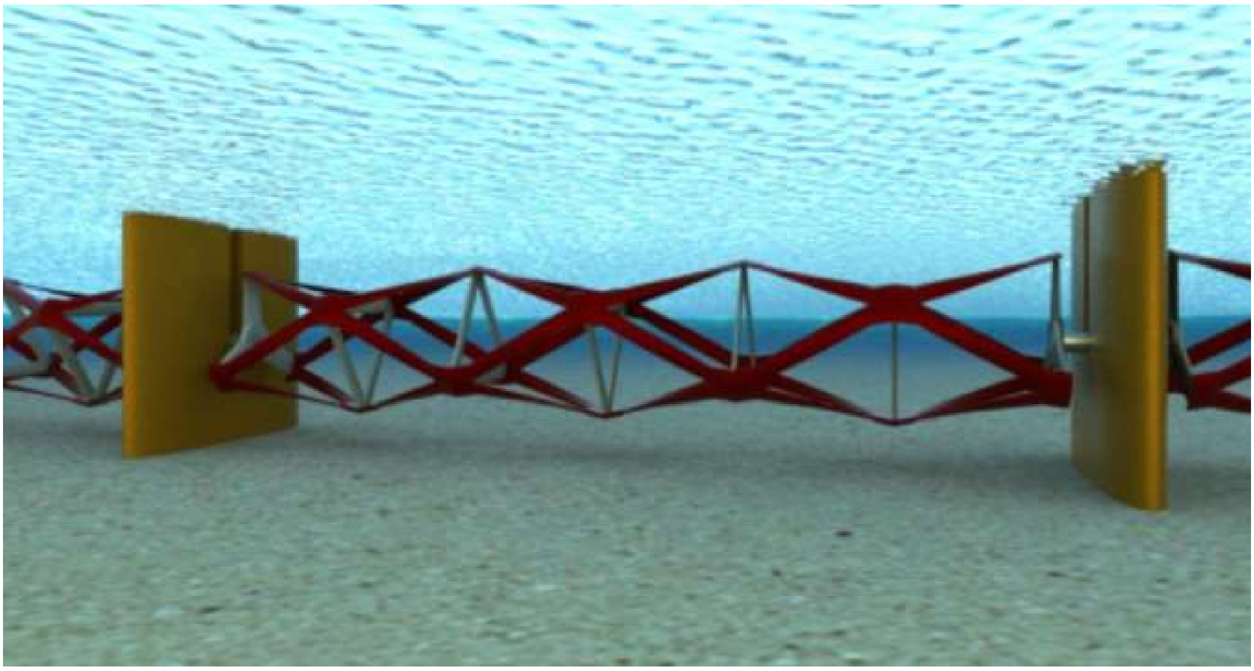

Figure 1.10 Kepler Energy Concept Inmage (Kepler Energy - Press Release, 2016)

1.3.2.2. Hydrovolts Inc

An American based company has made use the Savonius style rotor with up to a 1.5 m rotor diameter and 3 m long area, producing 12.5 kW of power in 3 ms^{-1} flow. This device is significantly smaller and is designed as a site delivered standard solution requiring minimal site preparation. Figure 1.11 shows the main designs major components. A demonstration project in 2012 deployed a 5 kW device for over a year, operating for 11 months of the year. Providing power to charge a battery bank.

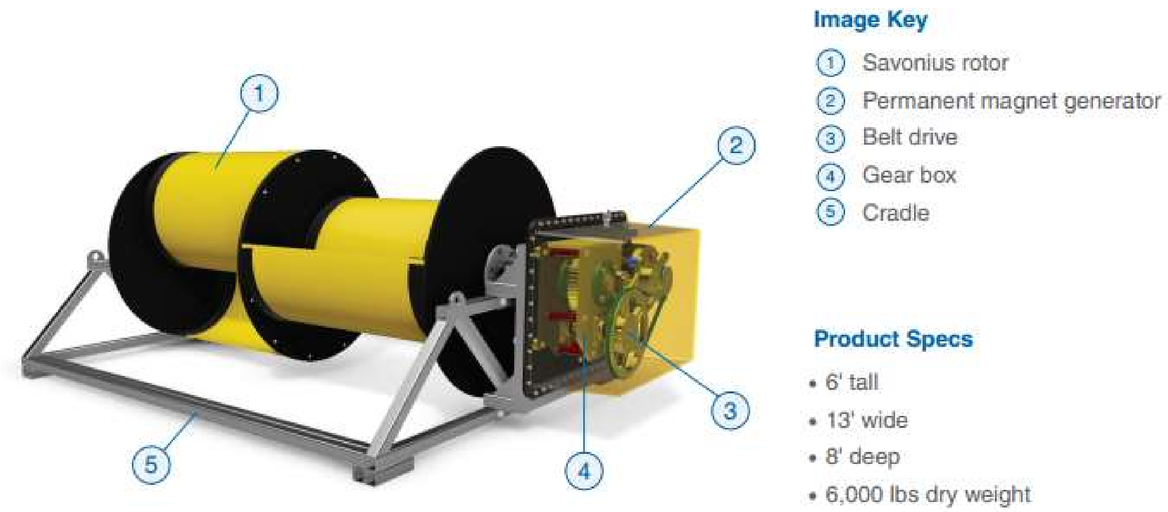

Figure 1.11 Hydrovolts Inc Canal Turbine Design (Hydrovolts Inc, 2012)

1.3.3. Horizontal Axis Tidal Turbines (HATT)

The wind industry which is recognised as being ahead of the tidal sector by a number of years has converged on the horizontal axis turbine as being the optimal solution for large scale deployments this is evident by the 2 GW of horizontal axis wind turbines, installed in the UK in 2014/15, and £1.25 billion invested (RenewableUK, 2015). This has supported the tidal sector in increasing the research knowledge in the common attributes of these devices. A sample of the approaches by commercial developers in applying these technologies to the tidal energy sector is given here.

1.3.3.1. Tidal Energy Limited

Tidal Energy Limited (TEL) are the innovators of the DeltaStream device. The device as suggested by the name hosts three turbines in a triangle formation, the frame forms a gravity base from a flooded tubular structure with an independent horizontal axis turbine set at each of the corners as can be seen in Figure 1.12 a). Each turbine is seated on a space-frame support structure and 210° yaw drive which enables the turbine to face into the ebb and flood tides. A 12 month full-scale deployment in Welsh waters successfully completed during December 2015, in Ramsey Sound, Pembrokeshire consisted of a single turbine mounted on a third of the delta frame as Figure 1.12 b) shows. The 400 kW device is connected to the shore where the power is currently dissipated. Future work include plans for an array of 10 DeltaStream units off the coast of St Davids Head, Wales (Tidal Energy Ltd, 2016).

Figure 1.12 Tidal Energy Limited a) DeltaStream concept b) Full-scale tubine demonstration (Tidal Energy Ltd, 2016)

1.3.3.2. *Alstom Ocean Energy*

Previously Tidal Generation Ltd (TGL) has been developing its technology since 2005 with numerous tests performed on iterations of its 500kW design in various waters. The devices features a floatable nacelle which is pulled down onto a freely pivoting support structure, at the opposite end of the nacelle to the turbine a thrust motor is featured. This motor is driven in order to pivot the turbine into the ebb and flood flow, then a locking mechanism activated to hold it in place. In 2013 TGL became Alstom Ocean Energy, and trials began on a commercial scale 1MW prototype turbine at EMEC, Orkney. The deployment of the turbine can be seen in Figure 1.13 at the beginning of its 18 month trial period. Alstom Ocean Energy now plan a grid-connected commercial array deployment of four turbines in the Isle of Islay.

Figure 1.13 Deployment of Alstom Ocean Energy 1 MW device at EMEC (Alstom Ocean Energy, 2013)

1.3.3.3. *Sustainable Marine Energy (SME)*

The Isle of Wight Company in the UK is a turbine platform developer which has partnered with marine propulsion experts Schottel hydro to produce the PLAT-O tidal turbine platform. The platform in its current form hosts 2 Schottels Instream Turbines, SIT which are rated to produce between 54 kW and 70 kW each, depending on configuration (Schottel, 2016). The PLAT-O platform is rated to 100 kW and is suspended in the mid-water column. The buoyant support structure is in turn tethered to the seabed and also offers some ducting for the turbine increasing performance. The demonstration of the PLAT-O device, as seen in Figure 1.14 is planned for deployment in 2016 at EMEC and will be grid connected. The platform does not feature any yaw mechanism and the turbines are supported by profiled stanchions which allow the turbine to be rotated through 180° to face flood or ebb tides.

Figure 1.14 Sustainable marine energy's PLAT-O demonstration device (Sustainable Marine Energy, 2016)

1.3.3.4. Open Hydro

The Open Hydro have an open-centred turbine with a ducted support structure. The device is designed to be a housed on a gravity based structure ultimately as shown in Figure 1.15 a). The turbine blades are symmetrical making it a bi-directional turbine. The test platform installed at EMEC in 2006 featured twin monopiles with surface piercing stanchions which facilitated maintenance and device development and retrieval as shown in Figure 1.15 b). Open hydro have since begun operations in the Bay of Fundy, Nova Scotia for a 4 MW array planned for 2016 (Cape Sharp Tidal, 2015).

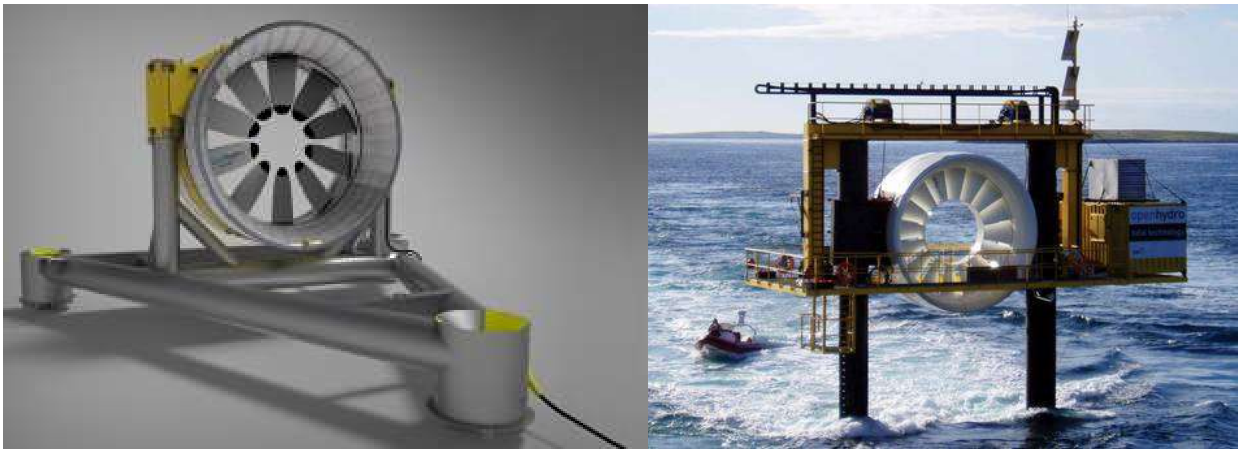

Figure 1.15 Open Hydro a) Full system concept b) EMEC deployment (European Marine Energy Centre, 2016)

1.3.4. Misc. Tidal Turbines

1.3.4.1. Nautricity

The spin-out company from Strathclyde University, Scotland has developed the Counter Rotating Marine Turbine, CoRMaT device as shown in Figure 1.16 a). The device features co-axial rotors connected to the generators stator and rotor. This configuration provides two primary benefits; the first being the increased differential rotation in the generator improving performance at lower flow velocities. The second when considered with the devices inherent buoyancy is the simplicity of its support structure. As the device has a neutral torque about its rotational axis, it can be tethered mid water column without a rigid frame as demonstrated by Figure 1.16 b) (European Marine Energy Centre, 2016) and making deployment in water depth up to 500m possible (Nautricity, 2013). Full-scale turbine testing of the 10m diameter, rated to 1 MW has been performed at EMEC in 2013 with grid connection and power conditioning (Nautricity, 2013).

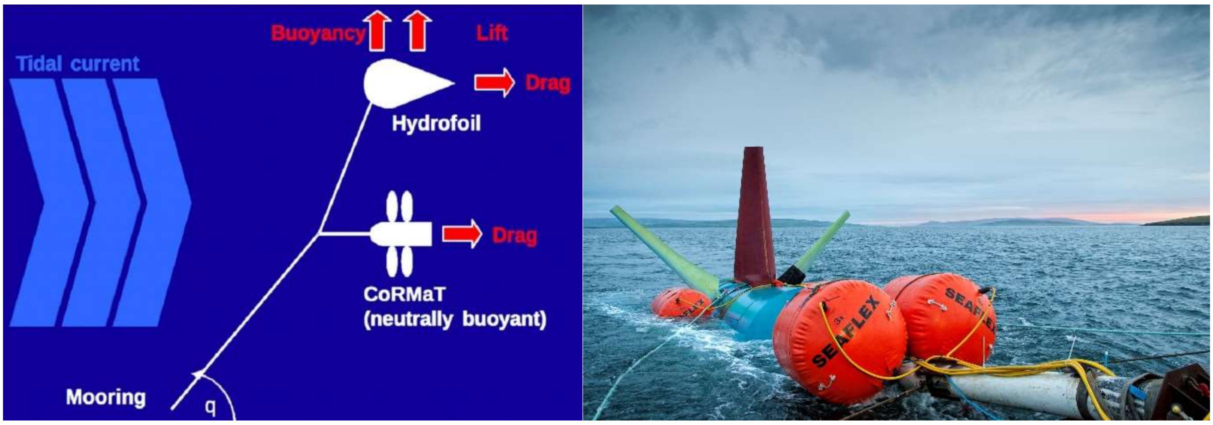

Figure 1.16 a) CoRMaT mooring arrangement b) EMEC testing at full-scale (Strathclyde University, 2013)

1.3.4.2. Minesto

The deep green device produced by Swedish company Minesto is a tidal kite. Designed to maximise output in deeper waters with lower flow speeds the tidal kite creates an artificial velocity 10 times greater than the surrounding flow, as it glides through the water. The power is extracted by a small ducted turbine which is mounted on the nose of the kite as seen in Figure 1.17 a). The full scale device has a 12m wing span and a turbine rated to 500 kW. Figure 1.17 b) shows the current testing features a 3m wingspan and has been operating in the Strangford Narrows, Northern Ireland. The kite follows a figure of eight configuration through the water during operation. Sweeping through the optimal portion of the water column. Full scale deployment of the deep green is planned for 2017 off the coast of Holyhead, Wales. The array will have a grid connected capacity of 10 MW.

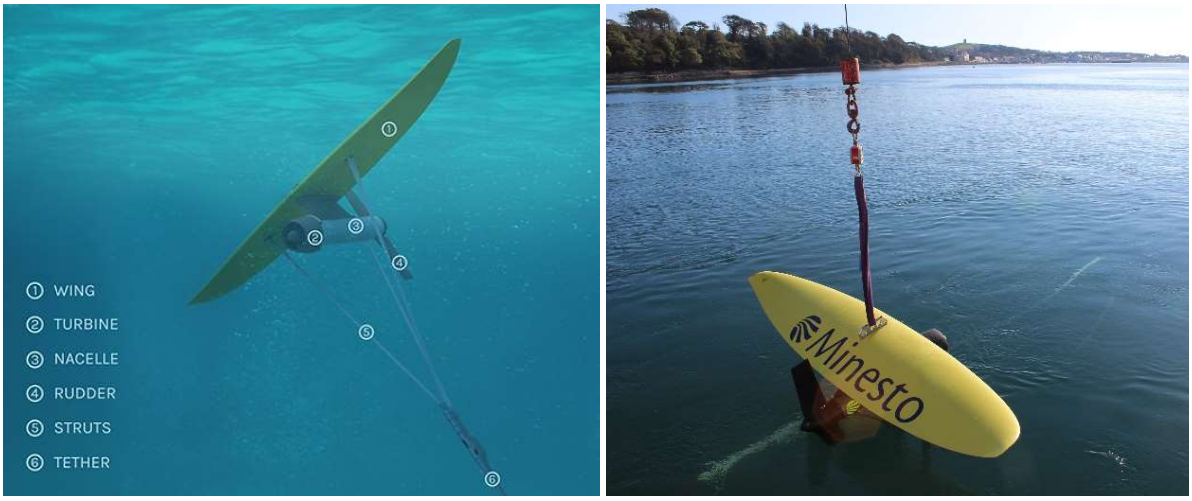

Figure 1.17 a) Minesto deep green device (Minesto, 2016) b) Quarter scale testing at Strangford, NI (Jannson, n.d.)

1.4. Tidal Stream Projects

The tidal stream technology is reaching commercialisation, with a number of projects being developed with private investment. Many of these projects are demonstration projects with single devices/ platforms being installed, whilst others are multi-device arrays using technologies already proven. A summary of projects underway are detailed in this section.

1.4.1. MeyGen Project, UK

The MeyGen project is one of the largest consented tidal arrays world-wide (MeyGen, 2015). The consenting currently grant 86 turbines, corresponding to 86 MW of output. The consenting area in the Pentland Firth, UK can be seen in Figure 1.18. The Island of Stroma and North coast of the Scottish mainland act to accelerate local flow through across the scoured bedrock of the ‘inner sound’ to velocities of 5 ms^{-1}.

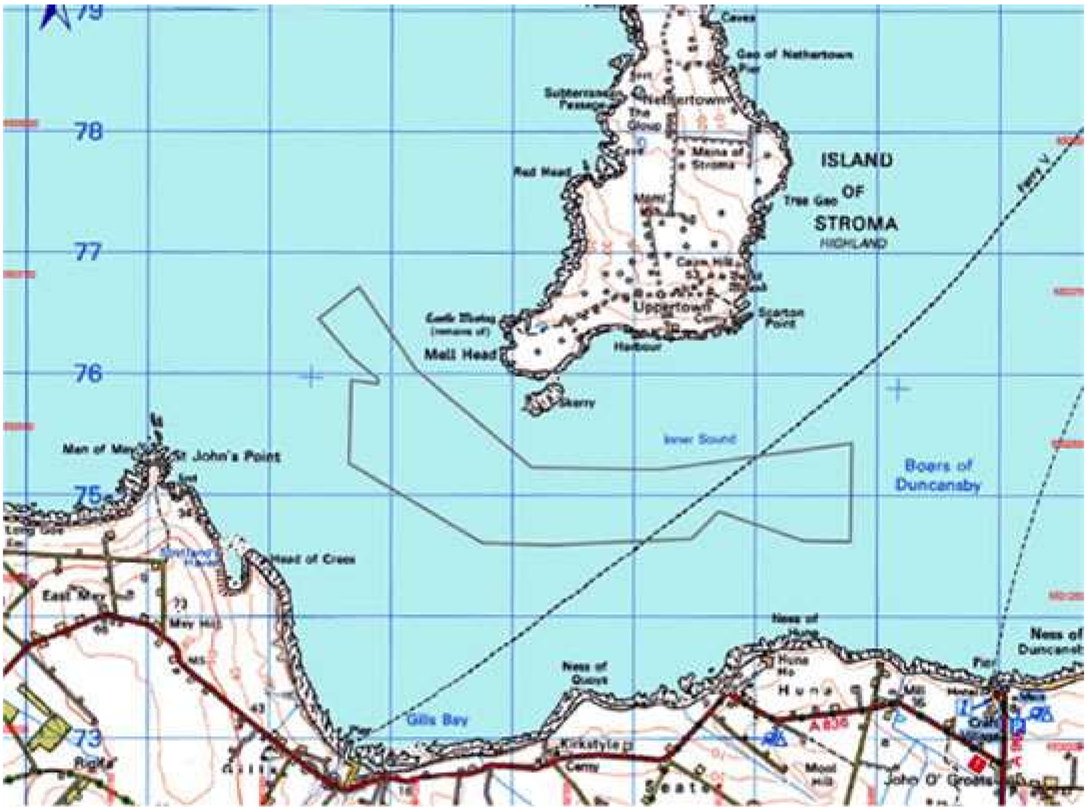

Figure 1.18 MeyGen Lease area Pentland Firth, UK (MeyGen, 2015)

The project is in phase 1A currently and the first turbine, an Andritz Hydro Hammerfest 1.5 MW device device, has been full installed and commissioned. Three Atlantis AR1500 devices are yet to be installed as part of phase 1A (Tidal Energy Today, 2016).

1.4.2. Cape Sharp Tidal, Canada

The OpenHydro and Emera Inc. project has recently deployed its first device in the Cape Sharp Project in the Bay of Fundy, Canada. Figure 1.19 shows the device during the deployment process. The current phase of the project plans to grid-connect 4 MW of tidal energy. Subject to planning consent the second phase will see capacity grow to 16 MW by 2017 and 50 MW by 2019 (Cape Sharp Tidal, 2015). The 73 m deep site experiences tidal flows greater than 5.5 ms^{-1} making it one of the most energetic sites globally.

Figure 1.19 OpenHydro 2 MW device deployment, Cape Sharp (Cape Sharp Tidal, 2016)

1.4.3. Brims Tidal Array, UK

The Brims Tidal Array is a venture between OpenHydro and SSE (Scottish and Southern Energy) which will feature a 200 MW array off the south coast of the Orkney island of Hoy (Rocks, 2016). The two phase project proposes 60 MW capacity installed by 2020 at a cost of £700 million for phase 1 and a further 140 MW at the same cost with an unconfirmed completion date (4C Offshore, 2016). The projects is expected to use the same technology as being deployed in Cape Sharp, as described in 1.4.2.

1.4.4. Holyhead Deep, UK

The project is based in Welsh water off the west coast of Anglesey. The deployment site features 80-100 m depths and 1.5 ms^{-1} flows, making it ideal for a Minesto 'Deep Green' installation. In June 2014 Minesto secured a leasing agreement and through regional funds have begun operations for the first installation. Planned for summer 2017 the first phase will feature 0.5 MW single device deployment. This will shortly be followed by two more devices increasing capacity of the array to 1.5 MW (Minesto, 2016).

1.4.5. Blackrock Demonstration, Canada

The Schottel Hydro subsidiary is collaborating with Fundy Ocean Research Center for Energy (FORCE) to deliver the Triton platform (Black Rock Tidal Power, 2016). The 2.5 MW capacity platform which will feature 40 SIT250 devices, manufactured by Schottel Hydro. Fabrication work has begun on the superstructure, as seen in Figure 1.20, and planned deployment is within 2017.

Figure 1.20 Fabrication of Verical Spars by Aecon Atlantic Industrial Inc. (Black Rock Tidal Power, 2016)

1.5. Summary of Tidal Stream Sector

The tidal stream industry is currently operating in the pre-commercial phase, with commercial developers operating at the technology readiness level of 6 or 7 (NASA, n.d.) with subsystem and full system deployed in tidal sites. As demonstrated in the section 1.3 many devices have been proven at full-scale prototype stage in sites such as EMEC, Scotland and Nova-Scotia, Canada. The sector is now concentrating on array scale deployments as identified by the planned projects identified in section 1.4. Large scale deployments will drive down the cost per of energy (£/MWh) increasing the competitiveness of tidal energy to other renewable technologies. Figure 1.3 in section 1.1.2 shows the £/MWh of technologies in 2012, the offshore wind sector (which has a cost of between £118/MWh and £133/MWh) is seen as the benchmark for establishing tidal energy as a competitive alternative. Recognising that advances in the offshore wind sector and established supply chain is going to bring the cost of energy down it is still expected that tidal stream energy can be competitive with a £100/MWh - £200/MWh expected to be obtained by 2020 (Energy Technologies Institute , 2015). The same report suggests up to a third of the cost of the energy will come from operation and maintenance.

It is important therefore to accurately predict the performance of tidal stream turbines and identify scenarios detrimental to turbine performance in order to further establish its commercial potential by inform the industry. From the devices shown in section 1.3 it is important to note the HATT devices are the dominant design with EMEC showing 42.5% of its tidal turbine device developers to have a HATT type device (European Marine Energy Centre, 2016). HATT developers can be separated into two primary design categories. Those devices which operates bi-directionally or devices that can yaw to face the flow. This design choice is a significant consideration as both options create detrimental operational scenarios such as support structure interaction or flow misalignment. Both will reduce performance and increase operational and maintenance costs. As such, the focus of this work investigates the performance of a tidal stream turbine under adverse operational conditions in order to determine detrimental performance characteristics and establish a criteria from which tidal developers can make critical design choices regarding turbine directionality, misalignment and numerical modelling short comings.

1.6. Thesis Layout

Chapter 1:	Introduces the drivers for research into tidal energy and the current status of the sector
Chapter 2:	Reviews the relevant literature, outlining the status of research in the marine energy and wind sector, to identify the knowledge gaps for this research.
Chapter 3:	Presents the applicable theory used to model the turbine and assess its hydrodynamic performance.
Chapter 4:	Describes the numerical methodology used to apply the theory presented in Chapter 3 to generate the CFD simulations.
Chapter 5:	Presents and discusses the performance characteristics of the turbine for various proximities between the turbine and support structure in an upstream and downstream configuration.
Chapter 6:	Presents and discusses the performance characteristics of the turbine for various angles of misalignment between the turbine and free stream velocity.
Chapter 7:	Explains the experimental methodology used to gather data from laboratory scale test and post processing procedure.

Chapter 8: Presents the experimental results from the laboratory scale test and discusses the experimental and numerical validation.

Chapter 9: Summarises the main conclusions from the work and the implications to the industry. Also makes recommendations for further work.

2. Literature Review

The critical review of relevant literature has been undertaken in this section in order to assist in developing the research envelope and outline past research relevant to this work. The review establishes which variables will be parameterised in order to establish their relation to the performance characteristics of a tidal stream turbine. A review of numerical modelling methods used in tidal stream turbine devices, and experimental studies on tidal stream turbines is also critically assessed in order to place this work in the context of previous research.

2.1. Numerical Modelling of Tidal Stream Turbines

Both numerical and experimental approaches have been conducted on devices and environmental conditions in the tidal energy sector. This section considers the research undertaken into tidal stream turbines using the former approach. A brief description of the technique and application used with respect to tidal stream turbines has been performed.

2.1.1. Actuator Disk Theory/ Betz Model

The actuator disk theory considers the swept area of a turbine as an infinitely thin disk. The theory makes the assumption that the flow is incompressible and mass is conserved through the system. The theory uses the axial induction factor (a) formed from the free stream velocity and velocity at the rotor. The theory enables the thrust on the disc to be calculated. Given the conservation of mass the change in kinetic energy upstream and downstream enables the power of a rotor to be calculated. The Betz model shows the maximum rotor performance is achieved when $a = 1/3$. This is known as the Betz limit and gives rise to a maximum Coefficient of Power, $C_P = 0.593$ (Ragheb & Ragheb, 2011).

The theory is used in the wind sector and has been applied to the tidal stream turbine designs. Work by Cambridge University (Whelan, et al., 2009) into a blockage correction method for the actuator disc theory has been used to show performance of a linear array with in shallow water, i.e. close proximity between the seabed and surface. The correction is made to the axial induction factor and is also applicable to the blade element momentum theory as discussed later in this thesis. The limitations established were applied to high Tip Speed Ratio (λ) cases which deviated from experimental results.

2.1.2. Blade Element Momentum Theory

The Blade Element Momentum Theory (BEMT) was developed from the wind industry (Manwell, et al., 2009). It combines the momentum theory with the blade element theory. The momentum theory builds upon the actuator disk theory by including angular momentum as well as the axial momentum. The addition of the angular momentum removes the assumption of the turbine acting as a disk and takes into consideration the rotational factors of the rotor improving the accuracy of the results. It also leads to other adaptations such as tip and hub losses which account for inefficiencies in performance of the rotor blades.

Studies by Southampton University have shown agreement within 5-15% between the BEMT code and experimental validation. Deviation between the C_P and C_T in experimental results and numerical predictions is consistently seen at the higher TSR, with the numerical models over predicting the power performance and under predicting the thrust performance in comparison to experimental results (Batten, et al., 2007). More recent work has quantified wave and yaw effects using BEMT (Galloway, et al., 2014). The complications of these dynamic scenarios limits the accuracy of the results by increases the error in the code. The 'skewed axial inflow correction' used in the work is highly dependent on the blade's rotational position (azimuth) and turbine performance was hampered with the inclusion of a wave climate. Further consideration of this work is undertaken in Section 0.

Work performed by Garrad Hassan (Bossanyi, 1997) on the dynamic inflow condition for BEMT models has been utilised by Strathclyde University to analyse the sensitivity of blade loading on TST in response to various geometric parameters (Nevalainen, et al., 2016). The Morris method of weighing the parameters effect on performance showed the turbine thrust loading varied significantly with changes to blade root pitch. The root pitch was varied by a range of ±5° relative to optimum pitch angle. Increasing the blade pitch, increased the eccentricity in the thrust loading. Other parameters considered include inflow variables including flow misalignment.

By coupling a BEMT code with Computational Fluid Dynamics (CFD), Swansea University (Malki, et al., 2013), aimed to maintain the computational efficiency of the BEMT code whilst enabling the wake of TST to be analysed. The CFD coupling enables the wake recovery of the turbine to be obtained. The findings of further work by Swansea University showed large wake recovery distances, up to 16.5 Diameters downstream of the turbine for 75% wake recovery. The relative performance of a turbine with a downstream stanchion or no stanchion was found to be 1.2% lower due to stanchion interaction. Whilst these results are noteworthy the published work did not show comparison to experimental results (Edmunds, et al., 2014). Other studies performed by Swansea showed the benefits of contra-rotating turbines in close proximity improving performance of a downstream device as the blockage ratio increased from 0.13 to 0.20 (Edmunds, et al., 2014).

2.1.3. Computational Fluid Dynamics

Computational Fluid Dynamics (CFD) differs to the previously mentioned techniques as it resolves the entire fluid flow field rather than the forces on the turbine alone. It is diversely used in the petrochemical and aerospace industries. The Navier-Stokes equations form the basis for the majority of CFD models, which generally assumes the fluid is Newtonian, though non-Newtonian fluid models are also available. Various CFD models are created depending on which terms in the Navier-Stokes are considered important. Ignoring the viscous terms yields the Euler equations, however for tidal stream turbine applications this is of limited benefit. More appropriate methods such as the Reynolds Averaged Navier-Stokes (RANS) include viscous models specific to solving the boundary conditions. In this instances those related to the surface of the turbine and its blades. The theory behind CFD will be considered in further detail in Chapter 2.6.

The commercial package StarCCM+ has been employed by Manchester University (Olczak, et al., 2016) in the resolving of RANS models for modelling the wake of an array of turbines. The work predicted the thrust performance of rotors in comparison to small scale experimental work. The work assessed an array of turbines in a 12 x 3 lattice, spaced such that the turbines downstream benefited from the acceleration around the upstream turbines. Predictions of the numerical model were within 20% for the second row of turbines and 38% for the third row of turbines. The work showed significant shortcomings in the software when relating to experimental results.

CFD models have been analysed by Cardiff university using the commercial package ANSYS FLUENT. This was used to study the performance of tidal stream turbines in a high shear profile (O'DOherty, et al., 2010). The paper uses velocity profiles taken from measurements of the Severn Estuary and the Anglesey Skerries. The input to the CFD model came from the 1/7th power law scaled to the average economically viable velocity over the swept area of the turbine. The work showed the significance of scaling laws in consideration of tidal energy sites and provided a comparative case study between two sites. Using this method a 30-40% difference in power is achievable between the realistic locations of a turbine in the water column. The study did not consider wave interaction near the surface as these sites were deemed first generation test sites with insignificant wave climates. Further work was recognised in considering surface interactions from waves.

Additional CFD work performed by Cardiff University into characterising the wake performance of a turbine has been performed more recently (Morris, 2014). The study initially identified the performance differences of a turbine when an increase in the solidity of the rotor is made. This resulted in an increase in the peak power and torque performances. The swirl characteristics of the wake were found to dependent on solidity up to 10 diameters downstream (Morris, 2014). This work was validated through experimental testing which is considered in more detail in section 2.2.1. The work by Morris (2014) continues into Fluid-Solid Interaction

(FSI) analysis of turbine blades, via a series of coupled quasi-static CFD and FEA models. It found the turbine performance decreased with excessive deflections at the tip of the blade. However performance of the turbine blade was seen to increase with slight deflections, and this was accounted for by the blade deforming into an optimal pitch angle (Morris, 2014). The FSI study performed by Morris, was furthered developed into a full two-way transient coupling in ANSYS CFX and Mechanical which resulted in the same performance increase on the rotors power being identified (Tatum , et al., 2015).

Seoul National University in South Korea have made advances in the application of Fluid-Solid Interaction to discover the effects of loading on tidal turbine blade performance (Park, et al., 2013). This work at a preliminary stage and has been compared with experimental work by Southampton University (Batten, et al., 2007). The blade deflection showed a drop in performance and conclusions highlighted the need for further consideration to blade design. The benefits of such modelling techniques are important and future work in this area will be important.

2.2. Experimental Testing

Experimental work is currently supported by the research community through primarily small scale devices at Technology Readiness Levels (TRL) 4-5 which correlates with laboratory testing and simulated operational environment (Day, et al., 2015). An assessment of existing laboratory tests conducted on scale HATT devices will put the work conducted in this research into context relative to past, and current research being undertaken. Consideration of the device scale, sub-system components and operating procedure, in addition to the instruments and testing facility used, will now be discussed in further detail below, for flume, towing tank and coastal experiments.

2.2.1. Flume Experiments

The use of re-circulating flumes offers advantages, as the inlet conditions can be varied in velocity and turbulence, and the use of a variety of flow straighteners have been demonstrated to vary the turbulence entering the working area. Additional customisations to flumes, relevant to tidal stream turbines, includes flow profilers which introduce a velocity shear profile through the working section (Tedds, et al., 2011). The benefit of testing in a flume include unlimited operational periods for testing system components for extended periods and repeating flow point measurements throughout the wake of a device (Tedds, et al., 2011). Many flumes include wave generation capacity, and wave current interaction is important to tidal stream turbine performance (Gaurier, et al., 2013). However the working area of flumes needs to be considered as it offers limitation, including high blockage ratio in the case of limited cross-sectional area, and/or the downstream wake capture area (Gaurier, et al., 2015).

Collaboration between Cardiff University and Liverpool University has facilitated the testing of a 1:20th scale turbine developed by Cardiff Marine Energy Research Group (CMERG) at the University of Liverpool's recirculating Flume. The 0.5 m diameter rotor was designed to accommodate the 2, 3 or 4 blades, to study the effects of changing solidity on swirl, in the wake of a turbine (Mason-Jones, et al., 2012; Tedds, et al., 2011; Morris, 2014). Figure 2.1 shows the turbine installed at Liverpool University. A Baldor brushless AC servomotor featured as the turbines alternator. It was driven by a control system which could incrementally increase the Torque Generating Current (TGC). This allowed the resistive torque of the alternator to be increased in order to obtain the corresponding rotational velocities for the turbine through an encoder feedback, hence obtaining the non-dimensional performance curves for torque and power. The thrust applied to the complete set-up was calculated from a load cell mounted at the top of the support structure, out of the water. This set up provided a good noise to signal ratio in the data sets (Morris, 2014). The pin and grub screw blade attachment allowed flexibility for different blade designs as well as various angles of attack to be set during set-up. The turbine reached the highest rotational velocities feasible at 1 ms^{-1} fluid flow. The experimental work showed that although there was a little power performance increase with increasing solidity, and there was a significant increase in the thrust (Mason-Jones, et al., 2012). The turbine wake length was found to be effected by solidity also. These results were used to validate CFD results (Tedds, et al., 2011; Morris, 2014).

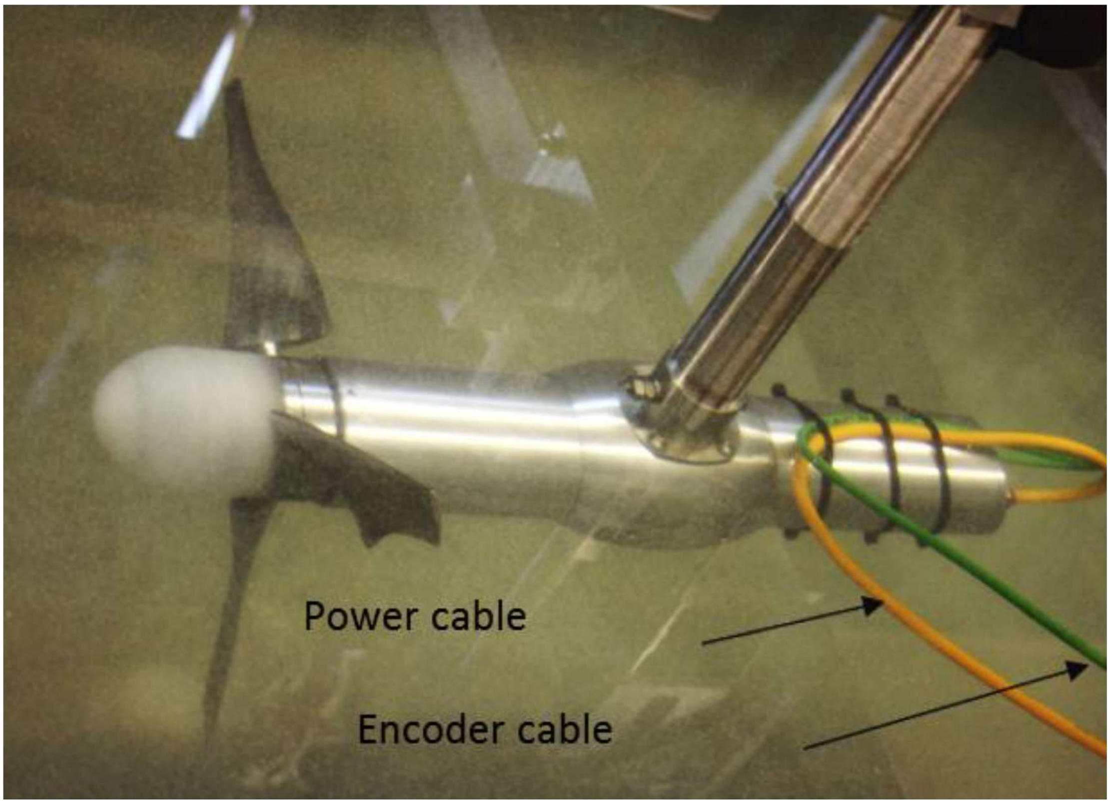

Figure 2.1 CMERG first generation Turbine (Morris, 2014)

In the work by Tedds et al (2011) and Morris (2014) significant shortcomings of the turbine were identified and can be seen in Figure 2.2. The figure shows the C_P performance of the rotor with error bound of ±1% in the ADV inflow instrument. The turbine instrumentation could only capture the performance of the turbine at rotational speeds after peak power performance was achieved. This was due to the alternator capacity, as the resistive torque approached peak power and peak torque, the TGC approached the alternators limit (3.6 A). This is turn overheated the alternator causing a shut-down to protect insulation on the windings of the alternator. The low sampling frequency of 0.92 Hz was also noted as being too low to obtain a meaningful amount of data points during a single rotation.

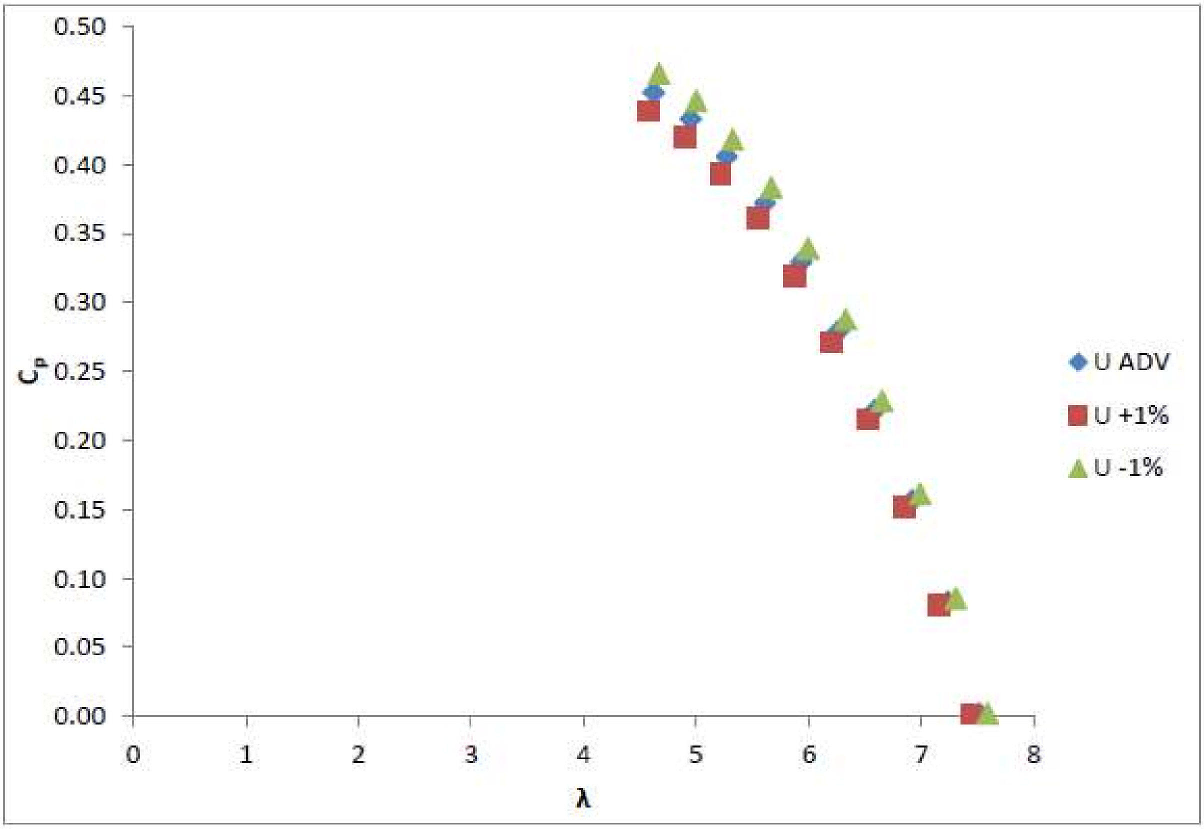

Figure 2.2 CP - λ for 2nd generation CMERG turbine (Morris, 2014)

A schematic of the Liverpool Universities re-circulating flume can be seen in Figure 2.3. The cross-sectional area of the work section is 1.4 m in width and 0.8 m in depth and has a length of 3.7 m. With a 0.5m diameter experimental turbine in the working section, the flume had a blockage ratio of 17.5%. As the blockage ratios is above the correctional threshold established (Whelan, et al., 2009) the results had to be post-processed to correct for this. The flume has flow straighteners which reduce the turbulence intensity in the working section to 5% (Tedds, et al., 2011). The facility uses an Acoustic Doppler Velocimetry (ADV) to record the flow velocity in the three co-ordinate axis. The accuracy of the data recorded with the ADV device was identified to be ±5% accurate for the resultant velocity (Tedds, et al., 2011).

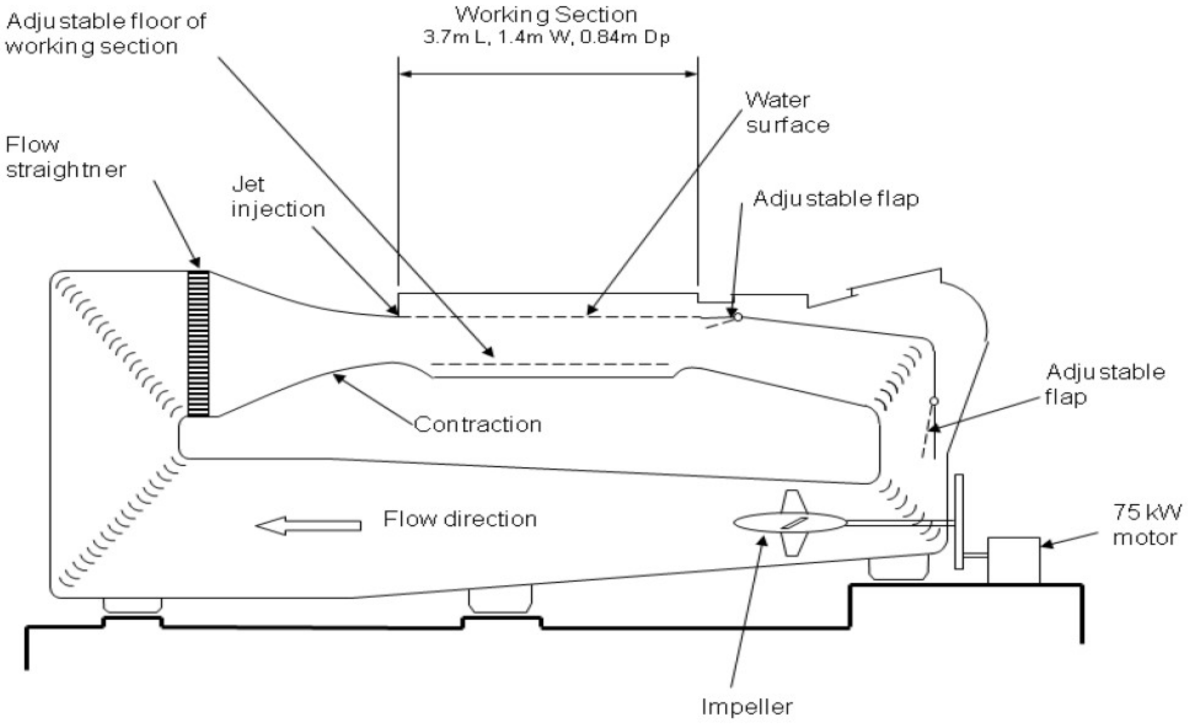

Figure 2.3 Liverpool universities re-circulating flume schematic (Tedds, et al., 2011)

Given these issues outlined above, the recirculating flume at Liverpool University offered testing for various geometrical set-ups. The constant proximity to the device and instruments during testing enabled quick adjustments, such as the number of blades and blade pitch angle, as well as the location of the ADV in order to capture the wake.

Another study undertaken by Sheffield university on a 1:143rd and 1:72nd scale experimental turbine was conducted in a water channel (Walker, et al., 2015). The turbine, being only 24 mm in diameter, was 3D printed using a laser sintering technique and featured four different support structures. The plastic rotor was driven by a current controlled 12 V motor drive with an infrared rotary encoder to record speed and rotational position. The set-up can be seen in Figure 2.4. The power of the turbine was ascertained by subtracting the power supplied to rotate the turbine at a known rotational speed with blades from the same case without blades present, in order to account for losses in the system. This provides the power contributed by the rotor blades, assuming losses in the system remain the same, with and without the blades (Walker, 2014). The error reported for the turbine torque and power measurements in the setup was reported as 11% (Walker, 2014).

The device is at a Technology Readiness Level, TRL of 3 as it is only a test of a sub-system of the full scale device, at a small scale.

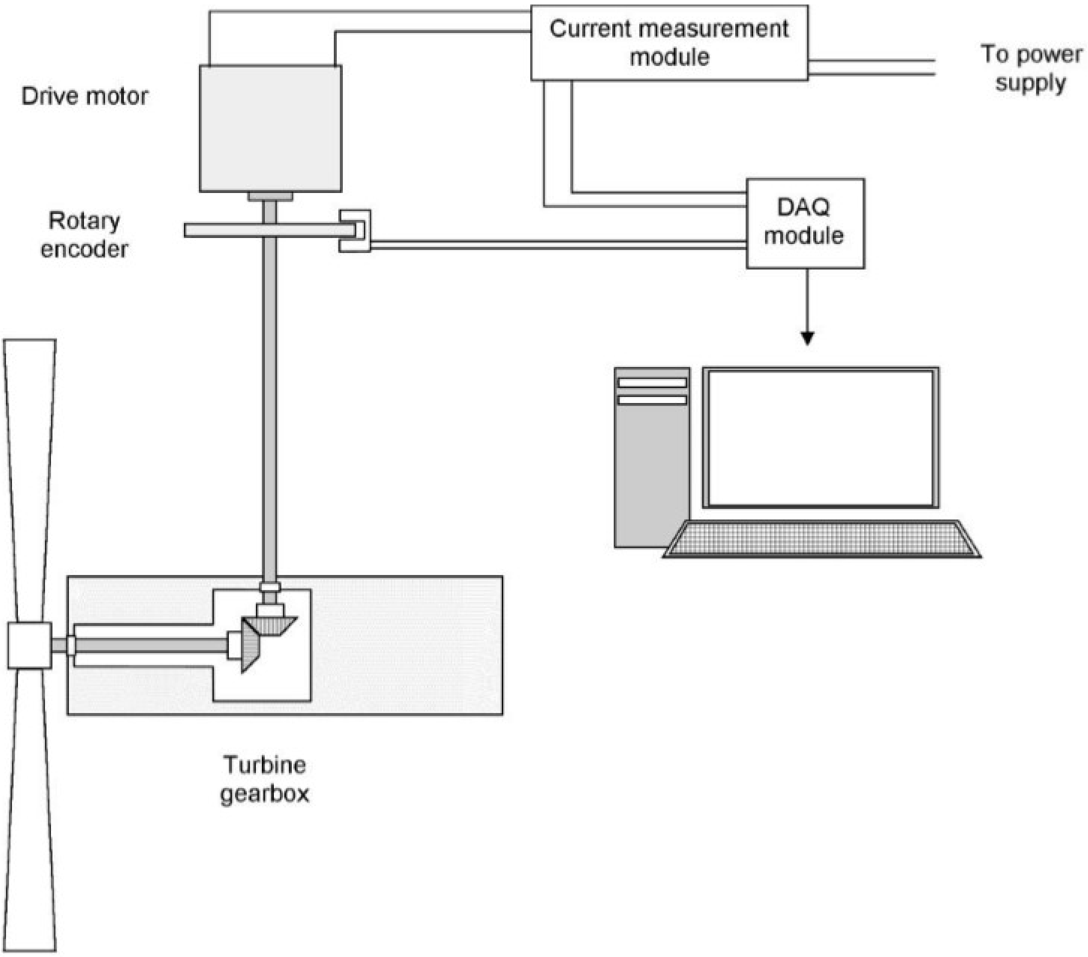

Figure 2.4 Experimental set-up of a 1:143rd scale turbine (Walker, 2014)

The facility used at Sheffield University was an 18 m long water channel with a cross-section of 0.5 x 0.6 m and a maximum velocity of 0.3 ms^{-1}. The blockage ratio was 7% and the turbulence flow measurements were thoroughly undertaken from Acoustic Doppler Velocimetry (ADV), Laser Doppler Velocimetry (LDV) and Particle Image Velocimetry (PIV) instruments. From the PIV flow measurements, errors were reported to be 6%.

The IFREMER Boulogne-sur-Mer flume in France and the CNR-INSEAN flume in Italy have tested the same 0.7 m diameter turbine (Gaurier, et al., 2015). The turbine features a gearbox and DC motor and is driven by a motor speed control unit. A torque meter is featured in the driveshaft behind the rotor, and a force/ moment load cell was mounted on the support structure, similar to the CMERG turbine. The rotational speed was controlled in order to obtain all the points on the performance curves, whilst the flume velocity was fixed for each series of tests at 0.6-1.2 ms^{-1} in increments of 0.2 ms^{-1} (Gaurier, et al., 2015). The flumes have a working section of 18 m and 10m in length for IFERMER and CNR-INSEAN respectively. They have cross-sectional working areas of 4 m width by 2 m depth and 3.6 m by 2.25 m respectively (Gaurier, et al., 2015). The testing was conducted under the FP7 Marinet 'round robin' project. The focus was on comparison of the same device in different facilities and provides a good understanding of the differences which require accounting for in experimental testing.

Further experiments performed at IFERMER undertook analysis of the wake behind a 1/15th scale device (Bahaj & Myers, 2013). The work was compared with a number of 1/20th scale actuator disks. The work found the near-field wake characteristics were highly turbulent with rotational structures generated from the turbine. However the far-field wake recovery was comparable to the actuator disk. It was found at these distances that the recovery was driven by the ambient turbulence and therefore further work with actuator disk arrays is justified.

2.2.2. Tow Tank Experiments

Towing tanks were traditionally established from the naval architecture and marine engineering industry. A typical towing tank facility can be seen in Figure 2.5 with a long tank spanned by a carriage capable of towing experimental apparatus through the water. These types of facilities are ideally designed for the testing of tidal stream turbines as they typically feature larger cross-sectional working areas than flumes. Also the uniform water provides idealised conditions for testing turbines without turbulence (Gaurier, et al., 2015). Most tanks typically feature beaches at either end or wave generating paddles and a beach. The latter setup facilitates super-imposed wave and current interaction. The decoupling of the two has its advantages in isolating the performance affects. However this approach does not simulate a true wave-current system. The limitations of tidal testing include the tank length, which coupled with the testing speed dictates the test period. Additional waiting time for the water to settle between runs can make the process somewhat laboured.

Figure 2.5 Kelvin Hydrodynamics Laboratory Towing Tank (Univeristy of Strathclyde, 2012)

The work performed in Strathclyde Universities Kelvin Hydrodynamics Laboratory (KHL) shown in Figure 2.5 featured a 1:20th scale (or 0.762 m diameter) three blade tidal turbine. The rotor was driven through a 1:10 step gearbox by a motor which was controlled to run at a pre-determined rotational speed. A torque and thrust transducer was located between the turbine rotor and gearbox (Doman, et al., 2015). Each blade also featured a strain gauge to record the root bending moments experienced by the blades. The tank had an operational cross-section of 4.6 m x 2.5 m and is 76 m long. The resulting blockage ratio was 15.8% and the flow speeds tested at ranged from 0.5 ms^{-1} to 1 ms^{-1}. The turbines pre-set rotational velocities curved the full range of TSR for the rotor. The results showed the peak power performance as being, C_P = 0.285 and at 1.00 ms^{-1} carriage velocity. The uncertainty in the power performance ranged from 1.7% to 6.8% and the increase in uncertainty occurred at high TSRs.

As part of the collaborative work the same tidal turbine device was tested in a number of testing facilities including KHL and CNR-INSEAN towing tanks (Gaurier, et al., 2015). The KHL tank has been described above, however the slightly smaller diameter of this turbine (0.7 m) provides a blockage ratio of 13.4% and this is significantly larger than the INSEAN tank which had a cross-sectional area of 9 m x 3.5 m setting a blockage ratio of 4.9%. The Italian facility is also longer at 220m (CNR-INSEAN, 2002). Comparison of the power and thrust performance characteristics between the two facilities found the KHL tank had higher peak performance, C_P = 0.43 and C_T = 1.21. The INSEAN tank had a peak performance of C_P = 0.41 and C_T = 1.16. The high thrust performance and differences between the two facilities were attributed to the blockage effects and by applying a blockage correction (Bahaj, et al., 2007) the peak C_P = 0.42 for the KHL facility and maintained at C_P = 0.41 for the CNR-INSEAN facility. Similarly peak C_T = 1.17 for KHL facility after blockage correction and C_T = 1.16 for CNR-INSEAN after correction. The paper discusses the possible need for blockage correction at high tip speed ratios even for blockage ratios below 5% (Gaurier, et al., 2015).

2.2.3. Coastal Experiments

Experimental work in the real tidal environment provides the benefits of realistic performance results rather than idealised performance seen in controlled environments. The coastal environment enable large scale testing to be possible, and a dependency on local bathymetry boundary affects can be avoided. However in order to benefit from these advantages of testing in the coastal environment, the test equipment must be robustly designed to withstand the hostile marine environment. Additionally flow characterisation becomes essential as it is unpredictable and therefore must be accounted for in the performance characterisation of the turbine (IEC 62600-200, 2012).

The work by Queens University Belfast shows the performance of two 1.5 m diameter tidal stream turbines in pushing tests at Montgomery Lake and moored coastal experiments at Strangford Lough in Northern Ireland (Jeffcoate, et al., 2015; Jeffcoate, et al., 2014). The two turbines were tested in-plane and in-line with one another to study the interaction of turbine arrays. The 1:10th scale devices offered unique insight into performance comparison between steady flow in the lake pushing tests and the unsteady tidal flow. The experiments showed a 30% reduction in electrical power performance at the moored tidal test site relative to the lake pushing tests. Also discussed in the work is the increase in uncertainty in the measurements due to the uncontrolled environment (Jeffcoate, et al., 2014). The work at Strangford lough has continued with full-scale experimentation of the Schottel Hydro device STG50 (Jeffcoate, et al., 2015). The commercial turbine rated to 50 kW produced a time averaged electrical output of 19 kW over the 4 month testing period and with full system efficiency reaching 35%.

2.3. Tidal Stream Resource

A number of attempts have been made to characterise the potential resource in the UK. The more significant contributions to defining the resource began in 1993 with the publication of the 'Tidal Stream Energy Review: UK, 1992-3' a desk study published by Energy Technology Support Unit (ETSU, 1993). The report outlined that there was clearly a large resource (58.0 TWh/yr) available in the UK waters yet the cost of extraction was not competitive at that time to economically justify tidal stream energy schemes. Moving forward to more recent analyses of the UK resource, the Carbon Trust commissioned Black and Veatch to perform a tidal stream resource assessment as well as technical assessments as part of the Marine Energy Challenge. Phase 1 of the report published in 2004, performed a literature review of tidal stream and marine current resources for the UK, Europe & throughout the rest of the world (Black & Veatch, 2004). The report identified the drawbacks of the farm method in 'predicting over-extraction' and introduced a flux method that takes the 'resource availability into account'. The result was a UK total 'technical extractable resource' of approx. 22TWh/y. The report identified that this figure was likely to be the upper limit of the 'technical extractable resource' and would in all likelihood never be fully reached. Phase 2 of the report published in 2005, focused on the accuracy of the findings from the phase 1 report by analysing the top ten influential sites and ‘validating the input data’ used to calculate the resource (Black & Veatch, 2005). This report provides the most complete assessment of the entire UK extractable resource to date. The findings identified many reductions in tidal stream flow speed, with an appreciation for these reductions; the report provided a figure of 18 TWh/y as the technical extractable resource on the continental shelf around the UK. However this report also identified the uncertainties in its calculations, which were determined as approximately +/- 30% for total resource. However with this uncertainty included, around 5% of the UK electricity demand can be met by the UK tidal resource, which as stated ‘can contribute meaningfully to the UK electricity demands’.

The extractable energy from the sites considered was based on device parameters such as system efficiency. However the resource has only been considered as a velocity magnitude and direction has been little considered. It is important to characterise the range of flow directions that occur at potential tidal energy site, as this will set the boundaries for investigating the impact of flow misalignment on a HATT.

2.4. Tidal asymmetry

In order to identify the extent of misalignment likely to occur at tidal sites the resource assessment techniques used can be configured to provide a broad view of the range of angles during ebb and flood flow. It is assumed for the purpose this review in literature a turbine would be installed facing the principle flood or ebb direction. Therefore any asymmetry between the flood and ebb flow will result in a misalignment between the flow and the axis of rotation of the turbine. The characteristics of tidal stream sites are still being ascertained. There is a need for defined directional fluctuations to be identified for yaw control systems and off-axis power projection in the case of a fixed-yaw turbine (Thomson, et al., 2012). Two techniques used to assess flow direction and magnitude over a tidal cycle are numerically and experimentally based. Literature available on both approaches is explored in the section below and the range of flow misalignment for various tidal sites identified.

2.4.1. From Resource Assessment Modelling

Regional Ocean Modelling System (ROMS) is employed by some research centres in assessing the tidal-stream energy resource (Lewis, et al., 2015). It was found that for two sites 3 km apart off the west coast of Anglesey, Wales, there is a 15.1° and 2.4° asymmetry between peak flood and ebb flow, as seen in Figure 2.6. This demonstrates the significant spatial variability of tidal asymmetry and the likely event of flow misalignment to a tidal stream turbine. The work goes on to establish the asymmetry at potential tidal energy sites in the Irish Sea. It is noted that at higher velocity sites (> 3 m/s) such as those identified as 1st generation sites have a median asymmetry of 20° (Lewis, et al., 2015). The 1st generation tidal sites are expected to be in shallower water, up to 40 m depths. It is noticed that for these depths there is a stronger percentage of ‘tidal current misalignment’ according to Lewis et al (Lewis, et al., 2015).

2.4.2. From Acoustic Doppler Current Profiler (ADCP)

The characterising of tidal stream sites is still being understood (Thomson, et al., 2012) however effort to standardise these characteristics has been made (IEC 62600-200, 2012). This standard was set in an effort to conform the method of ascertaining the flow characteristics of a site and thus predicting the resource as well as inform device developers of conditions required in the design considerations. The standard currently requires the tidal ellipse and principle flood and ebb flow directions to be reported as shown in Figure 2.7. Vessel mounted or bottom mounted ADCP devices are acceptable for collecting data, according to the standard. However directional heading must be obtained through a calibrated gyroscope such as a heading input or internal calibrated compasses for directional heading relative to the ADCP orientation (IEC 62600-200, 2012). An example this approach would be the vessel mounted ADCP used to determine the flow characteristics at Ramsey Sound in Pembrokeshire (Fairley, et al., 2013). The results found a 2° and 15° mean asymmetry between the flood and ebb tides for different transects taken in the sound. Whilst the analysis of these results are not presented in accordance with the IEC standard, they provide a valid example of asymmetry using the standard’s approach for headings. Example polar plots found using modelling and collected data can be seen in Figure 2.6 and Figure 2.7 as well as other sources (Iyer, et al., 2013).

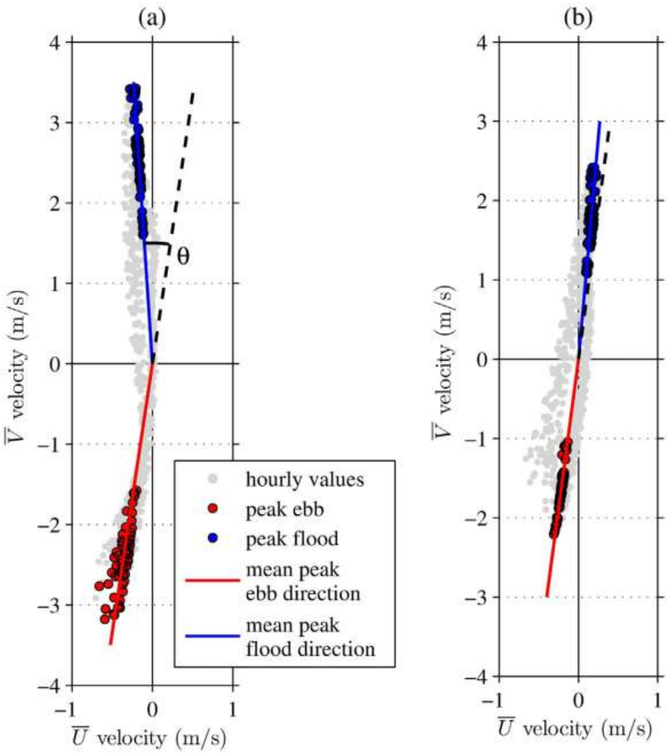

Figure 2.6 Tidal current asymmetry at site a) and b) off the coast of Anglesey, Wales using ROMS software (Lewis, et al., 2015)

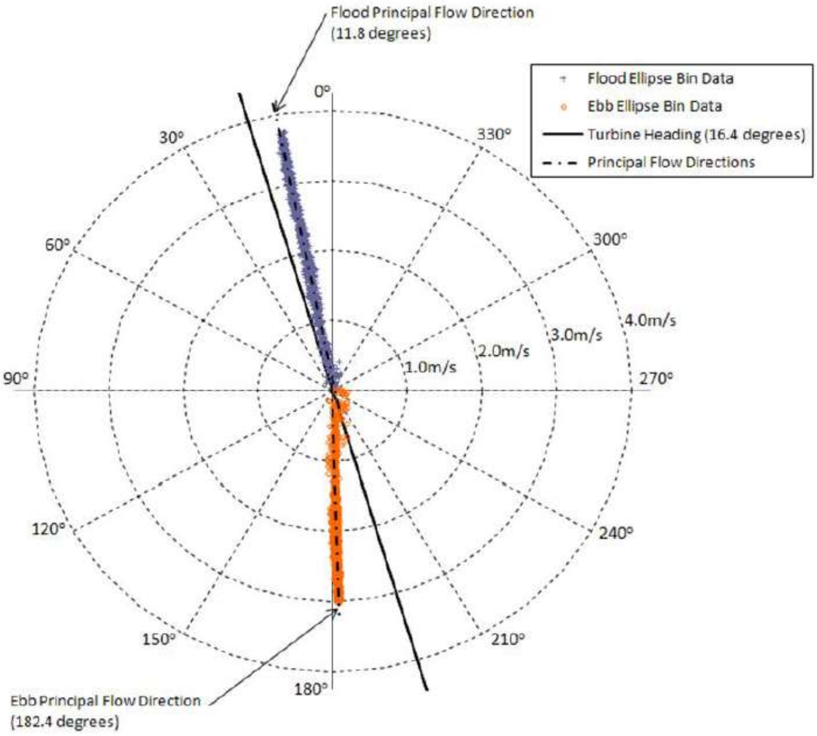

Figure 2.7 Tidal ellipse plot identifying principal ebb and flood directions (IEC 62600-200, 2012)

2.5. Support Structure Interaction

A turbine requires a support structure in order to remain in the flow, the options available are shown in Figure 2.8. Each has its own advantage and disadvantages for different project types and scales.

The surface piercing monopile enables the turbine to be located at various depths in the water column, whilst it also allows surface mounted control or power systems as well as making the device easier to maintain and retrieve on the surface. However it does create a shipping hazard and the drag created by the increased stanchion area causes additional loads on the foundations. Being able to support a turbine or multiple turbines makes this support structure likely to require greater structural stiffness, this may be achieved through increasing its size. A submerged monopole reduces shipping hazards and aesthetic appearance, however the same subsea installation work required for a monopile is required here. Additionally deployment and retrieval of the device becomes an operational consideration at the design stage.

The floating moored pontoon and seabed tethered devices will not be considered in this work as they both have features which allow them to face the incoming flow passively, in some cases. However it is also worth noting that surface mounted turbines are more exposed to wave interaction. As the wave direction can vary relative to the tidal flow it is possible to have flow misalignment through the rotor at the surface due to wave-current interaction. This is beyond the scope of this study however and maybe considered for future work.

The gravity based device requires careful consideration of its loading, however it does feature the benefit of not require permanent installation or subsea engineering works, making it more attractive from an environmental standpoint.

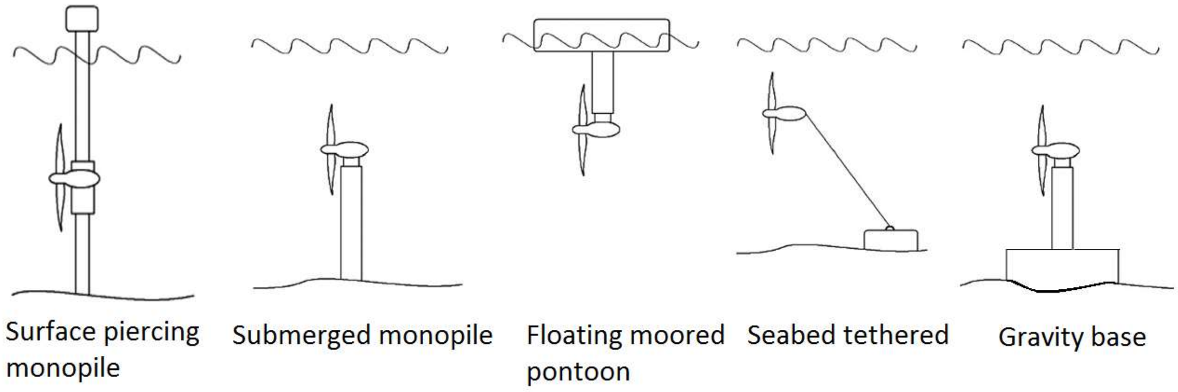

Figure 2.8 Support structure types (adapted from Nicholas-Lee & Turnock, 2008)

2.5.1. Directionality

Since the rotors are normally not placed in isolation, but are typically housed on a support structure, it is important not only to characterise the performance of the rotor, but also to fully understand the interaction of the support structure on the flow characteristics. Experience and knowledge gained from the wind industry has shown that the supporting structure always interferes with the fluid flow around the turbine blades due to the so-called tower dam effect as the flow is retarded in front of the supporting structure (Hau, 2006). However, little work has been published on the direct effect of a support structure on the performance of a TST, especially when the support structure is upstream of the plane of rotation of the turbine, as could be the case for turbines operating in dual-direction tidal flows. Prior work, carried out by Mason-Jones et al, (Mason-Jones, et al., 2013) initially investigated the effect of the stanchion geometry on the characteristic performance of a HATT, positioned 2 hub diameters or 3.6 m downstream of the rotor. Different cross-sectional geometries were used to study axial thrust loading on the stanchion. Five different cross-sectional geometries were tested with an additional model without any supporting structure to give baseline values. The effects of these different cross-sectional geometries on the axial thrust are shown in Figure 2.9, with a uniform velocity of 3.086m/s. Although a stanchion with an elliptical or hydrofoil cross-section can be seen to give the lowest combined turbine and stanchion thrust load. A circular stanchion would be cheaper for developers to manufacture and provides universal symmetry to the stanchion thrust load no matter which orientation. A profiled support will however have varying thrust loads relating to the incident angle of the flow. As such the study will be limited to a circular stanchion based on a compromise between the various factors.

It is noted that the study performed by Mason-Jones, et al. (2013) only considered the relation of the turbine relative to a downstream stanchion. In the case of a bi-directional turbine, the blades would rotate by 180° between flood and ebb tides, resulting in the turbine operating upstream and downstream of its support structure during a tidal cycle. Characterising the differences between the performances in these two scenarios is crucial. An alternative method of avoiding this situation would be to always face the blades into the free-stream velocity. This is reasonable within the wind industry where a yawing mechanism drives the nacelle and rotor to face the principle wind direction, this is simpler to incorporate and maintain on a wind turbine. In the tidal stream environment although it is feasible, to rotate the turbine to always face the oncoming flow, the added complexity and the harsh operating environment (Harding & Bryden, n.d.), let alone the increased capital costs and likely maintenance requirements, mean that the benefits from this option must be significant before this technology is incorporated. Hence it is important to fully understand the stanchion interaction effects on the turbine when upstream and downstream of the tidal stream turbine. Other reasons for considering a yaw drive will be discussed later.

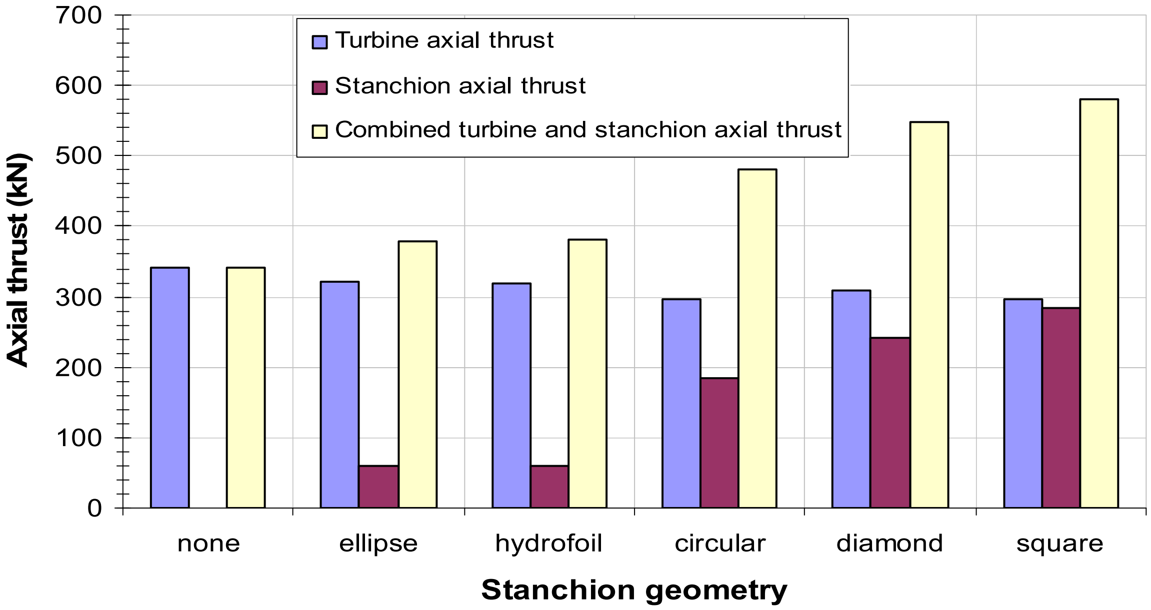

Figure 2.9 Effect of stanchion geometry on turbine power extraction and axial thrust (Mason-Jones, et al., 2013)

2.5.2. Proximity

Experimental and numerical work (Myers & Bahaj, 2009) considered the near field flow field of a turbine and support structure. Flow mapping 2.5 D to 5 D downstream of the turbine and stanchion were conducted. The research showed a deviation in the wake from the axis of rotation due to the stanchions presence. Shedding from the nacelle was also identified. The turbulence caused by both rotor and stanchion were clear, conclusions from the work indicated that removing the stanchion wake from the combined wake causes 'synergetic effects' in areas of heavy mixing. (Myers & Bahaj, 2009). Therefore it is important to consider the turbine and stanchion in a combined manner.

The study into turbine performance and support structure (Mason-Jones, et al., 2013) was only conducted at a constant proximity distance between the rotor and its downstream stanchion. This limitation's in the study opens up the opportunity for further work in defining the relation of a turbines performance to its support structure. One possible method would be to increase the clearance distance between the turbine and support structure developing the relation between the turbine performance and stanchion proximity. There will be an economic and physical limit to the maximum distance between the rotor and stanchion. Only by obtaining the characteristics of the turbine and flow for various clearance distances, however, can this benefit be defined and justification made for maximising this distance.

Existing experimental work on the proximity of a turbine to its support structure has been conducted at Sheffield University (Walker, 2014; Walker, et al., 2015). Two experimental procedures were carried out at 1:143 and 1:72 scale model operating in a water channel, which have shown an optimal operational position for between the rotating plane of the turbine and its support structure. Figure 2.10 shows that as the turbine and stanchion distance increases the turbine's coefficient of power increases up to a point and then proceeds to decrease as the distance continues to increase. Whilst the study was limited to the effect on coefficient of performance, it is likely that other performance characteristics are affected also. What was also not included in this work was a temporal description of the performance as the support structure is likely to impact each blade during the rotation and therefore cause a periodic signal in the performance time traces. This is important as regular power and thrust fluctuations have consequences to the drivetrain and structure life expectancy and maintenance regimes all impacting cost factors. It is therefore critical to further establish this interaction and provide the sector with anticipated issues from this interaction.

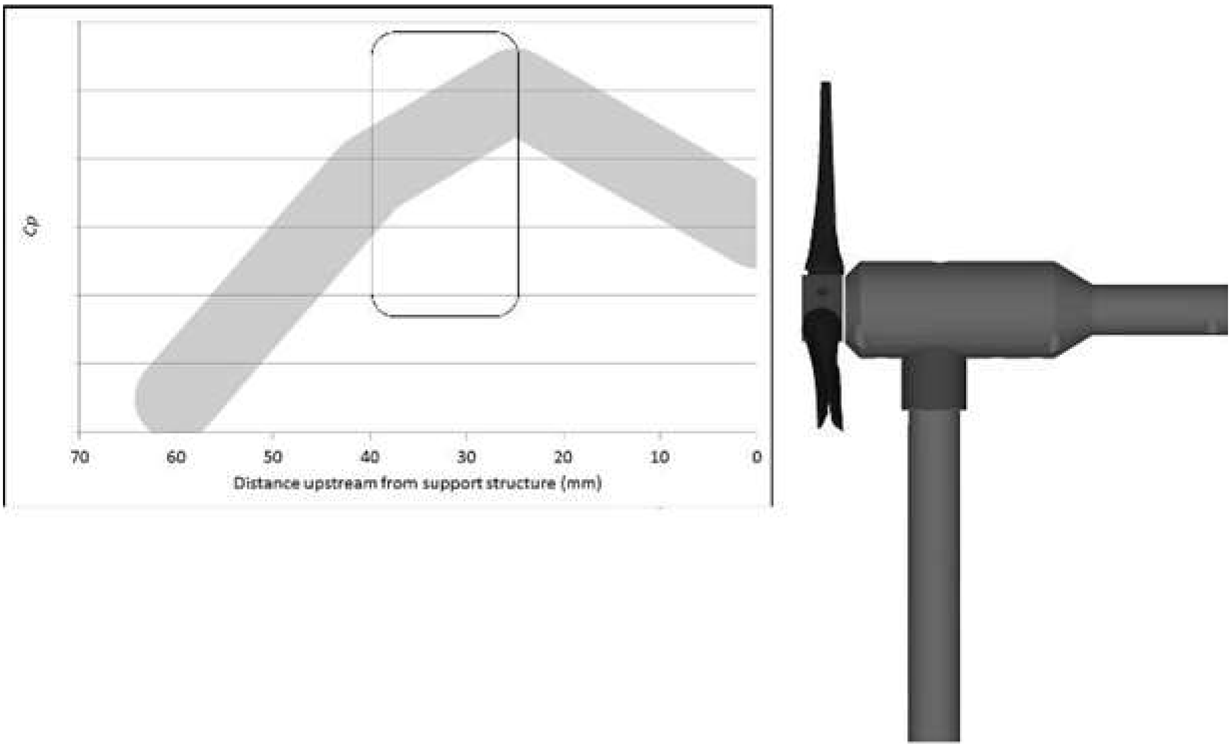

Figure 2.10 Turbines coefficient of Power with increasing distance from stanchion (Walker, et al., 2015)

Operational Yaw Angle

As identified in section 2.4, tidal asymmetry is spatially dependent even at one tidal site, it is also an important consideration to device developers. The rotational axis of HATTs will be orientated to operate facing the strongest flow direction, which is generally the ebb or flood flow directions, and as shown from section 2.4 the asymmetry in the tidal cycle (between ebb and flood) will lead to a misalignment. The misalignment between a turbine's rotational axis and the principle flow direction, can also be considered as the yaw angle, a term commonly found in the wind industry (Hau, 2006). The operational yaw angle is considered important from a turbine performance, capacity factor and structural loading perspective; as highlighted in other research (Harding & Bryden, n.d.). Many TST designs rely on near uni-directional flows and are therefore relatively unresponsive to small deviations due to asymmetry (Harding & Bryden, n.d.). Large deviations from the turbines axial plane can compromise the performance of horizontal-axis TSTs as reported by (Batten, et al., 2007). Furthermore, this is reinforced by Easton and colleagues (Easton, et al., 2010) who noted that these flow features could significantly affect a TST's operational efficiency. The most comprehensive study into yaw interaction with a TST is by Southampton University (Galloway, et al., 2014). The work considered the effect of wave and yaw angle on a scale HATT. The 1:20th experimental model was tested in a towing tank and used to validate a BEM numerical model. The BEM was seen to 'struggle' with the yawed turbine cases, the experimental loading was found to be non-linear (Galloway, et al., 2014). It is noted that in the experimental data, the increase in yaw angle from 0˚ to 22.5˚reduced both the mean in-plane and out-of-plane bending moments. The in-plane bending moment also increased in fluctuation amplitude, whilst the amplitude of the out-of-plane bending moments did not appear to change significantly. However the authors summarised that waves had a greater influence on loading than yaw angles and therefore focused the temporal results on the wave tests. As expected the authors found yawed cases resulted in reduced power capture and thrust (Galloway, et al., 2014). The work by Southampton University is comprehensive and provides a good insight into yawed flow. However, little consideration has been taken for the results of yaw angle on the support structure interaction. By identifying how the stanchion interaction effects on turbine performance changes with yaw angle it may be possible for device developers to identify when their turbine is operating at a yaw angle by the change in performance characteristics of the rotor.

2.6. Thesis aims and objectives

The literature reviewed in this section has identified some of the key research being undertaken into tidal stream turbines. The current numerical modelling techniques have been considered and the work in these areas has shown in each case experimental validation remains an important part. The use of CFD analysis on tidal stream turbines has a strong history at Cardiff University and makes it the prominent technique viable for the work in this thesis. The experimental work on-going shows some of the laboratory scale devices which have been tested and a few larger scale tidal testing campaigns which have been conducted and published. Consideration of the testing environment and the controllable parameters in the flow regime in order to relate to CFD analysis was shown to be important.

The evidence for tidal asymmetry has been identified as an issue and has lead into further consideration of turbine's operating in close proximity and orientation relative to their support structures and the effect of these two things on performance. The studies into these areas as previously established will be the focus of this thesis.

The aim of the work was to investigate the effect of support stanchion interaction and flow misalignment on the non-dimensional performance characteristics of a tidal stream turbine, using numerical modelling and experimental validation. This was achieved by the following objectives:

1. Comparison of the non-dimensional performance characteristics of a turbine upstream and downstream of their support structure at varying proximities.
2. Investigation of the significance of flow misalignment of the turbine on its non-dimensional performance characteristics.
3. Development of experimental apparatus and testing scenarios for numerical model validation.
4. Validation of a range of numerical modelling simulations with laboratory experiments.

3. Theory

This chapter presents the applicable hydrodynamic physics surrounding tidal stream turbines used to predict a tidal stream turbines performance and model its hydrodynamics, as well as its impact on the surrounding flow field. Firstly the notations of blade theory and fundamental physics is established, followed by the underlying equations used in the numerical modelling utilised in this study. The application in its context to tidal stream turbines is detailed. An overview of the relevant theory used to compare the performance of TST's is then define using non-dimensional performance characteristics such as the coefficients of torque, power, thrust and out-of-plane bending moments. The final section in this chapter outlines the correction factors required for axial flow misalignment which are of critical importance to this thesis.

3.1. Blade theory

The lift phenomenon is common to hydrofoils and aerofoils alike and the theory surrounding them is one and the same. As this theory applies to all tidal turbines that operate through inducing lift across a hydrofoil the theory presented here is well established in other sectors (Abbott & Von Doenhoff, 1949). The terminology developed has been translated to apply to rotary machinery in the case of a horizontal axis tidal turbine (HATT). Figure **3.1** shows the terminology and symbols used in this work. The free stream velocity (V) is defined as the principle flow, and is considered parallel to the axis of rotation of the turbine, in most cases. The tangential velocity (U_{Ta}) is the relative fluid velocity due to the rotation of the turbine and is dependent on the radial distance from rotational axis of the turbine and the rotational velocity (ω) of the turbine. The resultant velocity (U_R) is determined from equation [3.1]

$$U_R = \sqrt{V^2 + {U_{Ta}}^2} \qquad [3.1]$$

The angle of the resultant velocity relative to the free stream velocity (θ) as determined in equation [3.2]. The blade pitch angle (β) is the angle between the chord of the blade and the rotational plane the blade is acting in. The angle of attack (α) can be seen to be the remainder of the right angle between the tangential velocity and free stream velocity. It can otherwise be seen as the angle between the blade chord and the resultant flow velocity direction.

$$\theta = \tan^{-1}\left(\frac{V}{U_{Ta}}\right) \quad [3.2]$$

The blade chord length (C) is the distance between points A and B in Figure **3.1**. Point A can be considered the centre of the stagnation point at the tip of the blade when at an angle of attack of 0°. The point B is the trailing edge and the hindmost point of the blade. The lift (L) on the hydrofoil will always act perpendicularly to the resultant flow direction, whilst the drag (D) will always act parallel and in the same direction as the resultant flow. The blades thrust force (F_T) is the components of lift and drag that act in the axial direction of the turbine. The blades rotational force (F_θ) comes from the resultant, of the respective positive and negative contribution, of the lift and drag components acting in the plane of rotation of the turbine. The torque or in-plane Bending Moment (Q) of the turbine is the sum of these rotational forces acting at radial distances from the rotational axis.

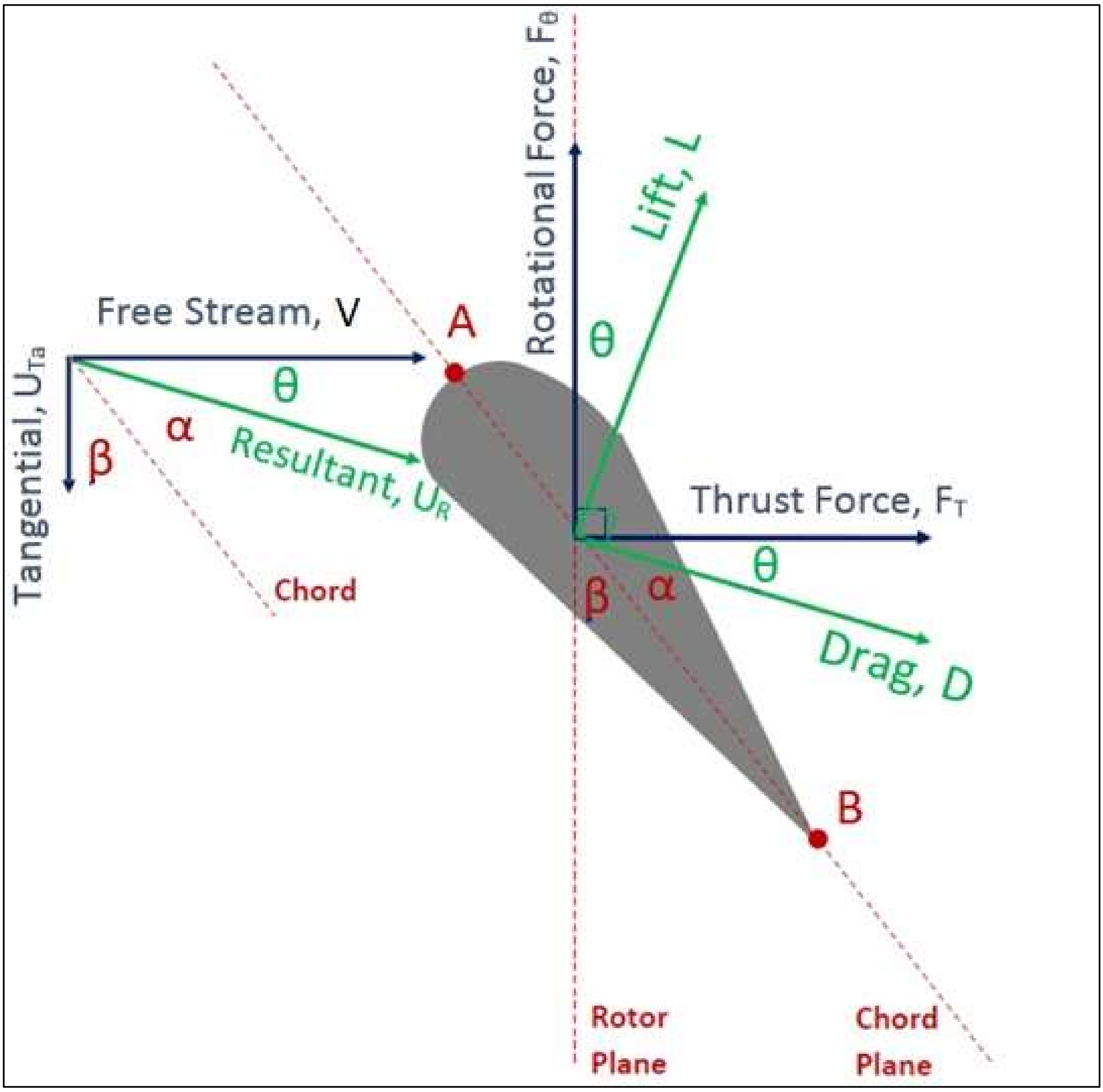

Figure 3.1 Blade Terminology Definition (adapted from Jeffcoate, 2014)

3.2. Reynolds Averaged Navier-Stokes Equations

The Reynolds Averaged Navier-Stokes (RANS) equations are derived from the transport equations and describe the motion of Newtonian fluids, the equations solve the velocity flow field for a given control volume and parameters. They can be considered as a differential equation dependent upon the preservation of continuity, momentum and energy, within a control volume. Equation [**3.3**] shows the continuity equation as found in ANSYS (Ansys, 2015), where the tensor notation are for a Cartesian coordinate system.

$$\frac{\partial \rho}{\partial t} + \nabla \cdot (\rho\, U) = 0 \qquad [3.3]$$

However the work in this thesis considered the fluid domain to be single phase and incompressible, thus simplifying the continuity equation to the form shown in equation [**3.4**] in three dimensional Cartesian form as derived in other work (Versteeg & Malalaserekera, 1995).

$$\frac{\partial u}{\partial x} + \frac{\partial v}{\partial y} + \frac{\partial w}{\partial z} = 0 \qquad [3.4]$$

The momentum equations as given by ANSYS (2015) is seen in equation [**3.5**] and follows Newton's second law; 'The rate of change of momentum of a fluid particle equals the sum of the forces on the particle' (Versteeg & Malalaserekera, 1995).

The forces on the particle stem from the surface forces such as pressure and viscosity, whilst body forces include; centrifugal and Coriolis forces.

$$\frac{\partial(\rho U)}{\partial t} + \nabla \cdot (\rho U \otimes U) = -\nabla p + \nabla \cdot \tau + S_M \qquad [3.5]$$

Where,

$$\nabla \cdot (\rho U \otimes U) = \begin{bmatrix} \frac{\partial}{\partial x}(\rho U_x U_x) + \frac{\partial}{\partial y}(\rho U_y U_x) + \frac{\partial}{\partial z}(\rho U_z U_x) \\ \frac{\partial}{\partial x}(\rho U_x U_y) + \frac{\partial}{\partial y}(\rho U_y U_y) + \frac{\partial}{\partial z}(\rho U_z U_y) \\ \frac{\partial}{\partial x}(\rho U_x U_z) + \frac{\partial}{\partial y}(\rho U_y U_z) + \frac{\partial}{\partial z}(\rho U_z U_z) \end{bmatrix} \qquad [3.6]$$

The momentum equation is represented in equation [**3.5**] as one equation, however it appears once for each axis in a three dimensional flow field problem. These three equations and the instantaneous continuity equation **[3.3]** form a closed set, with four variables. The four variables are three velocity components, u, v, w and the pressure, p. In order to solve these equations the case must be separated into averaged and fluctuating components. This however introduces further unknowns as seen in equation [**3.7**]. These are called the Reynolds stresses and appear in the momentum equations, as derived in Ansys (2015) and Versteeg & Malalaserekera (1995) and shown in equation [**3.8**]. In order to resolve the additional unknown Reynolds stresses, the Boussinesq approximation is used as discussed in section 3.3.3.

$$\frac{\partial \rho U_i}{\partial t} + \frac{\partial}{\partial x_j}(\rho U_i U_j) = -\frac{\partial p}{\partial x_i} + \frac{\partial}{\partial x_j}(\tau_{ij} - \rho\overline{u_i u_j}) + S_M \qquad [3.7]$$

and,

$$-\rho\overline{u_i u_j}) = \mu_t(\frac{\partial U_i}{\partial x_j} + \frac{\partial U_i}{\partial x_i}) - \frac{2}{3}\delta_{ij}(\rho k + \mu_t\frac{\partial U_k}{\partial x_k}) \qquad [3.8]$$

The averaged component of the flow and time varying component of the flow are dependent upon the time step size selected. In the case of a steady state model a pseudo time will be appointed.

3.3.1. Source Terms

The body forces in the momentum equation are found in the Source term (S_m) and in this study include Coriolis and centrifugal forces when in a rotating reference frame as described by equation [**3.9**] (Ansys, 2015).

$$S_m = -(2\rho\omega \times U) - (\rho\omega^2 r) \qquad [3.9]$$

3.3.2. Alternative rotation model

In ANSYS 2015 the alternative rotation model uses the absolute velocity in the rotational domain rather than the relative frame velocity. The main advantage of this function was to reduce the numerical error in situations where there were large radii in the rotating reference frame and when the axial flow velocity was large relative to the relative flow velocity in the rotating reference frame (Ansys, 2015).

3.3.3. Eddy Viscosity Concept

The eddy viscosity concept also known as the Boussinesq approximation relates the Reynolds Stress Tensor in the RANS equations to the strain (i.e. the deformation of a fluid package), as shown in equation [**3.8**], where the turbulent viscosity is a function of the turbulent kinetic energy and dissipation rate.

3.3. Turbulence Models

To solve the RANS equations a turbulence model is required, as a direct solution is currently unobtainable. Many models have been developed with significant advances depending on larger computational power such as the Large Eddy Simulations (LES) and Detached Eddy Simulations (DES). Due to the limitations of ANSYS licenses which restricted computational capacity the research is limited to the consideration of two equation turbulence models. The selection of the appropriate turbulence model is dependent on the physics of the scenario being modelled. Each model has different advantages and disadvantages. From past research the Reynolds Mean Stress (RSM) and Shear Stress Transport (SST) models have been used (Morris, 2014). In this research the SST model developed from the k-ω model, will be used as previous work shows good comparison with experimental validation (Morris, 2014) and is a well proven model in ANSYS CFX. In ANSYS CFX the SST model is beneficial as it can be transiently coupled to the mechanical package for a fully coupled Fluid-Solid Interaction model.

3.3.1. The k-ω Model

Developed by Wilcox (1986), the k-ω model solves two transport equations for each axis, one for the turbulent kinetic energy (k) and the other for the turbulent frequency (ω) (Ansys, 2015). The model is based upon the eddy viscosity concept which enables the derivation of the stress tensors required to solve the RANS equations.

The advantages of the Baseline (BSL) k-ω model include being computationally inexpensive, well established in industry and previously validated (Mason-Jones, 2010). It is an improvement on the k-ε model which is not well suited to rotational flows. It avoids some of the disadvantages of the traditional k- ω model, its blend function improves performance in far field rotational flows. The blend function allows transition from the k-ω model at close to rotational boundary surfaces to the k-ε model in the far regions (Menter, 1994).

One of the disadvantages of standard two-equation turbulence models is the requirement of a production limiter to avoid the build-up of turbulent kinetic energy in stagnation points (Ansys, 2015). This can be avoided however as discussed in section 3.3.2.

3.3.2. The Shear Stress Transport (SST) Model

The SST model takes the baseline k-ω model discussed above, but now accounts for the transport of the shear stress, as well as just predicting it using the eddy viscosity concept. This is important as it affects flow separation from surfaces and prediction of flow in adverse pressure gradients (Ansys, 2015). These are critical considerations when modelling the flow over a tidal turbine blade especially during the onset of stall conditions on the blade.

However a limitation identified in other work (Morris, 2014; Mason-Jones, 2010) shows the default Turbulent Kinetic Energy (TKE) dissipation rate in the SST model is high. This is an issue because the nature of the physical system being replicated is a true sea state which has a high background turbulence. For this reason the full system turbulence will not be considered and modelled and is a matter for further work. The SST model is heavily dependent upon two blend functions to transition between near surface boundaries and the free stream. These functions contain a y^+ term which is the distance to the nearest wall. As the distance from the wall increases the impact of the blend function on the fluid decreases.

3.3.3. Wall function

Near surface boundaries the effect of wall shear stress becomes dominant in the flow field. This is a log-law relation and is dependent upon the y^+ value as shown in equation [**3.10**] (Ansys, 2015).

$$u^+ = \frac{1}{k}\ln(y^+) + C \qquad [3.10]$$

Where u^+ is the near wall velocity, k is the von karman constant and C is a constant relating to the wall roughness. The y^+ for a k-ω model is shown in equation [**3.11** (Ansys, 2015).

$$y^+ = \frac{\sqrt{\tau_\omega/\rho} \cdot \Delta n}{v} \qquad [3.11]$$

Where the wall shear stress is τ_ω and Δn is dependent on the mesh at the boundary to give the dimensionless term to describe the distance from the wall. For highly accurate simulations a y^+ of less than 5 is recommended (Ansys, 2015), however due to the additional computational effort in solving such a fine mesh, previous work shows a y^+ of 300-500 being acceptable (Morris, 2014).

3.4. Non-Dimensional Performance Characteristics

A TST can be described by the non-dimensional performance characteristics, which is based on Froude's Momentum Theory for an actuator disk (Hansen, 2001). Non-dimensional performance characteristics originate from the need to compare the performance of parametrically differing situations. In the context of tidal stream turbines this can be used in a number of ways. They were originally designed to compare scale and geometrical differences of a device in ideal flow conditions. However in the development of the sector, this term has been broadened to include the comparison of differing flow parameters, no longer ideal flow. In order for these parametrisations to be compared effectively a standard must be maintained in order to keep the comparison tangible. The flow field in a true sea state will vary spatially in all three dimensions, relative to the rotor which requires a relative location to be decided where 'free flow' is occurring. This should be dimensioned relative to the turbine diameter (D) and placed in relation to the turbine, either perpendicular or in line with the axis of rotation of the rotor. The IEC standard (IEC 62600-200, 2012) has addressed these concerns and exacted parameters required to determine non-dimensional performance parameters in real tidal systems. The spatial requirement is a single value to define flow through the complete swept area of the turbine at this location. The IEC standard currently recommends a power weighted, area averaging method. What must also be considered is the temporal component of the velocity as the stochastic nature of a true flow regime will be highly temporal and this must be accounted for when characterising the performance of a TST. Current IEC standard (IEC 62600-200, 2012) requires between 2-10 minute windows with a frequency of at least 1 Hz to be collected in order to have statistically meaningful results for the time-averaged performance. IEC currently do not have a standard for characterising the performance of TST in tow tank facilities; however the ITTC (2008) have published recommendations. The advantage of a tow tank over other experimental facilities is by its very nature of being stationary water (given sufficient settling time) the fluid more closely represents the idealised set-up with no turbulence or stochastic nature and a uniform velocity profile meaning the volumetric average will be the same as just taking a single point and the upstream reference velocity can now be equated to the carriage velocity.

3.4.1. Coefficient of Torque

Equation [**3.12**] gives the torque coefficient (C_θ), which is the ratio of the torque generated by the turbine, Q to the maximum theoretical torque. The torque of the turbine is also known as the in-plane bending moment.

$$C_\theta = \frac{2.Q}{\rho.A.R.V^2} \qquad [3.12]$$

3.4.2. Coefficient of Power

The power coefficient (C_p) is the ratio of the extracted energy to the available energy over the swept area of the turbine and is given by equation [**3.13**].

$$C_P = \frac{2.Q.\omega}{\rho.A.V^3} \qquad [3.13]$$

3.4.3. Coefficient of Thrust

The thrust coefficient (C_t), given by equation [**3.14**] is the ratio of the axial load on the turbine to the axial load over the swept area of the turbine.

$$C_T = \frac{2.F_T}{\rho.A.V^2} \qquad [3.14]$$

3.4.4. Coefficient of Moment

A previous study, discussed earlier in section 2.5 (Mason-Jones, et al., 2013), showed the presence of asymmetric thrust loading and the compounded complexity with the presence of a stanchion. This work has been furthered by identifying the asymmetric loading as an out-of-plane bending moment for the turbine. By resolving the out-of-plane bending moments for each blade the resultant bending moment acting with a magnitude and direction on the driveshaft of the turbine was formulated (Frost, et al., 2015).

The axial thrust loads vary in magnitude along the blades in the radial direction. The sum of these loads can be equated to a point load acting at the centre of pressure on each blade. The disproportionality in these loads causes eccentricity in the total axial thrust; this is the out-of-plane bending moment which can be separated into its M_X and M_Y components as identified by the coordinate frame in Figure **3.2**. These loads must be accounted for in the stiffness of the turbine blades to cause minimal deflection, subsequently the loads are transferred through the rotor and onto the driveshaft. These loads will cause the driveshaft to deflect or misalign unless it is adequately sized and supported by adequately designed thrust bearings. In this instance loads are transferred through the driveshaft and support bearings onto the main support stanchion causing yawing, rolling and pitching motion at the support structures connection to the nacelle as identified in other work (Harper, et al., 2015).

The coefficient of the out-of-plane bending moment (C_M) is given by the ratio of the sum of the out-of-plane moments, as described in equation **[3.15**], acting on a turbine to the maximum theoretical out-of-plane torque (Hau, 2006). This is given in equation **[3.16**]. The direction at which the out of plane bending moment acts is given by equation **[3.17**] and gives a resultant angle of acting moment (θ_M) about the driveshaft of the turbine.

$$M_{xy} = \sqrt{\left(\sum M_x\right)^2 + \left(\sum M_y\right)^2} \quad [3.15]$$

$$C_M = \frac{2.M_{xy}}{\rho.A.R.V^2} \quad [3.16]$$

$$\theta_M = \tan^{-1}\left(\frac{M_y}{M_x}\right) \quad [3.17]$$

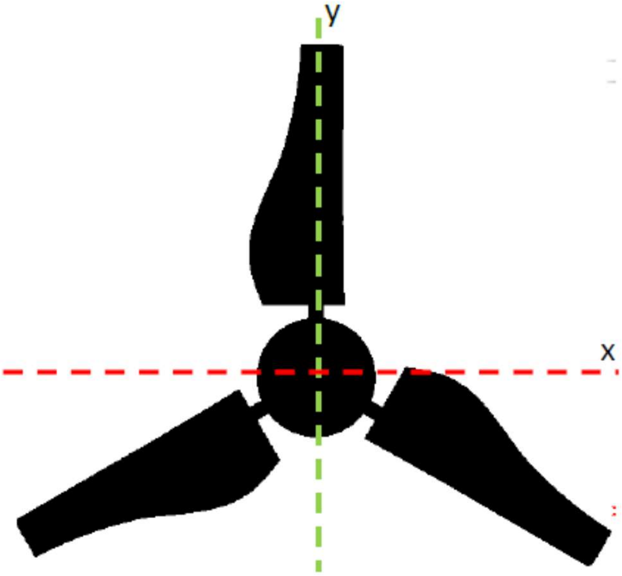

Figure 3.2 Axes for which out-of-plane bending moments are taken about

3.4.5. Tip Speed Ratio

The tip speed ratio (λ) is the ratio of the tangential velocity of the blade tip to the upstream velocity of the flow and is given by Equation **[3.18**]. Plotting the above performance characteristics against λ enables different devices to be compared regardless of the turbine diameter or flow conditions.

$$\lambda = \frac{\omega R}{V} \quad [3.18]$$

3.5. Transient Results Analysis

Due to the temporal nature of some data sets, both from CFD and experimental work, the mean (μ) and standard deviation (σ) values of a data set are used these are calculated using equations [**3.19**] & [**3.20**].

$$\mu(x) = \frac{1}{N}\sum_{n=0}^{n=N} x_n \tag{3.19}$$

Equation [**3.19**] describes the mean value for a time series with N data points.

$$\sigma(x) = \sqrt{\frac{\sum_0^N (x_n - \mu)^2}{N-1}} \tag{3.20}$$

Equation [**3.20**] shows the calculation of the standard deviation for the same time period with N data points and sample rate.

3.6. Correction for Blockage

In the non-dimensional performance characteristics stated in section 3.3.3; the theoretical maximum values in the denominator of the equations assumes ideal conditions. Ideal conditions being a uniform constant velocity perpendicular to the plane of rotation of the turbine. For non-ideal conditions however these input values must be accounted for and corrected. This is a significant issue, as identified from literature review in Section 2.2.2. The blockage ratio of an experiment is considered to be the ratio of the swept area of the turbine, A_T to the cross-sectional working area, A_{CS} as shown in equation [**3.21**].

$$Blockage\ Ratio = \frac{A_T}{A_{CS}} \tag{3.21}$$

The correction for blockage must be considered, especially where proximity to the facilities walls and free-surface significantly impact maximum extractable power attainable by a turbine. The identified threshold for implementation of blockage correction is 5% (Whelan, et al., 2009). Experimental or numerical modelling with a greater blockage ratio than this would require correction using blockage correction proposed by (Barnsley & Wellicome) and employed by Bahaj et al (Bahaj, et al., 2007; Whelan, et al., 2009).

3.7. Correction for Flow Misalignment

The necessity for maintaining ideal conditions in order to obtain a true non-dimensional performance characteristic means that the velocity must be considered again here for the occurrence of misalignment between the turbine and the principle flow direction.

Equation **[3.22**] describes the inflow velocity when the turbine's axial direction is in-line with the free stream. In circumstances of misalignment between the inflow direction and the rotational axis of the turbine a yaw angle (α) must be introduced to clarify the discrepancy. The inflow velocity will now be a component of the free stream velocity as described by equation **[3.23**].

$$V_{\alpha=0} = V \qquad [3.22]$$

$$V_{\alpha\neq 0} = V.\cos\alpha \qquad [3.23]$$

Alternatively the swept area of the turbine must be considered as it changes with misalignment from a circle to an ellipse; the vertical radius of the ellipse will remain the same. The horizontal radius will decrease as the yaw angle increases and this must be accounted for. The resulting equation for the projected area of a turbine in aligned flow and in misaligned flow can be seen in equations **[3.24**] and **[3.25**] respectively.

$$A_{\alpha=0} = \pi.r^2 \qquad [3.24]$$

$$A_{\alpha\neq 0} = \pi.r^2.\cos\alpha \qquad [3.25]$$

Where r is the radius of the turbine and α is still the yaw angle.

It is expected that both these corrections when applied to the theoretical maximum power, torque and thrust equations, the denominators in equations **[3.12**] - **[3.14**], would provide the performance drop due to misalignment. However as can be seen from Figure **3.3** whilst the normalised area corrected curves for torque, power and thrust all collapse onto one line, the velocity corrected cases differ from the area corrected cases. The torque and thrust velocity corrected cases experience the same nominal drop in performance with increasing yaw angle. However the power corrected case experiences a significantly greater drop. The reason identified for this is the contribution of the velocity squared terms in the torque and thrust equations and the cubed term in the power equation.

As a result of this numerical study of the maximum theoretical performances, it was determined that area correction method should be used in correcting for yaw turbine cases.

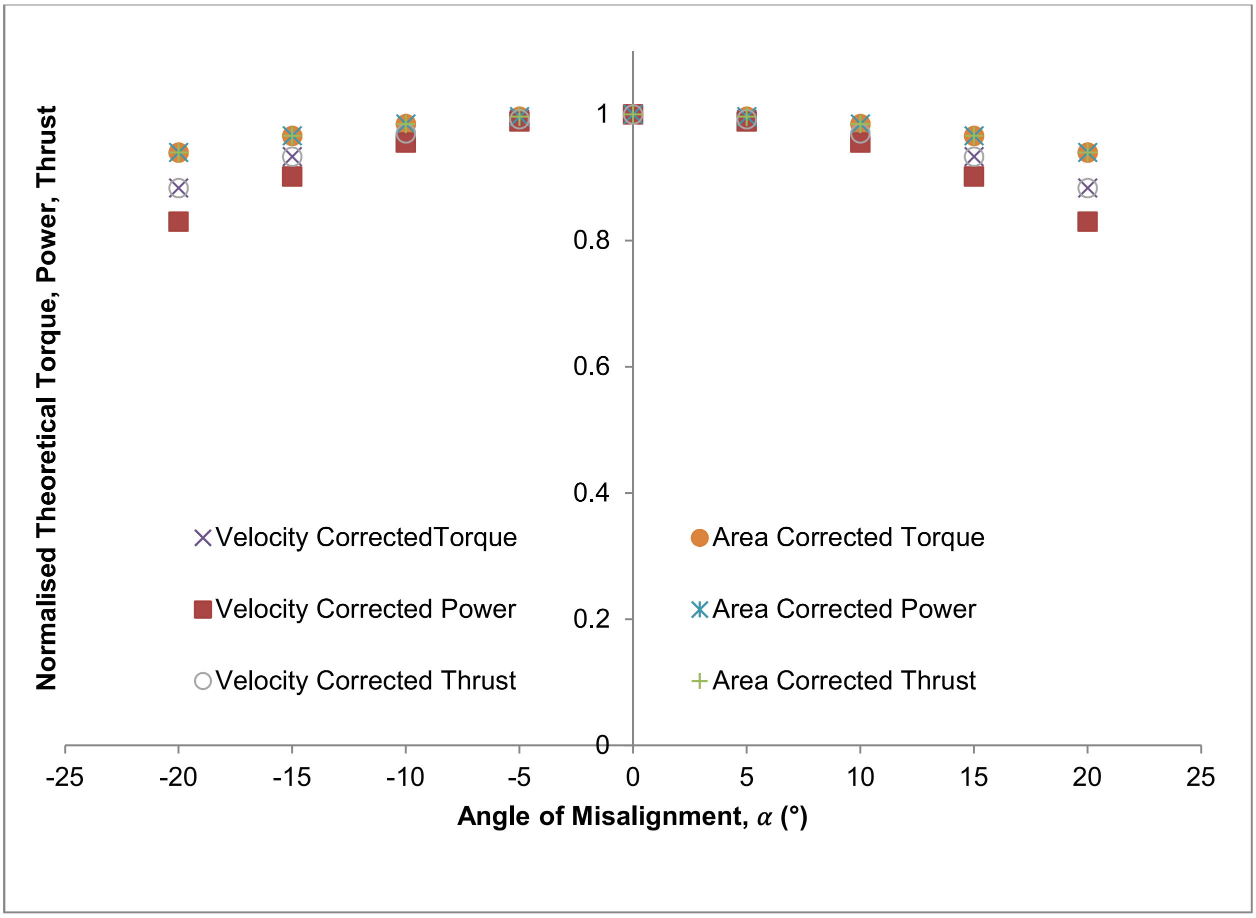

Figure 3.3 Normalised Torque, Power and Thrust for Yawed Turbine Cases

3.8. Reynolds Scaling

The Reynolds Number, a non –dimensional indicator of fluid characteristics, is important when considering the performance of turbines at different scales. The Reynolds number for both scales must be closely matched if the inertia and viscous forces are dominant in the flow (Journee & Massie, 2001). Reynolds number is dependent upon the density of the fluid, the principle velocity magnitude, the principal length and the kinematic viscosity as shown in equation [3.26].

$$Re = \frac{\rho V L}{\mu} \tag{3.26}$$

Both the density (ρ) and dynamic viscosity, (μ) are dependent on the fluid properties and the principle length (L) a property of the model geometry. The velocity is a unique component which is dependent on both the fluid properties and the geometries operating conditions. The principle length in relation to turbine design could be considered as the rotor diameter or blade chord length, both these options are discussed here.

3.8.1. Rotor-based Reynolds Number

In this case, the Reynolds number is a function of the turbine's diameter and the free stream velocity which the turbine is operating in. The turbine geometry used in previous work (Mason-Jones, et al., 2012) provided the critical Reynolds numbers for a full scale turbine, based on rotor diameter (10 m). The Reynolds number for this turbine geometry was derived from the change in coefficient of torque and power for various Reynolds numbers and identified the critical Reynolds number as $Re_{Crit} = 3x10^5$, however full Reynolds independence can be assumed after $Re = 5x10^5$. These results come from previous work performed (Mason-Jones, et al., 2012) and agree with experimental validation at 1:20th scale (Tedds, et al., 2011).

3.8.2. Chord-based Reynolds Number

The chord-based Reynolds number is a function of the blade chord length and resultant fluid velocity at that chord length. It is commonly used in propeller design (Gaurier, et al., 2015) and the blade chord should be considered at 70% of its length from the rotational axis of the propeller/ turbine (i.e. r/R=0.7), this is referred to as $C_{r/R}$. The resultant velocity and direction of the fluid at this radial length, $U_{r/R}$ and $\theta_{r/R}$ can be calculated from equation [3.1] and [3.2] respectively. The resultant velocity is dependent upon the free stream velocity and the tangential velocity of the turbine. The tangential velocity is in turn dependent upon the rotational velocity of the turbine. Therefore in order to determine the critical chord-based Reynolds number these terms are required. Substituting equation [3.1] into equation [3.26] and using $C_{r/R}$ as the principle length the relevant chord-based Reynolds numbers can be found. The blade chord Reynolds number is critical to the lift and drag coefficients of the blade, as low Reynolds number established the onset of stall (Abbott & Von Doenhoff, 1949).

Consideration of the turbine blade used in previous work (Morris, 2014), Table 0.1 in Appendi shows that the pitch distribution of the blade is such that the angle of attack of the blade remains approximately 10.5°. From this the diameter and chord based Reynolds numbers were calculated for the full scale (10 m) device and 1:20th scale device. It is clear that the full scale device Reynolds numbers are not achieved in the 1:20th scale device, at the velocities calculated in Table 0.1. However it is known from previous work by Mason-Jones, et al. (2012) that the critical rotor-based Reynolds number ($Re = 3x10^5$) equates to a chord-based Reynolds number of $Re_{crit} = 9.77x10^4$ which is achieved at the 1:20th scale for velocities greater than 1.00 ms^{-1}. Also the Reynolds independence is not achieved at the 1:20th scale until 1.50 ms^{-1}. These threshold will be significant for experimental comparison.

4. Numerical Methodology

The purpose of this chapter is to provide a detailed description of the set-up and execution of the numerical models using ANSYS research software. The turbine and various support structure geometries are described and the dimensions of the control volume and rotating domain used to host the various scenarios. The chapter continues by describing the mesh structure utilised and determine its quality using metrics discussed. Inclusion of the numerous input parameters defined to the ANSYS CFX program and how these relate to the theory described in Chapter 3 are reported as well. The final parts of this chapter discuss the processing and computational capabilities used as well as the post-processing procedure.

4.1. Model Geometry

The primary constituents of the complete turbine assembly are considered in this section as well as the geometries of the fluid domain. Figure 4.1 is annotated to show each of the primary constituents which will be discussed in this section.

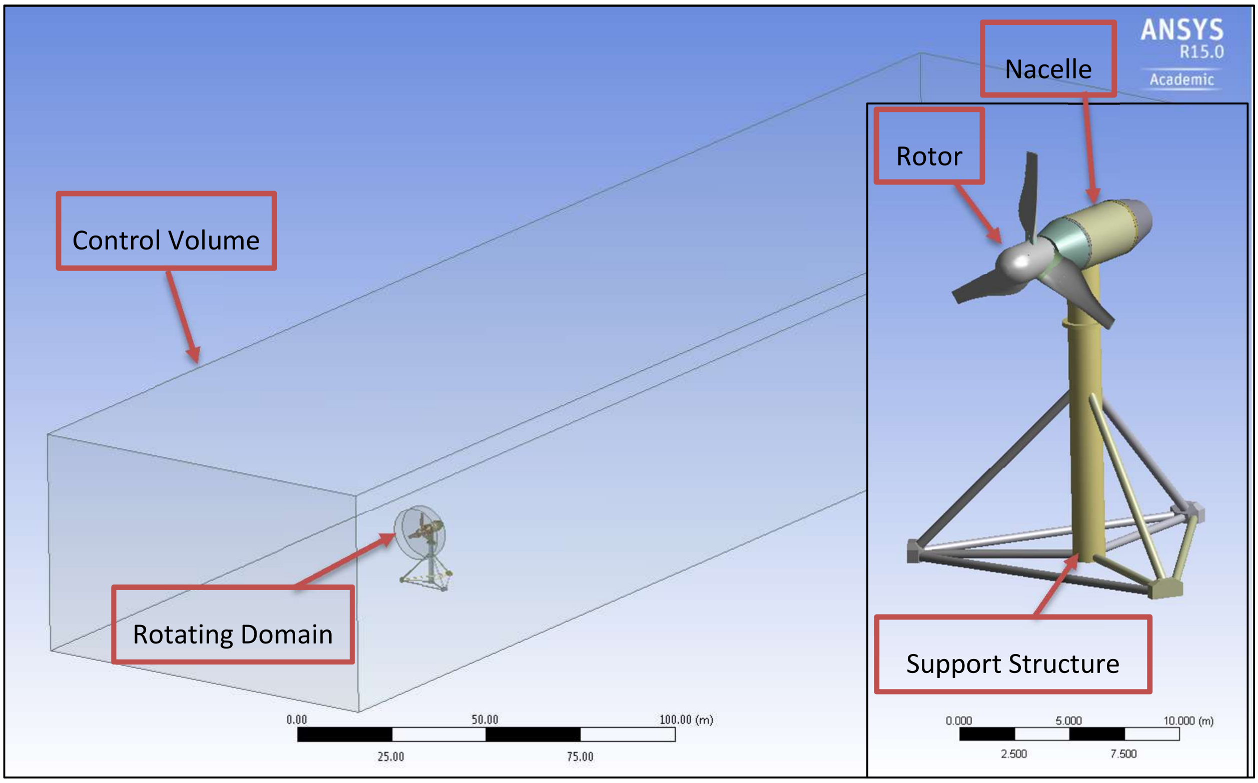

Figure 4.1 Primary Geometrical Components of Numerical Models

4.1.1. Rotor Geometry

The rotor used is a 0.5 m diameter, 3-bladed horizontal axis turbine which has been geometrically scaled up to industrial / full-scale 10 m diameter. The scaling maintained the ratio of hub to blade diameter. Further details of the original blade design can be found in previous published work (Egarr, et al., 2004). The blades are Wortmann FX 63-137 profile (developed by NREL for the wind sector) and are designed with 35° twist running along the length of the blade. The pitch distribution of the blade can be described by a cubic relation and maintains the 10.5° angle of attack along the blade facilitating self-starting by the rotor, the pitch distribution is shown in Table 0.1 in the Appendix. The blade profile can be seen in Figure 0.1 in the Appendix and its performance characteristics can be found in Figure 0.2 in the Appendix and are discussed in section 3.8.

The original 3D blade, as seen in Figure **4.2**, shows the three working sections which have been separated into root, middle and top faces as well as the connection pins and the hub faces. The blade length (L_B) is 3.91 m long from root to tip, the hub radius (R_H) is 0.89 m and the pin connector gap (L_P) between the root of the blade and rotor hub is 0.19 m. These three combine to make up the 10 m diameter full scale rotor.

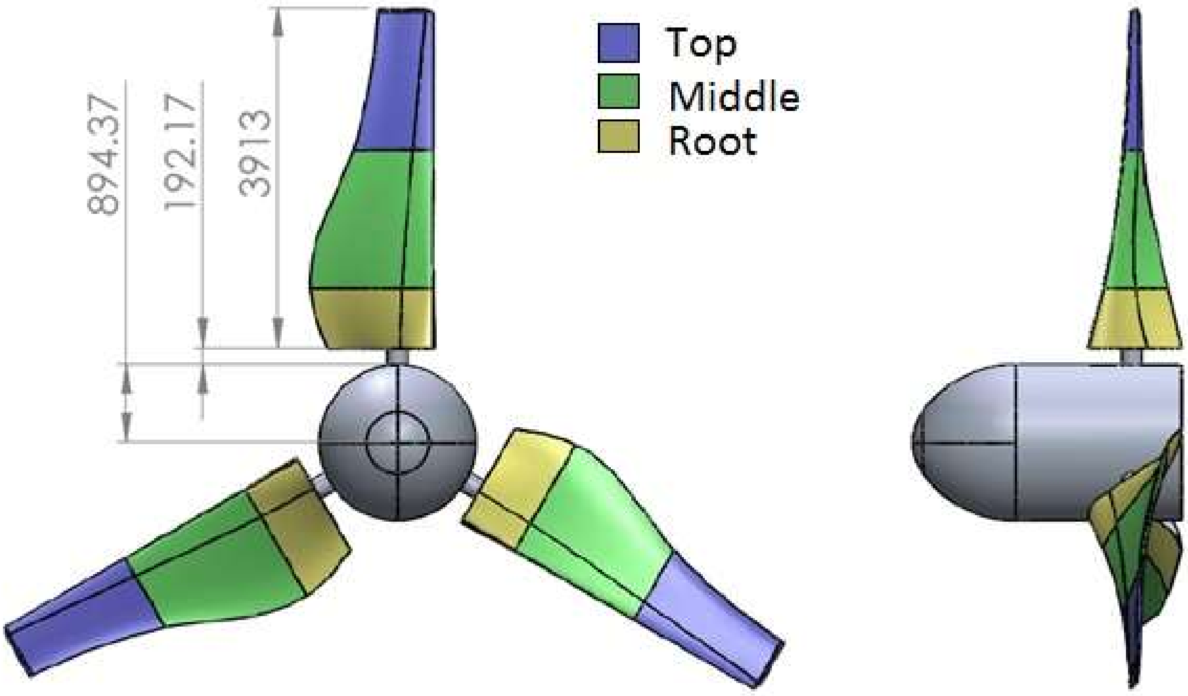

Figure 4.2 Original Turbine Geometry (mm)

Figure **4.3** shows a modified blade geometry at the root section, this design was made to improve aspects of the numerical modelling. The reasons for the modification to the root of the blades is due to the internal structure in the design of the rotor, the blades are assumed to be solid stainless steel as created for the lab scale model, this includes the pin connection. Work performed (Morris, 2014) on the stress and strain on the turbine blades showed that the pin connection caused stress concentrations that were not reflective of a true system. Whilst this work is to be recognised as valuable when referring to the design of this rotor, it is limited in its application to a true system. In order to improve this work therefore, the connection to the hub was re-designed with the profile at the root of the bladed being extruded into the hub, making a profiled connection. This removes the unnecessary hydrodynamic issues that were created in the gap between the end of the blade and external of the hub as well as enabling an internal design and connection of the blade to the hub to be later designed. FEA analysis of the root section will now be more realistic and the stress concentration of the pin alleviated.

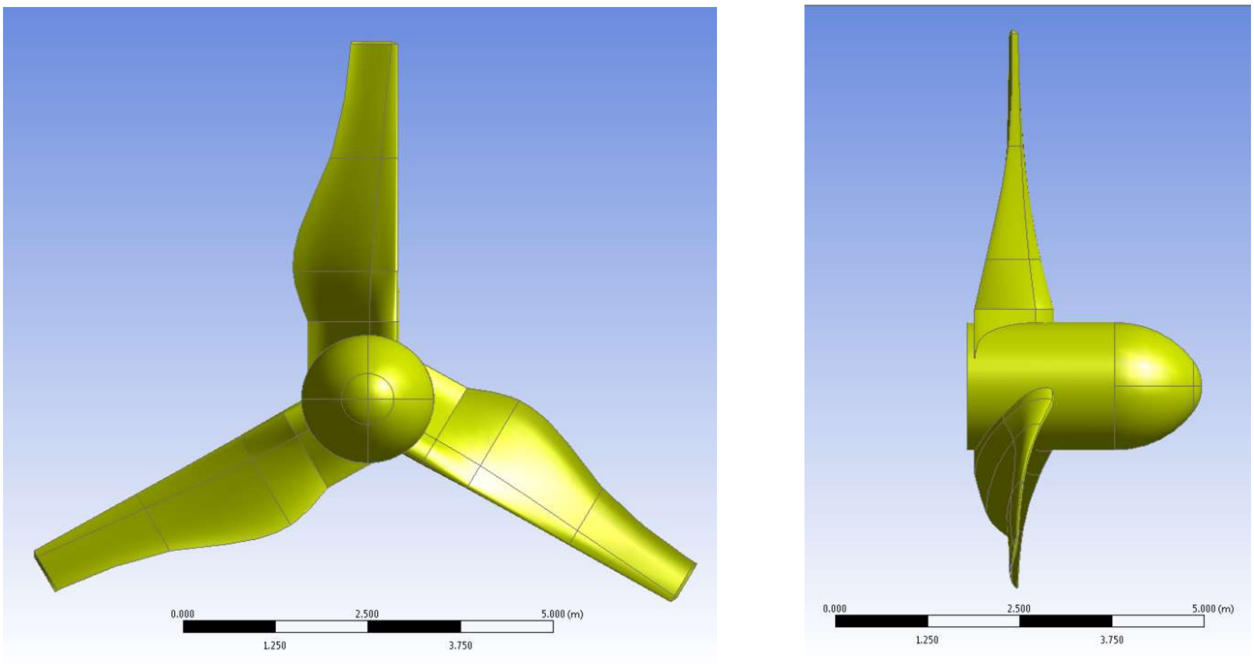

Figure 4.3 Modified Turbine Geometry

4.1.2. Support Structure Geometry

Previous work (Mason-Jones, et al., 2013) identified the cylindrical support structure offered the advantageous performance-cost benefits, being geometrically simple to manufacture whilst offering less interaction with the rotor performance and overall drag on the system. This shape was utilised in this study. From the literature review, however, a worst case scenario support structure and a realistic support structure were identified and modelled. These are described below.

4.1.2.1. Surface piercing monopile structure

The structure has taken from the early stage design by MCT used at Lynmouth (DTI, 2005), whilst this support structure design offers a worst case scenario for structure interaction. Being surface piercing increases the blade interaction and its diameter will emphasise the issue. The surface piercing monopiled cylinder, Figure **4.4** shows the turbine and structure with blade 1 of the turbine at Top Dead Centre (TDC). The diameter of the support structure is 2.4 m and was located at three different distances upstream or downstream of the turbine. The distances from the centre of the support structure to the trailing edge of the blades has been identified by notation L_i and has been varied equally upstream and downstream. The three distances from this point on will be known as L_1, L_2 and L_3 which correspond to 1.8 m, 2.8 m and 3.8 m separation respectively. This notation will be used throughout chapter 5.

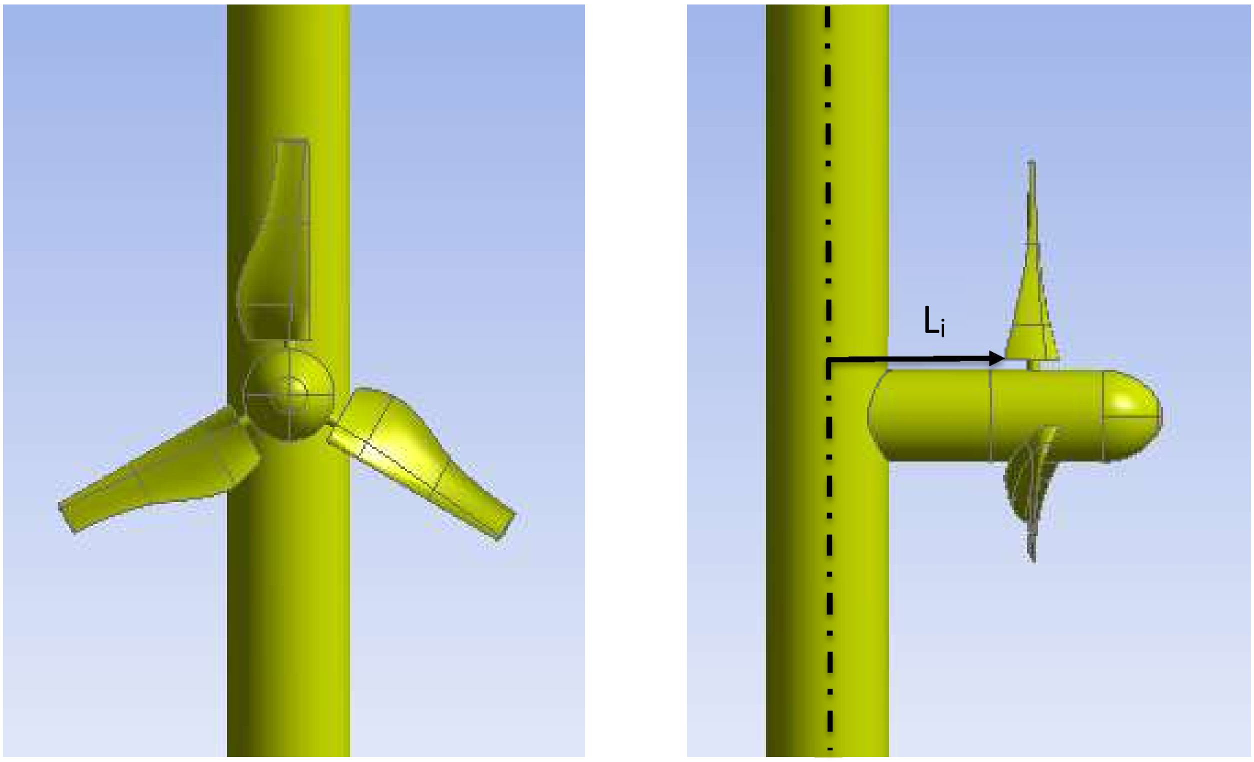

Figure 4.4 Monopile Structure

4.1.2.2. Tubular tripod structure

A less intrusive design was then also identified from literature and a replication of the Alstom support structure used at EMEC was modelled (see section 1.3.3.2 for more details). The design has a tripod structure about a central cylindrical support. The diameter of the central support is 1.5 m and the dimensions of the tripod have been included in Table 4.1. The modified turbine rotor is featured on this support structure as can be seen in Figure 4.5, the stanchion to rotating plane of the turbine is 1.36 D_{St} Upstream. The tripod structure does not interact with the blade passage, as the connection meets the structure 5 m below the axis of rotation. However, they were included in the model in order to ensure no interaction was made.

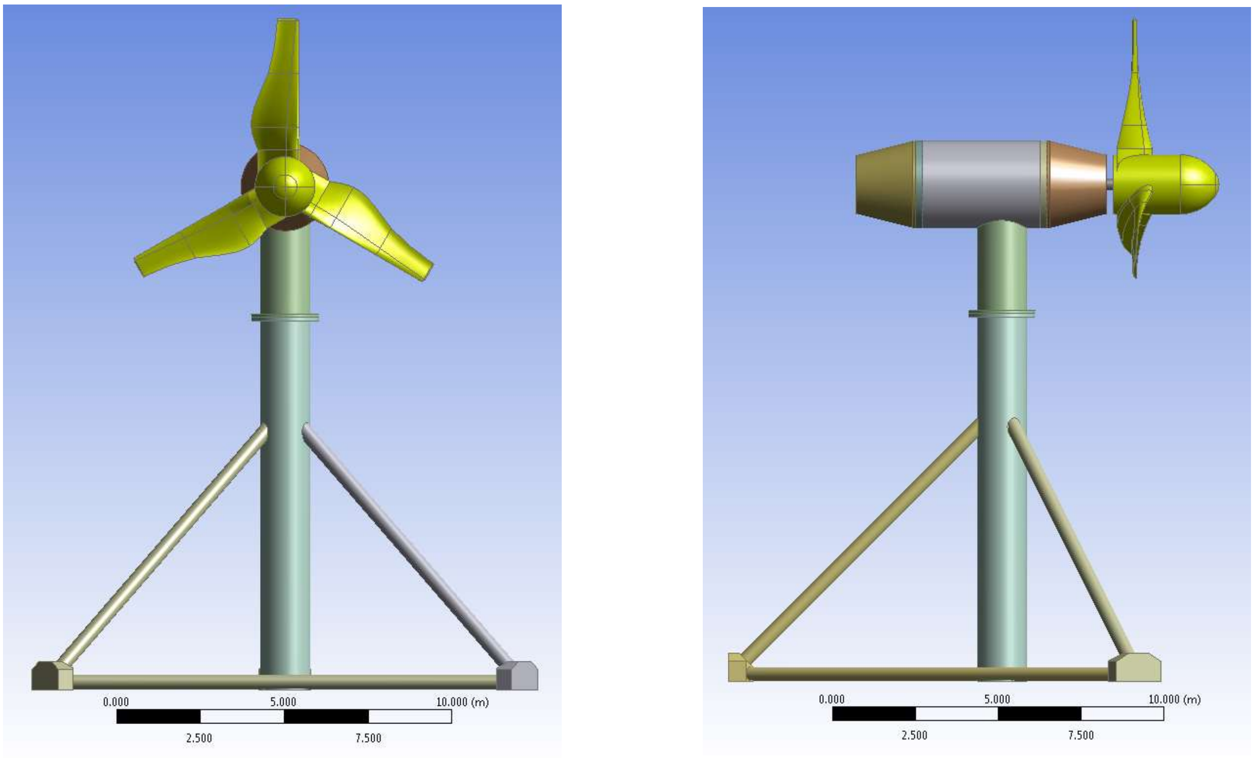

Figure 4.5 Tubular Tripod Structure Geometry

This geometry was modelled with various angles of misalignment between the principle flow axis and the rotational axis of the turbine, also referred to as yaw angles. Figure **4.6** illustrates this misalignment, where the angle, α is the yaw angle of the turbine and the sign convention for positive and negative yaw is established, negative being clockwise rotation and anti-clockwise being positive, when viewed from above. The green arrow shows the principle flow direction whilst the red lines identify the yawed turbine’s axis of rotation. Studies were performed for yaw angles, α = 0°, ±10°, ±15° and ±20°. This range was decided from cases identified in literature (see section 2.4.2 and 0) as likely to occur.

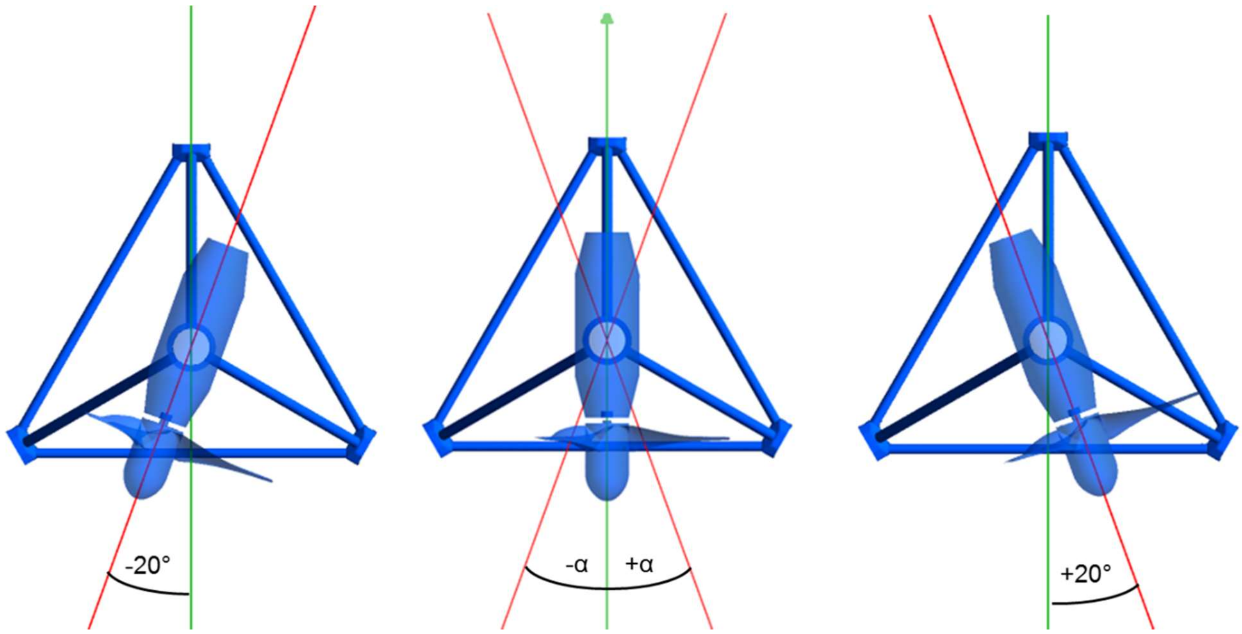

Figure 4.6 Identifying the Yaw Angle of a Turbine

4.1.3. Nacelle Evolution

The previous generation of the lab scale turbine used in previous work had a profiled nacelle which was the same diameter as the hub (Morris, 2014). The experimental turbine used in this thesis defined in Section 7.1 has a greater diameter nacelle than hub, with a taper section providing a linear transition between the hub diameter and full nacelle diameter. Table 4.1 displays the nacelles principle dimensions for the 10 m scaled model. In the numerical model a taper section was also included to the rear of the nacelle, this has the same geometry as the front taper section and was included in the scale model to offer a more realistic and hydrodynamic geometry.

Table 4.1 Tripod Support Structure Details

Geometry	Dimension	Value (m)
Central Support	Height (to axis of rotation)	15
	Diameter	1.5
	Distance to blades (from centre)	2.8
Angled supports	Length	12.5
	Diameter	0.35
	Connection Height (above seabed)	10
Horizontal supports	Length	15
	Diameter	0.35
Nacelle	Length	7.75
	Diameter	2.8

4.1.4. Rotating Domain

The cylindrical rotating domain encapsulates the turbine as shown in Figure 4.7 b, with a diameter of 14 m and a length of 5 m as recommended in previous work (Mason-Jones, 2010). The interface between this rotating domain and the stationary control volume is achieved by subtracting the rotating domain from the control volume using the Boolean function. This causes the surfaces of the rotating domain and the stationary control volume to occupy the same space. The interaction between the mesh at these surfaces is then controlled by the General Grid Interface GGI function of ANSYS CFX. This function allows the mesh of two surfaces that are connected to interact at the non-conformal interface (Ansys, 2015). This function was also applied between the turbine rotor and the cylinder.

4.1.5. Control Volume

The rotating domain encloses the turbine and has a non-conformal boundary considered later in Section 4.3.4, Figure 4.7 b) shows this. The control volume or ‘sea domain’ has boundary conditions on its external faces and encloses both the support structure, rotating domain and turbine as shown in Figure 4.7 a). The flow conditions were set at the inlet boundary upstream of the turbine and outlet boundary, downstream of the turbine. The control volume has a *height* x *length* x *width* of 60 x 400 x 100 m respectively. The cross-sectional area of the control volume is greater than those defined by previous studies (Mason-Jones, et al., 2013); the reason for this is to avoid wall interactions in the presence of the larger support structure. The turbine resides 100 m or 10 D (where D is turbine Diameters) downstream of the inlet and along the central plane of the model, 15 m above the seabed.

The Cartesian co-ordinate system used in all the models maintains the same reference system with X, Y and Z directions corresponding to U, V and W velocities.

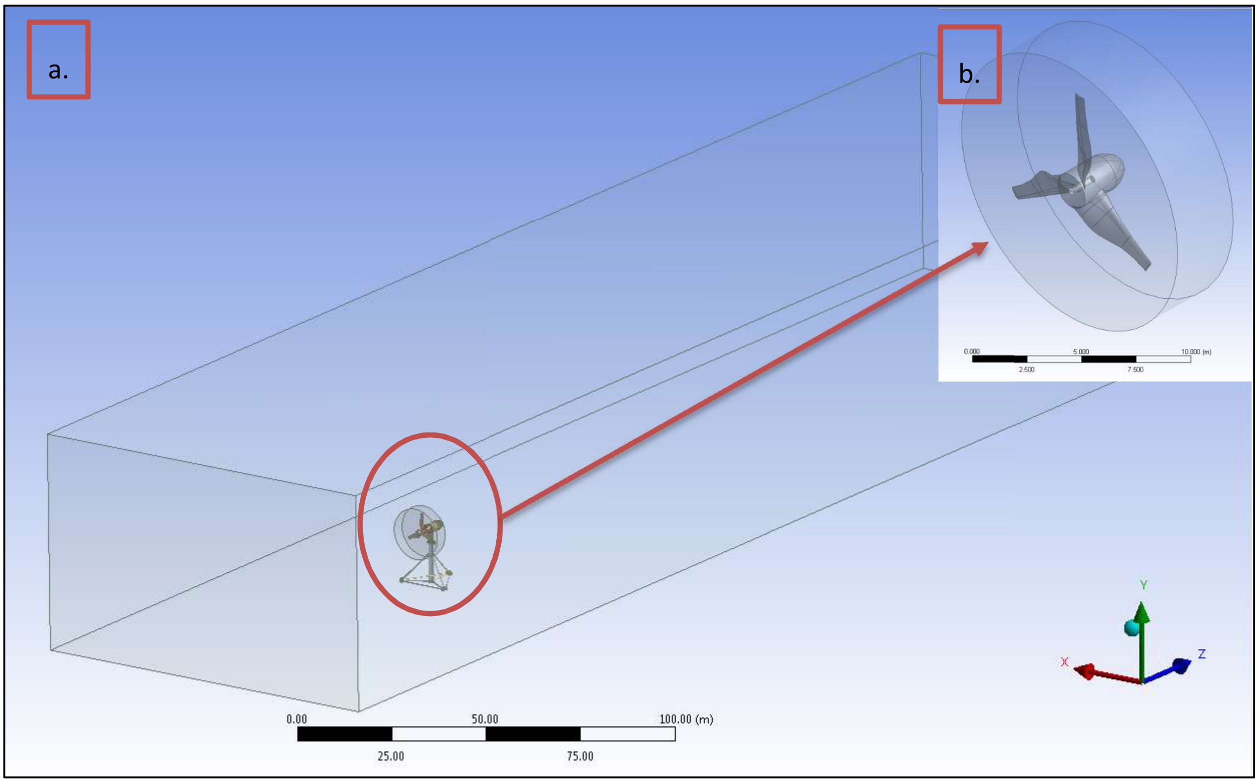

Figure 4.7 a) Control volume b) Rotating Domain, Turbine and Support Structure

4.2. Mesh

In order to solve the Navier-Stokes equations across the flow field of a model the domain is divided up into elements. For a 3D model these elements can be four shapes as seen in Figure **4.8**, the elements contain nodes at each corner, mid-length and centre (Ansys, 2015). The equations described in section 3.2 are calculated for each one of these centre nodes and this is used to generate the velocity, flow field and pressure distribution throughout the domain. In this section the mesh of the steady-state and transient models will be described. Due to different geometries however, the mesh metrics for each scenario differed. Nonetheless each mesh was deemed to lie within acceptable mesh quality metrics. The metrics used to assess the mesh quality were; number of elements, element skewness, and y^+. Skewness is a metric which defines how close to equilateral an element is. As defined in ANSYS help ‘a value of 0 indicates an equilateral cell and a value of 1 indicates a completely degenerate cell’ (Ansys, 2015). For this metric any cell with a skewness higher than 0.7 has been considered poor (Ansys, 2015). The y^+ is a post-processing metric and is defined in section 3.3.3, and was obtained from the stead state models run. These were recorded for both the control volume and rotating domain (see section 4.2.2.1 & 4.2.2.2).

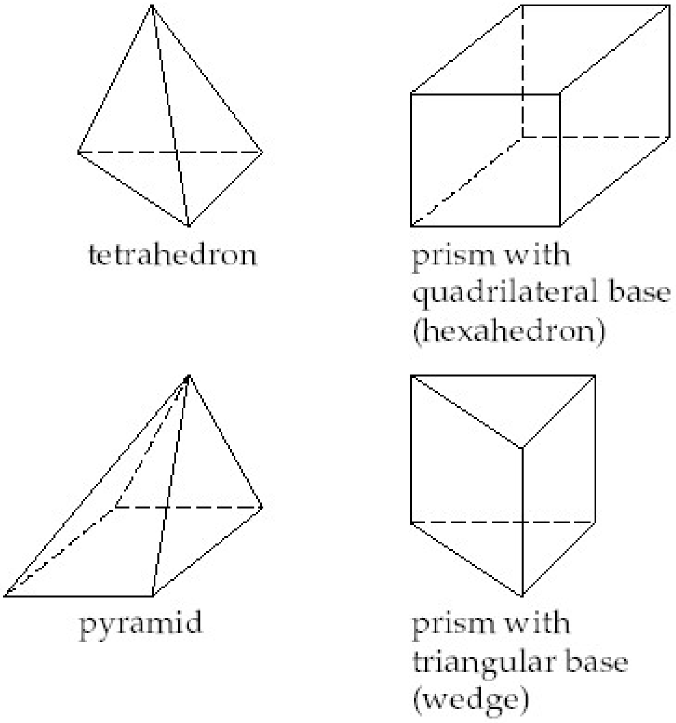

Figure 4.8 Mesh Element Shapes

4.2.1. Global Mesh Controls

The global mesh control was used to set parameters which influence the mesh structure across all the domains. Whilst ANSYS Meshing features a host of global mesh controls only those changed from the default settings will be commented on here. These controls remained common across all geometries.

The advanced size function was set to ‘On: Proximity and curvature’. This mechanism refines the number of elements set in the gap between two geometric entities as well as the ‘angles between normal for adjacent mesh elements’ as defined in Ansys Help (Ansys, 2015). The relevance centre refines the fineness of the mesh throughout the entire domain. Setting the relevance centre to ‘fine’ will increase the number of elements throughout the domain and specifically in areas of close proximity and tight angles. Ultimately this increases the accuracy of the results, however it costs in time and computational resource due to the larger mesh density, resulting from the increased number of cells.

The growth rate is also controlled by these parameters and by default would have a value of 1.2, however this was reduced to 1.1 which means with every successive layer away from a surface the edge length of the element will grow by 10% as suppose to the original 20% set. This will increase the fineness of the mesh about the surfaces of faces and improve the y^+ value.

No further functions were changed from the default in the global mesh controls.

4.2.2. Local Mesh Controls

These controls are applicable to identified features within separate domains, such the turbine blades and support structure. Both single and multiple nodes, edges, surfaces or bodies can be used to control the mesh, these options are identified in Figure 4.9. In these cases the same parameters were used for the control volume and rotating domain as detailed in sections 4.2.2.1 and 4.2.2.2. However due to changes to the turbine, nacelle and support stanchion geometries there were differences in the local mesh controls as detailed in section 4.2.2.3.

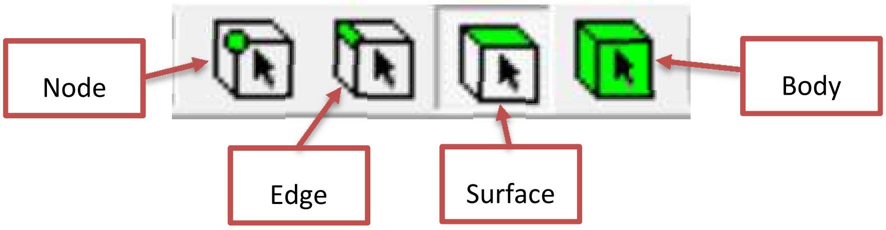

Figure 4.9 Local Mesh Control Tools

4.2.2.1. Control Volume

The mesh in the control volume consists of tetrahedral elements. Previous work (Mason-Jones, et al., 2013) made use of a ‘Body of Influence’ such as a cylinder running the length of the domain. This was used to structure the elements with a higher mesh density in the cylinder and a growth rate reducing the density with radial distance out from the cylinder, hence also improving the wake resolution in the results. A ‘Sphere of Influence imposes a local maximum size on all elements that are inside the boundary of the body’ as defined by Ansys Help Manual (Ansys, 2015).

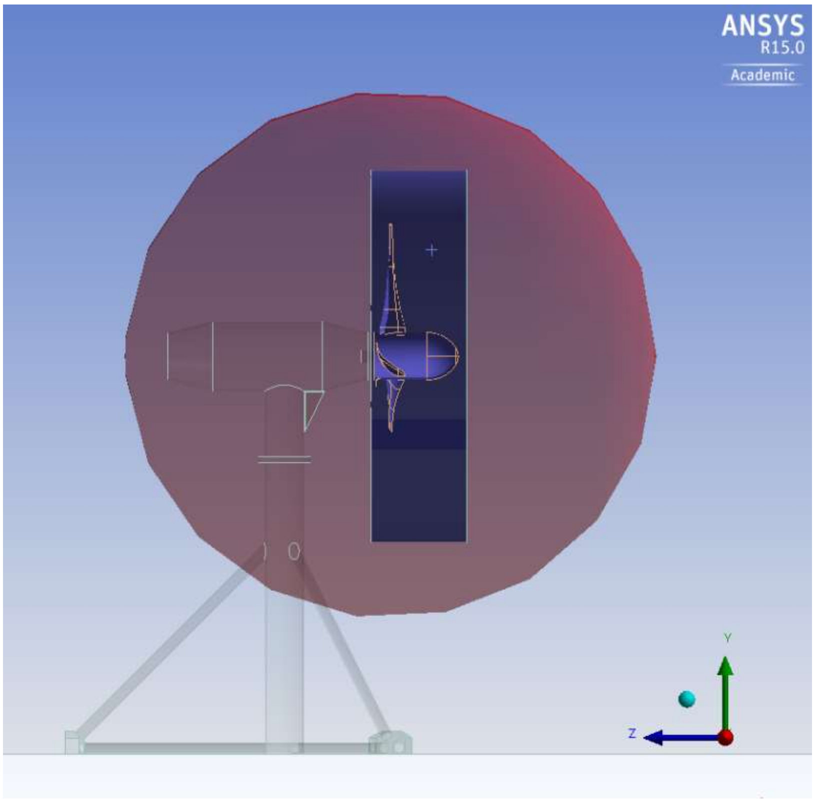

Figure 4.10 Sphere of Influence and Face Sizing’s

As the work in this thesis predominantly focuses on the interaction between the support structure and the turbine, the wake resolution beyond the hindmost part of the geometry was not prioritised, hence the use of a sphere of influence. The spheres centre was placed on the axis of rotation at the point where the blades connect to the hub. The radius of the sphere was set to 10 m, so that it envelopes the turbine blades and upper part of the support structure which interacts with the blades, as seen by red sphere in Figure 4.10. The element size was set to 0.2 m. This improves the fineness of the mesh locally between the turbine and support structure. The behaviour of the sphere of influence was set to soft, in order to avoid local face sizing’s and other body sizing’s being overridden.

In addition to this, the outer faces of the cylinder surrounding the rotating domain lie in the control volume. These three faces were given a face sizing of 0.2 m and have been shown by the purple area in Figure 4.10. A face sizing restricts the max edge length of the elements on this face, in this case to 0.2 m, which matches the faces sizes on the inner surface of the sphere of influence. The total number of elements in the control volume came to ~7.5 M with less than 0.1% of elements with a skewness greater than 0.7.

4.2.2.2. Rotating Domain

A body sizing of 0.2 m was used on the rotating domain to match the 0.2 m faces sizing applied to the outer faces in the control volume. This provides a consistency in the element sizes across the interface boundary which improves interpolation issues either side of the interface. A ‘patch conforming’ was applied to the body to ensure all faces are tetrahedrons, matching the external faces. Figure 4.11 shows the surface mesh, which matches the interface boundary. The small hole located at the centre of the flat surface in Figure 4.11 is the hole where the driveshaft crosses the interface boundary and therefore no mesh exists at this point.

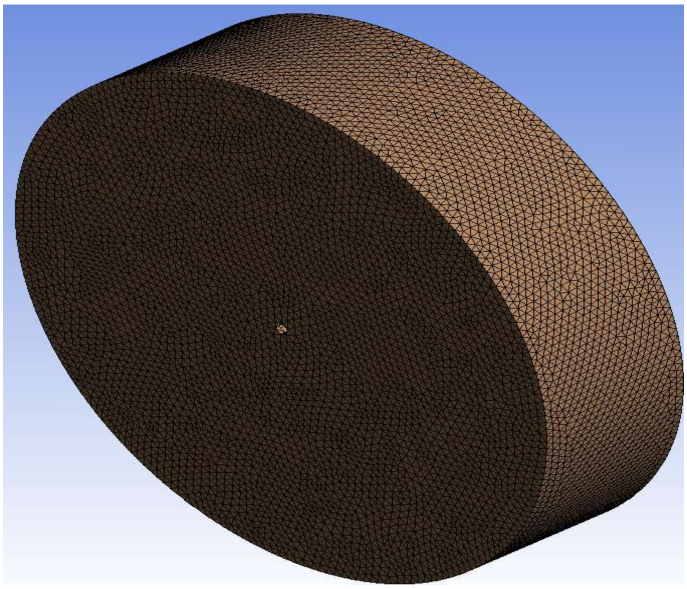

Figure 4.11 Surface Mesh of Rotating Domain

4.2.2.3. Turbine Geometry

The turbine geometry was meshed using multiple face sizing’s along the length of the blade and the hub, as well as using mapped meshes for the hub. Figure 4.12 a) identifies the 3 areas of meshing along the blade; the tip, middle and root. The concentration of smaller elements is made at the tip of the blades where the highest fluid velocities would be; the blade tips having a face sizing of 0.03 m, the blade middles having a face sizing of 0.06 m and the blade roots having a face sizing of 0.09 m. There is an inflation layer across the surface of the blade with a first layer thickness of 0.004 m followed by 10 successive layers with a growth rate of 1.1. These parameters were informed from previous work (Mason-Jones, 2010; Morris, 2014) which showed mesh independency. This was set in order to reduce the y^+ near the surface of the blade as much as possible, and resolve the boundary layer. The hub has a face sizing of 0.2 m. These local controls used tetrahedral, prism/ wedge and pyramid elements.

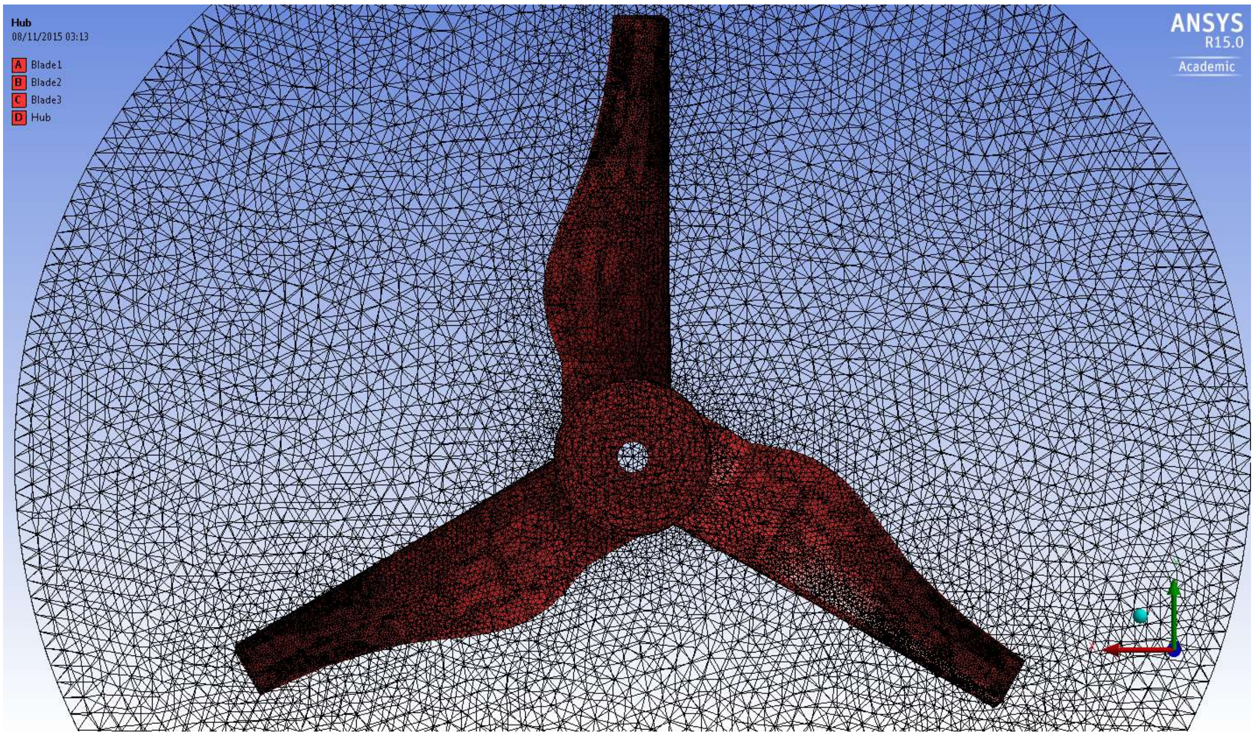

Figure 4.12 Turbine Rotor Surface Mesh

The rotating domain consisted of ~2.1 M elements, with 0.74% of the elements with a skewness of 0.7 of greater. The location of these elements is important, avoidance of poor elements on the leading edge and tip of the blade is important. The tip region of the blade is the source of the turbines greatest torque and thus power. Also the leading edge of the blade is critical to blade performance and poor mesh resolution here would reduce the accuracy of the solution. Figure 4.13 shows the distribution of elements with a skewness ≤0.7. It can be seen they are disbursed throughout the rotating domain and not concentrated about any geometrical feature. The y^+ on the leading edge of the blade and near the tip of the blade is 500 whilst the y^+ reaches 1500 at the root of the blade which is greater than the recommended y^+ identified in section 3.3.3 and in previous work on this turbine (Morris, 2014; Mason-Jones, 2010). However as it is less relevant region than the tip of the blade, this was considered acceptable. The nacelle and support structure surfaces were all meshed with a 0.2 m face sizing matching that of the hub and sphere of influence.

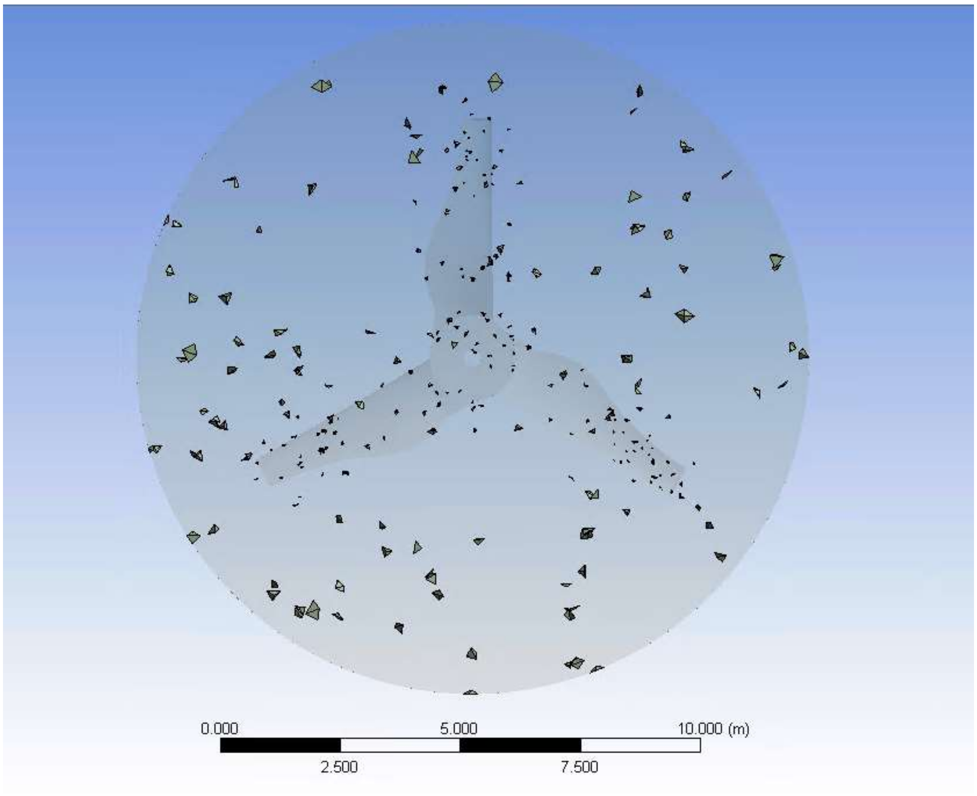

Figure 4.13 Skewness values higher than 0.7

4.3. Pre-processing

Before the numerical model simulation could be run, the physics of the problem to be solved had to be defined. This included all boundary conditions in the system as well as specification of the analysis and solver types. All of these parameters are defined in this section using the ANSYS CFX pre-processing software.

4.3.1. Analysis Type:

A steady-state (which is a time independent model) or a time dependent transient model can be run with ANSYS CFX. These options were utilised in the study for reasons discussed in each subsection.

4.3.1.1. Steady-State Model

ANSYS CFX uses a 'fully-coupled' solver, where the three-dimensional velocities and pressure are resolved simultaneously (Ansys, 2015). For a steady-state model this reduces the number of iterations, relative to other CFD codes which uses a linear, or semi-coupled solver where the pressure is guessed and then corrected in the next iteration. ANSYS FLUENT is an example of this solver approach (Ansys, 2015). ANSYS CFX steady-state models require no ‘real time’ information and instead operate on a pseudo time in order to solve the RANS equations (Ansys, 2015). The higher-order temporal features of the RANS equations are ignored simplifying the model and allowing convergence to be obtained quicker. The consequences of this are convergence problems if the flow contains temporal features. Identification of temporal features preventing convergence can be made manually by adjusting the pseudo time, if the period of the oscillation in convergence remains the same then it is a transient feature and must be run using the transient model type (Ansys, 2015). Due to the relatively in-expensive computational cost of this solver method, an initial insight into the performance criteria of the model was possible. Whilst a sufficient level of confidence was achieved and with awareness of potential temporal features preventing convergence, this solver method was selected for initial investigations of the different cases.

As previously mentioned in steady-state models a pseudo time is used. This term by default is an automatically assigned based on equation [4.1]. When the time step size is assigned manually it is recommended to assign δ upon a characteristic length (Ansys, 2015) and U as the mean velocity.

$$\Delta t \approx \frac{\delta}{U} \qquad [4.1]$$

Given the chord length of 0.896 m for the 10 m diameter turbine at 70% of the radius, as found in Table 0.1, in appendix and typical inlet velocity of 3.086 ms^{-1} in previous work (Mason-Jones, et al., 2013; Morris, 2014) the pseudo time was around 0.3 s. However it was found that the auto timescale was set to a much smaller value of 0.03 s by the ANSYS solver. Occasional cases where convergence proved to be an issue a manual time step size was applied, and half the auto timescale was used to improve convergence, or identify temporal features preventing convergence.

4.3.1.2. Transient Model

The advantages of the transient model are its use of real time information in which the model can capture the behaviour of temporal features in the flow field. The cost of this however is the requirement of additional computational power, memory and time to run the simulations. Therefore this analysis type was limited to use in specific cases where further details on temporal behaviour were required.

For transient analysis types the time-step size was a pre-defined parameter and was set by estimating a suitable time step size using equation [**4.1**]. Given the demand on computational resources from transient models a larger timescale than the auto timescale given to the steady-state models was set. As the number of rotations required in the transient model before results could be considered, the directionality study used values approximately 4 x greater, giving a Δt = 0.125 s. As discussed in results section 5.2.5, this time step size proved too course for transient solutions. Therefore in the subsequent transient models presented in Chapter 6 a finer time step size was used to give greater temporal resolution, at greater computational expense. To do this and maintain a reasonable overall simulation time the time step size was maintained as 0.125 s for the first 7 rotations of the simulation and then reduced for the final two rotations of the run to Δt = 0.025 s giving five times the temporal resolution. Results were only saved for the final two rotations of the model. The impact of changing the time step size on the model simulation period was significant with simulations exceeding 36 hour periods on the high performance computing machines.

4.3.2. Domain Properties and Fluid Models

The domains, both stationary and rotational were set with common fluid properties. The fluid was set to water and the relevant properties of this default fluid can be found in Table **4.2**.

Table 4.2 Default Properties of Water **(Ansys, 2015)**

Property	**Value**	**Units**
Density	998.2	$kg.m^{-3}$
Molecular weight	18.015	$kg.kmol^{-1}$
Viscosity	0.001003	$kg.m^{-1}.s^{-1}$
Reference Temperature	298	K

The buoyancy model was switched off as was the heat transfer functions, as these were deemed insignificant for the problem and would only add to computational time and expense. The turbulence model used was the k-ω Shear Stress Transport (SST) model, as described in section 3.2.

4.3.3. Boundary Conditions

The boundary conditions for the model vary depending on the case, however the inlet and outlet conditions were held constant.

4.3.3.1. Inlet Boundary

The inlet boundary face was set to have a constant velocity entering the control volume domain at 3.086 ms^{-1} which is the equivalent of 6 knots and is a good approximation of typical tidal flow available around the UK waters (Mason-Jones, 2010; Mason-Jones, et al., 2012). The turbulence intensity value at the inlet was set to 10% however as discussed by Morris (2014) most of the turbulence dissipates from the flow before reaching the turbine. The turbulence intensity at the plane of rotation is 0.1% which can be considered negligible.

4.3.3.2. Outlet Boundary

The outlet boundary was set to a pressure outlet and given a static pressure of 0 Pa. This offers no resistance at the outlet boundary and given the reference pressures in the domains was also set to 0 Pa, the only induction of flow comes from the inlet.

4.3.3.3. Walls and Surfaces

The boundary walls of the control volume were considered to be 'free slip' surfaces. This applies zero shear stress at the wall which will avoid the creation of a boundary layer. The seabed, which is the bottom face of the control volume, was set as a no slip wall with smooth wall roughness, creating a boundary effect. This is the default setting applied to all the surfaces of the turbine and support structure also.

4.3.3.4. Initial Conditions

The initial conditions for the models were set as Cartesian velocity components, in order to achieve convergence quicker the w-component was set to the inlet velocity, 3.086 $m.s^{-1}$. Whilst the u and v components were set to 0 ms^{-1}.

4.3.4. Interface and Rotational Domain

The interface settings differ for stead state and transient models. The steady-state models use a 'Rotational Periodicity' model, by specifying the rotational axis the model maps and provides a rotational transformation for fluid passing between the domains (Ansys, 2015). In this instance the steady-state CFD will capture a snapshot of the performance of the model in the assigned orientation.

The transient models on the other hand use a 'Transient Rotor Stator' interface, this is a sliding mesh interface. The approach accounts for the relative motion between the domains and all fluid flow interaction at the interface boundary, this is updated each timestep. This method will capture the temporal features of the rotating domain and provide a more accurate solution. However the method has a greater computational demand.

The interface was applied between the three internal faces of the stationary domain (control volume) and the three external faces of the rotating domain as described in section 0.

The rotational velocity of the domain however was set as a domain property and was therefore common for both the steady-state and transient domains. This parameter was varied in order to get the range of Tip Speed Ratios required in accordance with equation [**3.18**] The range spanned from 0 - 5 rad.s^{-1} depending on the desired λ, for the 10 m diameter turbine.

4.3.4.1. Stead State Interface

The steady state interface uses a *frozen rotor* model to connect the two meshes at the non-conformal interface. This fixes the relative orientation of the turbine in the rotating domain, which in this case is with blade 1 of the turbine at Top Dead Centre, TDC, as seen in both Figure 4.4 & Figure 4.5.

4.3.4.2. Transient Interface

The transient interface uses a *transient rotor stator* model to connect the interface. This model simulates the true transient nature of the turbine's rotation. The position of the rotating domain relative to the stationary domain is updated every time step, the displacement was dependent on the rotational velocity, ω, which was pre-defined as mentioned above.

4.4. Solver

4.4.1. Convergence Criteria

The numerical model simulations were run on various machines depending on availability. The largest of which was the High Performance Computing Wales, HPCW cluster in South Wales called Sandy-Bridge. The cluster featured an access to 64 nodes on an ANSYS research licence enabling parallel processing capable of handling large models and with 1.6 MHz memory speed per processor (Fewings, et al., 2014). The CFX solver is a Fortran 77 code which takes the definition file that is created at the end of the pre-processing in ANSYS CFX and compiles the machine code which runs the simulation. This section will define the parameters set to determine model convergence for both the steady-state and transient model simulations.

The convergence criteria were set using the Root-Mean Square (RMS) residuals for the continuity equation and the momentum equation in the three principle Cartesian axes against iteration count. These terms are defined in section 3.5. Different magnitudes were specified between the steady state runs and the transient models.

A convergence residual target of 1x10^{-08} was set for the stead state models. This criteria was set for all four equations. Where the residuals converged above the set criteria, however, these cases were assessed and accepted if the residuals became asymptotic to the x-axis around 1x10^{-06}. No convergence residuals target was set for the transient models, however the same convergence criteria was maintained. As can be seen from Figure **4.14**, the models were sitting at a converged value above 1x10^{-06} when the time step size was 0.1 s, however when the time step is reduced to 0.025 for the final two rotations the residuals drop and plateau below the 1x10^{-06} threshold.

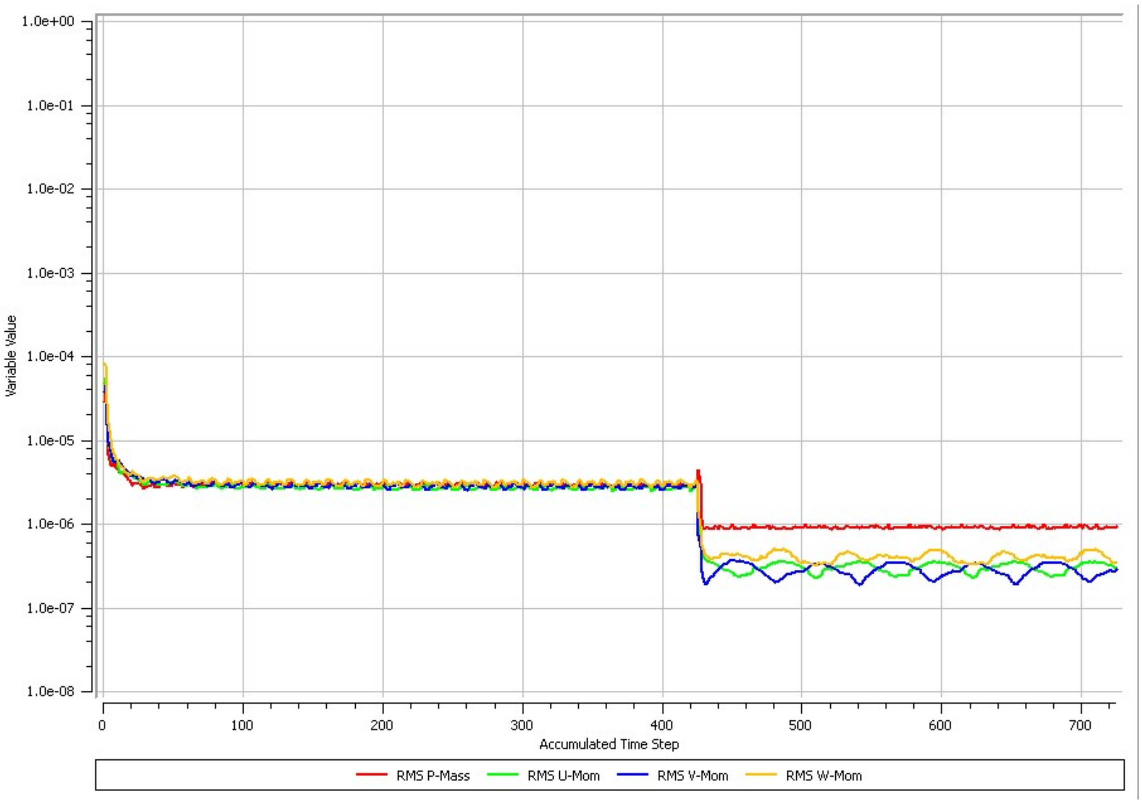

Figure 4.14 Continuity and momentum equation RMS residuals

Additional convergence criteria for both steady state and transient models were based on monitor points throughout the domain, plotting the velocity relative to the stationary domain against iteration/ accumulated time. The locations of these velocity points is shown in Figure **4.15** and are along the axis of rotation, 50 m upstream, 50 m downstream, 250 m downstream. Figure **4.16** shows a typical plot of the velocity monitors for a steady state run. The flow field is seeded throughout the domain with the initial values as defined in section 4.3.3, the velocity monitors therefore all begin at this initial value at the start of the iterations. Monitor point ’50m upstream’ remains at the inlet velocity through-out the run as it is upstream of any disturbance. However the downstream velocity monitor points each drop in magnitude as the wake of the turbine propagates downstream with every iteration or accumulated time advancement. Until a steady or repeating pattern is sustained, this is an indicator the model has converged for this part of the domain.

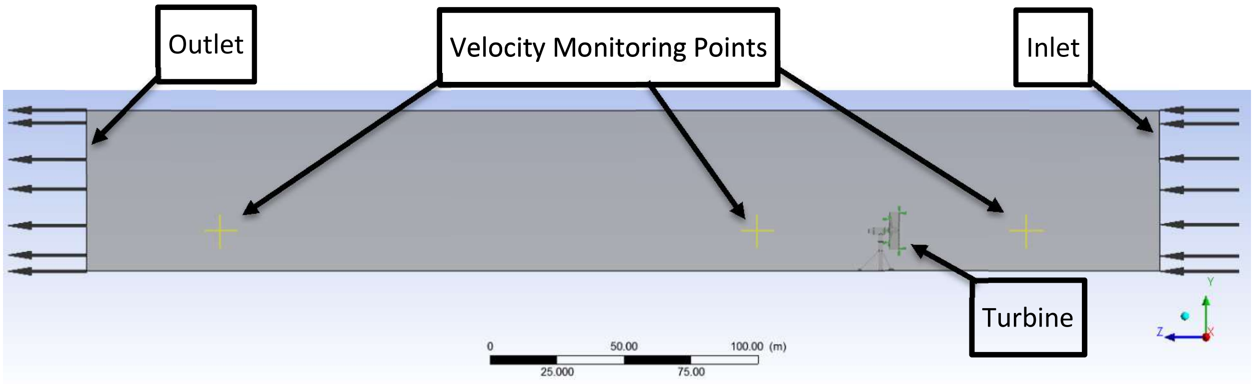

Figure 4.15 Monitor Point Locations in control volume

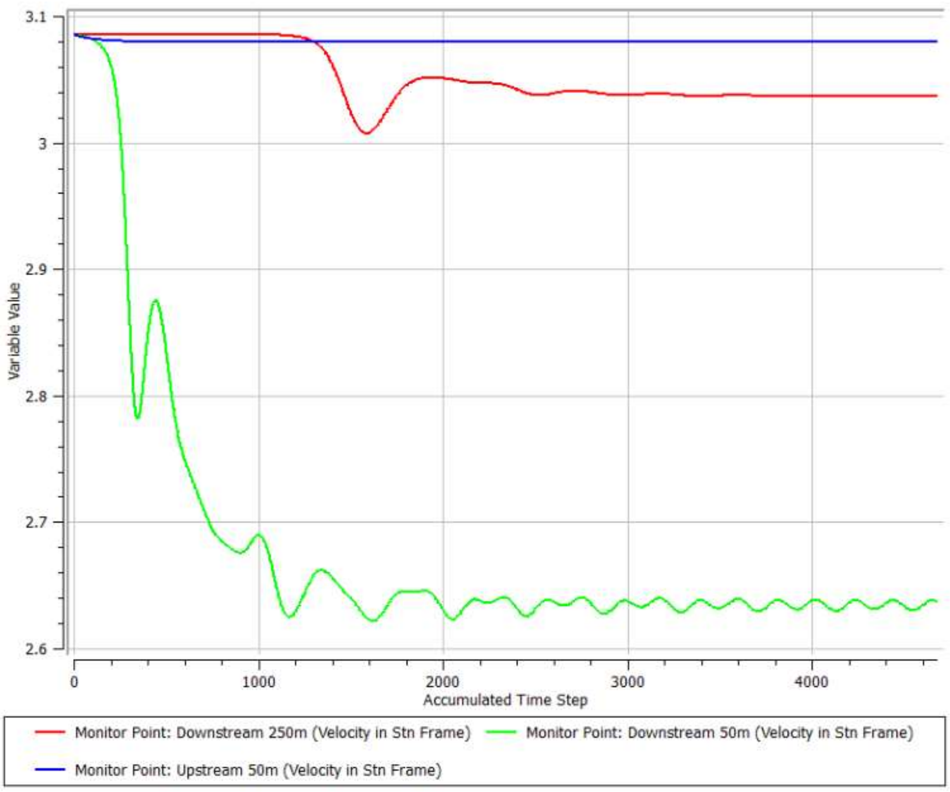

Figure 4.16 Velocity Monitors from Steady-State run

4.5. Post-Processing

4.5.1. Extracting Forces and Bending Moments

Once the solver was complete and the model converged, ANSYS CFD-Post software was used to extract the performance characteristics and other results. The performance characteristics were obtained through using a CFX Expression Language (CEL). These expressions are a function of CFD-Post and enable the thrust, torque and bending moment values to be extracted from specified geometry locators. For transient models these expressions can be plotted as a function of time and provide the temporal results. The expression statement consist of a series of functions as shown in equation **[4.2]**.

```
[<Phase>.]<Function>[_<Axis>[_<Coord Frame>]]()@<Location>
```

[4.2]

The ‘*Phase’* identifier is used for multiphase flow and so was not needed for the model outputs. The *Function*s used was either a force or a bending moment (in-plane or out-of-plane). The ‘*Axis’* in which the force was taken or about which the torque was taken is identified here. The ‘*Coord Frame’* refers to the co-ordinate reference frame and was taken as the global co-ordinates with the exception of models with turbines in axial misalignment. In which case a custom co-ordinate system was used in order to capture axial results. The '*Location*' refers to a surface location for which the results will be compiled, for example Blade 1, 2 and 3 were separate surfaces.

4.5.2. Calculating Torque, Power, Thrust and Out of Plane Bending Moment

CFD outputs were analysed to provide the performance characteristics identified in Section 3.3.3. The dynamic torque of the turbine is determined from the summation of the temporal or time averaged contributions from each blade and the hub. The power was calculated by multiplying the torque by the rotational velocity of the turbine. For thrust, the summation of all the forces in the axial direction on each of the blades and the hub was made. The resultant out-of-plane bending moment was calculated by outputting the bending moments for each of the blades about the x and y axis as outlined and identified in section 3.4.4 and Figure 3.2. The coefficient of the out-of-plane bending moment was then calculated using equation **[3.15**] & [**3.16**]. The direction of the resultant bending moment is calculated by equation [**3.17**].

The non-dimensional performance characteristics were then calculated from these values using equations **[3.12**] to **[3.18**], in Section 3.3.3.

4.5.3. Turbine Wake

The near field wake was considered in this study, although the domain was set up to capture 30 diameters downstream of the turbine. As shown in other work (see section 2.1) without realistic tidal flow conditions the wake details extend further downstream than is realistic. As the boundary flow inputs have been limited to a plug flow and a 10% TI, combined with the issues of TKE dissipation identified as an issue with the SST turbulence model, the wake extent downstream is expected to be an overestimate of a true tidal system. These limitations are recognised and therefore any studies into the velocity flow field is limited to near field where the shear stress forces remain dominant. Or in the case of far field effects, the wake is considered representative and can be used for comparative purposes between scenarios.

5. Directionality & Proximity Results

The Chapter compares the power performance of the 'base' case, that is the original turbine geometry as described in section 4.1.1, with previous work using the same geometry (Morris, 2014). The chapter continues with results and discussion showing the optimal proximity between the turbine rotor plane and its support stanchion. As well as establishing the effects of operating a turbine upstream or downstream of its support structure. Through these results and discussion the objective is to establish the preferential arrangement for both proximity and orientation of the turbine relative to the support structure. The results are separated into steady-state and transient components, the former provide insight across the whole operating range of the turbine whilst the latter specifically considers the peak performance case in more detail. Given the limitations previously discussed the wake characteristics of the various scenarios are also considered. The model geometry used is a stanchion which passes through the entire water column. The stanchion diameter, $D_{St} = 2.4$ m and the turbine was located at three distances either upstream (closer to the inlet than the stanchion) or downstream of the stanchion (stanchion closer to the inlet than the turbine). The three distances are $L_1 = 1.8$ m, $L_2 = 2.8$ m and $L_3 = 3.8$ m, as defined in Section 4.1.2. Further details on the steady-state model set-up parameters can be found in Section 4.3.1.1.

5.1. Steady State

The use of steady-state models was made to provide the non-dimensional performance characteristics of the geometry across a full range of λs. The turbine was orientated with a blade at Top Dead Centre (TDC) as described in Section 4.1.

5.1.1. Torque

The coefficient of torque, $C_{\theta.}$ was considered for the seven different geometrical scenarios identified and then repeated at various values of λ by varying the rotational velocity of the turbine, whilst keeping the inlet velocity and turbine geometry constant for each steady-state simulation run. Therefore the same mesh was maintained for the rotating domain for the remaining simulations and changes to the control volume mesh was made to accommodate the various stanchion geometries. Figure 5.1 shows the C_θ-λ performance for the no stanchion case and L_{1-3} downstream and upstream cases. The seven cases all follow the same trend, displaying three key points, the initial rise from λ = 0, where all the cases have slightly different start-up torques. Followed by a peak C_θ value between λ = 2- 2.5. Following this, all cases show a linear decline in C_θ as the turbine's rotational velocity increases. The point at which $C_\theta = 0$, is the freewheeling point. Whilst all the data sets, have this same trend, the specific values differ between cases and this is noteworthy. The reference case to which all the other cases were compared with is the no stanchion case. This has a start-up $C_\theta = 0.038$, which then increased to peak C_θ with a magnitude of $C_\theta = 0.116$ at $\lambda = 2.5$, before descending to $C_\theta = 0$ as the turbine approaches freewheeling at $\lambda = 6.8$. Table 5.1 shows the key differences between the cases from a numerical perspective. It is clear from both Figure 5.1 and Table 5.1 that the upstream orientation is preferred, in terms of the maximum torque, for all cases in comparison to their downstream counterparts. In the upstream orientation, the closer the proximity of the stanchion to the turbine, the greater detrimental impact is seen on the turbine's performance. In the downstream orientation this trend does not persist where case L_2 downstream has approximately 2% greater C_θ performance than the L_3 downstream case.

Table 5.1 Comparison of key points from C_θ - λ data sets

Case	Peak C_θ	Percentage drop	λ at peak C_θ
No Stanchion	0.116	0.0%	2.5
L_1 Upstream	0.096	17.2%	2
L_2 Upstream	0.106	8.6%	2.5
L_3 Upstream	0.109	6.0%	2.5
L_1 Downstream	0.088	24.1%	2
L_2 Downstream	0.094	19.0%	2.5
L_3 Downstream	0.092	20.7%	2.5

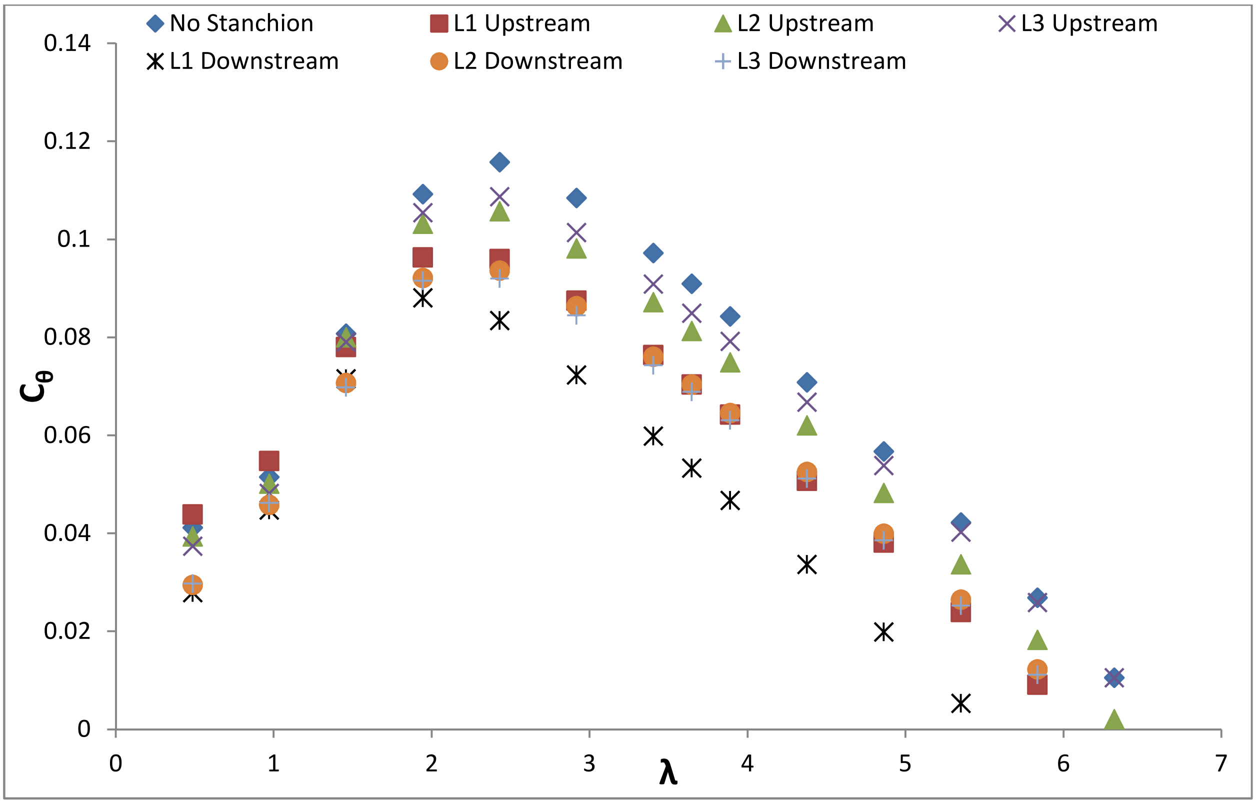

Figure 5.1 C_θ-λ for upstream and downstream cases at varying stanchion clearance distances

5.1.2. Power

Figure 5.2 shows the C_P-λ performance of the no stanchion case, with previous numerical modelling scenarios (Morris, 2014) using the same turbine geometry and similar set-up as described in Section 2.1.3. Both data sets follow the same trend with peak performance at λ = 3.65. The rise in performance with increasing λ is also similar, however the deviation as λ approaches freewheeling is apparent. This deviation was attributed to the different software used in the numerical modelling technique. This comparison shows caution must be taken regarding the freewheeling point and at high λ values. However as a comparison tool results around peak power performance can be considered to be consistent with previous work (Morris, 2014).

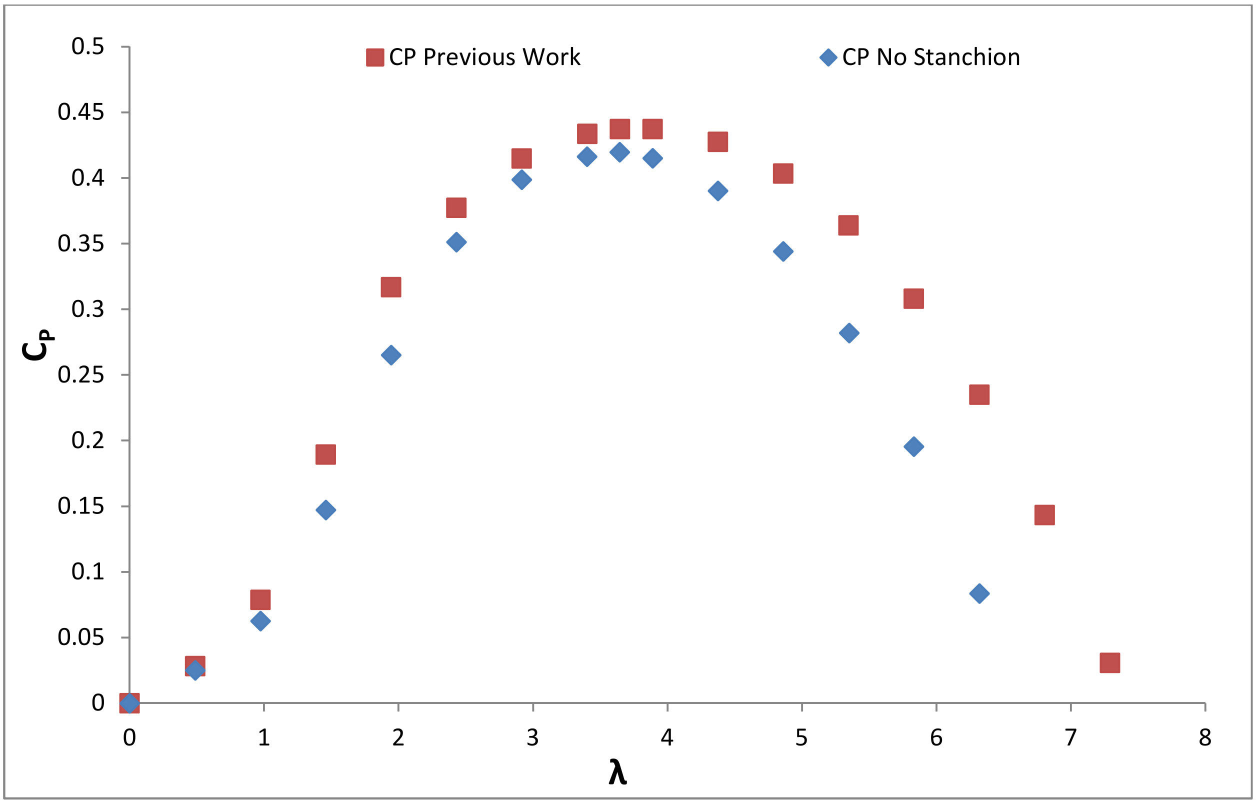

Figure 5.2 Comparison of same rotor geometry performance from previous work and current model

The coefficient of power (C_P) for the three proximities both upstream and downstream at the three distinct distances can be seen in Figure 5.3. As with the C_θ-λ curves, there is a distinct shape to all the data sets. The trend follows this pattern; $C_P = 0$ when the turbine is stationary and there is close C_P performance found between all cases at low λ. A rapid increase in C_P as well as divergence in the data sets is then found before plateauing to a peak C_P around λ= 3 - 4. The data points then decrease and converge somewhat as the turbine approaches free-wheeling at λ = 6.6.

From Figure 5.3 and Table 5.2 it is clear that the introduction of a stanchion can be seen to detrimentally effect the C_P. Table 5.2 shows that the upstream cases perform with greater C_P at each clearance distance than their downstream counterparts. It is also noted that with greater proximity between the stanchion and turbine, the greater is the detrimental impact on C_P. The exception to this trend however is the L_3 downstream case which has a 1% lower C_P than the L_2 downstream case.

Table 5.2 Comparison of key points from C_P - λ data sets

Case	Peak C_P	Percentage drop	λ at peak C_P	Freewheeling λ
No Stanchion	0.4196	0.0%	3.645	6.6
L_1 Upstream	0.3164	24.6%	3.402	6.2
L_2 Upstream	0.3605	14.1%	3.645	6.4
L_3 Upstream	0.3786	9.8%	3.645	6.6
L_1 Downstream	0.2585	38.4%	2.916	5.5
L_2 Downstream	0.3122	25.6%	3.645	6.3
L_3 Downstream	0.308	26.6%	3.402	6.2

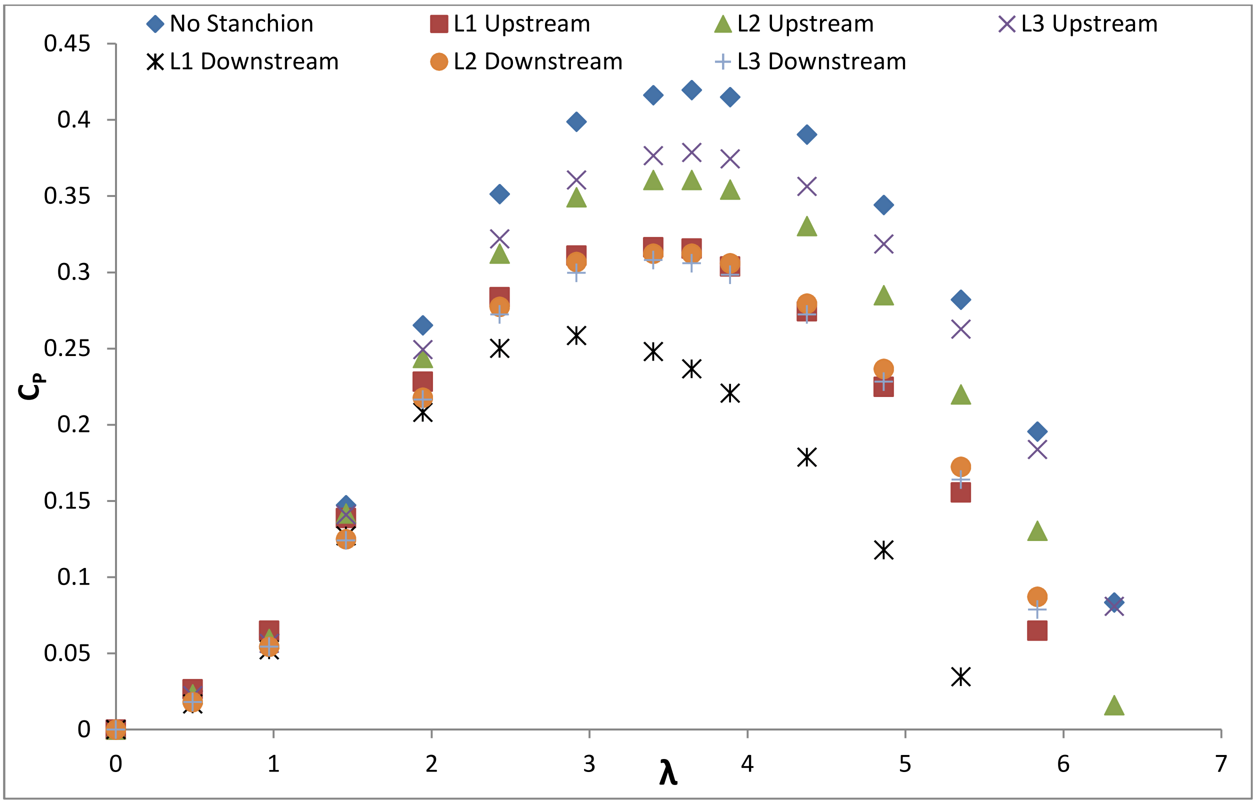

Figure 5.3 C_P-λ for upstream and downstream cases at varying stanchion clearance distances

5.1.3. Thrust

The coefficient of thrust, C_T for the No Stanchion and L_1, L_2 and L_3 cases both upstream and downstream are shown (Figure 5.4). The No Stanchion turbine had a $C_T = 0.248$ at $\lambda = 0.5$. C_T increases as the λ increases and begins to plateau as the λ reaches peak around 6.3 with a C_T of 0.844. The overall trend to the upstream and downstream cases is similar to the No Stanchion case. The upstream cases all have a greater C_T at start up at $\lambda = 0.5$. The increase in C_T as λ increase is greater for the No

Stanchion case and so at highest values of λ the upstream cases with greatest clearance distance (L_2 and L_3) are comparable to the No Stanchion case. These are followed by the L_2 and L_3 downstream cases which are the next lowest in C_T. The L_1 upstream is then next in magnitude followed by the L_1 downstream case. Table 5.3 shows the peak C_T values and percentage drop relative to the no stanchion case.

Table 5.3 Comparison of key points from C_T - λ data sets

Case	Peak C_T	Percentage drop	λ at peak C_T
No Stanchion	0.844	0.00%	6.5
L_1 Upstream	0.716	15.17%	6
L_2 Upstream	0.788	6.64%	6.5
L_3 Upstream	0.819	2.96%	6.5
L_1 Downstream	0.632	25.12%	5.5
L_2 Downstream	0.75	11.14%	6
L_3 Downstream	0.745	11.73%	6

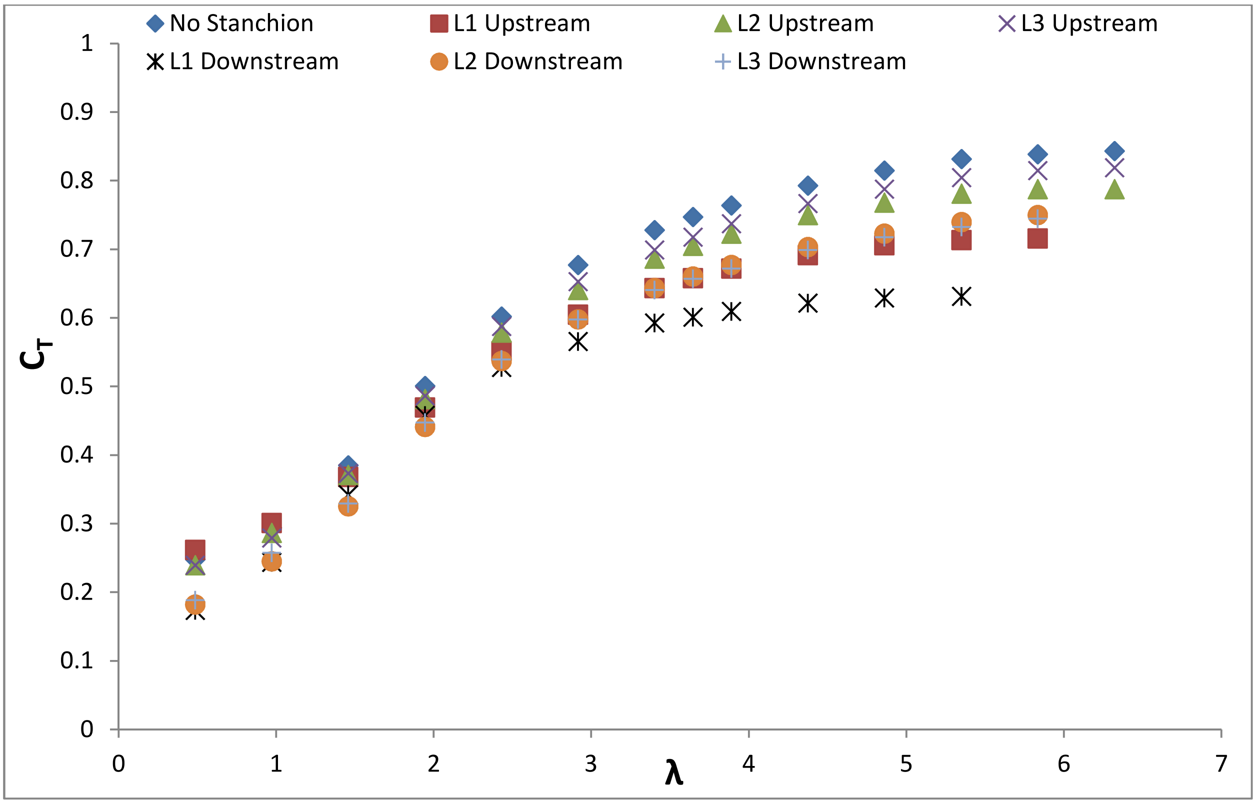

Figure 5.4 C_T-λ for upstream and downstream cases at varying stanchion clearance distances

5.1.4. Discussion

Sections 5.1.1 to 5.1.3 have established the significant detrimental impact of operating a turbine downstream of its support stanchion. It is clearly shown that for the C_θ and C_P characteristics, the downstream turbines continually underperform relative to their upstream counter-parts. It is noteworthy however that the L_2 downstream case performs better than the L_3 downstream case with respect to power and torque. This may be due to its placement coinciding with a vortex shedding, increasing the velocity locally. However since the difference is only slight it maybe within the tolerances of the CFD model. The magnitude of C_T in the downstream cases is lower, which is preferred.

In addition the closer the proximity of the turbine to the support structure, the greater the detrimental impact to the C_θ and C_P characteristics of the turbine. This has also been shown in small scale flume experiments (Walker, et al., 2015) which has already been considered (Section 0). Findings by Walker, et al (2015) concur with what the findings for the upstream cases in the above results. The C_P improves with increasing separation between the stanchion and the turbine up to a maximum clearance at L_3. The maximum clearance distance L_3 is equivalent to 1.6 D_{St} it is therefore expected that the reduction in C_P was not noticed as the results were still operating within the range of increasing performance. Caution must be taken however in comparing the turbine performance between different geometries at different scales, as discussed in Section 3.8. Similar characteristics have been identified in the wind industry with tower clearances of 1 to 1.5 stanchion diameters (Burton, et al., 2001).

5.2. Transient

To progress the understanding of stanchion interaction beyond previous work (Mason-Jones, et al., 2013), the turbine performance was studied during the rotation of the turbine in a transient model. The same parameters and geometry as the steady-state study was used. The transient models were simulated at a constant angular velocity of 2.25 $rad.s^{-1}$ ($\lambda = 3.65$), which equated to peak power.

The transient results shown in this section plot the non-dimensional performance characteristic against the rotational position of Blade 1. The azimuth, φ of blade 1 is considered for two complete rotations after the residuals have reached a stable convergence criteria, with 0° and 360° being blade 1 at TDC. The same seven cases are considered here as in Section 5.1, the No Stanchion case, the three upstream cases and the three downstream cases. The mean (μ) and standard deviations (σ) were taken using equations [**3.20**] and [**3.21**] from Chapter 2.6 across the plotted data range and not the complete data sets, to avoid skewed results from the start up.

5.2.1. Torque

The C_θ has been plotted against blade 1 azimuth, φ. Figure 5.5 shows C_θ for the No Stanchion case and L_1, L_2 and L_3 upstream cases. It can clearly be seen that the No stanchion case far exceeds the performance of the other cases. The mean values, plotted as dashed lines in Figure 5.5, show the increase in performance as the clearance between stanchion and turbine rotating plane increases. The amplitude of the fluctuations in the signal also reduces with the increase in distance. Table 5.4 shows the increase in the mean as the clearance distance increases. It also shows the diminishing returns, given by the percentage change in the mean value. Whilst the standard deviation was seen to be higher than the no stanchion case for the L_1 and L_2 clearance distances, however the L_3 appears to have a reduction in σ.

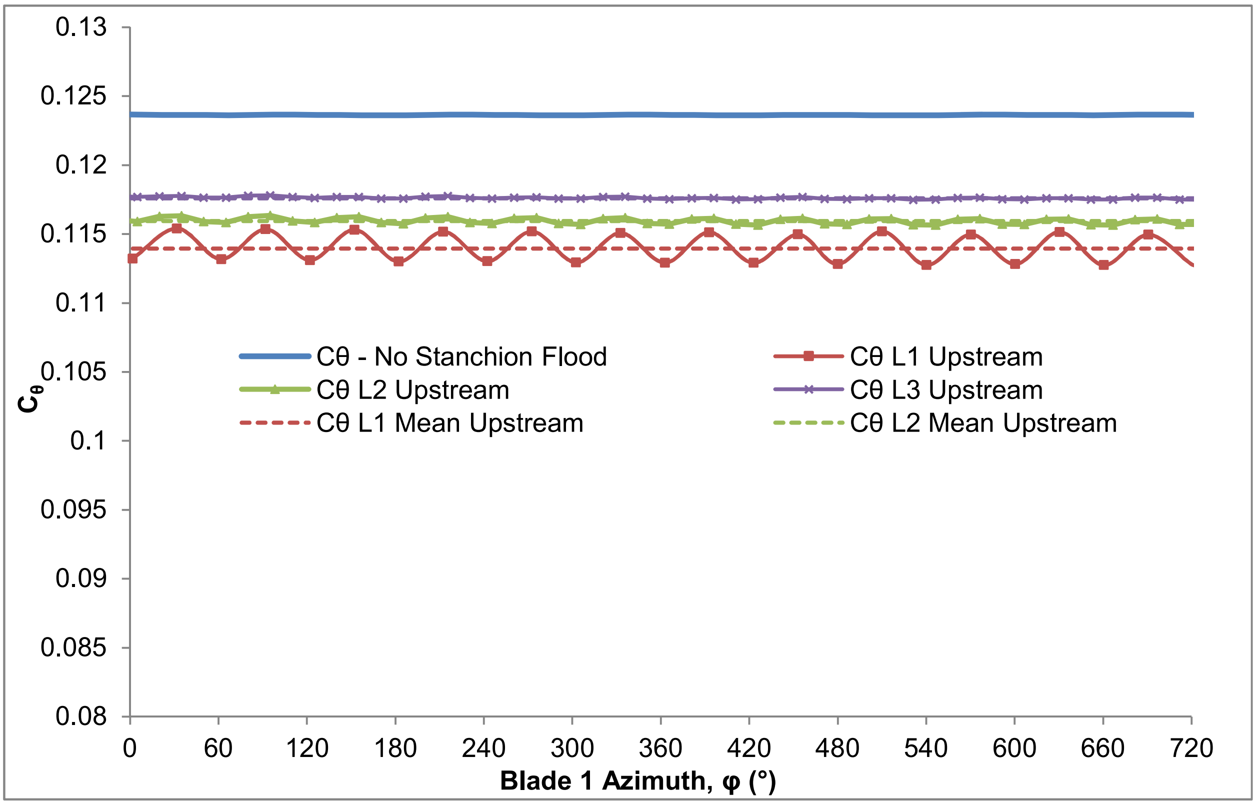

Figure 5.5 C_θ-φ for No Stanchion and upstream cases

Table 5.4 Mean and Standard deviation of upstream cases C_θ values and percentage change from no stanchion case

Upstream	**C_θ - μ**	**μ - percentage change**	**C_θ - σ**	**σ - percentage change**
No Stanchion	0.124	0.0%	0.0001606	0.0%
L_1	0.114	-8.3%	0.0008354	420.2%
L_2	0.116	-6.7%	0.0002049	27.6%
L_3	0.118	-5.4%	0.0000620	-61.4%

Figure 5.6 shows C_θ during two rotations of the turbine for the No Stanchion case and L_1, L_2 and L_3 downstream cases. The No Stanchion case is the same as in Figure 5.5 with a C_θ of 0.124 and negligible SD. Clearly the downstream cases show closer mean and higher amplitudes of fluctuations than their upstream counter-parts. The mean performances shown by the dashed lines are much closer. Table 5.5 showed that the mean values do not increase significantly with clearance distance. However it would appear the benefits of increased clearance distance on the standard deviation of the results improved significantly between L_2 and L_3 downstream.

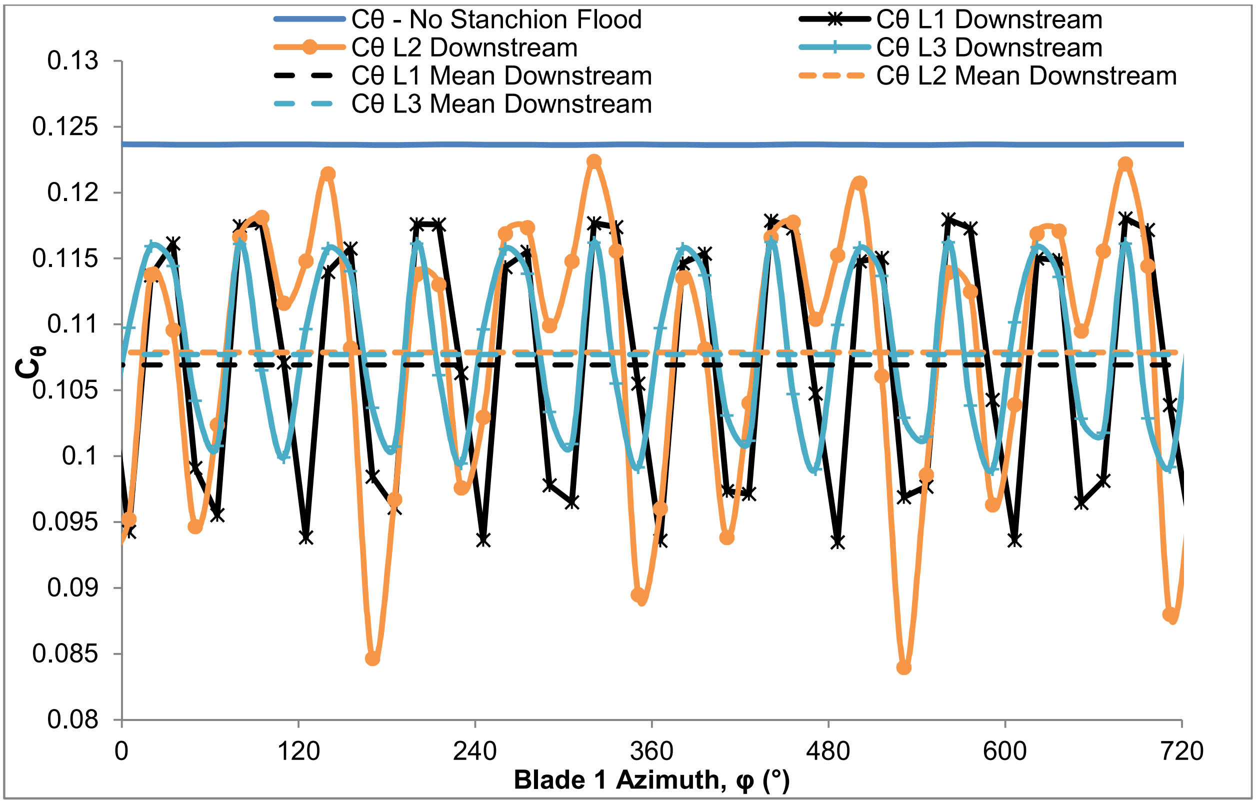

Figure 5.6 C_θ-φ for No Stanchion and downstream cases

Table 5.5 Mean and Standard deviation of downstream cases C_θ values and percentage change from no stanchion case

Downstream	**C_θ - μ**	**μ - percentage change**	**C_θ - σ**	**σ - percentage change**
No Stanchion	0.124	0.0%	0.0001606	0.0%
L_1	0.107	-14.2%	0.0098028	6004.6%
L_2	0.108	-13.0%	0.0099942	6123.8%
L_3	0.107	-13.6%	0.0065803	3997.8%

It is evident that the mean C_θ performance of the upstream turbines is greater than the downstream turbines for each of the proximities; L_1, L_2 and L_3. It is also clear that the σ of C_θ for the upstream cases is much lower than their respective downstream counterparts. The downstream cases have greater σ. The L_3 downstream case has the lowest σ, which is almost ten times greater than the worst upstream counterpart, L_1.

5.2.2. Power

The C_P is calculated in the same way as in Section 5.1.2, it is the product of the rotor torque and rotational speed of the turbine, divided by the theoretical available power. In this section it has been plotted against blade 1 azimuth. Figure 5.7 shows the No Stanchion case in comparison to the three upstream cases for two full rotations. The No Stanchion case shows the highest mean C_P of 0.423 and negligible SD over the two rotations. It is evident from the downstream cases that increase distance between the rotating turbine plane and stanchion benefits the mean CP of the turbine and reduces fluctuations. This is shown in the percentage change in performance as seen in Table 5.6. It was noticed from Table 5.4 and Table 5.6 that the percentage changes in the mean and standard deviation of C_θ and C_P were the same, and this is as expected.

Table 5.6 Mean and Standard deviation of upstream cases C_P values and percentage change from no stanchion case

Upstream	**C_P - μ**	**μ - percentage change**	**C_P - σ**	**σ - percentage change**
No Stanchion	0.423	0.0%	0.0005464	0.0%
L_1	0.388	-8.3%	0.0028424	420.2%
L_2	0.394	-6.7%	0.0006971	27.6%
L_3	0.400	-5.4%	0.0002109	-61.4%

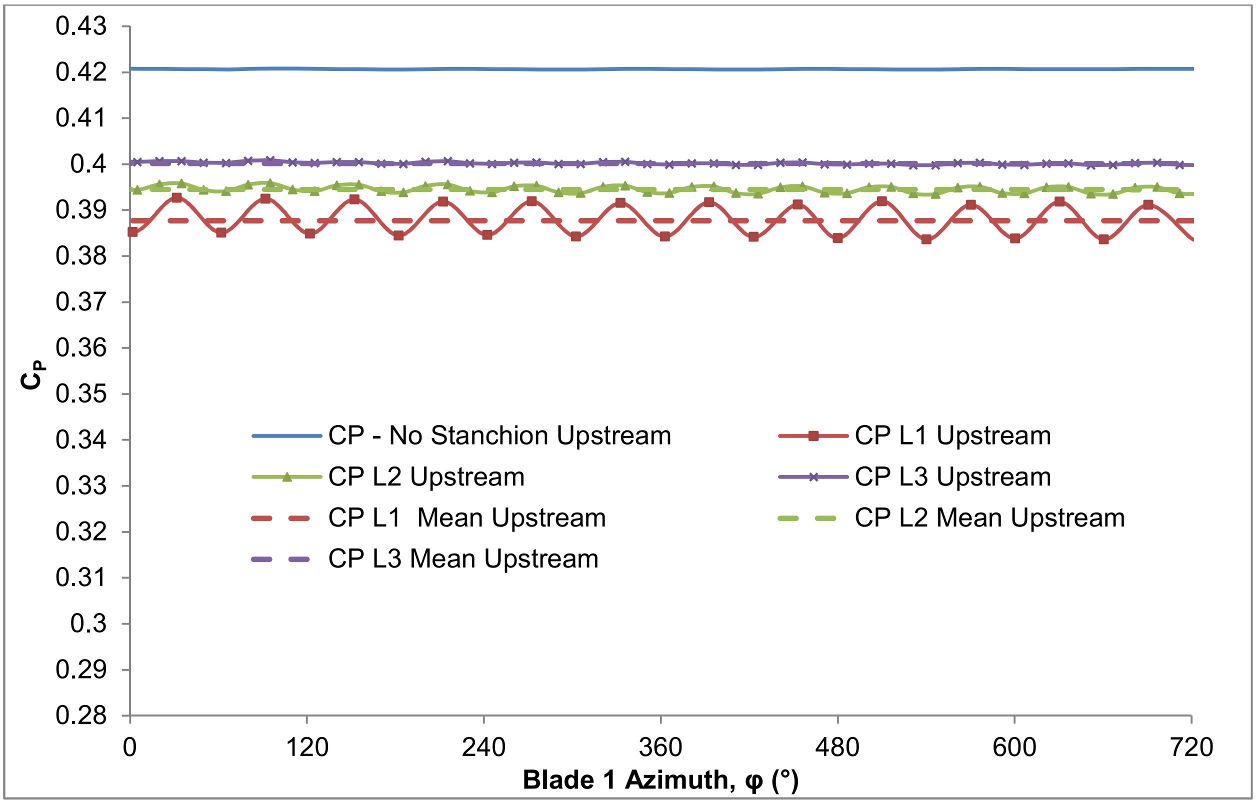

Figure 5.7 C_P-φ for No Stanchion and upstream cases

Figure 5.8 has the same axes as Figure 5.7 with the No Stanchion and downstream cases plotted instead. The No Stanchion case remains the same as in Figure 5.7 with the highest mean C_P of 0.421 and negligible σ over the two rotations. For the downstream cases it can be seen that the performance is significantly affected by the stanchion at all clearance distances. Interestingly, the mean values of all the downstream cases have a similar mean value and similar fluctuations. The highly fluctuating nature of the C_P is due to the high levels of interaction between the turbine and support structure. There are 6 peaks and 6 troughs in the plotted data per turbine rotation. Due to the high timestep size used, the peaks of the curves may not have been captured fully, however the trend remains clear. The peaks occur when one of the three blades is aligned to the horizontal, as this is when all three blades are clear of the support structures, this happens at Blade 1 azimuth of approximately 30°, 90°, 150°, 210°, 270° and 330° whilst the troughs occur around 0°, 60°, 120°, 180°, 240° and 300° when a blade is in line with the stanchion at Top Dead Centre (TDC) or Bottom Dead Centre (BDC). The L_2 downstream case appears to have the greatest fluctuation in C_P and this is confirmed in

Table 5.7 which shows σ = 0.034 the highest of all the downstream cases. Table 5.7 also confirmed that the mean C_P does not improve with increased distance, as the L_2 downstream case shows the least percentage change of all the cases. The troughs in the C_P-φ plot occur as a result of the blade entering the stanchion shadow, in this low velocity field (as already established from Section 5.1.4) the torque on the blade drops, reducing the total torque and therefore the power produced by that blade and in turn the total turbine.

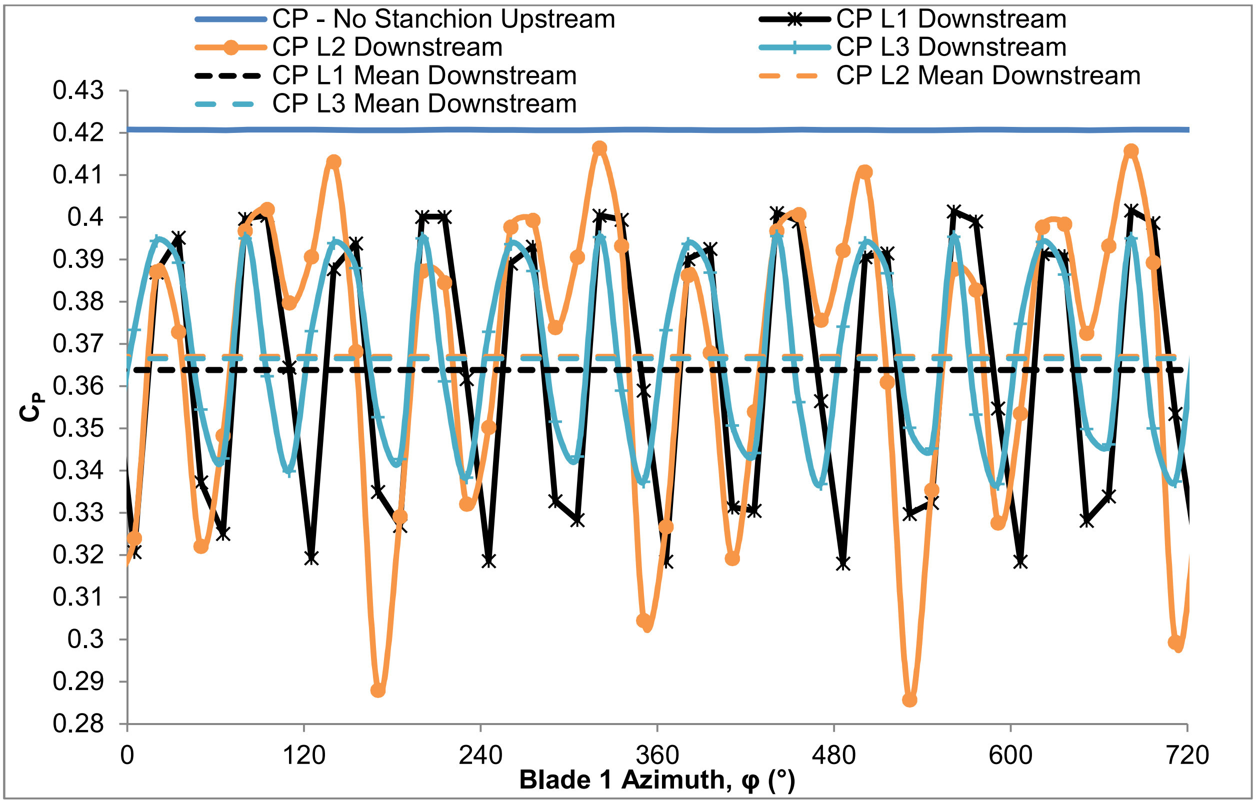

Figure 5.8 C_P-φ for No Stanchion and downstream cases

In Figure 5.8 the irregular peaks were due to the timestep size providing insufficient resolution in the curves, missing the sharp peaks. Higher resolution by reducing the timestep will be required to capture the performance during a rotation. The lack of resolution was worst seen in the L_2 downstream case is due to the significance of the amplitude fluctuation. This occurs in the rest of the transient results and is seen most clearly in the downstream cases. Further discussion on this point is made in Section 5.2.5.

Table 5.7 Mean and Standard deviation of downstream cases C_P values and percentage change from no stanchion case

Downstream	**C_P - μ**	**μ - percentage change**	**C_P - σ**	**σ - percentage change**
No Stanchion	0.423	0.0%	0.0005464	0.0%
L_1	0.363	-14.2%	0.0333536	6004.6%
L_2	0.368	-13.0%	0.0340049	6123.8%
L_3	0.365	-13.6%	0.0223894	3997.8%

5.2.3. Thrust

The coefficient of thrust, C_T is calculated in the same way as in Section 5.1.3, and has been plotted against blade 1 azimuth. C_T-φ is shown for the No Stanchion case and the L_1, L_2 and L_3 Upstream cases in Figure 5.9. The No Stanchion turbine case has a C_T of 0.828 and a negligible SD. Upstream cases can be seen to have lower C_T values than the no stanchion case, with the lowest coming from the smallest stanchion clearance, L_1 upstream. The lower C_T values are positive result and will reduce the structural strength and stiffness of the turbine blades and support structure making it cheaper to fabricate. However what is also evident from Figure 5.9 is the increase in the fluctuation of C_T with closer clearance distances. This is evident in Table 5.8 which shows the σ of C_T signal to be greater at L_1 and least at L_3.

Table 5.8 Mean and Standard deviation of upstream cases C_T values and percentage change from no stanchion case

Upstream	**C_T - μ**	**μ - percentage change**	**C_T - σ**	**σ - percentage change**
No	0.828	0.0%	0.0005475	0.0%
L_1	0.762	-8.0%	0.0035497	548.3%
L_2	0.769	-7.2%	0.0008846	61.6%
L_3	0.775	-6.5%	0.0002601	-52.5%

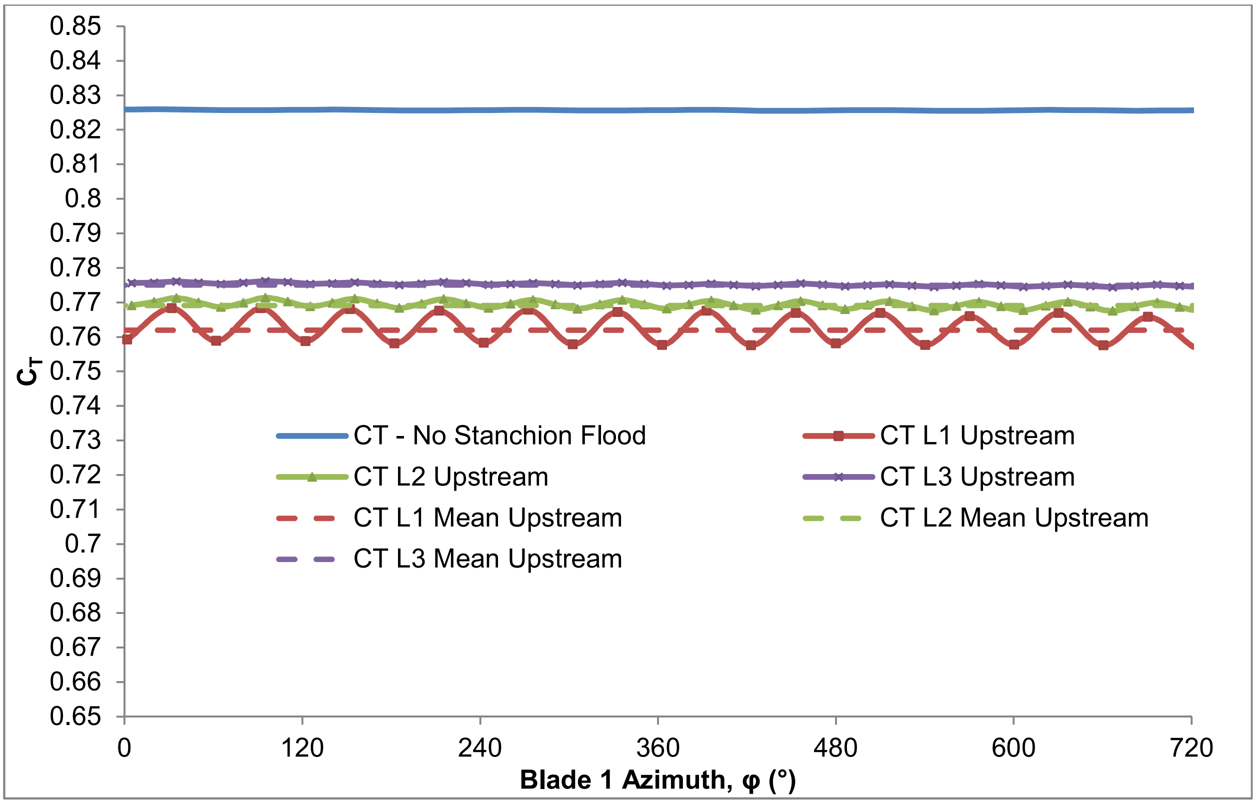

Figure 5.9 C_T-φ for No Stanchion and Upstream cases

Figure **5.10** has the same axes range as Figure **5.9**, only showing the No Stanchion case along with the three downstream cases. The No Stanchion case remains the same as in Figure **5.9** with a C_T of 0.826 and negligible SD. The L_1 downstream case has a mean C_T of 0.709 which is 14.2% lower than the No Stanchion case, and it has a SD of 0.039. The L_2 downstream case has a mean C_T of 0.729 which is 11.7% lower than the No Stanchion case, and it has a SD of 0.031. Whilst the L_3 downstream case has a mean C_T of 0.731 which is 11.5% lower than the No Stanchion case, and it has a SD of 0.026.

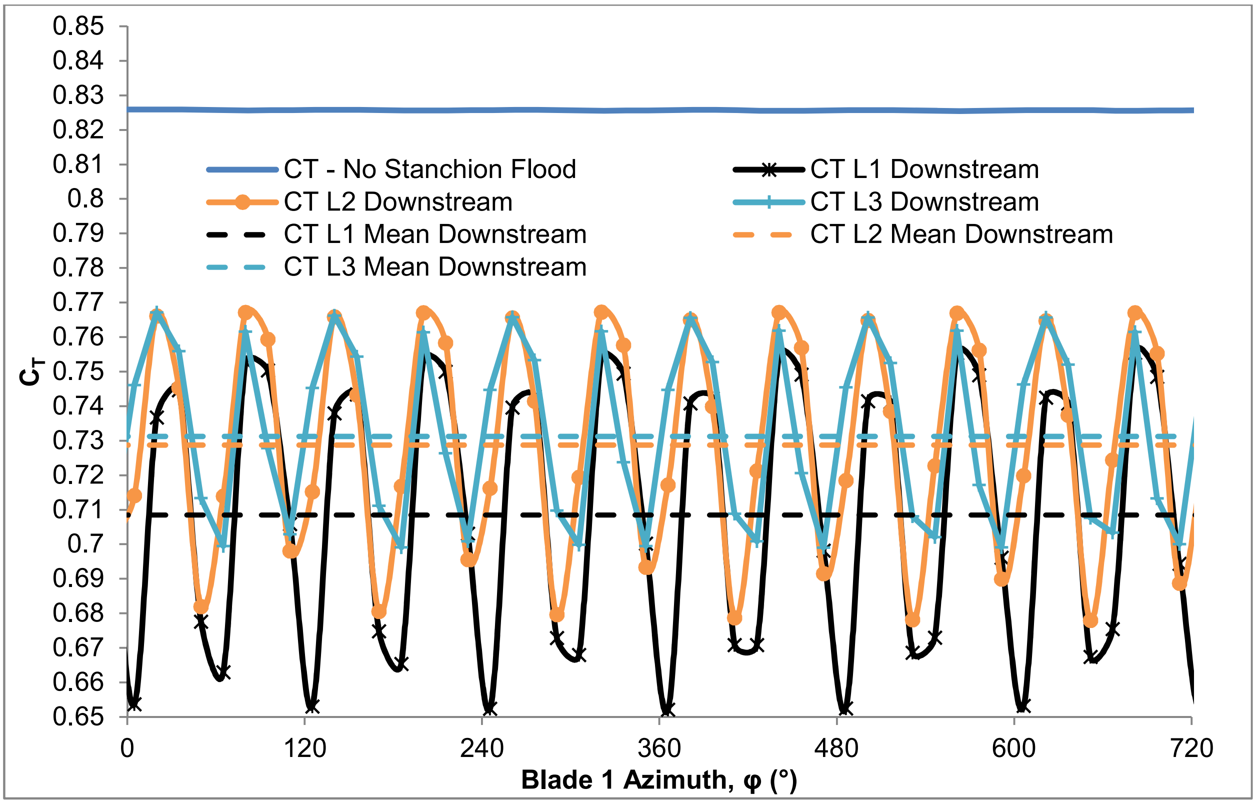

Figure 5.10 C_T-φ for No Stanchion and Downstream cases

Table 5.9 Mean and Standard deviation of downstream cases C_T values and percentage change from no stanchion case

Downstream	**C_T - μ**	**μ - percentage change**	**C_T - σ**	**σ - percentage change**
No Stanchion	0.828	0.0%	0.0005475	0.0%
L_1	0.708	-14.5%	0.0393244	7082.4%
L_2	0.728	-12.1%	0.0320672	5756.9%
L_3	0.730	-11.9%	0.0262410	4692.7%

The upstream cases all have a higher mean than the downstream cases, which in the case of C_T is not preferable. On the other hand the upstream cases have a lower σ, meaning the fluctuations in the load were less significant and preferable to the higher fluctuations found in the downstream cases. The preference toward a higher mean load and lower fluctuations could be made, because high load fluctuations are known to be the cause of fatigue failure (ASM International, 2008) and these loads will apply to the blades, and will be transferred to the main shaft bearings and into the support structure. It is therefore a design requirement of all these components to be designed for suitable static and dynamic loads. A higher static load which experiences less dynamic fluctuations will likely be preferable to the alternative given the C_P and C_θ benefits of the increased upstream clearance. The variation in high peak, low peak is caused by the time step size being too large giving poor resolution for the transient study, as discussed further in Section 5.2.5.

5.2.4. Out-of-Plane Bending Moments

The out-of-plane bending moment is calculated as described in section 3.4.4 it is then converted to a non-dimensional characteristic, C_M of the turbine using equation [**3.16**]. Consideration of the C_M provides insight into the structural loads the blades, drive-shaft and bearings will have to accommodate, as well as the support structure, ultimately.

When there is No Stanchion present the resultant bending moment from the blades about the rotating axis is small but present as can be seen from Figure **5.11**. This slight inherent bending moment may come from the geometry of the blades however its magnitude (mean C_M of 0.001 or Out-of-plane bending moment of 2203 kNm) is such that it is negligible in comparison to when there is a stanchion present. The angle at which the out-of-plane bending moment acts fluctuates about a mean of 333.4˚ with the number of peaks corresponding to the number of blades.

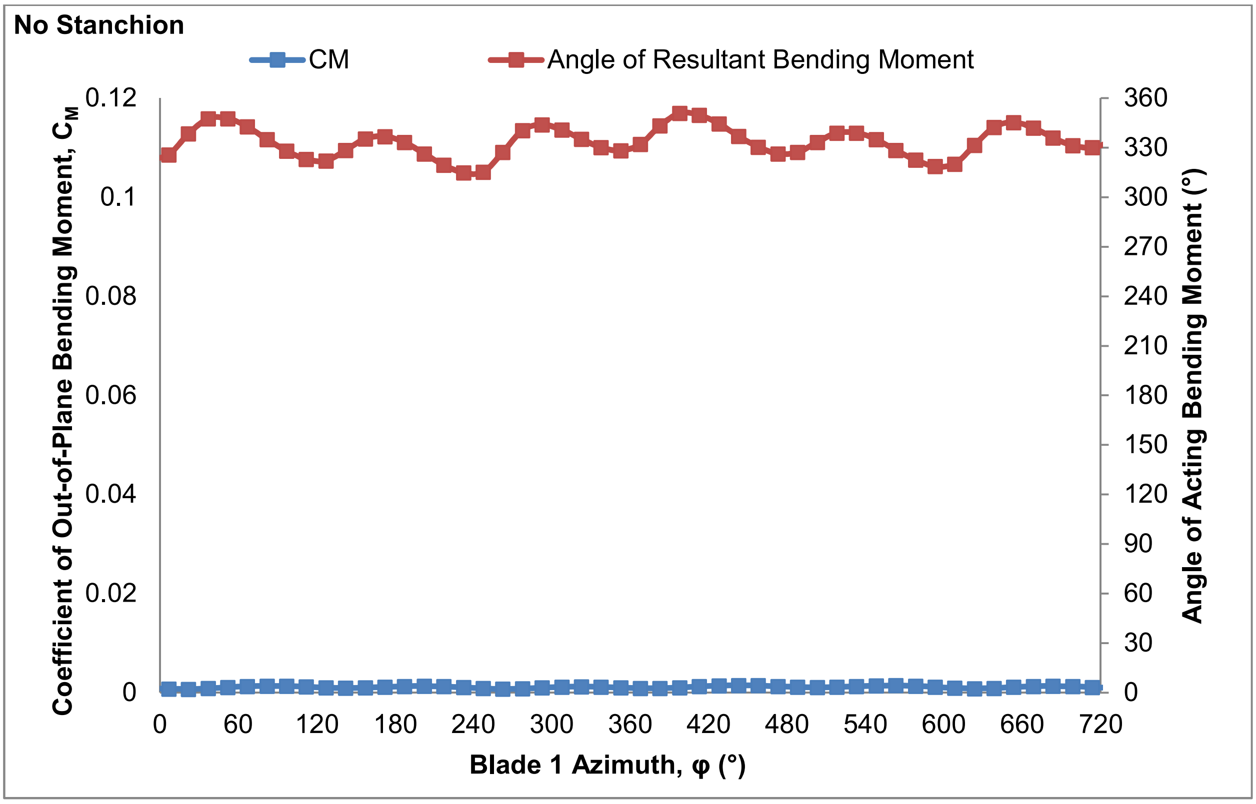

Figure 5.11 C_M-φ No Stanchion Case

Figure 5.12 shows the C_M for the three upstream cases; L_1, L_2 and L_3. The mean C_M is higher than the no stanchion case for all the upstream proximities, with increased clearance the mean C_M drops. The fluctuation in the signals can be seen to decreases as the clearance distance increases. Table 5.10 shows the mean, μ and standard deviation, σ of the cases. The percentage change of the mean C_M relative to the no stanchion case is clearly significant for all proximity cases. There is a clear increase in reduction in the out-of-plane bending moment between L_2 and L_3. The standard deviation in the signal is an indication of the fluctuations, a similar pattern to the mean C_M is detected in the standard deviation.

Table 5.10 Mean and Standard deviation of upstream cases C_M values and percentage change from no stanchion case

Upstream	**C_M - μ**	**μ - percentage change**	**C_M - σ**	**σ - percentage change**	**Angle of acting bending moment - μ**
No Stanchion	0.001	0.00%	0.0002	0.00%	333˚
L_1	0.02	1900.00%	0.005	2400.00%	207 ˚
L_2	0.019	1800.00%	0.002	900.00%	193 ˚
L_3	0.006	500.00%	0.001	400.00%	176 ˚

Figure 5.13 shows the C_M for the three downstream cases; L_1, L_2 and L_3. The mean C_M is higher than the no stanchion case for the downstream proximities, with increased clearance the mean C_M drops. The fluctuation in the signals can be seen to decreases as the clearance distance increases. Table 5.11 shows the mean, μ and standard deviation, σ of the cases. The percentage change of the mean C_M relative to the no stanchion case is clearly significant for all clearance distances. There is a distinct difference between the mean percentage change from L_1 and L_2 case, and from L_2 and L_3 case. The L_3 case has a greater C_M than the L_2 however it does have the lowest standard deviation, making it the most favourable downstream position.

Table 5.11 Mean and Standard deviation of downstream cases CM values and percentage change from no stanchion case

Downstream	**C_M - μ**	**μ - percentage change**	**C_M - σ**	**σ - percentage change**	**Angle of acting bending moment - μ**
No Stanchion	0.001	0.00%	0.0002	0.00%	333˚
L_1	0.039	3800.00%	0.028	13900.00%	176˚
L_2	0.029	2800.00%	0.021	10400.00%	194˚
L_3	0.030	2900.00%	0.020	9900.00%	193˚

The upstream and downstream cases all have greater C_M than the No Stanchion case. The upstream cases all have significantly lower mean C_M and standard deviation in comparison to the downstream cases. The angle of acting bending moment in both cases crosses the 0°/360° line three times during a single rotation; this is what causes the step like response, seen in Figure 5.12 and Figure 5.13. The cause for the change in direction of the step up/ set down for the angle of acting bending moment curve between the upstream and downstream cases is due to the global reference frame remaining constant and the turbine being rotated through 180°. The cause of the increase in out-of-plane bending moment with proximity to the stanchion is a result of the bias thrust loading on the blades. As the plane of rotation of the turbine approaches the support stanchion the reduction in thrust caused by the structure increases. This results in a greater imbalance of thrust between the blades, with the two blades not in line with the stanchion having a much greater thrust and thus increasing the out-of-plane bending moment.

The downstream turbine sees a much greater out-of-plane bending moment than the respective upstream turbine cases. There are two causes for this:

1. The support stanchion shadow effect is much greater downstream, meaning the turbine blade in-line or closest to the stanchion has a significantly lower thrust relative to the upstream turbine blade in the same position.
2. The support stanchion also causes and acceleration of the flow to either side, which increases the thrust on the two blades out of line with the support structure

These two factors further increasing the imbalance of thrust and consequently the magnitude of the out-of-plane bending moment.

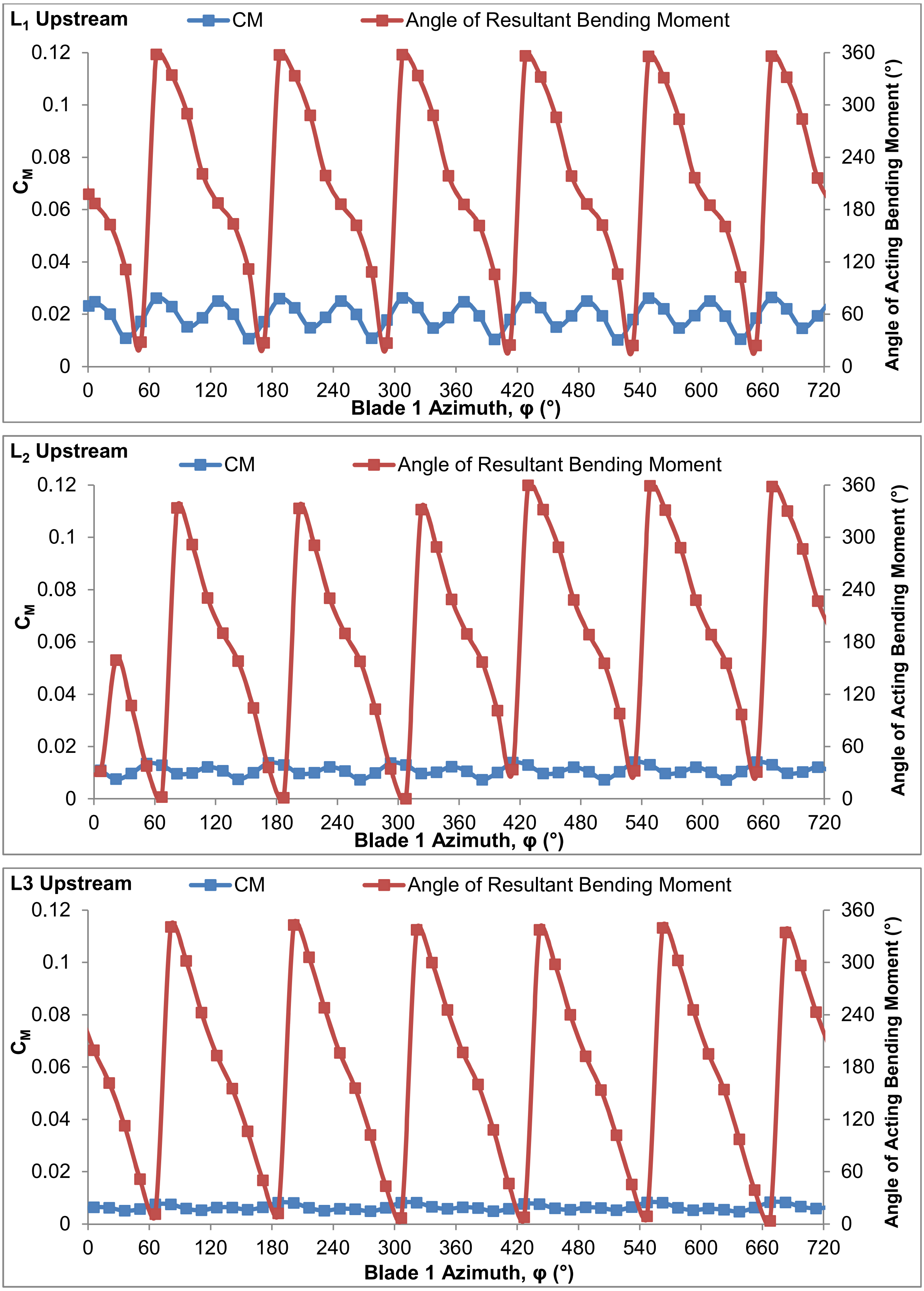

Figure 5.12 C_M-φ for L_1, L_2 and L_3 Upstream Cases

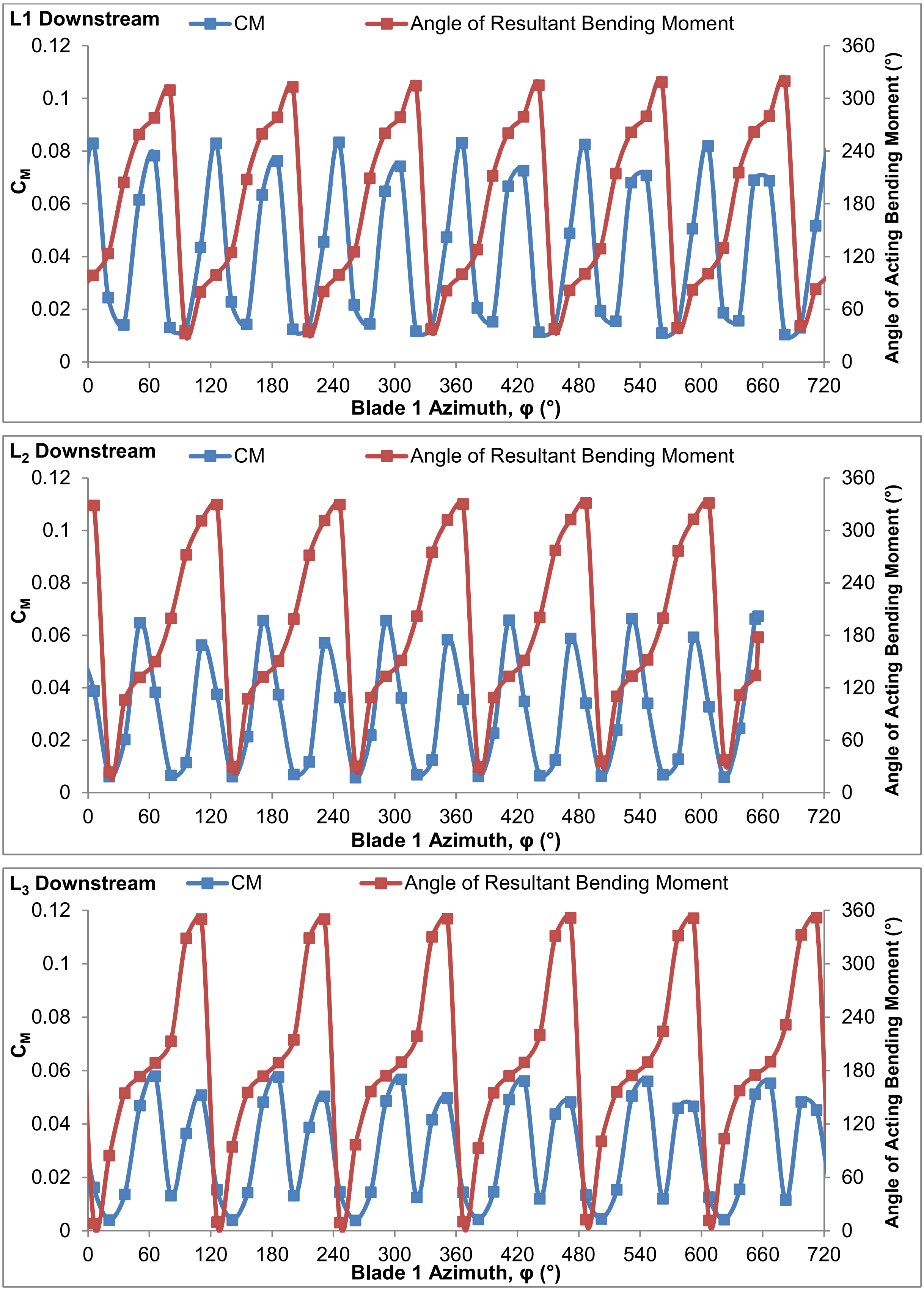

Figure 5.13 C_M-φ for L_1, L_2 and L_3 Downstream Cases

5.2.5. Discussion

The transient results have confirmed there is a benefit in operating upstream of the stanchion and with an increasing clearance distance between rotor and stanchion, mean performance characteristics improve. Improvement in mean performance values are a small benefit in comparison to the reduction in fluctuations of the performance characteristics as well as out-of-plane bending moments on the rotor, that the upstream with larger clearance offers. This is shown by the increase in σ in the transient results between upstream and downstream orientations, which is an order of five times greater in the downstream configuration. The implications of these results are significant as they will lead to the reduced fatigue life of system components. The fluctuations in the in-plane (torque) and out-of-plane bending moments will detrimentally impact the fatigue life of the gearbox and thrust bearings. The blade life expectancy may also be reduced if not considered during the design stage. The power fluctuations will increase demand on power conditioning. In order to operate a turbine in a continually upstream configuration the device must be actively or passively yawed to face the oncoming flow. As shown in Section 1.3.3 a few HATT devices have such an arrangement.

In addition to the advantages of a continually upstream turbine arrangement, it can be seen that the greater the distance between the plane of rotation of a turbine and the support structure the better for mean performance and lower σ.

5.3. Wake Characteristics

The pressure and velocity flow field around the turbine in the near wake supports the performance characteristics shown for the transient results in Section 5.3.1. The far-field flow, downstream of the turbine, shows the recovery of the flow and is an indicator to array spacing and is taken from the steady-state results, at close to peak power, in Section 5.3.2.

5.3.1. Near-field wake

Figure **5.8** and Figure **5.10** have been magnified to look at the pitch and amplitude of the fluctuations in C_T and C_P over a third of a rotation for the downstream case as can be seen in Figure 5.14 a) and b). What is clear is that the curves are not symmetrical as the blade passes through the shadow of the stanchion. There is a sharp increase in the thrust and a more gradual drop as the blade passes out of the shadow. The shape of the C_T curve is reflected in the C_P curves with a rapid drop off of power as the blade passes through the shadow of the stanchion and a more gradual rise as the blade passes out of the shadow. In addition the peak values on both sets of curves are not coincident, such that the smaller the clearance the more delayed the lows and highs of the fluctuations.

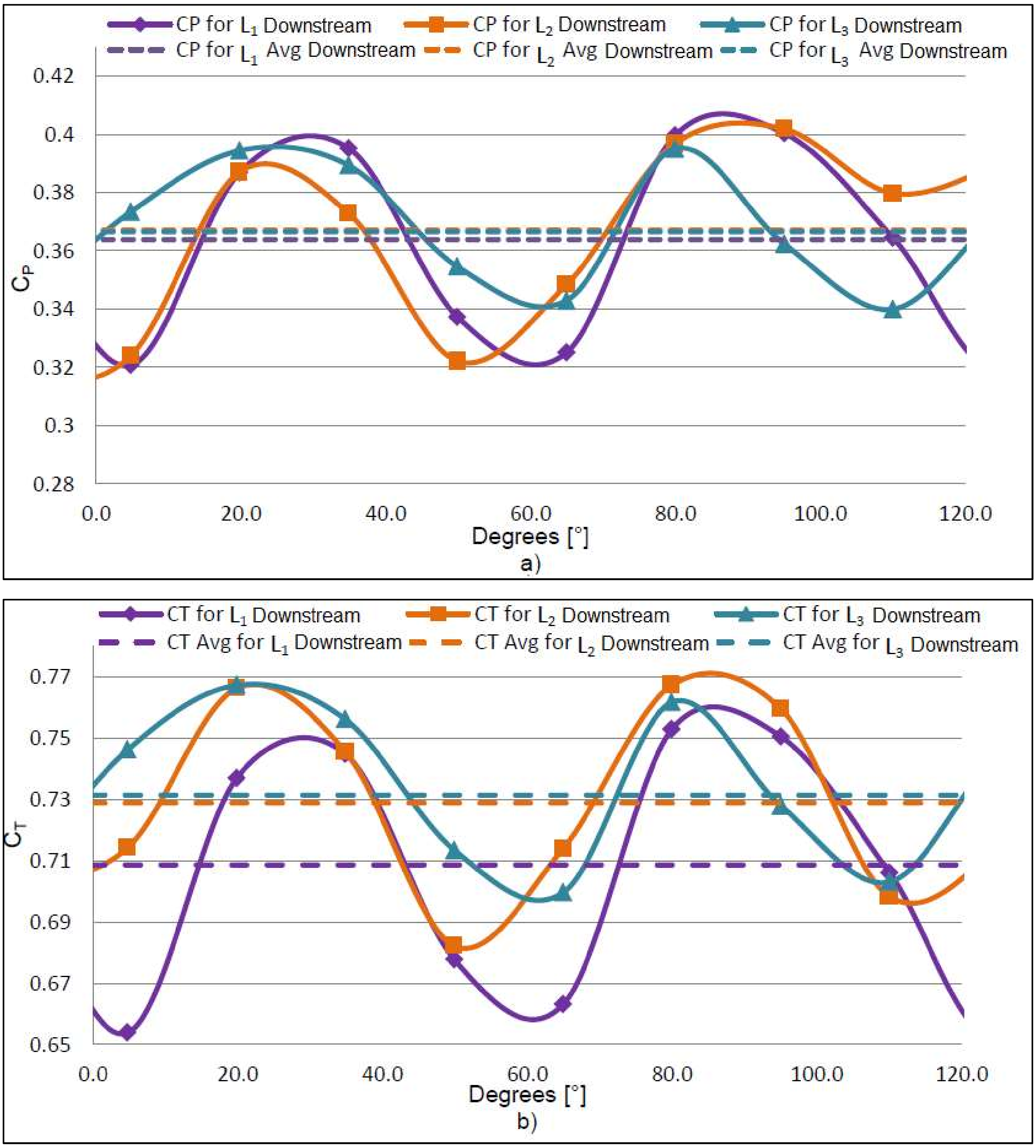
a)

b)

Figure 5.14 Detail of the fluctuation in a) CP and b) CT for a third of a rotation

The cause for this asymmetry in the performance characteristics as a blade passes the support structure can be identified through the near field wake analysis shown in the velocity contour plots in Figure 5.15. The contours are taken from the transient CFD model, using a contour plot in the horizontal plane, 3 m above the axis of the turbine. The white circles in the figure indicate the stanchion and a blade profile can be seen to be moving passed the stanchion as the time series progresses. As the blade passes the stanchion a low velocity region forms between the stanchion and the blade. The closer the blade is to the stanchion, the stronger this low velocity region attaches between them. These regions, as has been highlighted in Figure 5.15, do not attach until the blade has almost passed the stanchion and remain attached until a distinct distance after the blade has passed beyond the stanchion. The blade therefore remains de-powered for longer on exiting the region affected by the stanchion.

Figure 5.15 Velocity Contours for L1 Upstream clearance at increasing time steps

5.3.2. Far-field wake

Figure 5.16 shows the variation of axial velocity for the length of the control volume and clearly marks the disruption to the flow caused by the introduction of a TST and stanchion compared to just the TST at peak power extraction. The centreline velocity has been normalised to the free stream velocity, whereas the length has been normalised to the 90% recovery for the TST without a stanchion. Hence the wake length at which 90% recovery of the turbine in isolation is 1.0. This method of normalising allows a direct comparison of the recovery rate for the presence of a stanchion in different configurations also. In all cases zero is the rotational plane of the blades. As the fluid approaches the turbine, or the stanchion in the case of the downstream flow, there is a rapid reduction in the velocity as a result of the additional blockage upstream of the turbine for all cases, as would be expected. In addition, this reduction starts further upstream and the initial recovery, immediately downstream of the stanchion, is faster for the turbine downstream of the stanchion when compared to the turbine upstream of the stanchion. When considering the effects of the clearance distance, it can be seen that there is less disruption to the upstream velocity when the stanchion clearance is only L_1 and the downstream wake recovery also varies with clearance distance, particularly in the near field region of the turbine. The fluid velocity must clearly drop to zero as the axis passes through the turbine hub. Immediately behind the hub of the turbine there is a recirculation zone, which forces the velocity to peak and then drop. For the downstream case, the magnitude of the peak and drop is greater than the upstream, causing a larger difference in the velocity between the peak and trough. Subsequent to the initial recovery, there is a further reduction in the velocity which is seen in all the curves. However the reduced velocity is, as expected, greater as a result of the increased blockage when compared to that of the turbine only curve. However the curve for a clearance of L_2 is very close to that of the turbine only scenario. Further downstream the wake recovery merges for each upstream and downstream cases. As the clearance distance becomes longer so the distance at which the wake reaches the 90% recovery length reduces, such that by a clearance distance of L_3 the recovery occurs at L90/Lns90 ~1, the same as if no stanchion were present.

Given the stated limitations of far field wake analysis discussed in Section 4.5.3, Figure 5.16 is a useful plot for investigating the optimal spacing of TST array in the linear direction as it shows the minimal downstream stream spacing to ensure the flow is sufficiently recovered. Although the recovery lengths are not independent of rotor - stanchion proximity, these differences are minimal and as such, the array spacing would not be adversely affected by any of the stanchion clearances investigated. In fact L_2 upstream condition appears to have favourable wake recovery length with over 90% recovery achieved sooner than that of the no stanchion condition, investigation into the reasons why this is occurring maybe considered in future research, however it is suspected that this maybe geometry and set-up specific and cannot be translated to other cases.

The plotted line for the downstream separation is affected first as the rotating plane is downstream of the stanchion and so it is the stanchion causing the initial drop in velocity as flow separates around it. This also explains the longer initial recovery time of the upstream cases shown in the plots as they are hindered by the stanchion after passing through the turbine.

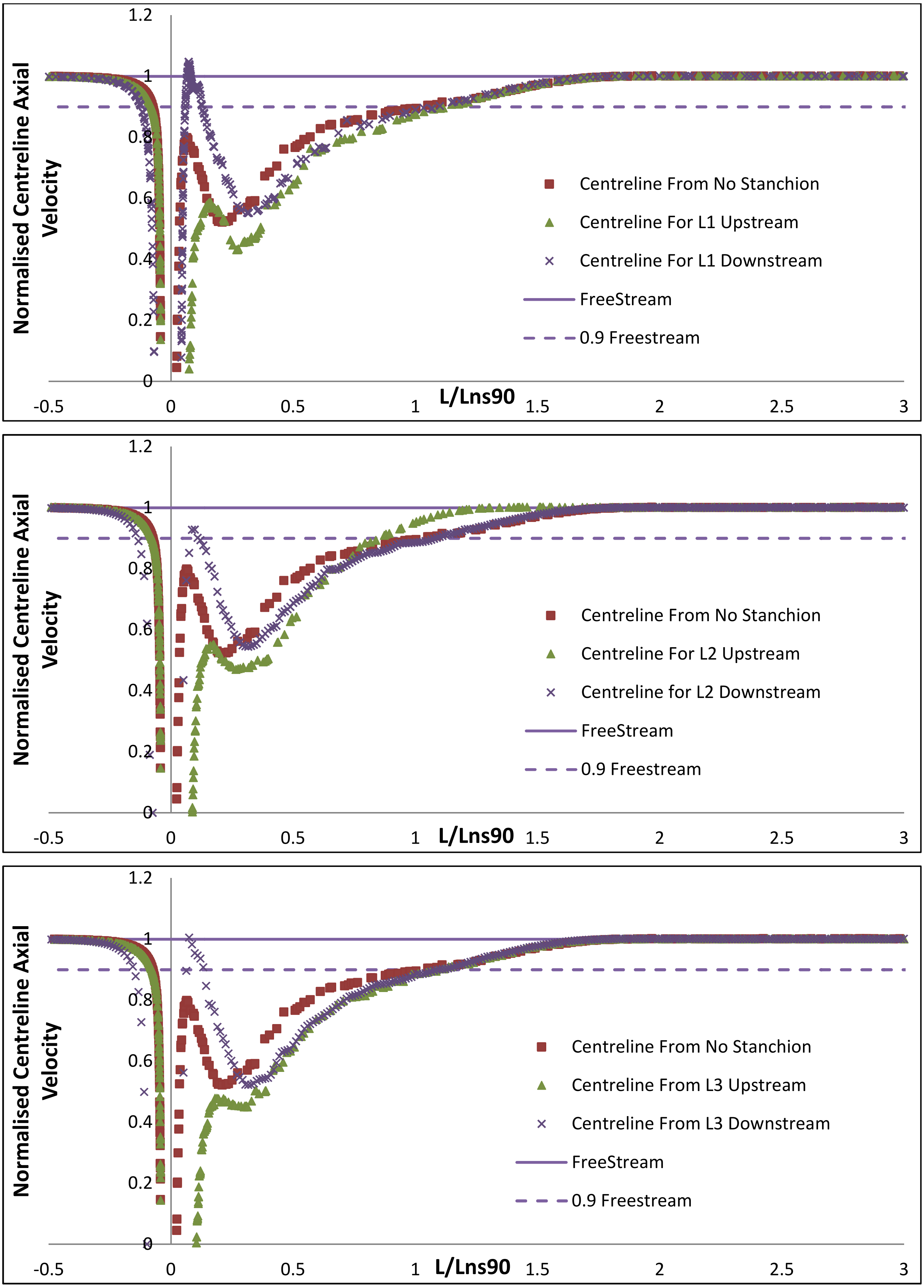

Figure 5.16 Downstream axial velocity recovery for turbine with and without a stanchion.

5.4. Summary

The steady state (section 5.1) and transient results (section 5.2) can be compared at the same tip-speed ratio, λ = 3.5. Comparison of the corresponding performance values from both these sections provides an insight into the differences between the two modelling techniques. Table 5.12 and Table 5.13 clearly show the performance differences of the modelling approaches. It can be seen that for the no stanchion case the performance characteristics are consistently lower for the steady state model. Additionally the steady state results showed consistently greater percentage changes for each of the directionality and proximity cases relative to their transient counter-part results. As a single blade from the steady-state models is at TDC (in-front of the surface piercing stanchion) it was expected that the overall torque and power and thrust performance of the turbine would be lower relative to the mean values over a rotation from the transient models. This has been shown to be the case. As established, this is due to the stanchion interaction, as the stanchion has a more significant impact in the downstream orientation it was expected that the downstream steady state cases would be affected more significantly. It is observed however that the steady state results have the same pattern as the transient results, with upstream continually outperforming the downstream cases and increasing clearance distance between rotor and stanchion improves performance. The coefficient of the out-of-plane bending moment was calculated for the transient results and shows further reason to avoid downstream operation, not only to avoid increased mean loads but also greater fluctuation in the loads. Further work is required to validate both results sets against experimental results to determine the significance of their differences. This will be considered in Chapter 8 - Experimental Results.

Table 5.12 Turbine peak performance characteristics at λ = 3.65 for steady-state CFD results

λ = 3.65	Upstream - percentage change			No Stanchion	Downstream - percentage change		
	L_3	L_2	L_1		L_1	L_2	L_3
C_θ - μ	-6.6%	-11.0%	-23.1%	0.091	-41.8%	-23.1%	-24.2%
C_P - μ	-9.8%	-14.1%	-24.6%	0.420	-43.5%	-25.6%	-27.1%
C_T - μ	-4.0%	-5.7%	-12.0%	0.748	-19.5%	-11.6%	-12.2%

Wake characteristics were considered to provide insight in the cause of the performance drop in the near field and identified the attachment of a low-velocity stagnation point at the front of the stanchion to the upstream passing blade, causing the reduction in blade performance. Interestingly the attachment of the low-velocity contours remains as the blade passes beyond the stanchions projected area creating a lag in the performance drop which is dependent on the spacing. The far-field wake characteristics showed stanchion proximity does not significantly impact wake recovery and therefore is not a significant concern for array spacing.

Table 5.13 Turbine mean performance characteristics at $\lambda = 3.65$ for transient CFD results

$\lambda = 3.65$	Upstream - percentage change			No Stanchion	Downstream - percentage change		
	L_3	L_2	L_1		L_1	L_2	L_3
C_θ - μ	-5.4%	-6.7%	-8.3%	0.124	-14.2%	-13.0%	-13.6%
C_P - μ	-5.4%	-6.7%	-8.3%	0.423	-14.2%	-13.0%	-13.6%
C_T - μ	-6.5%	-7.2%	-8.0%	0.828	-14.5%	-12.1%	-11.9%
C_M - μ	500.0%	1800.0%	1900.0%	0.001	3800.0%	2800.0%	2900.0%

Given the results, both steady state and transient, it has been established that operating a turbine in a continually upstream manner, to always be facing the incoming flow in-front of the turbine, is the optimal orientation. Working under the premise of the transient results provide a closer image of the performance of a true system; the recommendations to industry are to operate TST in a continually upstream manner. The spacing between the supporting structure and turbines rotating plane should also be maximised within structural limitations to maintain high rotor performance and reduce fluctuations in loading, however evidence of the diminishing returns from increased clearance distance may justify a clearance between L_2 and L_3 for this scenario. In order to achieve these recommendations, the design should incorporate a yaw mechanism to accommodate the upstream alignment of the turbine and flow for both ebb and flood phases of the tide.

Further benefits may be gained from continual flow alignment in an upstream manner, such as is found on the Alstom device (Alstom Ocean Energy, 2013). If the flow is not bi-directional between flood and ebb or if there is a drift in the direction of flow during a tidal cycle, as is shown to occur in Section 2.4, should the yaw mechanism account for these misalignments and what advantage is gained from this? This is what is explored in the following chapter.

The findings from this chapter have been published by (Frost, et al., 2015) and are supported by previous work conducted by (Mason-Jones, et al., 2013).

6. Flow Misalignment Results

The results and discussion in this chapter determine the effects of axial flow misalignment, or yaw angle, on the performance characteristics of the turbine. The same turbine was used as in the previous chapter, however the turbine's support structure was replaced with the tripod structure for reasons discussed in Section 4.1.2. The timestep size for the transient models has also been reduced in order to address the resolution in the results during a single rotation. The results of the aligned turbine as well as ±10°, ±15° and ±20° yaw angle cases are shown and discussed. Section 4.1 shows the geometrical arrangement of the yaw angles, and is shown clearly in Figure 4.6. For both steady-state and transient numerical models, non-dimensional performance characteristics are presented and discussed.

The objective of this chapter is to inform the industry of potential detrimental performance and loading conditions that occur due to misalignment, and the extent of the impact with increasing misalignment. This work will emphasise the need for the industry to consider the tidal flow regimes in which turbines are placed, not only with regards to velocity magnitudes but direction also as discussed in Section 0.

6.1. Steady-State

In this section the results for the steady-state models are shown. This was undertaken using the stanchion and turbine geometry identified in Section 4.1. The swept area of the turbine and velocity in the denominator of the non-dimensional performance characteristic equations [**3.12**] were maintained as for the aligned case (no yaw angle). This was performed for the aligned turbine and the ± 10°, ± 15° and ± 20° misaligned cases.

6.1.1. Torque

The coefficient of torque (C_θ) for the following cases have been taken from steady state ANSYS CFX models. A C_θ-λ curve was plotted by increasing the rotational velocity of the turbine for each of the data points. C_θ was calculated using the sum of the torques about the axis of rotation for the three blades and the hub using equation [**3.12**] as established in Section 3.4.1.

Figure 6.1 shows that for all alignment cases there is a similar trend in the data set. The C_θ has a cut in of approximately $C_\theta = 0.042$ for all cases. The data sets then diverge as the λ increases, with all cases having a peak C_θ at $\lambda = 2.5$. There is then some convergence between the data sets again as λ continues to increase towards freewheeling. Freewheeling for the aligned case occurs at λ = 6.8. The value of C_θ continues to decrease below the zero line; the reasons for this is in ANSYS CFX the rotational velocity, ω is an input defined prior to solving as described in section 4.3.3 and if it exceeds the freewheeling value of the turbine, the turbine will begin to act as a pump, being driven by the motor rather than the hydrodynamic loads of the flow. The specifics for these key points in the curve have been highlighted in Table 6.1.

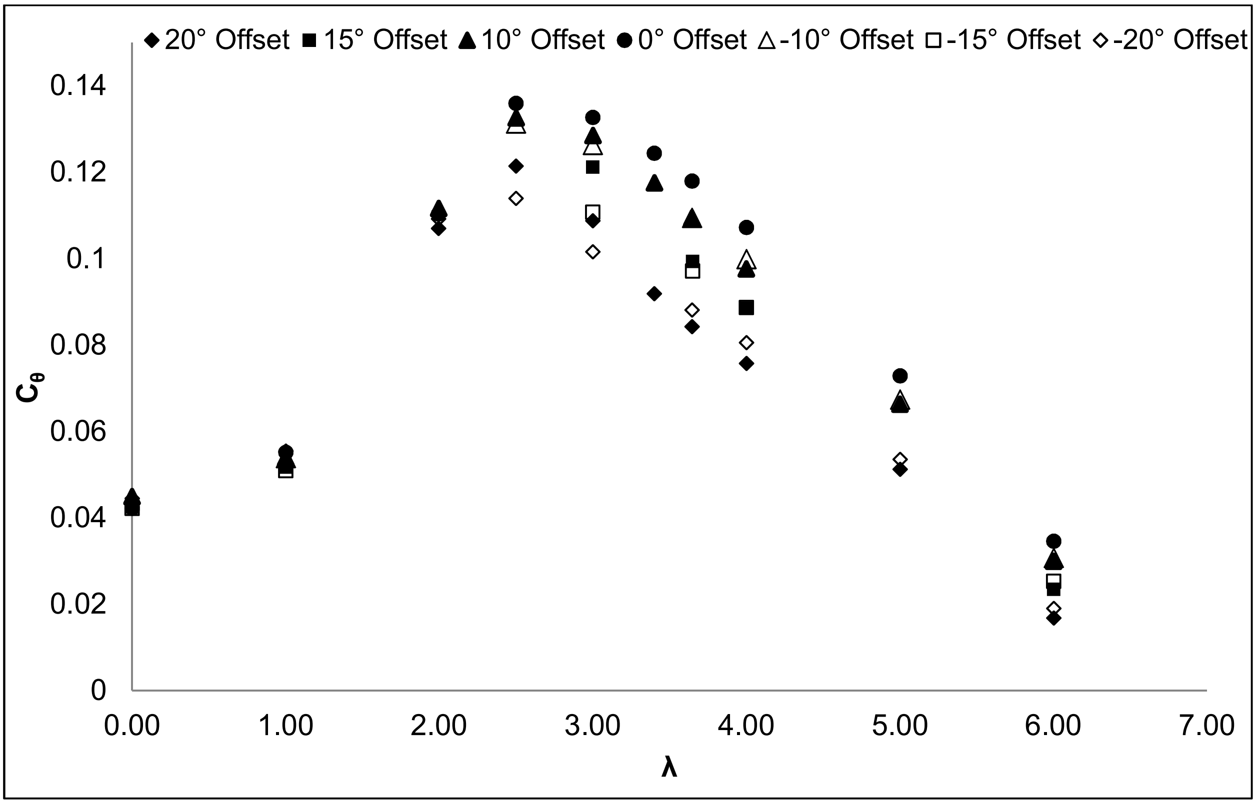

Figure 6.1 C_θ - λ for 0°, ±10°, ±15° and ±20° Misaligned Turbine Cases

Table 6.1 Key points on C_θ - λ figure for various yaw angles

Yaw angle (°)	Cut in C_θ	Peak C_θ	Percentage change in C_θ	Freewheeling λ
+20	0.044	0.121	-11.03%	6.5
+15	0.042	NA	NA	6.6
+10	0.045	0.132	-2.94%	6.7
0	0.042	0.136	0.00%	6.8
-10	0.045	0.131	-3.68%	6.7
-15	0.042	NA	NA	6.6
-20	0.044	0.114	-16.18%	6.5

It is clear that the aligned turbine offers the greatest peak performance for C_θ with a value of 0.136 at $\lambda = 2.5$. The value then drops successively between ±10˚, ±15˚ and ±20˚ as seen in Table 6.1. This is likely due to the reduced upstream velocity that is now perpendicular to the flow. The relationship between the inlet velocity and velocity passing through at a normal to the turbine has been defined in equation [3.23]. The cut-in C_θ does not vary significantly between the cases, the ±10˚ and ±20˚ cases experienced a 5% and 6% increase in cut-in C_θ. There is a more notable trend with the freewheeling point, for the aligned turbine C_θ reached freewheeling at a λ of 6.8, this then reduced with respective increases in the angles of misalignment to 6.7, 6.6 and 6.5. In the steady-state models Blade 1 was left at TDC. This means the relative pitch angle of the other blades to the principle flow direction varies. As a result different torques will be produced by each blade. The net effect of this is a reduced rotor torque efficiency as has been shown.

6.1.2. Power

The coefficients of power for the following cases have been taken from steady state ANSYS CFX models. A C_P-λ curve was plotted by increasing the rotational velocity of the turbine for each of the data points. C_P was calculated using the sum of the torques multiplied by the rotational velocity of the turbine using equation [**3.12**] as established in section 3.4.1.

Figure 6.2 shows the C_P-λ curve for the aligned turbine with profiled blade roots and the tripod stanchion. For all the data sets $C_P = 0$ when the turbine is stationary, as expected, the data sets then follow a similar trend, increasing to a peak as λ increases. However due to the varying angle of misalignment between the curves/ datasets diverge with varying peaks. The data sets then decline as λ increases towards freewheeling.

It can be seen from Figure 6.2 and Table 6.2 that increasing the angle of misalignment increases the detrimental impact on the turbine’s coefficient of power. It can be seen not only to reduce the peak C_P but also compress the C_P-λ curve with the freewheeling point being reached at an earlier λ. It also can be seen that at the higher yaw angles, the negatively yawed turbine has a lower C_P than its positively yawed counterpart. This is likely to stem from the rotational direction of the turbine creating some differences.

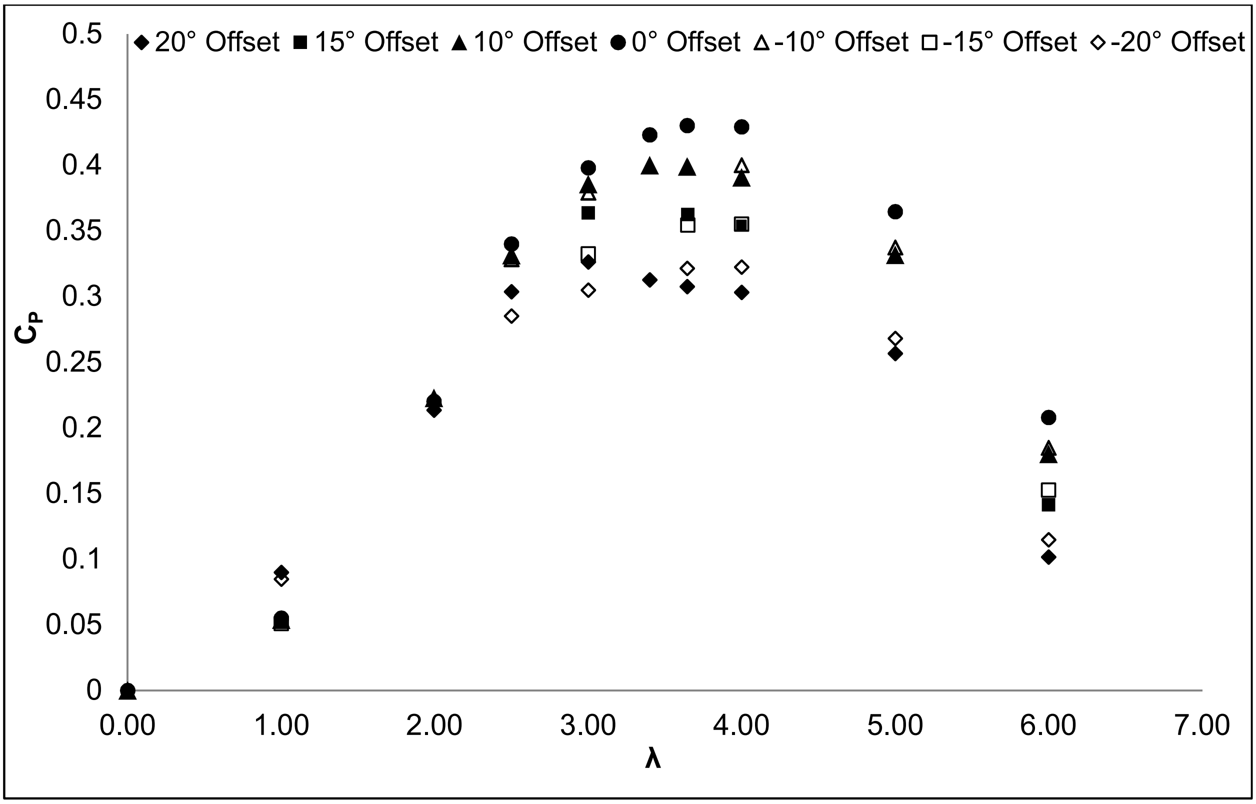

Figure 6.2 C_P - λ for 0°, ±10°, ±15° and ±20° Misaligned Turbine Cases

Table 6.2 Key points on C_P - λ figure for various yaw angles

Yaw angle (°)	λ of Peak C_P	Peak C_P	Percentage change in C_P	Freewheeling
+20	3.00	0.333	-22.56%	6.5
+15	3.65	0.363	-15.58%	6.6
+10	3.40	0.399	-7.21%	6.7
0	3.65	0.43	0.00%	6.8
-10	3.65	0.399	-7.21%	6.7
-15	3.65	0.354	-17.67%	6.6
-20	4.00	0.322	-25.12%	6.5

6.1.3. Thrust

The coefficient of thrust for the following cases have been taken from steady state ANSYS CFX models. A C_T-λ curve was plotted by increasing the rotational velocity of the turbine for each of the data points. C_T was calculated using the sum of the axial forces (thrust loads) for each of the blades and the hub using equation [**3.12**] as established in section 3.4.1.

Figure 6.3 shows the C_T-λ curve for the aligned turbine with profiled blade roots and the tripod stanchion. All the datasets have a $C_T \sim 0.271$ when the turbine is stationary, at $\lambda = 0$ and then increases to peak C_T. In some cases C_T then declines slightly as the turbine approaches freewheeling. However this does not occur to all of them. For the aligned case the turbine's peak $C_T = 0.85$ at $\lambda = 4$. This is followed by a slight decline as freewheeling is achieved. The key points in the other datasets have been summarised in Table 6.3. There is a beneficial drop in C_T with increasing yaw angle, however this must be weighed against the reduction in C_P which is much more significant.

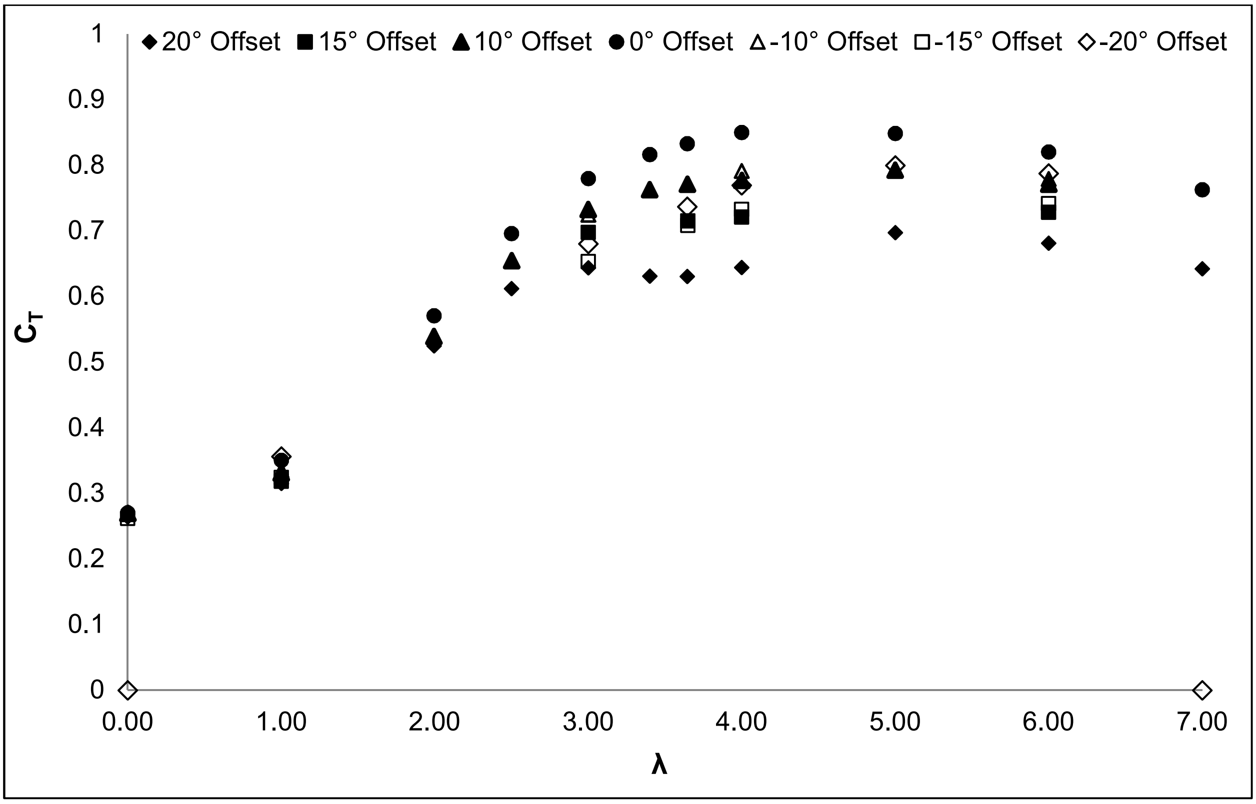

Figure 6.3 C_T - λ for 0°, ±10°, ±15° and ±20° Misaligned Turbine Cases

Table 6.3 Key points on C_T - λ figure for various yaw angles

Yaw angle (°)	Cut in C_T	λ of Peak C_T	Peak C_T	Percentage change in C_T
+20	0.266	5.00	0.697	-18.00%
+15	0.266	6.00	0.742	-12.71%
+10	0.267	5.00	0.792	-6.82%
0	0.27	4.00	0.85	0.00%
-10	0.267	4.00	0.792	-6.82%
-15	0.265	6.00	0.729	-14.24%
-20	0.266	5.00	0.8	-5.88%

6.1.4. Out-of-Plane Bending Moment

Figure 6.4 shows the magnitude of resultant shaft bending moments at the rotor end of the driveshaft. As can clearly be seen, in this blade orientation with blade 1 at top dead centre, there is a significant increase in the bending moment with the inclusion of flow misalignment. The relation of C_M with λ is inconsistent for all the datasets, making a general trend difficult to identify. However there is a clear increase in C_M as misalignment increases. This is apparent for both positive and negative yaw angles. The aligned turbine experiences a peak bending moment of 16 kNm at λ = 3. The bending moment for the +10° misaligned turbine peaks at λ = 5 with a magnitude of 80 kNm. This is significant, as whilst the reduction in C_P is small there is a 400% increase in the bending moment even over a small misalignment. Increasing the misalignment up to +20° misaligned turbine also peaks at λ = 5, with a significantly higher magnitude of 150 kNm.

The negative misalignment cases show similar trends to the positive cases, with respect to the bending moment increasing with an increase in misalignment. The trend in the shape and magnitude of the bending moments over the range of λ for the -10° and -15° are also similar showing that there is reasonable independence of the misalignment at these angles. However, the -20° peaks at 190 kNm at λ = 5; a 27 % increase over the +20° misalignment case.

Overall comparing the peak bending moments over the whole working range results in an increase from the aligned case of 400% at ±10°, ~570 % at ±15° and between 800 and 1300% at ±20°, respectively.

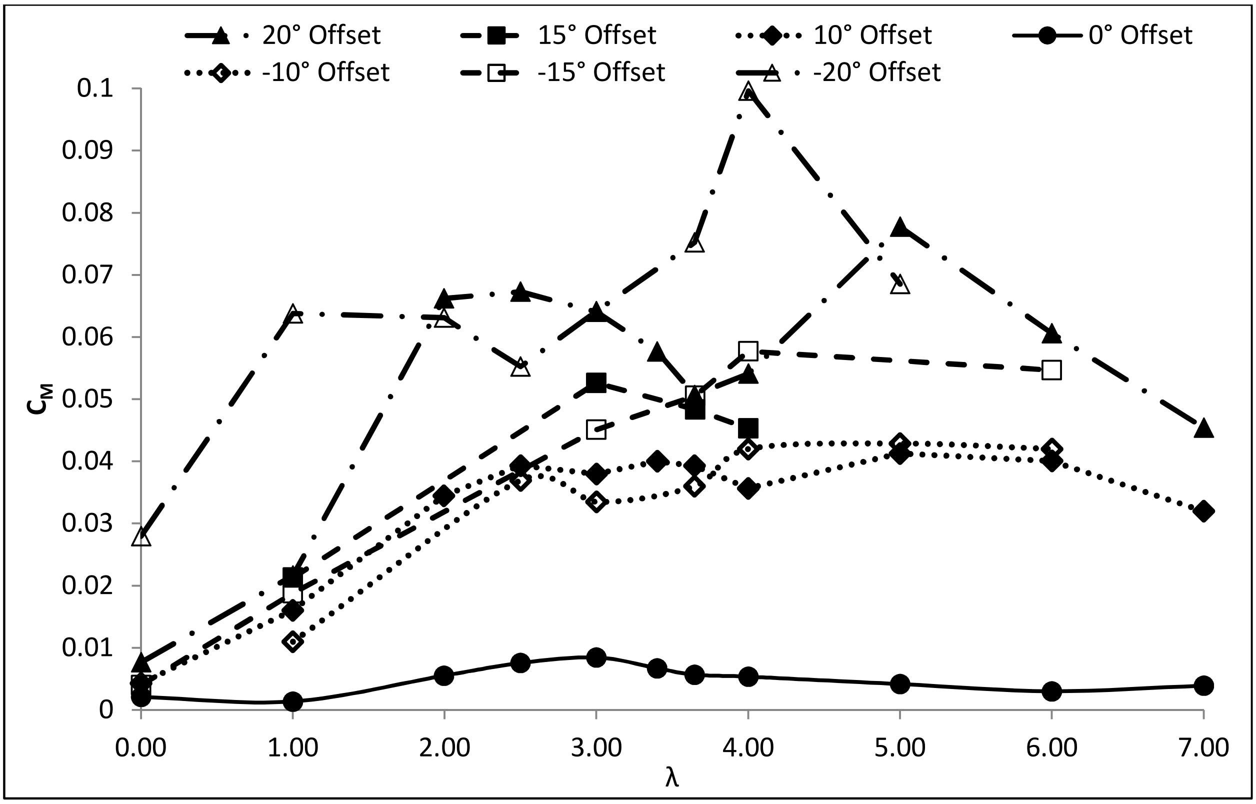

Figure 6.4 Coefficient of resultant shaft bending moment against λ for turbine misalignments

6.1.5. Discussion

It is evident from the performance characteristics shown that the misalignment between a turbine and the principle flow direction has a detrimental impact. The peak coefficients of torque and power both drop as low as 11% and 25% respectively in comparison to their aligned cases. The reduction in coefficient of thrust is a positive from a loading perspective, however only 18% reduction is a not a significant gain when compared to the drop in C_P.

A significant result that requires further investigation is the deviation of the positively and negatively misaligned cases from one another. It appears that at low and high rotational velocities there is little deviation between polar misalignments, however at and around peak C_θ and C_P a significant deviation occurs. At peak C_θ the positive misaligned cases perform better than the negatively misaligned cases, however at peak C_P the reverse is true. It is suspected that the direction of misalignment influences the performance due to the rotational direction of the turbine. Further investigation into this by considering the pressure contours about the Blade at TDC are shown in Figure 6.5. These contour plots show a horizontal plane passing through the turbine, 3m above the axis of rotation. The aligned turbine cases and positive and negative yaw angles cases are shown (Figure 6.5). It appears that the separation between the high and low pressure sides of the blades breaks down as the relative velocity at the tips of the turbine blades increases. The contours for a TSR of 2 are all very similar with a high pressure region on the front face of the blade (the bottom faces in Figure 6.5) and a low pressure region on the back face of the blade. There is a slight change however as λ increases to 3.65, which is close to peak power. It can now be seen that a low pressure region has begun to form on the front face of the blade. The low pressure region is small for the aligned and +10° yawed case, but is considerably larger for the +20° yawed turbine case. Conversely, the -10° yawed case and -20° yawed case seem to require higher tip velocities before the low pressure contours begin to appear on the high pressure side of the blade. This aids in explaining the reason for the increased performance in the negatively aligned case.

Figure 6.5 Pressure contours at 3m above rotational axis on Blade 1

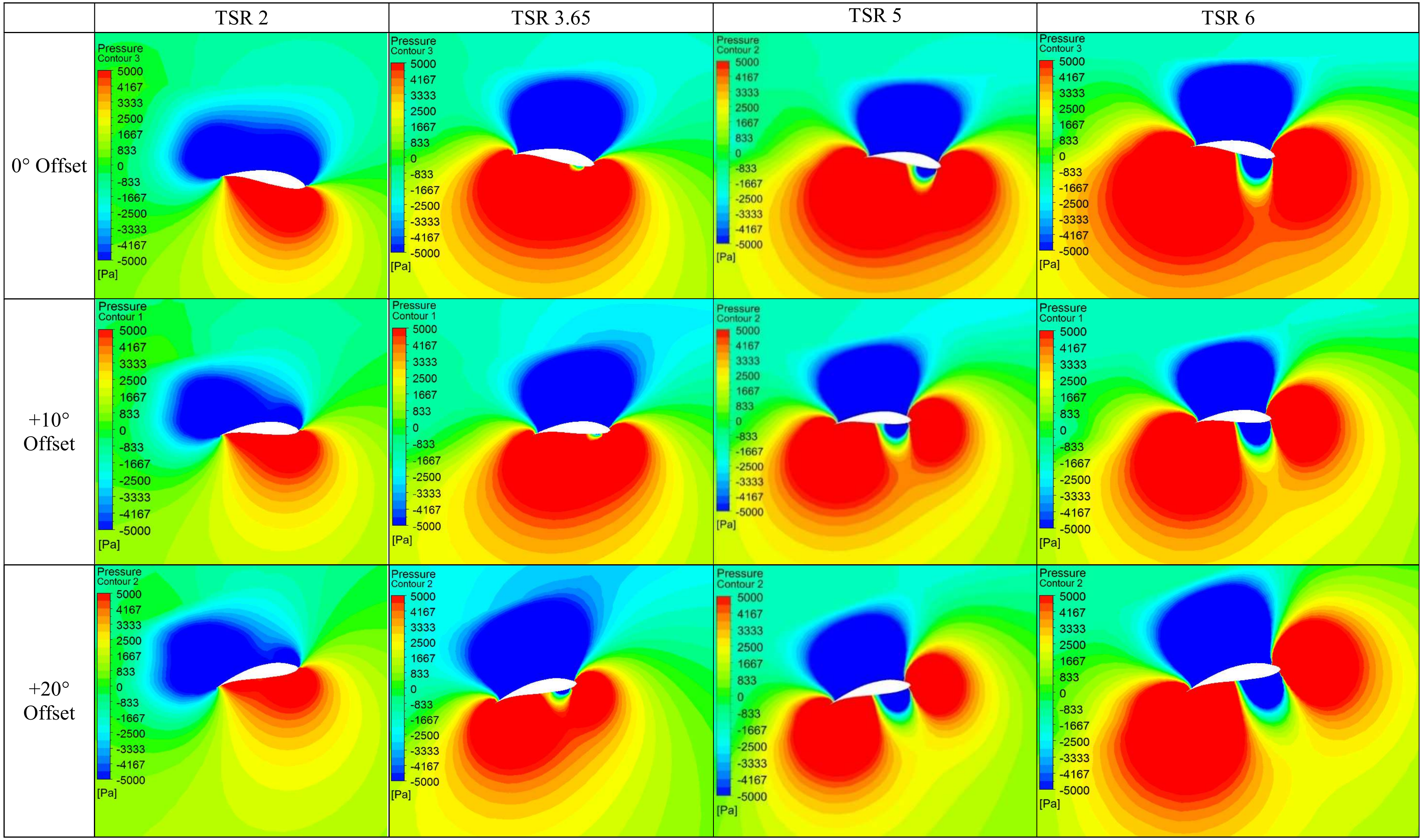

	TSR 2	TSR 3.65	TSR 5	TSR 6
0° Offset	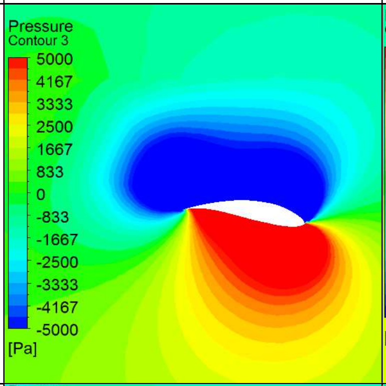	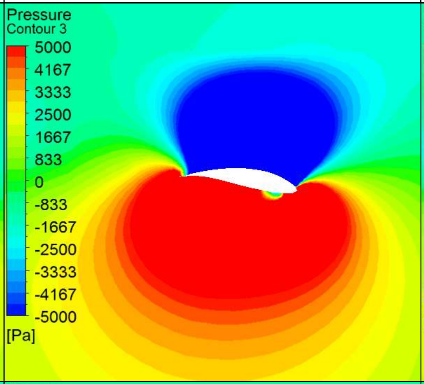	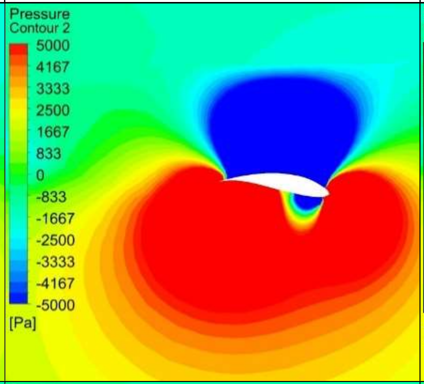	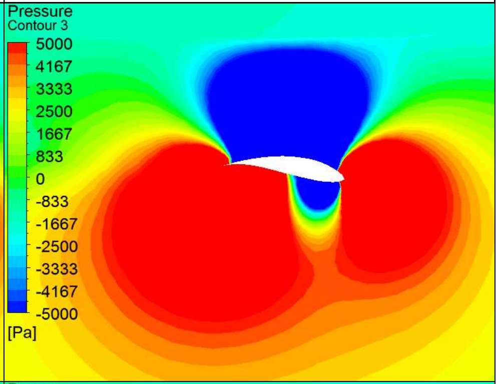
-10° Offset	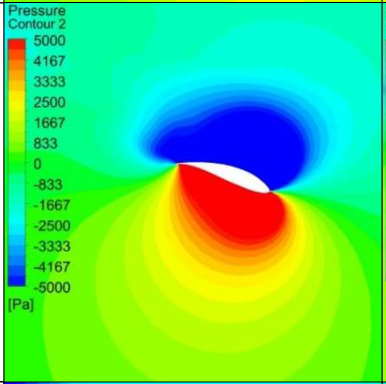	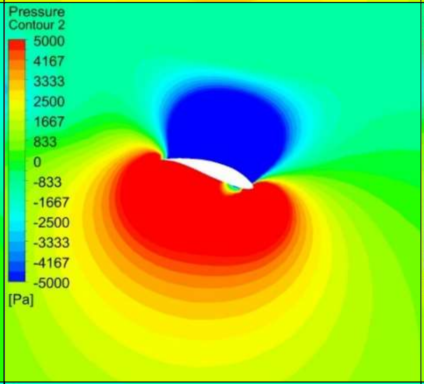	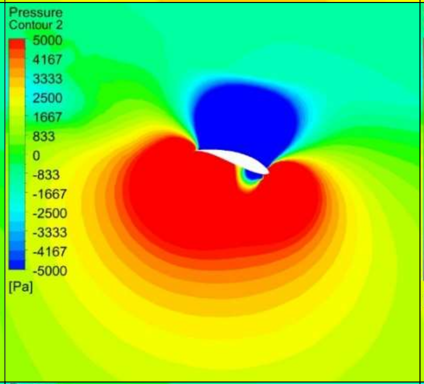	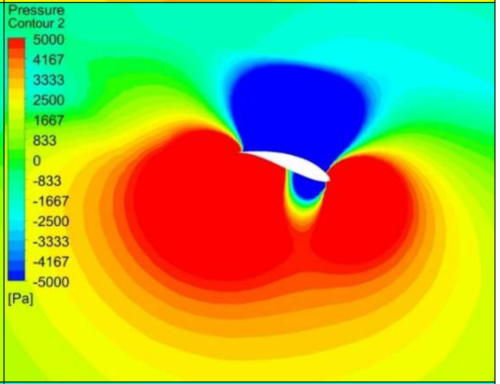
-20° Offset	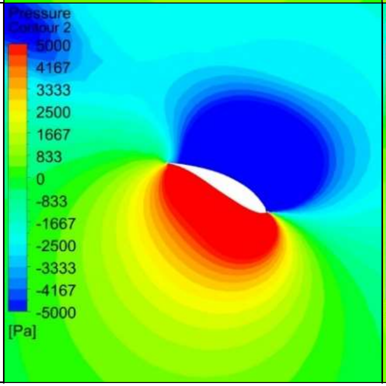	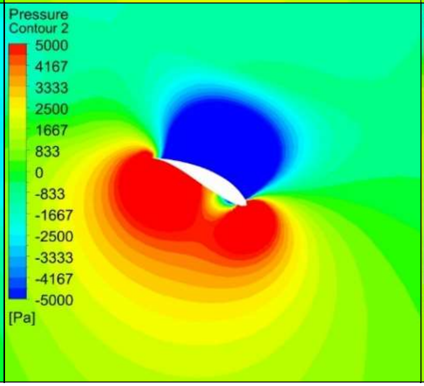	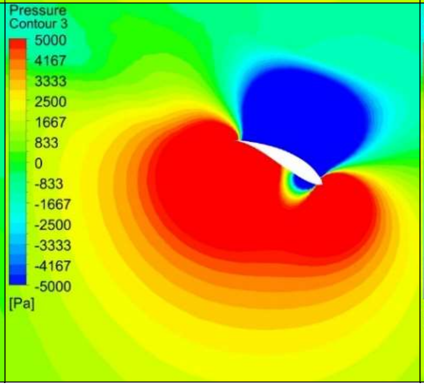	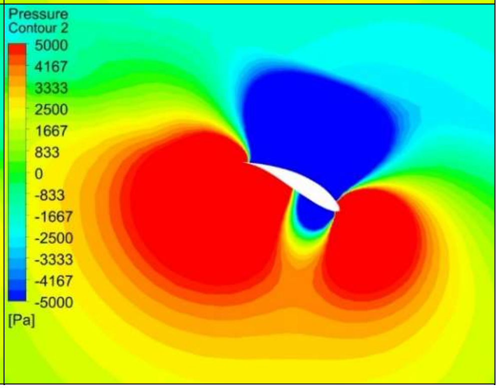

6.2. Transient

As identified in Section 2.1.2, the rotational position of the turbine is significant when considering a turbine operating at a yaw angle. To further investigate the effect of misalignment/ yaw angle on turbine performance during rotation a transient model with the same parameters and geometry as the steady-state study was utilised. The transient models were analysed at $\lambda = 3.65$, which corresponds to the angular velocity of peak C_P as identified by the steady-state models. This provided results for a full range of blade rotational positions. Further transient models were run for $\lambda = 3$ and $\lambda = 5$, however these results are not discussed here but are used later in Section 8.1.

The transient results shown in this section plot the coefficients of torque, power, thrust and out-of-plane bending moments of each blade and the hub against the azimuth/ rotational position of blade 1, for a given angular velocity. The azimuth (φ) of blade 1 is considered for a complete rotation, with 180° being blade 1 at Bottom Dead Centre (BDC), and is directly in-line with the support stanchion and 0° and 360° being blade 1 at TDC, with no stanchion interaction. The figures in this section run from 180° to 540°, which is one full rotation. The rationale for the start being at BDC is due to it being the earliest point after the model had stabilised from which to take results. The same angles of misalignments are considered here as in Section 6.1, the aligned turbine case and ±10°, ±15° and ±20° misaligned turbine cases. The mean (μ) and normalised standard deviation (σ) were taken using equations [**3.19**] and [**3.20**] respectively from theory section across the plotted data range and not the complete data sets, in order to avoid skewed results from the start up.

6.2.1. Torque

The C_θ has been plotted against blade 1 azimuth, φ. The aligned case can be seen in Figure 6.6 with the total C_θ for the entire rotor swept area shown on the LHS axis and the torque of the individual blades on the RHS axis. The total turbine C_θ performance having a mean of $\mu = 0.123$ and standard deviation of $\sigma = 0.004$. Consideration should be given to the performance of blade 1, as the blade passes approximately BDC, $\varphi = 183°$. The torque contribution from the blade drops to a trough of 71.9 kNm. This is as expected due to stanchion interaction as discussed in Section 5.2 previously. The asymmetry in blade 1 torque curve is noteworthy, after the blade passes the stanchion the performance recoveres slower than when approaching the stanchion at BDC. The peak performance occurs at 393° which is equivalent to 33° relative to TDC, with a torque of 78.0 kNm. Blades 2 and 3 experience the same peaks and troughs in performance with a phase difference of 120° due to geometry. Therefore only blade 1 will be looked at from here onwards and symmetry in the blade performance is expected with 120° phase difference.

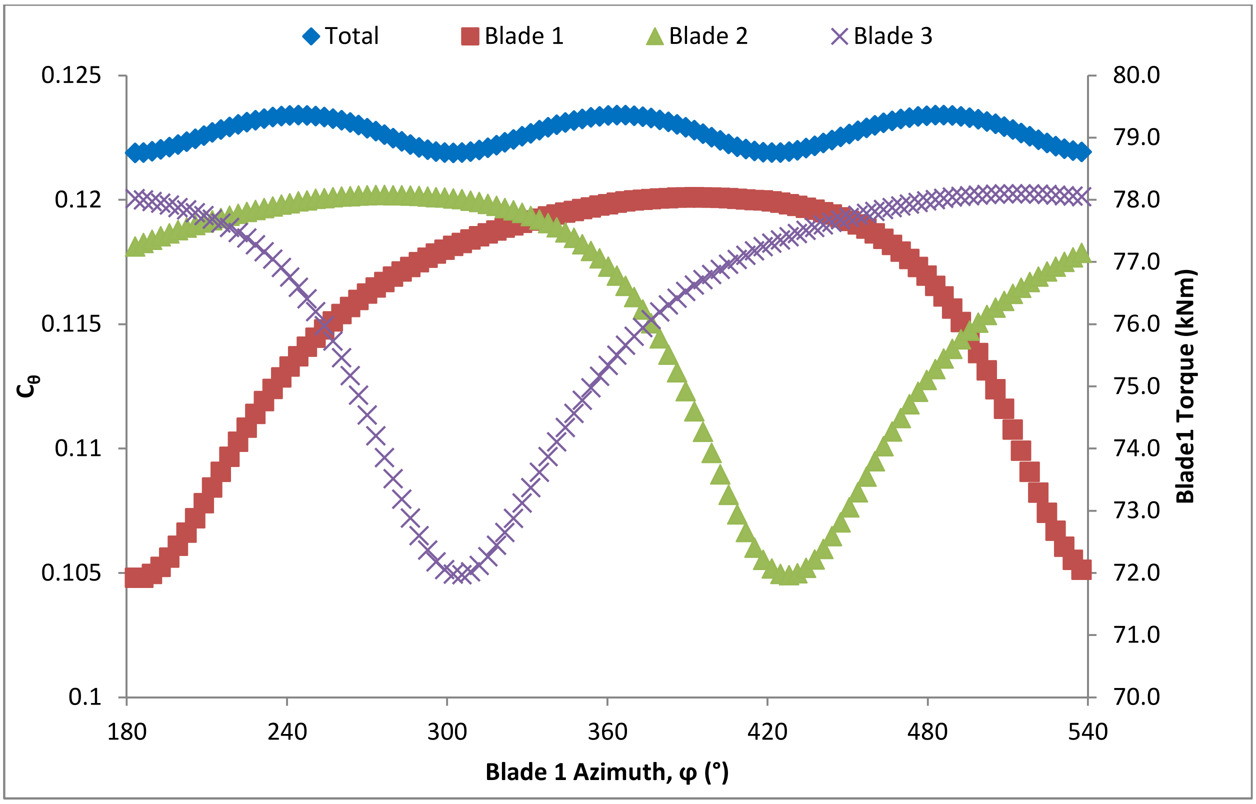

Figure 6.6 C_θ - φ for 0° yaw angle (aligned case) at λ = 3.65

Figure 6.7 shows C_θ-φ for the aligned case and all the yaw angle cases at peak power. The aligned turbine has the highest torque and there is a clear negative trend with positive or negative yaw angles. The ±10° and ±20° yaw angle cases have similar mean values, however there is a significant difference between the ±15° yaw angle cases. Table **6.4** shows the changes in mean, standard deviation and the phase shift between all the cases. The mean is a percentage change relative to the aligned case and confirms the negative trend with increasing yaw angle. The standard deviation was calculated by normalising the data set against its mean and then applying equation [**3.20**]. The standard deviation clearly reduces as the turbine is yawed in the negative direction, conversely it increases as the turbine is yawed in the positive direction. The phase shift is taken as the change in azimuth of the first peak in the curves. There is a clear positive and negative shift with a positive and negative yaw angle.

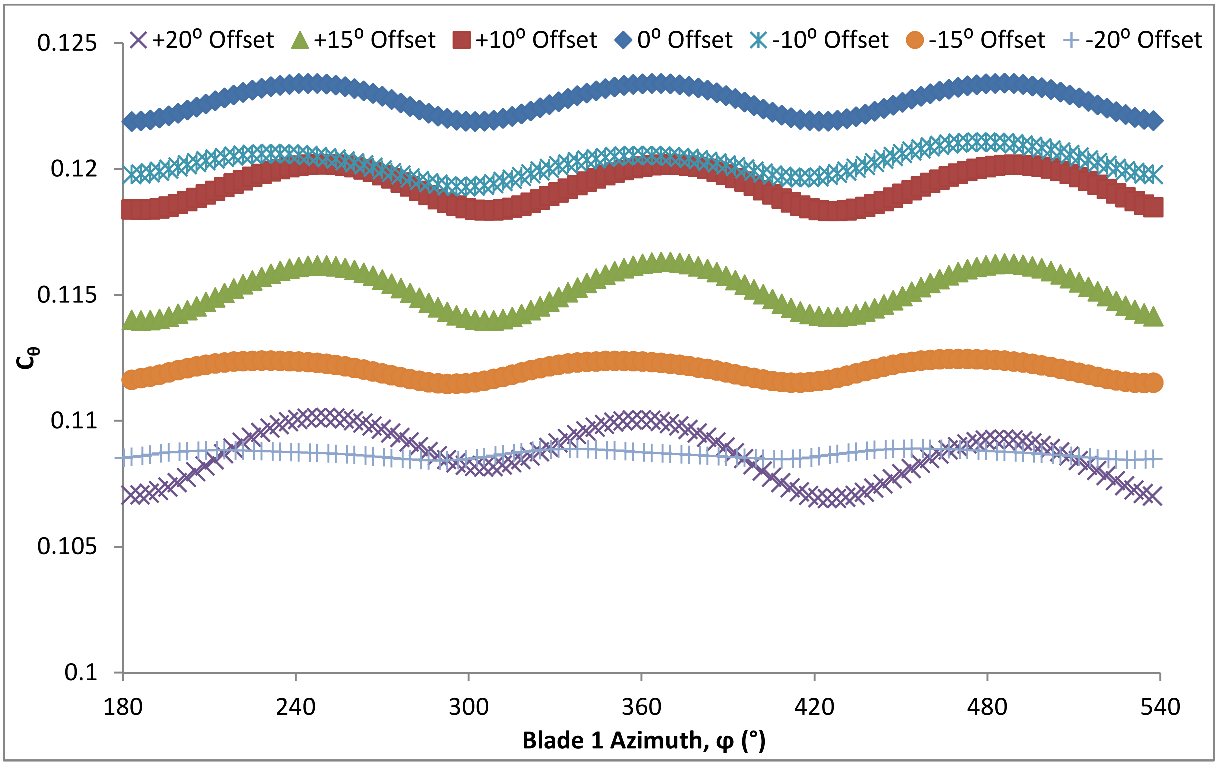

Figure 6.7 C_θ - φ for all yaw angles at λ = 3.65

Table 6.4 Change in C_θ mean, standard deviation and phase with misalignment

Yaw Angle	**C_θ - μ**	**C_θ - σ**	**C_θ – Φ (°)**
+20⁰	88.48%	0.009244	6.15
+15⁰	93.88%	0.006708	3.22
+10⁰	97.24%	0.00545	6.45
0⁰	100.00%	0.004404	0
-10⁰	98.02%	0.003832	-12.89
-15⁰	91.31%	0.002868	-16.11
-20⁰	88.58%	0.00135	-31.58

Studying the individual performance of blade 1 in kNm for all the yaw angles, as seen in Figure 6.8, the 0° yaw angle (aligned) case has already been reported and is the same as in Figure 6.6. The +10° yaw angle has a peak of 78.5 kNm which is unexpectedly higher than the aligned case. The peak occurs at φ= 334°, this is 59° earlier in the rotation than the aligned case. The trough has a value of 65.9 kNm and occurs at φ= 189° which is only 6° later than the aligned case, and remains due to the stanchion interaction. As expected the -10° yaw angle has a very different blade 1 torque performance through 1 rotation. The peak occurs much later than its positive counterpart, being 90° later than the aligned case with a magnitude of 77.5 kNm at φ= 483°. The performance of blade 1 for the -10° yaw angle no longer experiences its greatest drop in torque as it passes the stanchion, but now is at an azimuth of 363° with a magnitude of 72.7 kNm, the trough remains ~1 kNm higher than the aligned case and ~6.8 kNm higher than the +10° yaw angle case. The +15° and +20° yaw angles have respective peaks of 77.9 kNm and 76.1 kNm, both at φ= 328°. Both cases are lower than the aligned case, and occur earlier in the rotation than the aligned case. The troughs in blade 1 torques for +15° and +20° yaw angles have a magnitude of 60.9 kNm and 53.3 kNm at φ= 189° and φ= 192° respectively. The troughs are lower than the aligned case and occur slightly later in the rotation than the aligned case, probably because the point at which the blade passes directly in-front of the stanchion is later. The -15° and -20° yaw angle cases have a peak torque of 73.4 kNm and 73.3 kNm at φ= 483° and φ= 490° respectively. Both these instances are lower than the aligned case and later in the rotation, interestingly they are very similar in magnitude to one another. Consideration of the troughs in -15° and -20° yaw angle cases shows a different story, with a magnitude of 65.4 kNm and 60.2 kNm at φ= 370° and φ= 374° respectively. Both these results have a much lower trough than the aligned case and both occur ~180° from the aligned case close to TDC. This re-enforces what was seen with the -10° case, the negative yaw angle detrimentally impacts the blade as the blade passes TDC. Consideration of the power performance will be conducted in the next section.

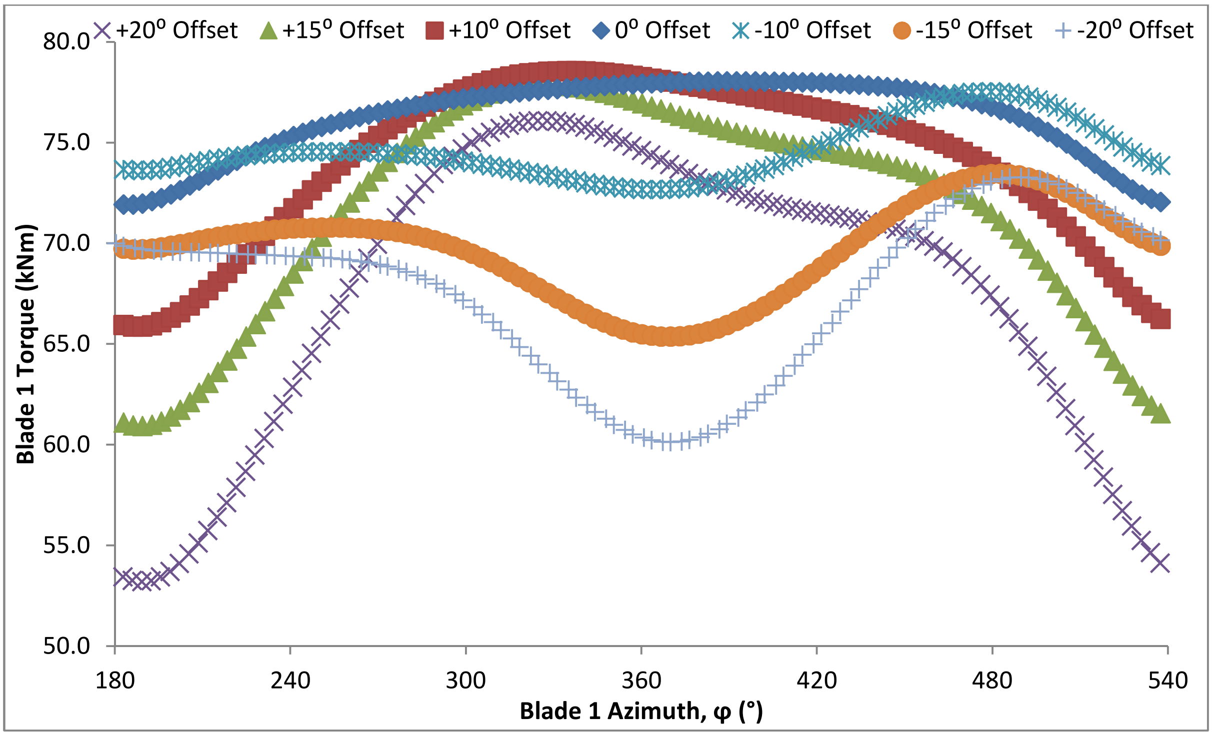

Figure 6.8 Blade1 Torque - φ for all yaw angles at λ = 3.65

6.2.2. Power

The C_P has been plotted against blade 1 azimuth, φ. The aligned case can be seen in Figure 6.9 with the C_P of the entire rotor shown on the LHS axis and the power provided by each blade in kW is on the RHS axis. The total turbine C_P performance has a mean of $\mu = 0.447$ and standard deviation of $\sigma = 0.004$. The curve experiences three peaks and troughs in performance and can be seen to coincide with the peaks and troughs of the power contributed by the individual blades. Considering the performance of blade 1, as the blade passes approximately BDC, φ= 183° the power is 161 kW. The peak power contribution of blade 1 occurs at φ= 393° for the aligned turbine with a magnitude of 176 kW. As is expected the same phase difference between the blades occurs with the power performance as with the torque performance previously. For this reason then only the rotor as a whole and blade 1 will be considered for the rest of this section.

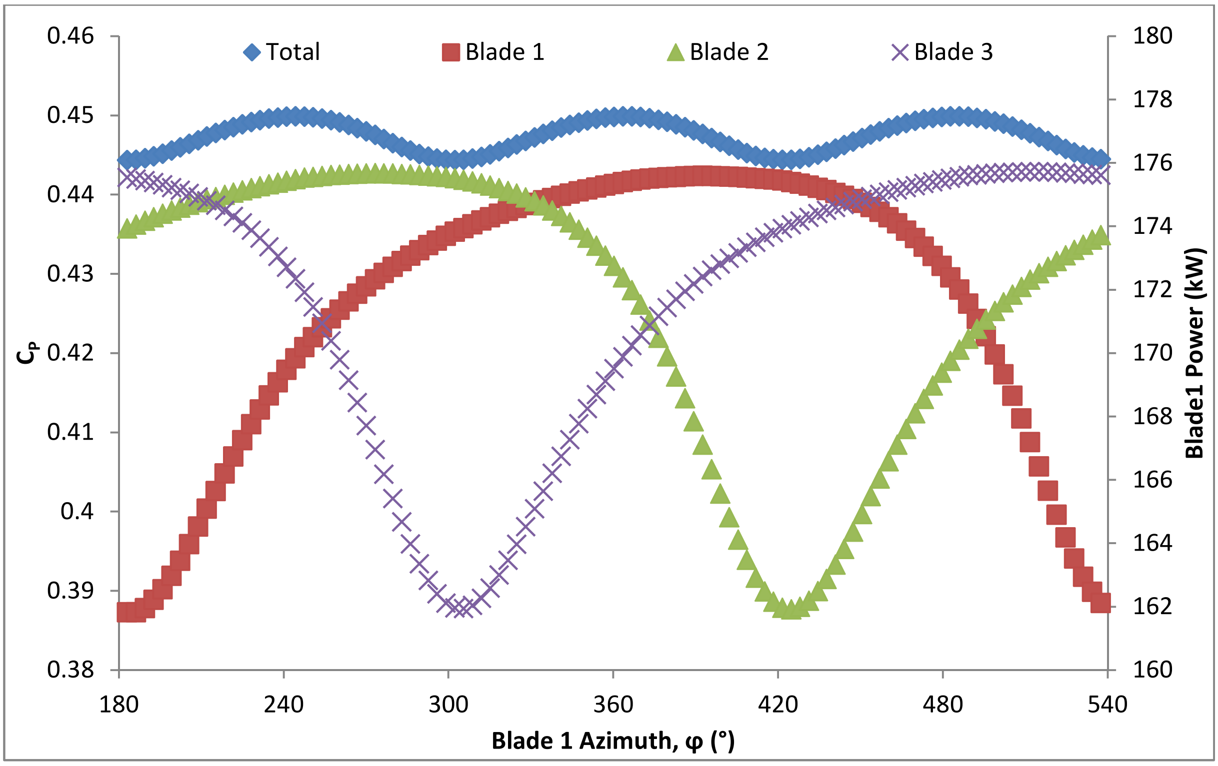

Figure 6.9 C_P - φ for 0° yaw angle (aligned case) at λ = 3.65

The C_P-φ curves for all the turbine's yaw angle cases are shown in Figure 6.10, the aligned case is the same as in Figure 6.9. There is a clear negative trend with increasing yaw angle, both positive yaw and negative. The difference in the positive and negative yaw angles of the same magnitude (ie ±10°) shows that the blades are sensitive to yaw direction. Table 6.5 shows the change in mean C_P as well as standard deviation and phase with changing yaw angle. The mean has been shown as a percentage change relative to the aligned case, whilst the standard deviation is taken from the normalised data set against its mean value. The phase shift is taken as the change in azimuth of the first peak. There is clearly a trend in both the mean percentage change and standard deviation.

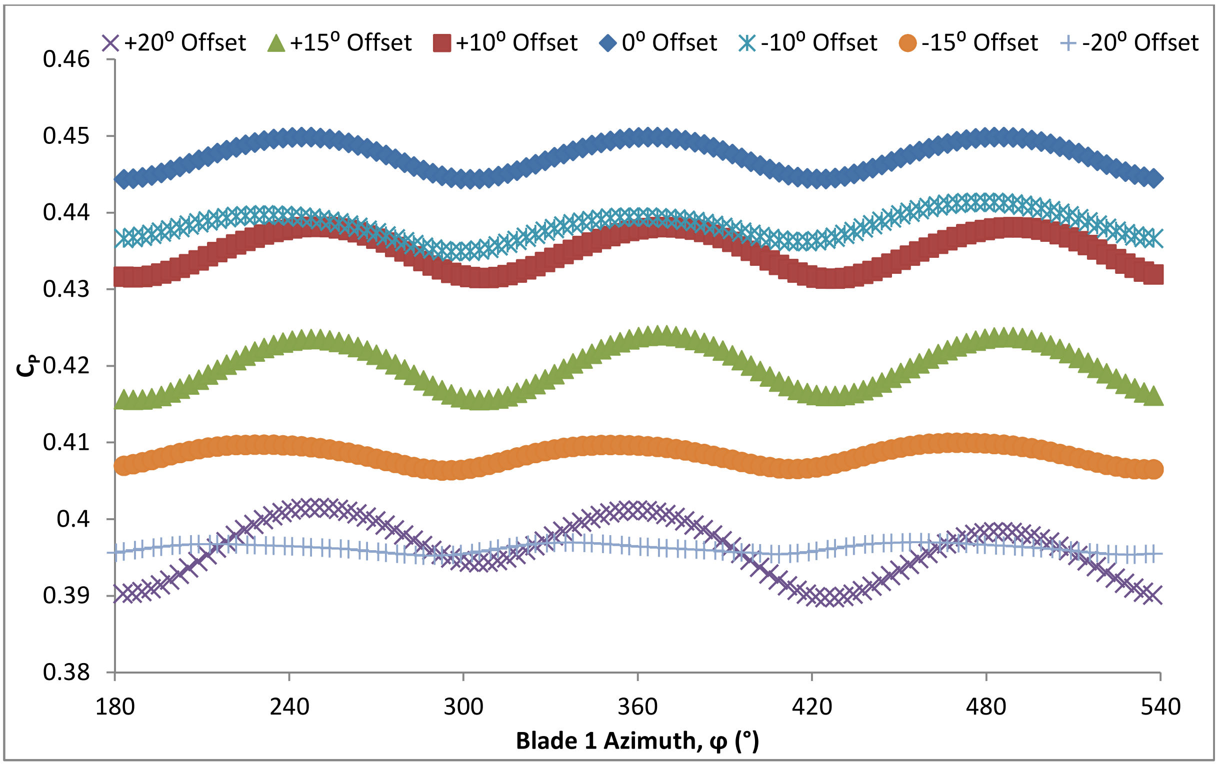

Figure 6.10 Total C_P - φ for all yaw angles at λ = 3.65

Table 6.5 Change in mean C_P, standard deviation and phase with yaw angle

Yaw Angle	μ	σ	Φ (°)
+20⁰	88.48%	0.009	6.0
+15⁰	93.88%	0.007	3.0
+10⁰	97.24%	0.005	7.0
0⁰	100.00%	0.004	0.0
-10⁰	98.02%	0.004	-13.0
-15⁰	91.31%	0.003	-13.0
-20⁰	88.58%	0.001	-31.0

Figure 6.11 shows the power contribution from blade 1 for all yaw angle cases at a λ value corresponding to peak power. As the power is taken from the product of the torque and rotational velocity of the blade, the trends seen in this figure are the same as in Figure 6.8. Given the same

trends, Figure 6.11 is included in this analysis to emphasise the -10° yaw angle case which can be seen to have the highest power when passing the stanchion at BDC.

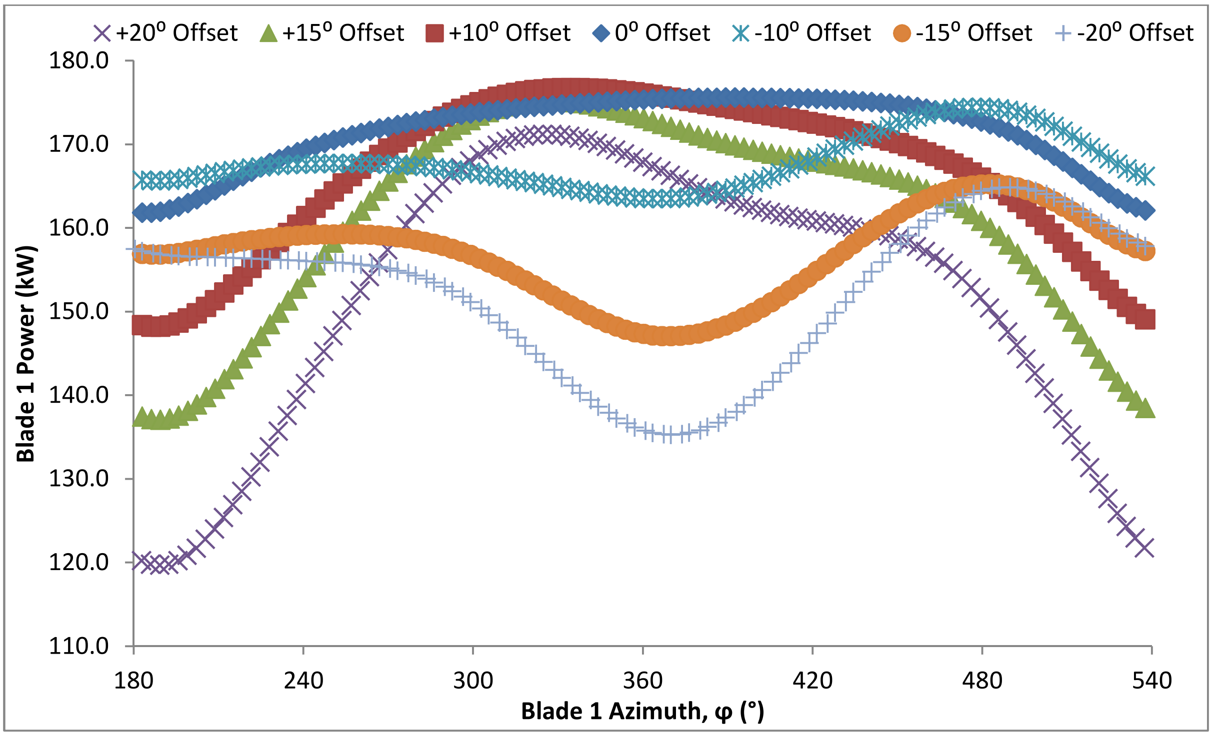

Figure 6.11 Blade1 Power - φ for all yaw angles at λ = 3.65

6.2.3. Thrust

The C_T has been plotted against blade 1 azimuth, φ. The aligned case can be seen in Figure 6.12 with the C_T of the entire rotor shown on the LHS axis and the power provided by each blade in kN is on the RHS axis. The aligned turbine case has a C_T performance with a mean of $\mu = 0.847$ and standard deviation of $\sigma = 0.003$. It can be seen from Figure 6.12 the thrust contribution from each blade is identical, only phase shifted through 120° due to the geometry. When the performance of blade 1 is considered in isolation, for the aligned case, the blade experiences a peak thrust load of 106 kN at

447° and a trough in thrust load down to 100 kN at 199°. Notably the onset of peak thrust occurs after the onset of peak power and likewise for the troughs in thrust and power.

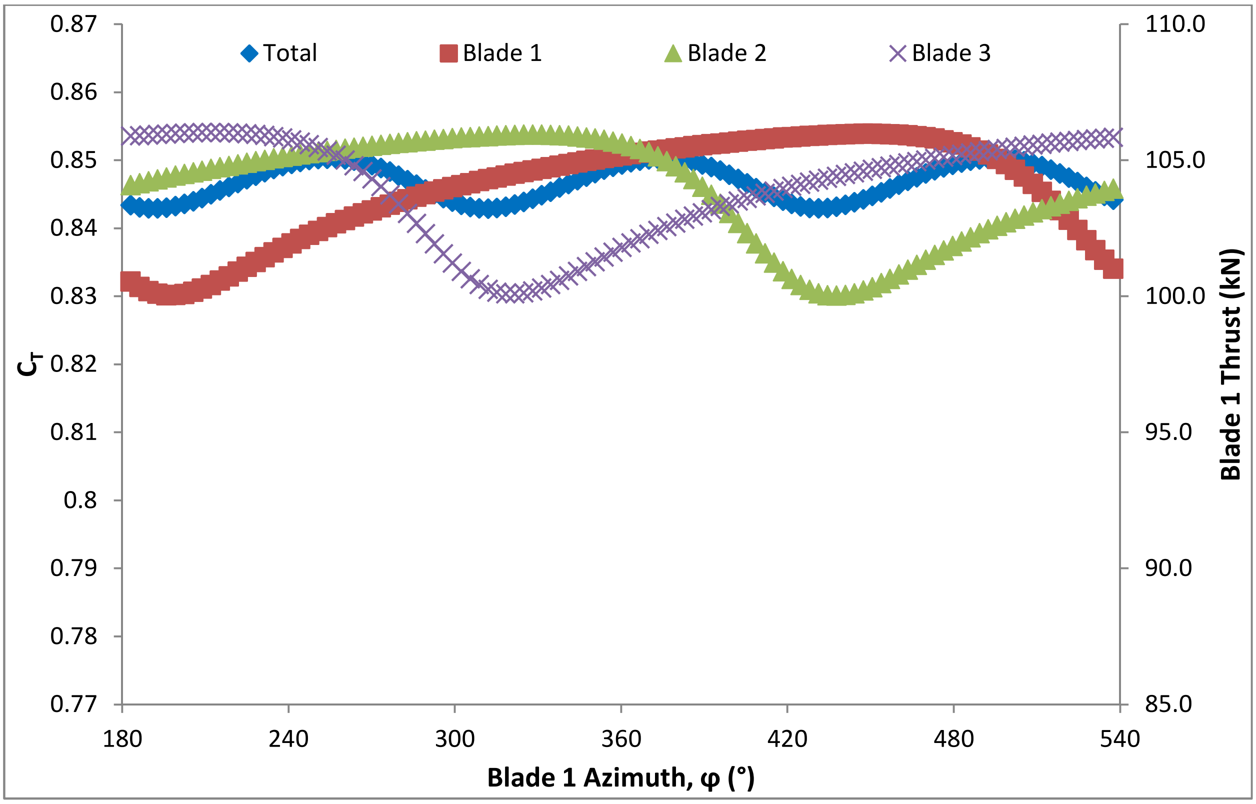

Figure 6.12 C_T - φ for 0° yaw angle (aligned case) at λ = 3.65

The C_T-φ of the turbine for all yaw angle cases is shown in Figure 6.13. The aligned case has already been described in the previous figure and remains the same. The mean C_T value increase as the turbine goes to ±10° yaw angle. However the standard deviation increases for the +10° and decrease for the -10°. There is also a noticeable phase shift when compared to the aligned case, in Figure 6.13. The phase has advanced for the +10° yaw angle case and retreated for the -10° yaw angle case. The corresponding means, standard deviations and phase differences for each of the cases is shown in Table **6.6**. The mean values are shown as a percentage change from the aligned case, and the standard deviations are formed from normalising the data set against its mean. Whilst the phase shift, Φ is the number of degrees the first peak has advanced or retreated relative to the aligned case. The mean values agree with what was identified in Figure 6.13, whilst the standard deviations are shown to increase as the positive yaw angles increases, and decrease as the negative yaw angle increases. The phase shift is incoherent, with the -15° yaw angle showing a positive phase shift, which was unexpected.

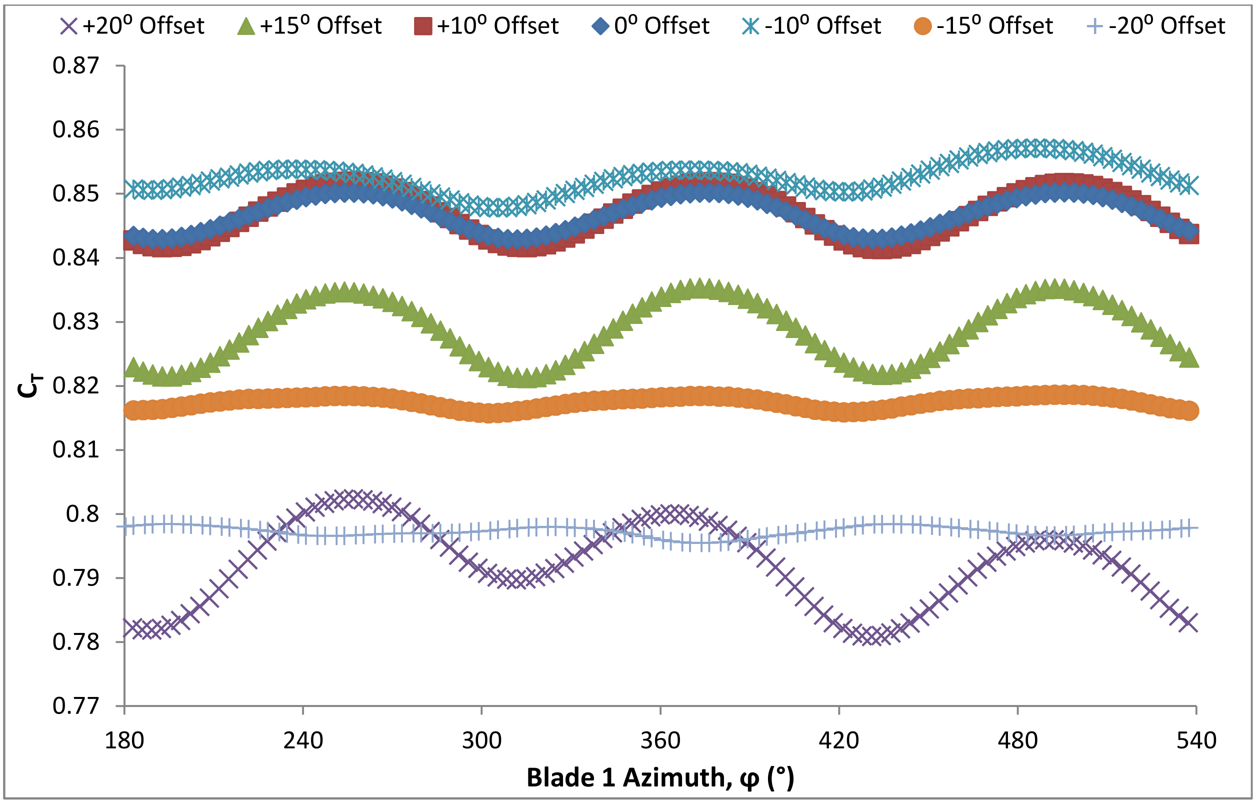

Figure 6.13 Total C_T - φ for all yaw angles at λ = 3.65

Table 6.6 Changes in mean C_T, standard deviation and phase with yaw angle

Yaw Angle	C_T - μ	C_T - σ	C_T – Φ (°)
+20⁰	93.48%	0.008	2.9
+15⁰	97.86%	0.006	0.0
+10⁰	100.02%	0.004	3.2
0⁰	100.00%	0.003	0.0
-10⁰	100.72%	0.003	-16.1
-15⁰	96.55%	0.001	3.2
-20⁰	94.16%	0.001	-58.0

Figure 6.14 considers the thrust load on blade 1 for all yaw angle cases. There is a distinct trend between the positive and negatively yawed cases. The positive yaw cases have a peak in thrust load around φ= 488° whilst the negatively yawed cases all have a peak thrust load around φ=330°. The troughs of the positive yaw cases are no longer at BDC but now occur at around φ=370°, close to TDC. For the negatively yawed cases the troughs remain close to BDC as expected. The negatively yawed cases have lower troughs relative to their positively yawed counterparts.

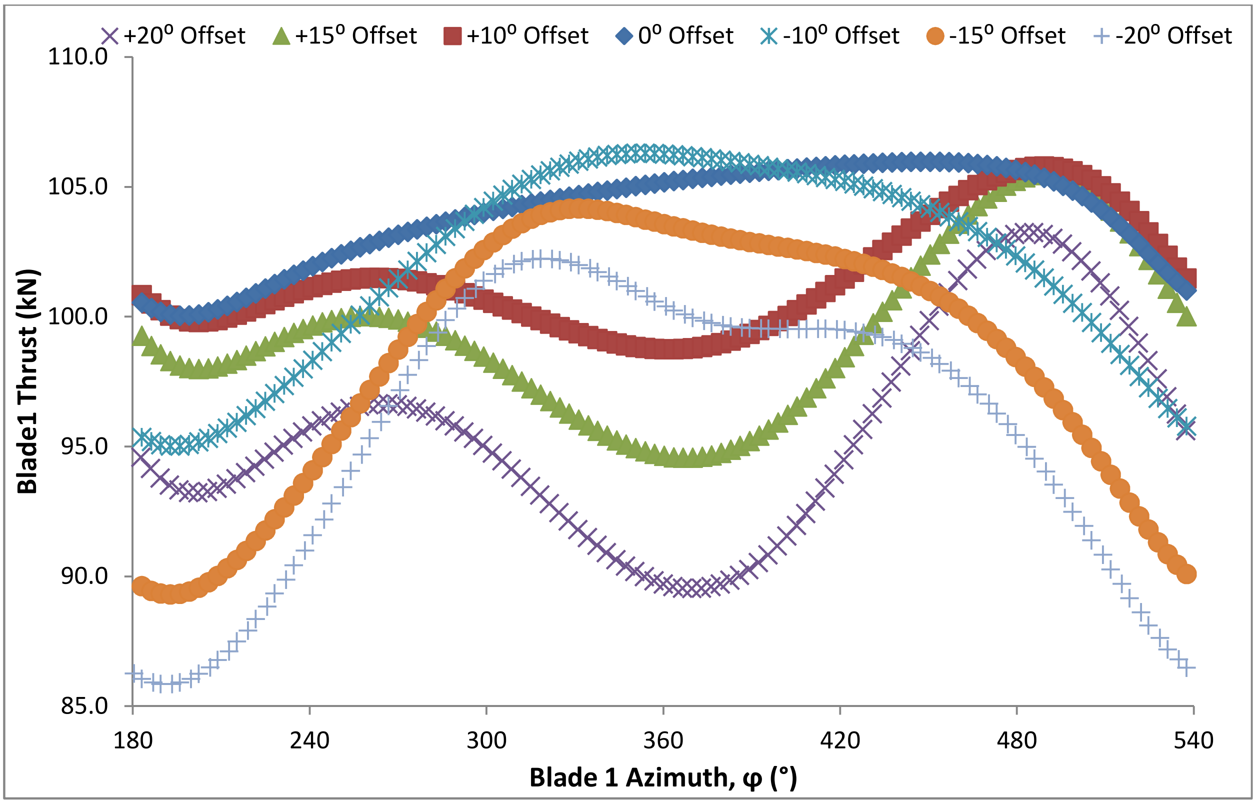

Figure 6.14 Blade1 Thrust - φ for all yaw angles at λ = 3.65

6.2.4. Out-of-Plane Bending Moments

The out-of-plane bending moments are calculated using equation [3.14] and the angle at which the out-of-plane bending moment is acting is calculated using equation [3.15]. Figure 6.15 shows the coefficient of out-of-plane bending moment for the aligned case on the LHS axis and the angle of acting bending moment on the RHS axis. The aligned case has a mean C_M of $\mu = 0.008$ and a mean acting angle of 312˚. The C_M for the aligned case has a standard deviation of $\sigma = 0.243$, whilst the acting angle has a standard deviation of $\sigma = 0.048$. Figure 6.15 as expected is similar to that of Figure 5.11, the no stanchion case considered in Section 5.2.4. However the presence of a stanchion interfering at BDC gives rise to a higher C_M as well as greater fluctuations in C_M. The peaks in C_M have a 120˚ interval, with the first occurring when blade 1 is at φ= 212˚ which is 30˚ past BDC. This is likely to be the point at which the difference in thrust load between the three blades is at its greatest giving rise to large out-of-plane bending moments. The angle of acting bending moment fluctuates around its mean of 312˚.

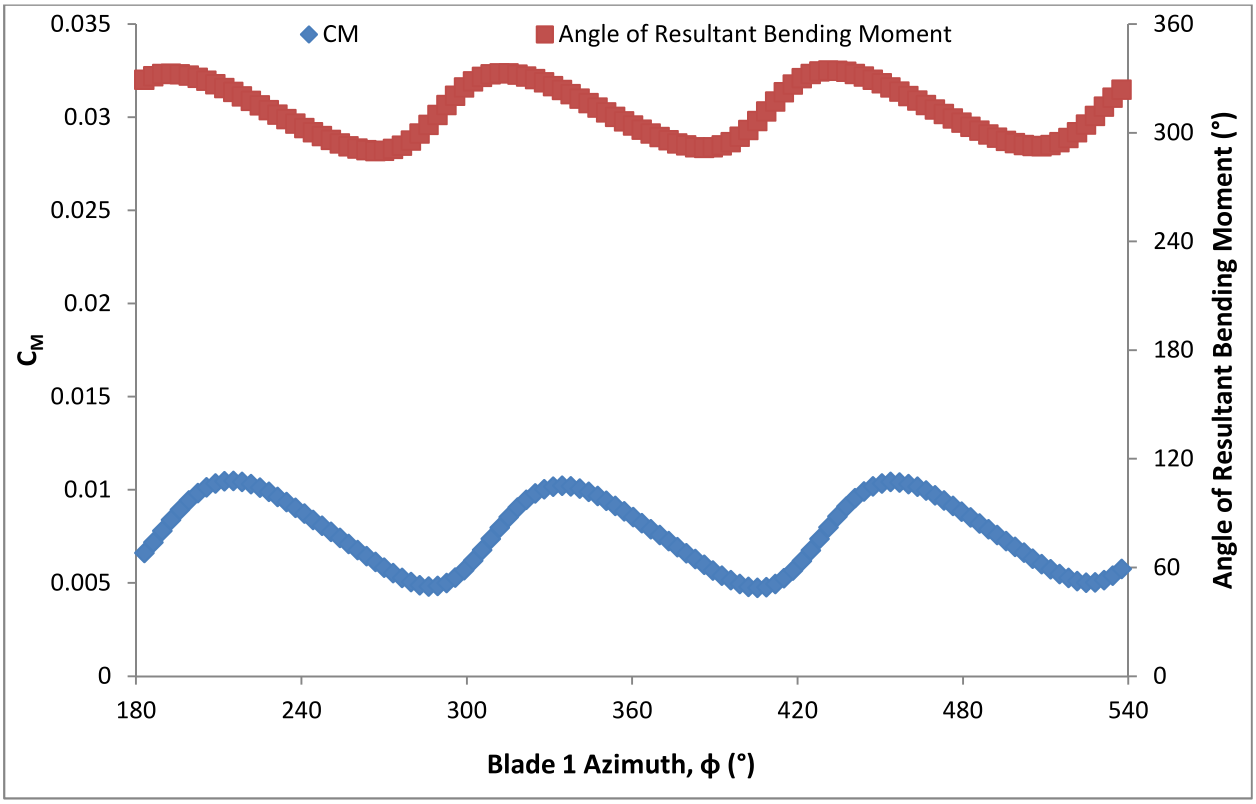

Figure 6.15 C_M and angle of resultant BM against azimuth for aligned case

Figure 6.16 & Figure 6.17 shows the C_M and acting angle of out-of-plane bending moment for the positively and negatively yawed cases respectively. It is clear that with increasing yaw angles, either positively or negatively away from the aligned case, the C_M value increases. There are also slight changes in the form of the C_M curve with increasing yaw angle. The shape appears to become more symmetrical about its peak or trough and less of a falling bias as seen in the aligned case. Table 6.7 shows the percentage increase in C_M with misalignment which increases to 351% of its original value in the worst case. The table also shows that the aligned case has a higher standard deviation for the C_M in the aligned case than the yawed cases. The percentage change in the angle of acting bending moment is not as important as the standard deviation for the acting angle of bending moment, which is more significant in the positively yawed cases and becomes less significant for negatively misaligned cases.

Table 6.7 Mean and standard deviation for the C_M and acting angle for all cases

Yaw Angle	C_M - μ	Angle - μ	C_M - σ	Angle - μ
+20°	308.82%	73.02%	0.181	0.051
+15°	241.15%	73.03%	0.174	0.050
+10°	170.27%	76.20%	0.175	0.055
0°	100.00%	100.00%	0.243	0.048
-10°	220.63%	57.95%	0.132	0.029
-15°	307.51%	60.35%	0.134	0.030
-20°	351.16%	63.36%	0.130	0.030

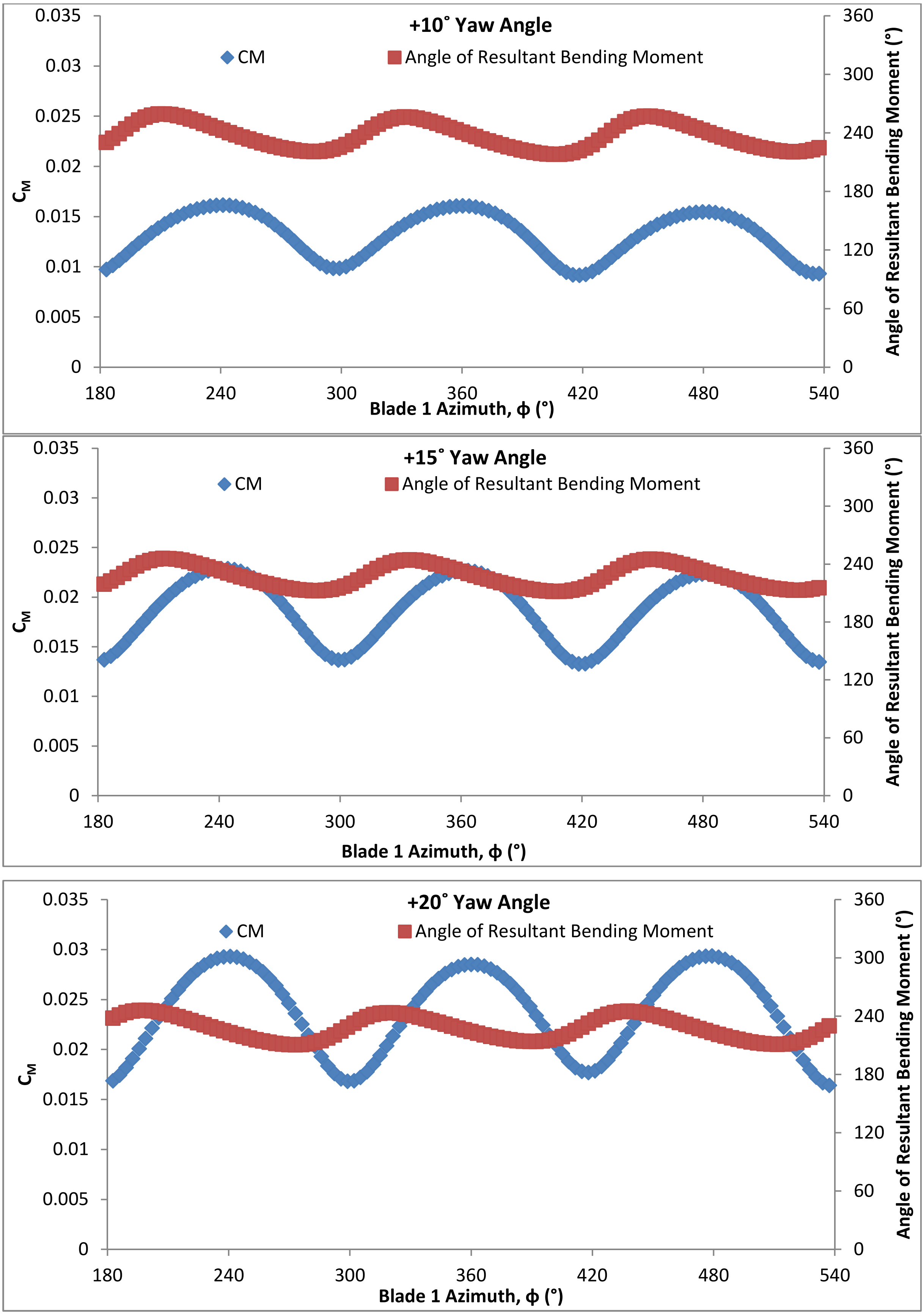

Figure 6.16 C_M and acting angle of BM against azimuth for positive yaw cases

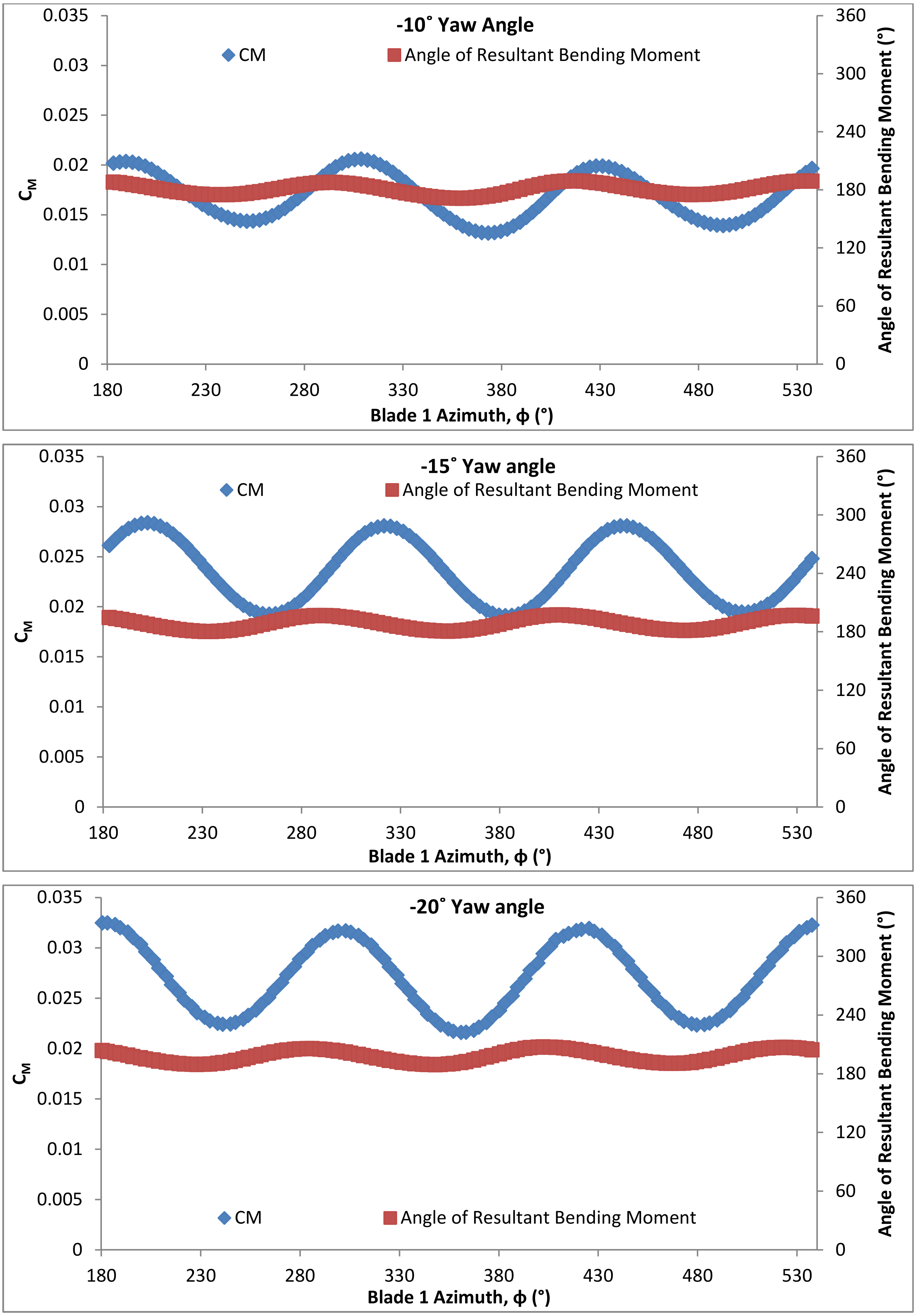

Figure 6.17 C_M and acting angle of BM against azimuth for negatively yawed cases

The final thing to consider is the contribution of a single blade to the out-of-plane bending moment, this is shown in Figure 6.18. The trend for all the cases appears to be very similar with the most significant difference being the negatively yaw angle cases having an 180˚ degree phase shift. The peak and trough occur at TDC and BDC respectively for the aligned and positive yaw angle cases, and then in reverse for the negative yaw angle cases. In addition, all cases appear to have the same minimum values, however the aligned case has the greatest maximum value and this maximum is reduced as the yaw angle increase between cases.

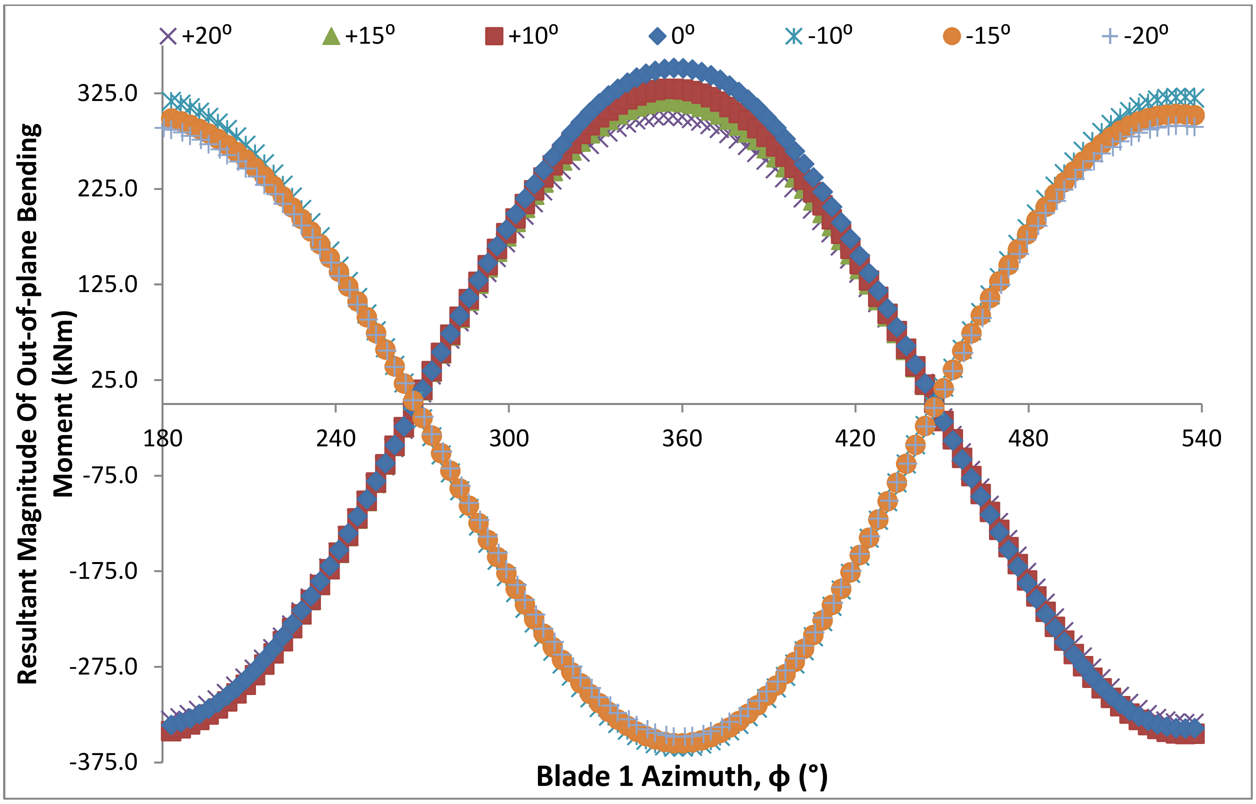

Figure 6.18 Resultant Magnitude of out-of-plane bending moment for blade 1 during a single rotation

6.2.5. Discussion

This section has shown the performance characteristics of a tidal stream turbine aligned to the flow and at yaw angles of ±10˚, ±15˚ and ±20˚. It has been shown that with increasing yaw angle, either positive or negative the mean coefficients of torque and power drop, as would be expected. Insight into the performance of a single blade during rotation has shown the cause of the deviation between the positively yawed turbine cases to the corresponding negatively yawed turbine cases. The blade performs better when passing the stanchion if there is a negative yaw angle, the yaw angle of -10˚ was shown to be optimum at near BDC. There is a resulting reduction in the standard deviation of the total C_T and C_P values with negative yaw angles.

The coefficient of thrust showed that with increasing yaw angle there is a slight increase in thrust up to ±10˚, this is then reduced as the yaw angle increases toward ±20˚. There is again a reduction in the standard deviation with negative yaw angle making it more preferential to positive. The results for the coefficient of out-of-plane bending moments showed that there is a significant increase in mean values with yaw angle and this is considerable higher for negative yaw angle compared with positive yaw angle. The implications of this will be to the fatigue life of the bearings. Any form of yaw angle will have a detrimental impact, due to the increase in the mean value, however the standard deviation in the acting angle of the out-of-plane bending moment shows that for positive yaw angle cases the increased load will be spread across a greater arc in the bearing than for the negative yaw angle cases. This however would require further work on bearing fatigue life prediction to confirm.

6.3. Summary

This Chapter has shown the significance of flow misalignment on the performance of tidal stream turbines. It has been established that an increasing yaw angle decreases the non-dimensional performance of the turbine. The steady state CFD models showed a reduction in the performance curves with the most significant difference seen around the peak C_θ and C_P values. Figure 8.17, Figure 8.19 and show the difference between the steady state and transient CFD performance at λ = 3.65. The change in non-dimensional performance of the transient CFD results are summarised in Table 6.8 these show that the most significant change to the performance characteristics was to the coefficient of moment, the increasing yaw angle created significantly higher out-of-plane bending moments.

Table 6.8 Turbine mean performance characteristics at λ = 3.65 for transient CFD results

λ = 3.65	**Yaw angle**						
	-20˚	**-15˚**	**-10˚**	**0˚**	**+10˚**	**+15˚**	**+20˚**
C_θ - μ	-11.4%	-8.7%	-2.0%	0.123	-2.8%	-6.1%	-11.5%
C_P - μ	-11.4%	-8.7%	-2.0%	0.447	-2.8%	-6.1%	-11.5%
C_T – μ	-5.8%	-3.5%	0.7%	0.847	0.0%	-2.1%	-6.5%
C_M - μ	251.2%	207.5%	120.6%	0.008	70.3%	141.2%	208.8%

The application for industry suggests that operating a yaw mechanism to actively track the flow may not be justified from a purely performance perspective. However the design of the slow speed drive-shaft and thrust bearings (being closer to the rotor), must take into the consideration the significantly higher out-of-plane bending moments identified at higher yaw angles. Passively tracking devices will benefit from these performance differences and may prove to have a competitive advantage. Furthermore, the results showed the performance of a turbine in positive or negative flow misalignment (see Figure 4.6 for sign convention on yaw angle) were not symmetrical. The performance in negative flow misalignment surpasses their positive counterparts. It is logically reasoned that the result is due to the rotational direction of the turbine. This is a significant result for devices being installed by the industry which are not actively or passively tracking the flow. These devices may see increased performance across their lifetime if the rotational direction and positioning tolerances of their device on the seabed is so configured that any likely flow misalignment will experience the least performance losses seen on the negative flow misalignment identified in this chapter. These findings required experimental validation (which can be found in Chapter 8). Further work would consider the performance of differing blade profiles to identify if these trends apply to more industrial relevant rotor designs.

Secondly, the results allude to a performance advantage in having the blade actively varying in pitch angle throughout the rotation. Varying blade pitch angle during rotation is already seen in the wind industry (Muljadi & Butterfield, 2000). The ability to individually change the pitch angle of each blade during rotation could significantly reduce the stanchion effects as well as address other performance issues such as flow misalignment and wave – current interaction. This is an area for further work and support from the wind industry, and rotor design from the aero-space sector may be useful in this venture moving forward.

7. Experimental Methodology

This Chapter outlines the details of the experimental testing methodology using a 1:20th scale laboratory model tidal turbine developed by Cardiff Marine Energy Research Group (CMERG) for use in both flume and tow-tank experiments. The experimental methodology and next generation turbine have both been built upon the previous experiences of CMERG (Morris, 2014; Mason-Jones, 2010), with the objective of gaining further insight into the performance of a turbine for validation of the numerical models. A description of the advances made in the next generation experimental turbine design, following on from the review in section 2.2. This Chapter defined the experimental procedure and facilities used in completing the test regime outlined. The final section of this Chapter will define the post-processing performed to obtain the final results from the data collected.

The 1:20th scale turbine is 0.5 m in diameter and has been developed to comply with a Technology Readiness Level (TRL) of 4 in accordance with the recognised TRL definitions (NASA, n.d.). The turbine was developed in a parallel project, within CMERG (Allmark, 2016), which incorporates condition monitoring instrumentation. The manufactured turbine was also used for the experimental validation of the numerical models presented in this thesis. The validation experiments described and later discussed in this thesis were undertaken, by the author, in one of the tow-tanks at CNR-INSEAN in Rome, Italy (CNR-INSEAN, 2002) through the MaRINET Trans-National Access (MaRINET FP7, n.d.).

7.1. CMERG Experimental Turbine

Figure 7.1 shows the CAD schematic and post manufactured experimental turbine. The schematic representation of the experimental turbine includes the key components incorporated into the design and are outlined in this chapter.

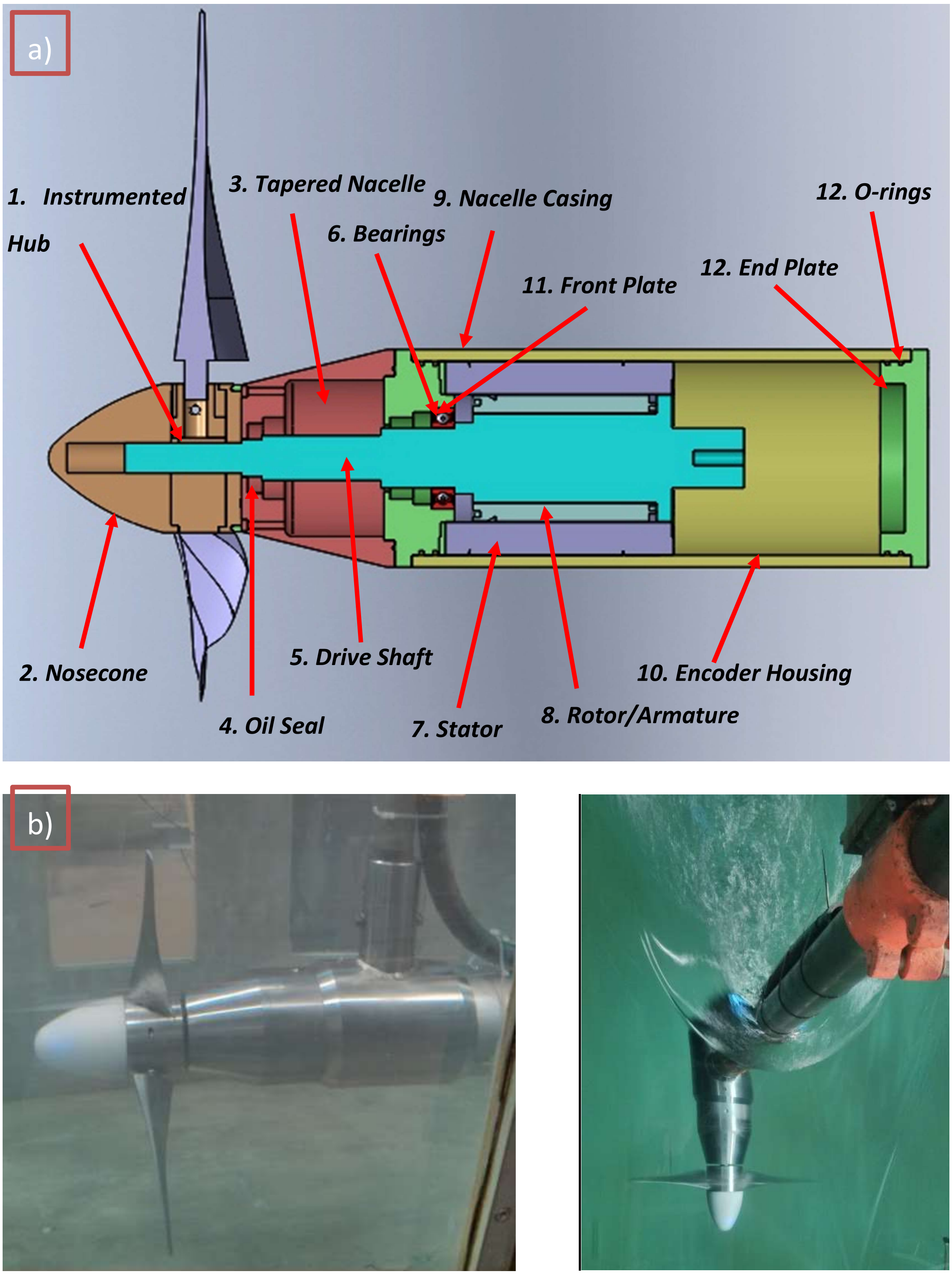

Figure 7.1 CMERG experimental turbine a) CAD section view b) Device during testing

7.1.1. Experimental and Numerical Geometry

Both the experimental and numerical geometries used are very similar in design. Some of the differences however are worthy of note. The nose cone of the experimental model was adapted to fit the instrumentation required for the blade thrust and torque. The differences are limited to the nose cone profile and the hub to rotor diameter ratio remains the same. The root connection of the blades added in the CFD model is not present in the experimental model, however as very little power is captured at the root with this blade profile this is unlikely to cause significant differences. The stanchion is connected with a collar that has not been modelled in the CFD, however the low profile nature of the collar is unlikely to be an issue.

7.1.2. Instrumented Hub & Nose Cone

Since the use of three blades has been established as the optimal arrangement in previous work (Morris, 2014), the hub was designed for this optimum blade number and so has three blade slots. The instrumented hub (annotation 1 in Figure 7.1 CAD schematic) features strain gauge flexures as can be seen in Figure 7.2. The flexures are configured to deflect in response to the axial thrust load on the blade and the bending moment about the axis of the blade root. The blade will experience hydrodynamic loading during operation. This loading will be distributed along the blade in the radial direction from the hub. The axial cup, identified in Figure 7.2, is made of brass and is designed to mitigate the moments that will occur from this remote load and respond purely to the axial thrust being applied to the blade. The advantage of this design principle over alternative systems, which calculate the bending moment on the blade relative to its root, is that the centre of pressure is not required to calculate the axial thrust. As with all aspects of the turbine, the calibration of this instrumentation is reported in section 7.4. The strain-gauge flexures for the axial thrust have a working range of 0 – 80 N and bending moment about the axis of the blade root was designed to have a working range up to 0.34 Nm. The location of the strain-gauge flexures makes only positive loading possible. The instrumented hub was designed for a sampling frequency of 250 Hz in order to capture data within a rotation at high RPMs.

The nose cone (annotation 2 in Figure 7.1) is hollow and hosts the Arduino board which amplifies the gain from the strain gauges and stores them in a synchronised file on an SD card. The board also synchronises acceleration data from accelerometers mounted in the axial, and two radial directions perpendicular to one another.

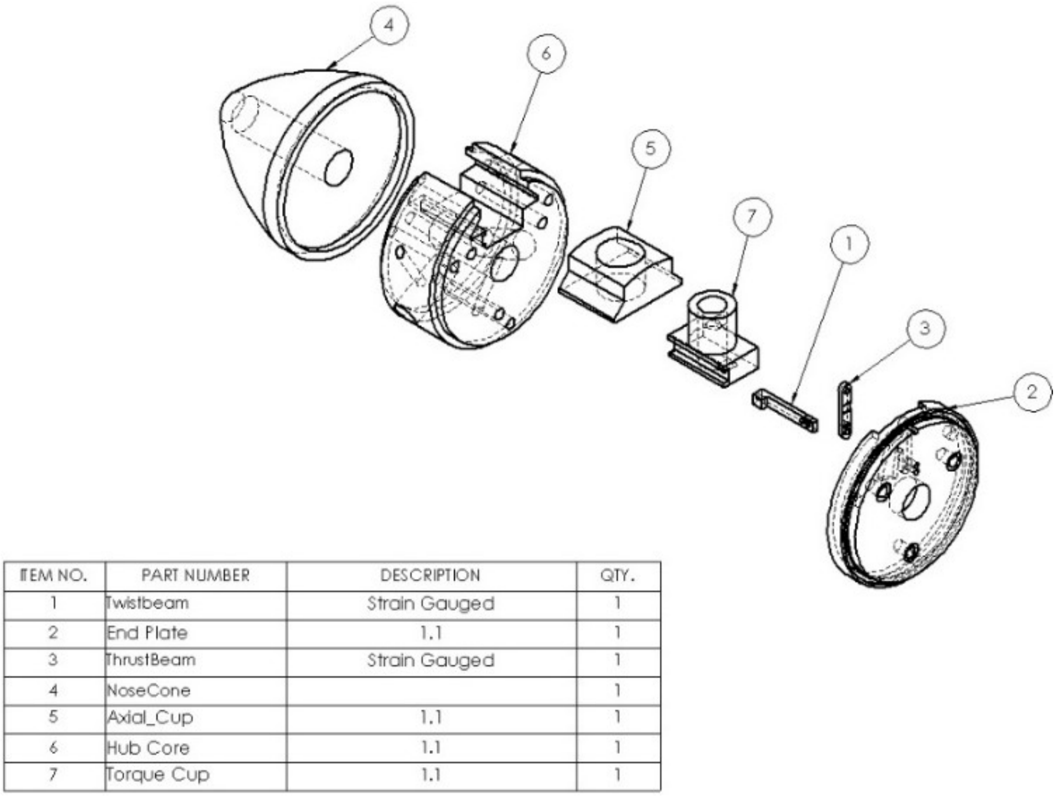

ITEM NO.	PART NUMBER	DESCRIPTION	QTY.
1	Twistbeam	Strain Gauged	1
2	End Plate	1.1	1
3	ThrustBeam	Strain Gauged	1
4	NoseCone		1
5	Axial_Cup	1.1	1
6	Hub Core	1.1	1
7	Torque Cup	1.1	1

Figure 7.2 Instrumented Hub Assembly Drawing (Allmark, 2016)

As there is only one instrumented holder slot for the blades, the blade in this location will from hither to be referred to as Blade1.

7.1.3. Alternator

Figure 7.1 shows the rotor and stator of the alternator as annotations 7 and 8 respectively. In order to obtain the full non-dimensional performance curves an alternator capable of operating at the low rotational speeds and high torques experienced for this diameter rotor was required. The Bosch-Rexroth synchronous torque motor MST130E-0035, was selected as the ideal alternator for the expected torque applications. The operational envelope can be found in

Table 7.1 and Figure 7.3 (Bosch-Rexroth, 2015) which shows that the rated and maximum torque and rotational velocity will meet the requirements of the rotors peak torque and power, thus capturing the full non-dimensional performance curves. The motor control instrumentation was driven through labview (Allmark, 2016) and set to a sample frequency of 10 Hz, with the exception of the Torque Generating Current (TGC) and rotational position, which were logged at a sample frequency of 250 Hz, thus providing much higher resolution, required for temporal analysis.

Table 7.1 Operating Data for Alternator

Parameter	Symbol	Value	Units
Rated torque	M_N	22.5	Nm
Maximum torque	M_{max}	65.0	Nm
Rated power	P_N	600	W
Maximum power	P_{max}	880	W
Maximum velocity at maximum torque	①	100	RPM
Rated velocity	②	350	RPM
Maximum velocity	③	700	RPM

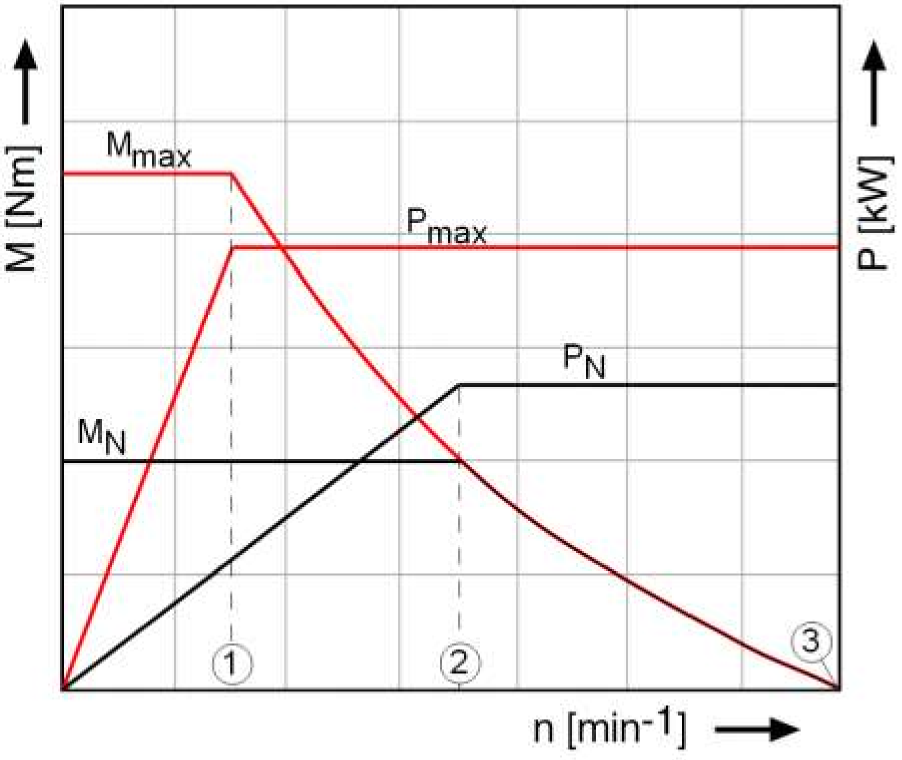

Figure 7.3 Operating Behaviour of Alternator

7.1.4. Turbine Housing

The turbine's housing was made of four stainless steel parts as identified by annotations 3, 9 11 and 12 in Figure 7.1 CAD schematic. The front tapered section (3) houses the oil seal, front bearings and slip-ring. It has a 19° draft angle to transition between the maintained hub diameter from previous work (Morris, 2014; Tedds, et al., 2011) and to accommodate the larger alternator. The stainless steel end plate (11) sits between the tapered section and main housing with two sets of O-rings to offer a second layer of protection against a potential failure of the oil seal. The nacelle casing (9) is tight fitting to the alternator's rotor and offers good thermal conductivity properties essential for dissipating heat from the alternator to the surrounding fluid. The stainless steel end plate (11) also has two O-ring seals and a potted gland which takes the necessary cables to the surface for the Data Acquisition (DAQ) and drive systems.

7.1.5. Data Acquisition (DAQ) System

The turbine's set up had various instruments transmitting data from the different sub-systems of the device. A National Instruments, NI PXIe-8135 unit was used to collect the various digital and analogue data streams in a succinct manner. The PXI was driven as a data card using the Labview software on a Laptop to gathered and synchronise the various data streams at the various sample rates with the relevant time stamp. Further details on the DAQ architecture can be found in published work (Allmark, 2016). Table 7.2 shows all the channels recorded during the testing, the channels variable name, signal type, measurement units, SI units and sample frequency are identified.

Table 7.2 Data collected

Channel	**Variable Name**	**Signal Type**	**Rated Range**	**Recorded Units**	**Converted Units**	**Sample Frequency**
1	Fluid Velocity in x-	Analogue	0-5	V	$m.s^{-1}$	NA
2	Fluid Velocity in y-	Analogue	0-5	V	$m.s^{-1}$	NA
3	Fluid Velocity in z-	Analogue	0-5	V	$m.s^{-1}$	NA
4	Stanchion Thrust	Analogue	0-5	V	N	NA
5	Wave Probe	Analogue	0-5	V	m	NA
6	MotorData1 (Encoder Position)	Digital	0-360	°	-	250
7	MotorData2 (TGC)	Digital	0-5	V	Nm	250
8	PLC Time	Digital	NA	s	s	10
9	PLC Motor position	Digital	0-360	°	-	10
10	PLC Motor Torque	Digital	0-90	Nm	Nm	10
11	PLC Motor Power	Digital	NA	W	W	10
12	PLC Motor Voltage	Digital	NA	v	v	10
13	PLC Motor TGC	Digital	NA	A	A	10
14	PLC Motor Temp	Binary Switch	I/0	-	-	10
15	PLC Motor Velocity	Digital	0-700	RPM	$rad.s^{-1}$	10
16	Hub Acc in x-direction	Analogue	0-5	V	$m.s^{-2}$	250
17	Hub Acc in y-direction	Analogue	0-5	V	$m.s^{-2}$	250
18	Hub Acc in z-direction	Analogue	0-5	V	$m.s^{-2}$	250
19	Blade 1 Thrust	Analogue	0-5	V	N	250
20	Blade 1 Twist	Analogue	0-5	V	Nm	250

7.2. Experimental Facilities

CNR-INSEAN is a former naval design facility, near Rome in Italy. Through the FP7 Marinet project (MaRINET FP7, n.d.) the CMERG turbine was used in a testing programme at the facility. CNR_INSEAN host two tow test tanks, of 470 m and 220 m in length (CNR-INSEAN, 2002). The tow tank used in this work was the 220 m long tank, which had a cross-section of 9 m in width and 3.5 m in depth. The blockage ratio of the turbine in this tank was 0.62% which meets the requirements of the facility to mitigate the blockage effects (Whelan, et al., 2009; Gaurier, et al., 2015). Being a towing tank the water is still and therefore little or no turbulence was expected in the water provided sufficient settling periods were given between runs, meeting another facility requirement. The carriage has a maximum speed of 10 ms^{-1} with ±0.15% accuracy (CNR-INSEAN, 2002). This highly accurate towing speed will meet the requirements for improved inlet velocity data required by the testing facility. Speeds of 10 $m\ s^{-1}$ far exceed requirements for this system, a velocity of around 1 ms^{-1} will be used and will have an accuracy of ±0.0015 ms^{-1}, assuming a linear error. The turbine was mounted such that the rotational axis of the turbine was 1 m below the water surface. The stanchion had an Outside Diameter (OD) of 70 mm and Inside Diameter (ID) of 50 mm. It was clamped 1 m above the water surface which gave a total stanchion length of 2 m from the rotational axis to the first clamp. This 1 D clearance between the top of the rotors swept area and surface was to avoid free-surface effects and maintain sufficient bed proximity clearance. The turbine position can be seen relative to the carriage and tank in Figure 7.4.

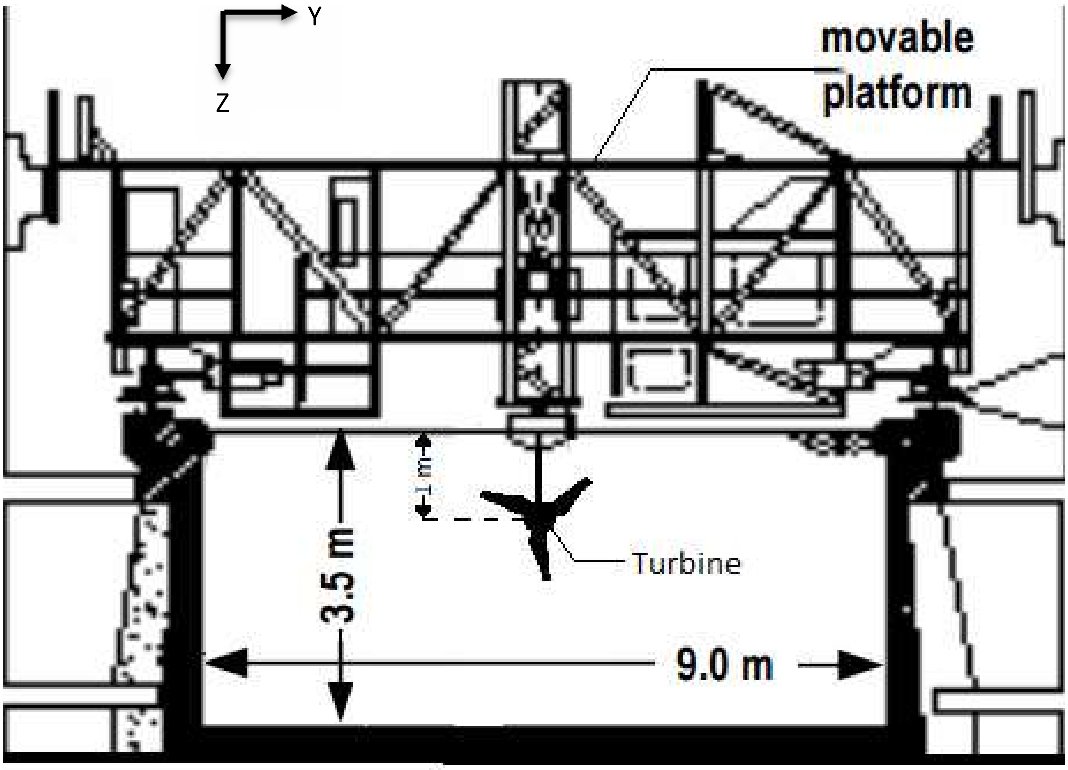

Figure 7.4 CNR-INSEAN tank dimensions and turbine mounting, not to scale (adapted from CNR-INSEAN, 2002)

7.2.1. Carriage Speed

The carriage speeds used during the experiments were 0.5, 0.75, 1, 1.25 and 1.5 ms^{-1}. The turbine was operated in only one-direction as the turbine itself would have needed to have been rotated through 180^{0}. Hence the carriage was returned to its start position, at a speed of 0.5 ms^{-1}. The slower return towing speed was to reduce reverse thrust loading on the turbine and allow time for the tank to settle between runs. The tanks 220 m length provided an operational distance of 190 m, as the increase sample periods require smaller test periods for statistical significance the test period was set to 90 seconds, including the acceleration and retardation of the carriage. These test parameters enabled a number of tests to be conducted in one length of the tank depending on the carriage velocity as detailed in Table 7.3.

Table 7.3 Tests conducted per run of tank

Carriage Velocity (m/s)	Distance for 90s test (m)	Number of Tests per tank length
0.5	45	4
0.75	67.5m	2
1	90	2
1.25	112.5	1
1.5	135	1

7.2.2. Reynolds Independence

Operating in a Reynolds independent regime was critical in enabling validation between the small scale experimental turbine and full scale turbine modelled in CFD. The use of the blade chord Reynolds number has been made in this thesis, for reasons that have been discussed in Section 3.8. Appendix, Section A shows the range of chord-based Reynolds number at 70% of the blade length achieved for the operational velocities in these experiments was between 4.88×10^4 and 1.46×10^5. It was assumed the variation in tank water temperature does not fluctuate significantly and therefore provides a constant dynamic viscosity was used. The critical chord-based Reynolds number for this rotor was shown (Section 3.8) to be a value of 9.77×10^4 this was achieved at a carriage velocity of approximately 1.00 ms^{-1} for the full range of λ.

7.2.3. Optical System

The use of an optical alignment system and reflective markers enabled the accurate alignment of the turbine for yaw angle testing. The turbine was then manually rotated to the required yaw angle by observing the change in angle on the optical tracker. The resolution of the system gives an angular accuracy of 10% and 15% at $\alpha = \pm 10°$ and $\alpha = \pm 20°$, based on the geometrical set-up.

7.3. Test Program

The experimental test programme was designed with inherent flexibility due to the tight constraints of the 6 day test window. Table 7.4 shows the test run relevant to this thesis and in Appendix C all the testing achieved in the given test campaign.

Table 7.4 Relevant Tests Conducted

Velocity (ms^{-1})	Range of λ	Yaw angle (˚)
0.50	1.5, 2.5 ,3.0 ,3.5 ,4.0 ,4.5 ,5.5	0
0.75	2.5 ,3.0 ,3.5 ,4.0 ,4.5 ,5.5	0
1.00	1.5, 2.5 ,3.0 ,3.5 ,4.0 ,4.5 ,5.5	0
1.00	1.5, 2.5 ,3.0 ,3.5 ,4.0 ,4.5 ,5.5	±10
1.00	1.5, 2.5 ,3.0 ,3.5 ,4.0 ,4.5 ,5.5	±20
1.25	2.5 ,3.0 ,3.5 ,4.0 ,4.5 ,5.5	0
1.50	1.5, 2.5 ,3.0 ,3.5 ,4.0 ,4.5 ,5.5	0
1.50	2.5, 3.5, 4	±10
1.50	2.5, 3.5, 4	±20

7.4. Calibration

Consideration of the instruments used in the 1:20th scale turbine and their calibration is made in this Section. The uncertainty in the calibrations is reported in section 7.5.

7.4.1.1. Calibrating the Alternator

Channel 7 in **Error! Reference source not found.** provides MotorData2, which is the applied variable for calculating the alternators TGC in Amps using calibration equation, [7.1]. The gradient ***b*** = 0.31 and the intercept ***a*** = -1.2. These values were provided from the alternator manufacturer (Bosch-Rexroth, 2015). To obtain the torque of the alternator in Nm, the TGC is multiplied by a torque constant, T_C = 6.66 also provided (Bosch-Rexroth, 2015). After calculating the torque of the alternator a correction is required to find the torque of the rotor. The correction (Allmark, 2016) accounts for frictional losses in the alternator, and can be seen in equation [7.2]. The same occurs for calculating the power generated by the rotor, using equation [7.3], where ω is the rotational velocity in RPM (0.10472 converts RPM to $Rad.s^{-1}$), and T_i denotes the TGC of the current data point. The polynomial equations used for the correction of frictional losses were derived from experimental work where the turbine was driven in water without the blades.

$$\boldsymbol{M_y = (b \times M_x) + a} \qquad \textbf{[7.1]}$$

$$\boldsymbol{T = T_c . T_i - \left(-8x10^{-6}\omega^2 + 0.0056\omega + 0.6811\right)} \qquad [7.2]$$

$$\boldsymbol{P = (T_c \times T_i\omega \times 0.10472) - \left(0.0002\omega^2 + 0.1289\omega - 1.5592\right)} \qquad \mathbf{[7.3]}$$

The torque and power readings were taken repeatedly for each rotational velocity set and the resulting polynomial functions derived from curve fitting of the data as shown in Figure 7.5 (Allmark, 2016). The scatter seen at each rotational speed lies within 2.5% and 5.5% of the full turbine rating for power and torque respectively, sources for this scatter may include the PID control system being suboptimal (Allmark, 2016).

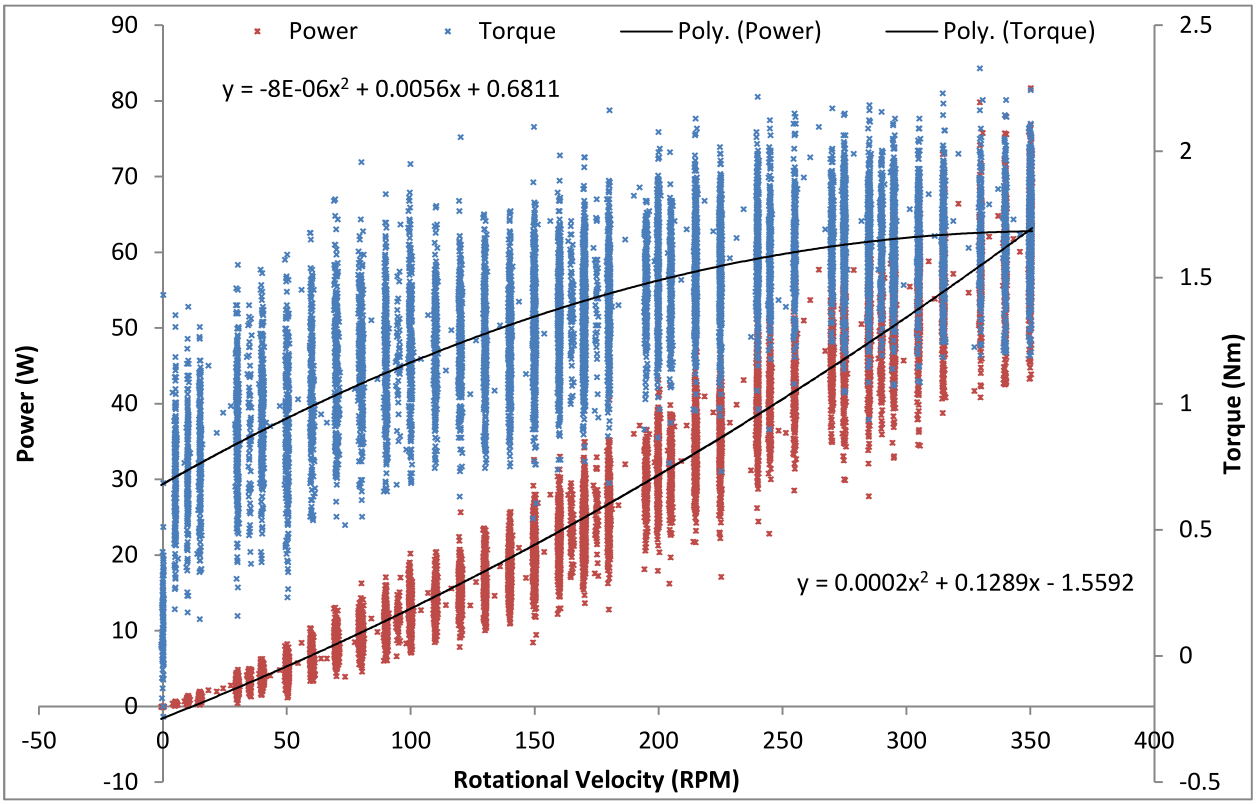

Figure 7.5 CMERG Turbine Frictional losses

7.4.1.2. Calibration of the Encoder

Channel 6 in **Error! Reference source not found.** is MotorData1 which is the rotational position of the driveshaft from the encoder. This was converted to degrees using the linear calibration equation 7.1. Where ***b* =** 72, and ***a* =** *0* both these constants came from the encoder manufacturer (Heidenhain, 2014).

7.4.1.3. Calibration of the Instrumented Hub

The thrust gauge in the instrumented hub described in Section 7.1.1 was calibrated manually by applying a load, (F_L) at a distance (D_L) from the strain-gauge and the output voltage was recorded. The experimental procedure for the calibration can be found in the Appendix. The procedure generated a series of datasets produced from the average of the results, for the different distances at which the load was applied from the root of the instrumented hub. Figure 7.6 shows a data set where V_R is the voltage range and F_L the load applied. The uncertainty bands were calculated using the standard deviation of the residual data as defined in (ITTC, 2008) using the matlab code outlined in other work (Doman, et al., 2015). The gradient of the curve is, b = 0.043 and the intercept, a = 0.004 which was deemed negligible. It can be seen that there is a slight, but negligible hysteresis between all the loading and unloading data sets, the R^2 value was found to be 0.9943.

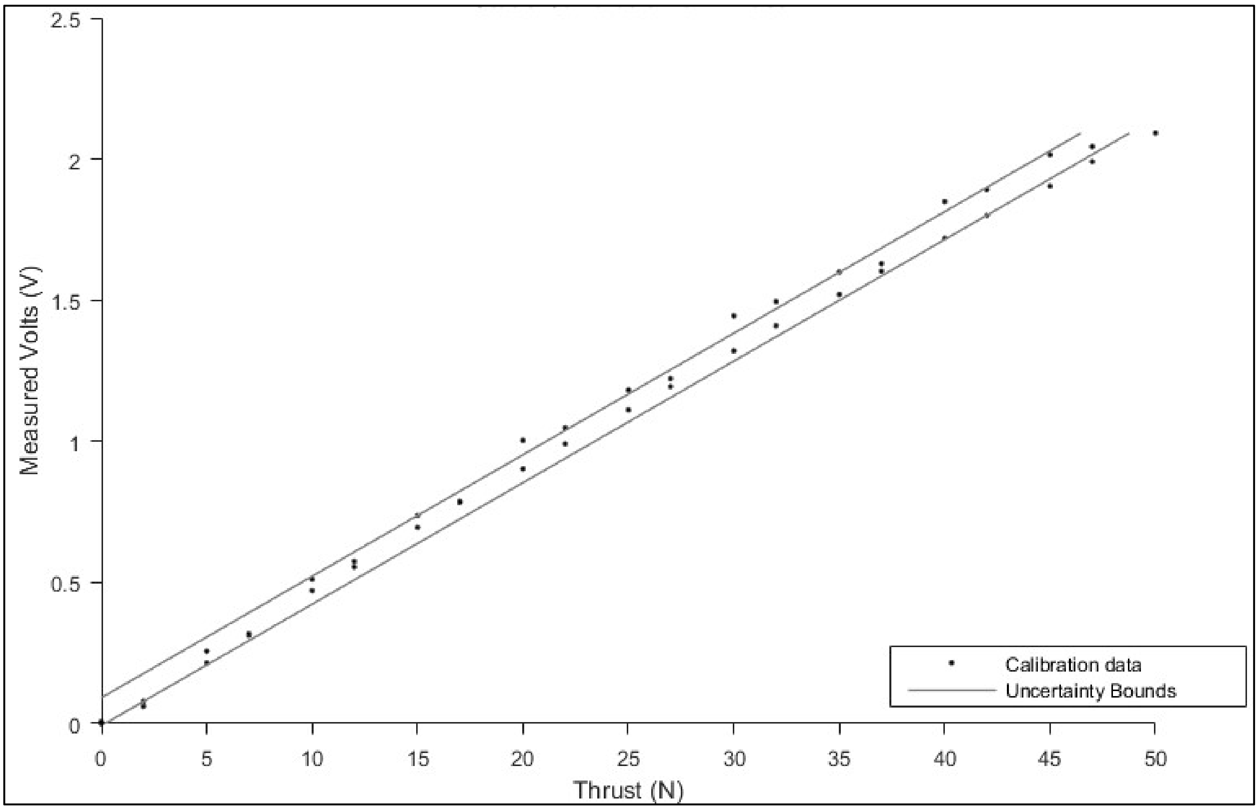

Figure 7.6 Instrumented hub calibration results

The equation for the line is in the same form as equation 7.1 where F_L is the output variable and V_R is the desired variable. To obtain the thrust from the instrumented hub, the voltage from the strain gauge flexure in the instrumented hub will be recorded for Blade1. The blades thrust will then be determined as a post process using equation 7.4.

$$\boldsymbol{F_L = \frac{(V_R - a)}{b}} \qquad \textbf{[7.4]}$$

Where F_L is now the thrust on Blade1 in N, V_R is the measured voltage from the strain gauges and the gradient and intercept have come from the mean values in Figure 7.6.

7.5. Uncertainty Analysis

This section determines the systematic and random errors found in directly measured variables and their propagation to desired output variables. The work follows the recommendations of ITTC documentation (ITTC, 2008) and the IEC standard (IEC 62600-200, 2012) as well as similar work performed by (Doman, et al., 2015). The methodology of determining random error is also defined from sample results. The methodology has been demonstrated through the example of determining the uncertainty for the thrust on the blade using the calibration described in section 7.4.1.3.

7.5.1. Systematic Error

The systematic error identifies the total bias uncertainty in the applied measurement, M_x from equation 7.1. Using the instrumented hub calibration as an example the total bias uncertainty in the calibration is determined from the propagation of bias, as identified in equation [7.5]. As the calibration set-up utilised a force multiplier, the lever arm length should be included in the uncertainty analysis (ITTC, 2008).

$$\mu_B = F_L \sqrt{\frac{{\mu_{Bm}}^2}{m^2} + \frac{{\mu_{Bg}}^2}{g^2} + \frac{{\mu_{Bl}}^2}{l^2}} \qquad [7.5]$$

A list of all the variables used in finding the bias of uncertainty can be found in Table 7.5 (Doman, et al., 2015; Ansys, 2015; CNR-INSEAN, 2002). The first three parameters are used in calculating the bias uncertainty for the instrumented hub calibration, where F_L has been taken as the mean applied load from the calibration procedure, F_L = 24.15 N.

Table 7.5 Bias in Parameters

Parameter	Symbol	Value	Bias, μ_B	Units
Hanging Masses	m	5	0.0025	kg
Gravitational Acceleration	g	9.81	0.0014	$m.s^{-2}$
Lever Arm Length	l	0.2	0.0005	m
Turbine Radius	R	0.25	0.0005	m
Carriage Velocity	V	Variable	0.0005	$m.s^{-1}$
Water Density	ρ	998.2	0.0011	$kg.m^{-3}$

7.5.2. Random Error

The precision uncertainty of the measure variable, M_y in equation 7.1 is determined from the standard error of the estimate as found in equation [7.6] (Doman, et al., 2015; ITTC, 2008), where n denotes the size of the data set and *i* indicates the current data point in the set. The measured variable is *y* whilst the applied variable is *x*. As in equation 7.1 the constants *a* and *b* represent the offset and gradient of the calibration. For the instrumented hub calibration, the mean values from section 7.4.1.3 were used to calculate a precision uncertainty for the complete calibration.

$$\mu_P = x_{SEE} = \sqrt{\frac{\sum_{i=1}^{n}(y_i - a - b.x_i)^2}{n-2}} \qquad [7.6]$$

7.5.3. Error Propagation

To obtain the 'combined standard uncertainty' the bias and precision uncertainties presented in equation [**7.5**] and [7.6] are combined into equation [**7.7**]

$$\mu = \sqrt{{\mu_B}^2 + {\mu_P}^2} \qquad [7.7]$$

The combined uncertainty is the square-rooted of the sum of the bias uncertainty squared and precision uncertainty squared. This uncertainty analysis was undertaken for the instrumented hub and alternator, the rotational encoder's uncertainty was provided by the supplier (Heidenhain, 2014). In all three cases the uncertainty for bias, precision and combined have been provided in Table 7.6.

Table 7.6 Uncertainty values for calibrated instruments

Variable	**Mean Value**	$\boldsymbol{\mu_B}$	$\boldsymbol{\mu_P}$	$\boldsymbol{\mu}$	**Percentage of mean**
Blade Thrust, N	24.15	0.0617	1.1487	1.15	4.7%
Torque, Nm	1.01	0.0051	Not Available	Not Available	-
Rotational Velocity, rad.s^{-1}	14.01	0.0005	Not Available	Not Available	-

Table 7.6 shows that the uncertainty in the blade thrust is less than a percent of the mean values used in the calibration. This gives confidence in the procedure. The torque and rotational velocity uncertainties were not available from Bosch-Rexroth or Heidenhain. For this reason the uncertainty of the blade thrust values was continued however uncertainty in the other parameters is subject to further research being conducted in order to obtain these uncertainty characteristics.

The percentage uncertainty in the non-dimensional thrust performance parameters was calculated using equations [**7.8**] which were formed from the uncertainty function for each of the components in equations [**3.15**].

$$\mu_{CT}{}^{2} = \sqrt{\left(\frac{\mu_T}{T_{mean}}\right)^2 - \left(\frac{\mu_\rho}{\rho}\right)^2 - \left(\frac{\mu_A}{A}\right)^2 - \left(\frac{2\mu_V}{V}\right)^2} \times C_T{}^{2} \qquad [7.8]$$

7.5.4. Confidence intervals

The mean value for a data set is taken in the manner described in section 1.6. In order to set confidence intervals for these values, the distribution of the data set must be considered. In assuming Gaussian distribution for all data sets, as shown for sample data in Section 7.6.1, the mean value of the data set will be at the peak of the PDF curve. The confidence interval for each data set was calculated for 95% confidence, this equates to plus and minus approximately twice the standard deviation from the mean as expressed by equation [**7.9**] (Coleman & Steele, 2009).

$$\mu \pm 1.96\sigma \qquad [7.9]$$

The variables μ and σ have been calculated from equations [**3.19**] and [**3.20**] in section 3.5. This method has been used to produce the error bands for time average results in Chapter 8

7.6. Data Processing

Following data collection the raw data required processing to obtain the final results. **Error! Reference source not found.** shows all the variables collected, and the units recorded. The raw data was post-processed into their respective SI units by applying the calibration equations and correction factors using Matlab software. The scripts used can be found in the Appendix Section D however a description of the post-processing procedure is detailed in this section.

After each experiment the data sets were downloaded from the SD card in the arduino and collated with the data from the alternator into a .tdms file with common time stamps. This is done by the National Instruments PXI unit. The file was converted to a .txt file with a structure as defined in **Error! Reference source not found.**, using the channel numbers as column headers.

In **Error! Reference source not found.** channels 1-5 were not used for the experimental work in this thesis as these channels were set-up for recirculating flume tank experiments with inputs from ADV and a force block. The flow measurements were not required in the CNR-INSEAN tests as this was dictated by the carriage velocity. By the nature of being a towing tank the velocity in the z and x direction which are shown in Figure **7.4** will be zero. The velocity in the x-direction came from the carriage velocity which was specified in Section 7.2.1. No stanchion force block was available for the tests and the wave probe data only used in tests with waves present. In addition channel numbers 20, which was the twisting or bending moment of the blade about its locating pin in the hub, was not used due to damage to the twist strain gauge. All other channels were monitored and/or used in the analysis, as described in the following section.

7.6.1. Sample Data sets

Some sample data sets are shown here in order to aid establishing the reason for these processing procedures. Prior to displaying the data in this section the only post processing performed was the calibration equations applied as defined in Section 7.5. These sample results all come from the same 1 ms^{-1} velocity tests with a λ of 3.5. Figure 7.7 shows a sample time series of torque, thrust and rotational velocity for the aligned 1 ms^{-1} test case. Figure 7.7 has been separated by vertical lines identifying the three sections of the data set.

1. Start-up – this section of the data has been ignored in the results as the carriage was accelerating.
2. Middle – this was the section used in the results and to ensure either end were not included it has been taken as the middle half of the data set, leaving a quarter for start-up and end.
3. End – this was generally a sudden stop in the data as the recording is ended however in some cases where the carriage reached the end of the tank before the recording was stopped there was a deceleration period identifiable. This section of the data sets has been ignored.

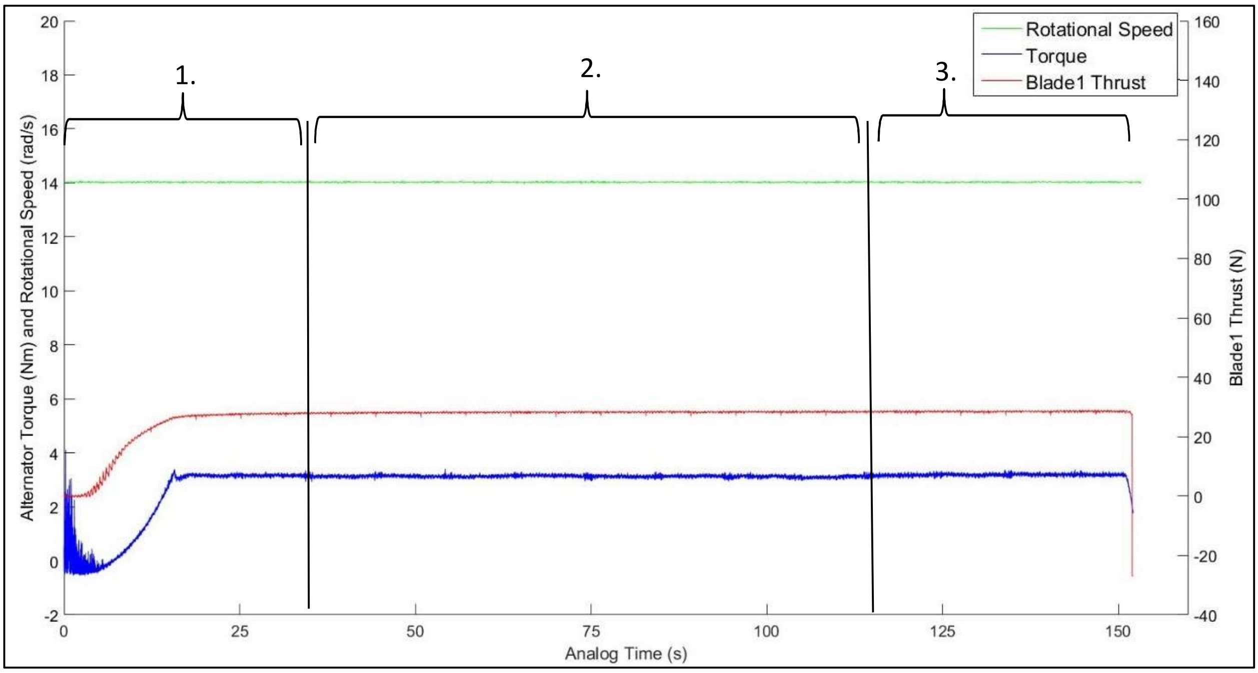

Figure 7.7 Raw data set of complete test

The middle section in Figure 7.7 was used to determine the performance characteristics. The coefficient of torque, power and thrust along with tip speed ratio, were calculated using equation **[3.12**] to **[3.14**] and [**3.16**] respectively. The numerators of the non-dimensional performance characteristics were calculated from the middle section. The numerator for the coefficient of thrust, C_T (equation **[3.14**]) was taken as the blade1 thrust multiplied by the number of blades, which was three. The carriage velocity has been reported as a constant for each test and was used accordingly to calculate the denominator, along with the other constant such as water density (ρ_W = 998.2 kg.m^{-2}) and rotor diameter (R = 0.25 m). Figure 7.8 to Figure 7.11 shows the coefficients of torque, power and thrust for the middle section, using the same test case as Figure **7.7** along with their respective Probability Distribution Functions (PDF). The mean for the entire portion and 95% confidence intervals have also been plotted. The mean values will be used to plot the time averaged results, where the 95% confidence intervals are set as the error bars for each data point.

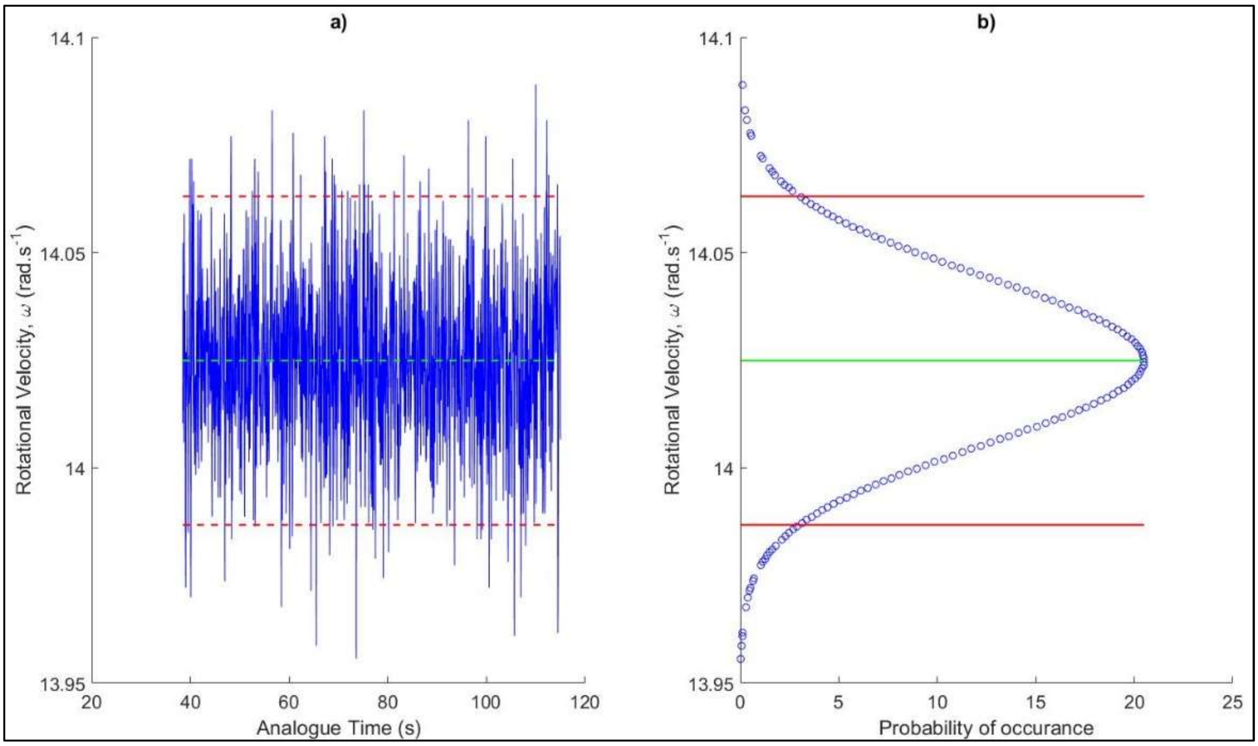

Figure 7.8 a) Rotational velocity, ω with mean and 95% confidence intervals b) Corresponding PDF

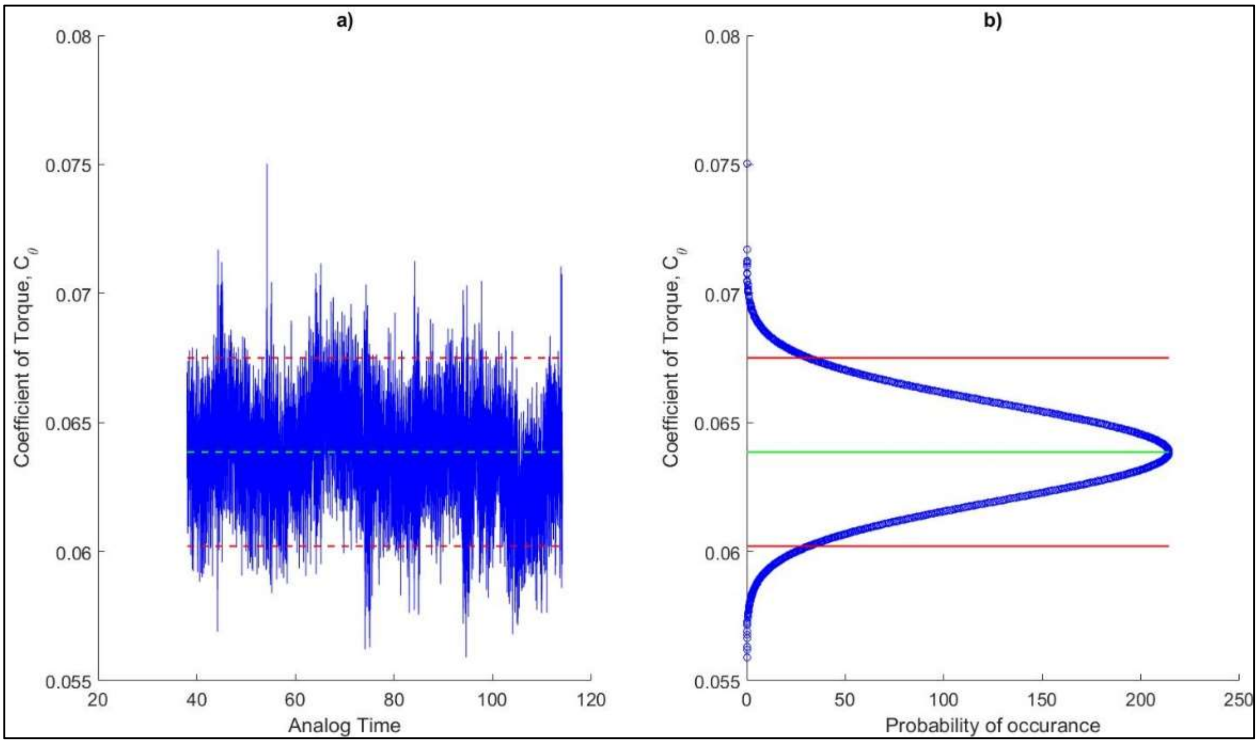

Figure 7.9 a) C_θ with mean and 95% confidence intervals b) Corresponding PDF

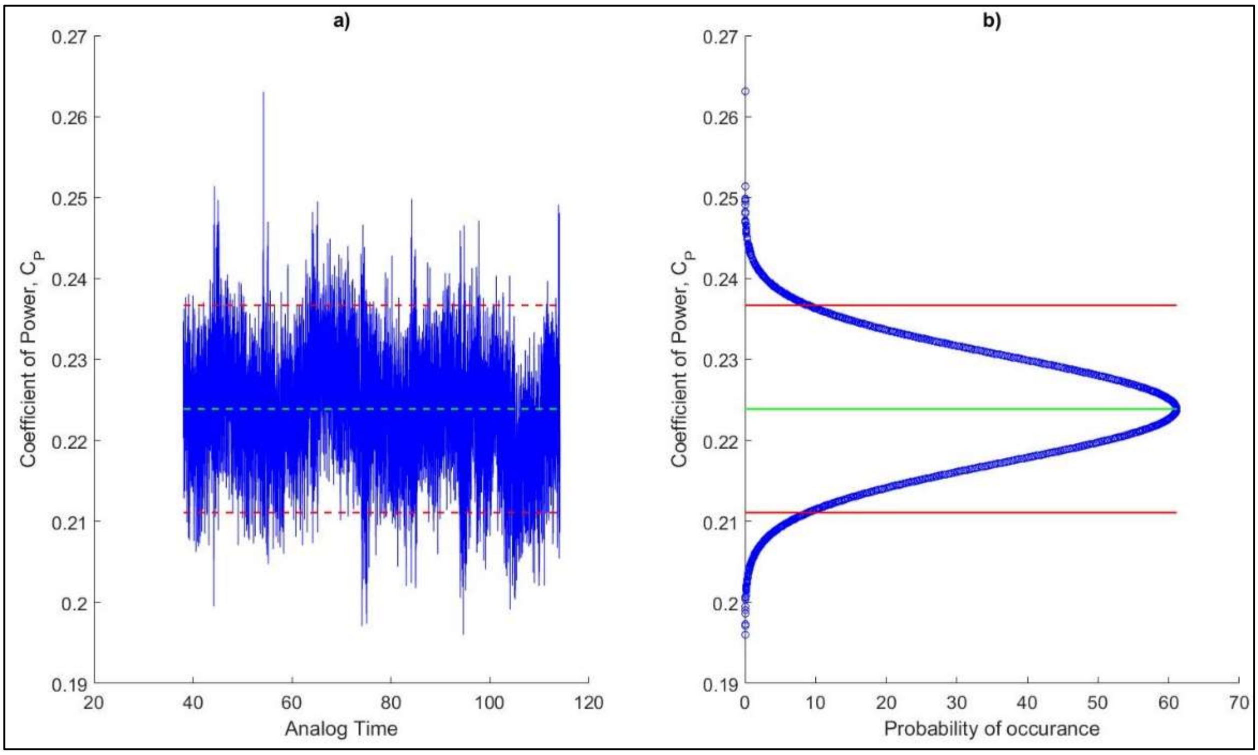

Figure 7.10 a) C_P with mean and 95% confidence limits b) Corresponding PDF

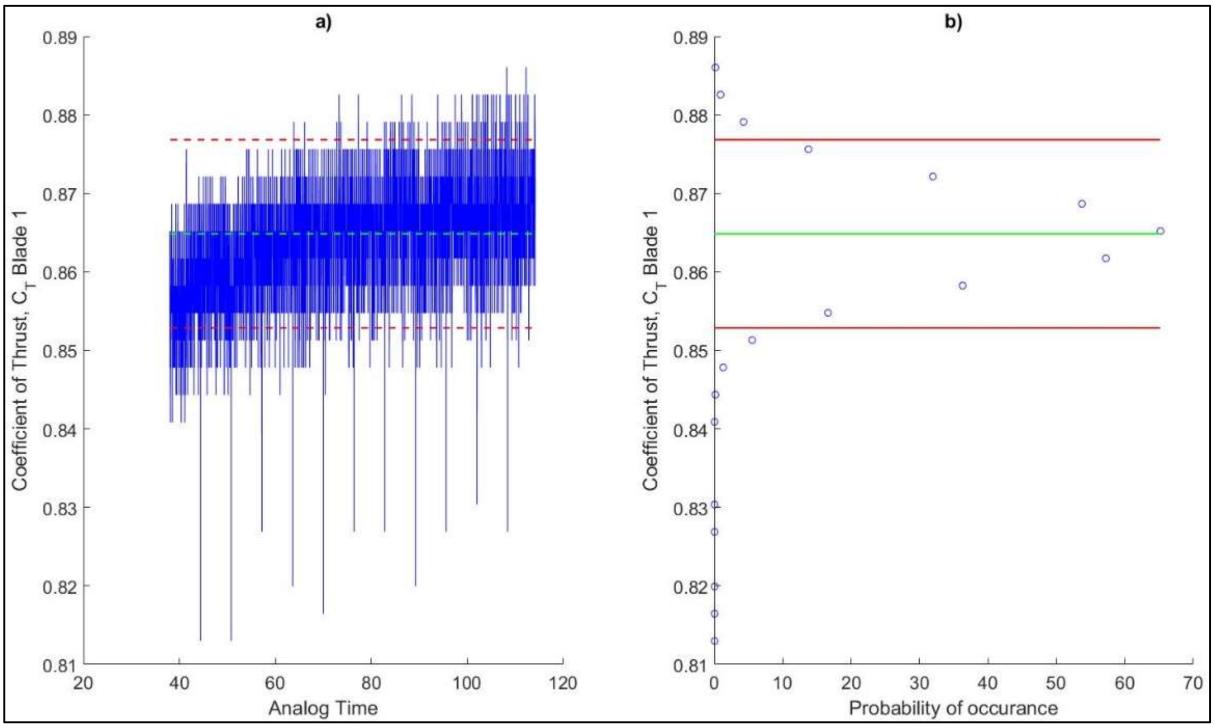

Figure 7.11 a) C_T with mean and 95% confidence limits b) Corresponding PDF

As discussed in Section 7.5.4 the confidence limits are determined with the assumption of Gaussian distribution in the data. The PDF plots in Figure 7.8 to Figure 7.11 shows that for each variable, rotational velocity, and the coefficients of torque, power and thrust the distribution of the sample data sets holds true to the definition of Gaussian distribution (Coleman & Steele, 2009). However it was noticed that for the coefficient of thrust (Figure 7.11) the distribution appears sparse of data points. This is due to banding in the data set, a result of the bit size used to store the data in the Arduino which limits the resolution. This was not adjustable as a post-process, however improvement of the blade thrust data resolution should be considered for further work. These are the limits that will be used to set error bars in the time averaged results section (Section 8.1).

The middle portion of the time series for torque, power and thrust results were passed through a low pass, moving average filter, with a window size equivalent to a period of 0.124 s. This was calculated using the *'filtfilt'* function in matlab, the function is represented by equation [7.10] (Matlab, 2015). The function is a moving average filter, and will remove high frequency noise from the data, the filter has been used to smooth features that are higher than the blade-stanchion passing frequency. Figure 7.12 shows the middle portion of the data sets with both filtered and unfiltered rotational velocity, torque, power and thrust results for comparison.

$$y_i = \frac{\left(x_i + x_{i-1} + \cdots + x_{i-(Window\ Size-1)}\right)}{Window\ Size} \qquad [7.10]$$

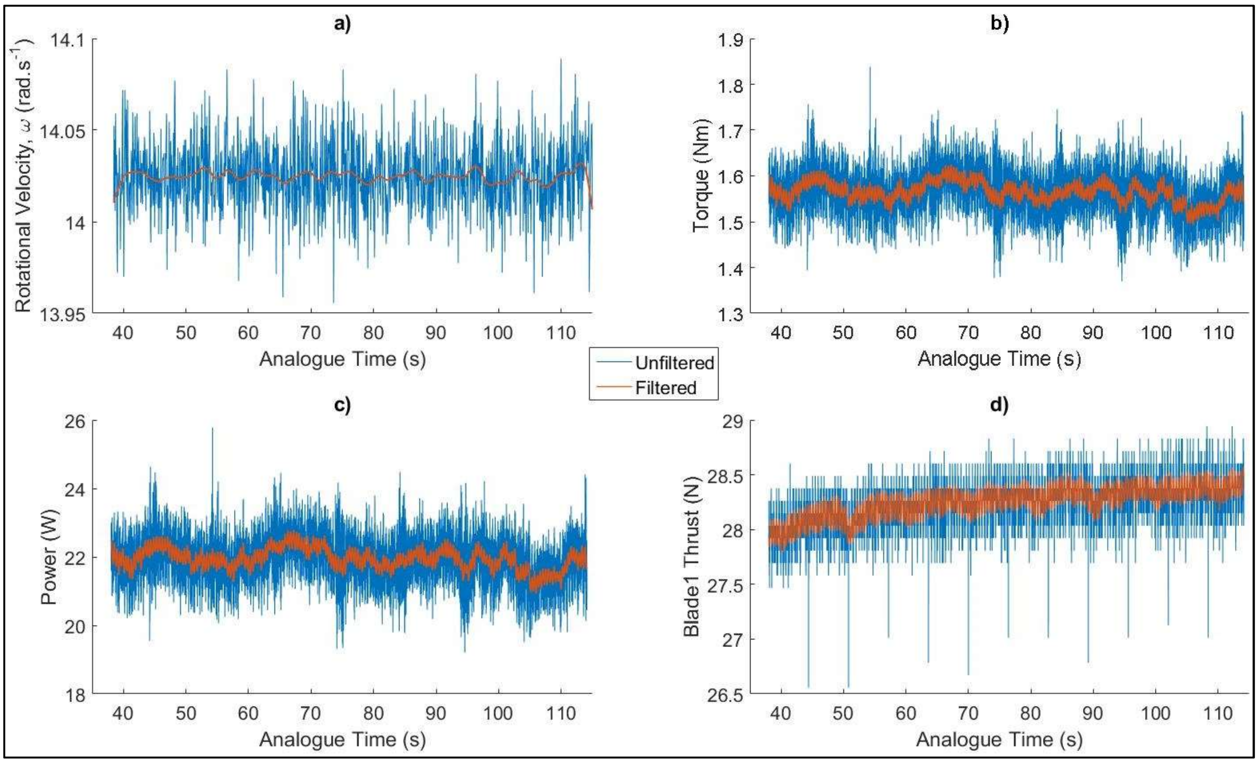

Figure 7.12 Filtered and unfiltered values for a) Rotational Velocity b) Torque c) Power and d) Thrust

Temporal results were formed from the middle portion of the datasets, using the rotational position of the turbine. The high frequency datasets (250 Hz) provide detail on the turbine performance during rotation. The rotational position of blade 1 (in degrees) was plotted against the turbines torque, power and blade 1 thrust for all the datasets in the middle portion. The blue data points are the unfiltered data sets, whilst the orange data points are after the low pass filter was applied to the data.

Identifying the significant trends and rotational dependent features were not feasible for the temporal results. In order to gain insight into these results the Power Spectral Density, PSD of the middle third of the data set was calculated to plot the periodogram for the results. The process uses the Discrete Fourier Transform (DFT) function in Matlab to transpose the time domain data into the frequency domain. The periodogram provides the power intensity of the signal at each given frequency. It is useful for identifying the excitation frequencies of a signal by their amplitude. Equation [7.11] defines the process for calculating the PSD and this is typically plotted for the Nyquist range of the data (Matlab, 2015). As the signal is symmetrical in the positive and negative frequency range, only half the positive side was plotted as this showed all the data of interest.

$$\hat{P}(f) = \frac{\Delta t}{N} \left| \sum_{n=0}^{N-1} x_n e^{-i\,2\pi\, f_n} \right|^2 \qquad [7.11]$$

Where Nyquist range is;

$$-\frac{1}{2\Delta t} < f \leq \frac{1}{2\Delta t} \qquad [7.12]$$

All the results for the experimental work were processed using the methodology discussed in this chapter. The experimental results and discussion can be found in Chapter 8.

8. Experimental Results

This Chapter analyses the experimental results from the laboratory scale test conducted at CNR INSEAN. The experimental procedure and methodology can be found in Chapter 7 which also outlines the test regime conducted relevant to this work.

The performance characteristics of the turbine was investigated, using the data collected as both time averaged and temporal to reflect the steady-state and transient results from numerical modelling. The discussion of each set of results is considered in two parts, firstly the interpretation of the results themselves in isolation, followed by the validation they provide for the CFD results. The discussion includes the impact of these findings in the wider context of the thesis as well as the relevance to industry. Possible reasons for discrepancies between the CFD and experimental work are highlighted for addressing in further work.

8.1. Time Averaged Results

As described in Section 7.2.1, each run of the tank was performed at a pre-defined carriage speed and pre-defined rotational velocities of the turbine. This was done to correspond with relevant Tip Speed Ratio (TSR) value, the mean performance for the turbine can therefore be found for each λ and plotted to give the non-dimensional performance curves as established in Section 3.3.3. The mean value and 95% confidence limits were obtained as described in Section 7.6.

It is worth highlighting that in the following results section some tests cases have shown the Bosch-Rexroth motor to be driving the rotor rather than being driven by the fluid. This is identified in the Matlab script by the sign convention. A positive voltage in the torque transducer indicates the motor is driving the rotor, a negative voltage from the torque transducer indicates the rotor is being driven by the fluid. Whilst these data sets have been shown in the Torque, Power and Thrust curves they have been disregarded for the respective coefficients curves. The reason for disregarding these cases is that when the motor is driving the rotor, energy is being added to the fluid and the rotor is performing as a pump. In these situations the coefficients will not collapse onto one curve as expected.

8.1.1. Torque

The mean torque over the middle portion as described in Chapter 7 has been taken to provide each data point. Figure 8.1 shows the alternator torque prior to the application of the frictional losses in the drivetrain for various carriage velocities at pre-determined rotational velocities. The 95%

confidence limits can be seen as the error bands connected with each data point. As the carriage velocity increases, the turbine's rotational velocity must increase to maintain the same λ value in the non-dimensional performance criteria. The 0.50 ms^{-1} carriage velocities can be seen to be negative along with the highest rotational velocity points at 0.75 ms^{-1} and 1.00 ms^{-1}. These points are being driven by the alternator, and causes the negative torque value from the alternator. This means the turbine is acting as a pump for these data sets and therefore cannot be used to determine the rotors performance characteristics. For this reason these point will not be considered further.

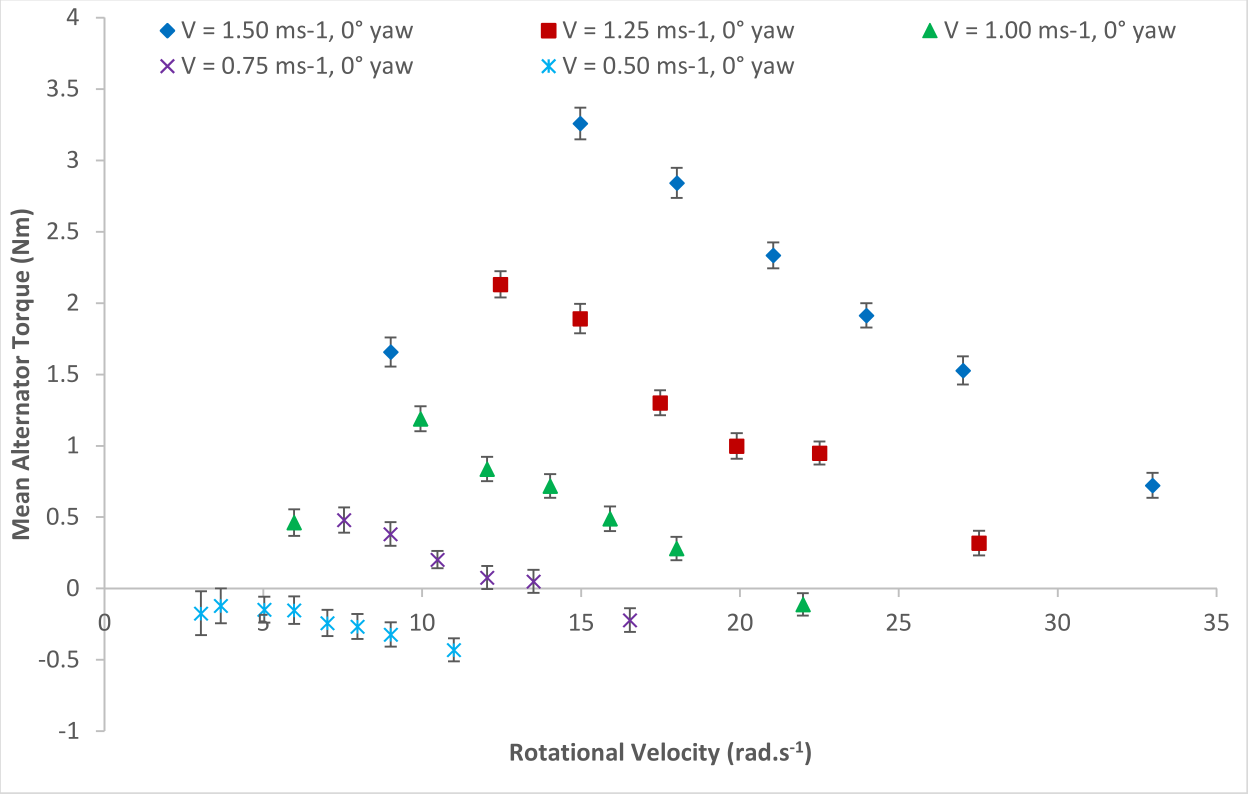

Figure 8.1 Mean and standard deviation of alternator torque with increasing turbine rotational velocity for 0° yaw angle

The alternator calibration was then applied to the data to account for losses in the turbine and thus provide the rotor torque. These mean values were then used to calculate the C_θ-λ curve as can be seen in Figure 8.2. The figure shows the coefficient of torque collapses closely onto one curve, with the 95% confidence bands overlapping in most cases. The two exceptions being the 1.00 ms^{-1} case at a λ = 3 and the 0.75 ms^{-1} at a λ = 4.5. However these outliers are not significant to the trend of the data. The turbine has the highest torque at a λ = 2.5 with a $C_\theta = 0.158$.

For comparison with CFD the steady state C_θ-λ curve from Section 6.1.1 has also been plotted with a trend line. It can be seen that the steady-state CFD has under predicted the peak torque, however it does show a close comparison past the peak, before diverging again as the turbine approaches freewheeling. The transient CFD mean data points at λ = 3, 3.65 and 5 have also been included from Section 6.2.1 and shows closer agreement with the experimental results than the steady-state.

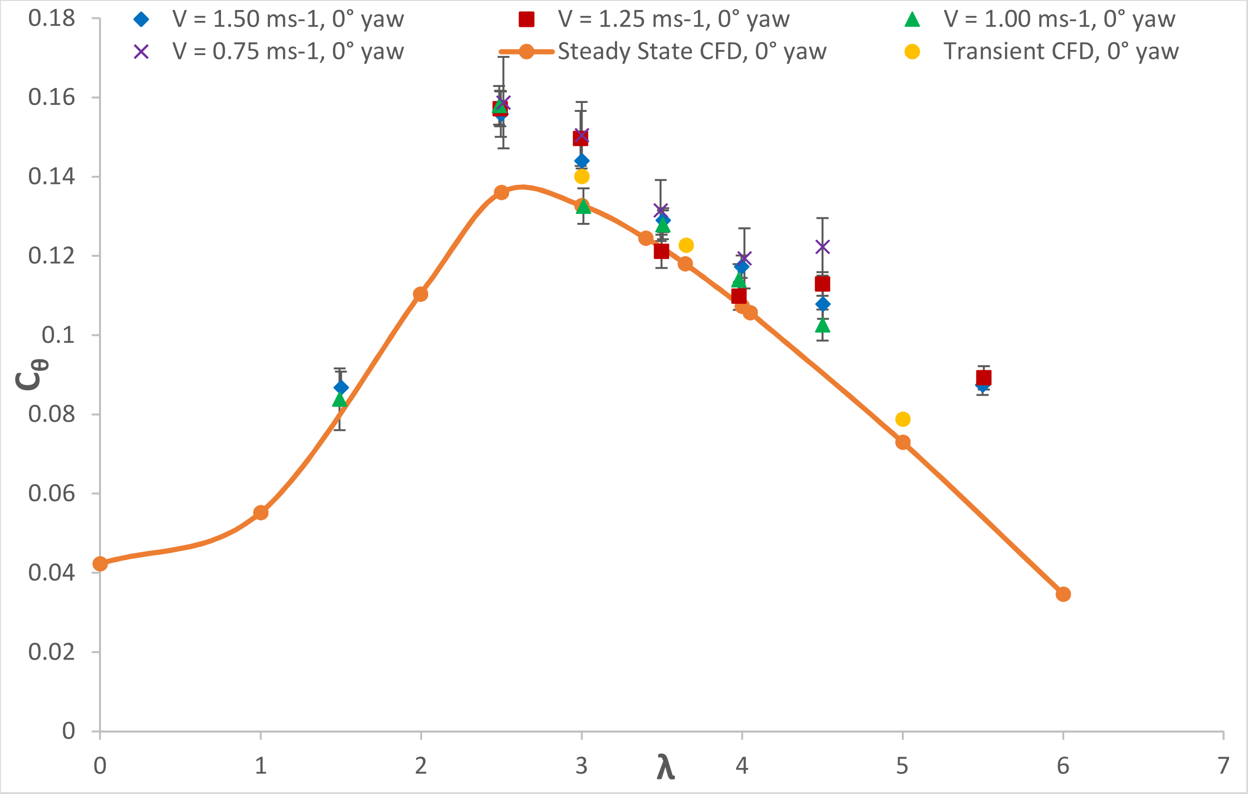

Figure 8.2 Coefficient of Torque with increasing λ for 0° yaw angle in comparison to steady state and transient CFD

The mean torque values for ±10˚ yaw angles on the experimental turbine are plotted in Figure 8.3 as non-dimensional C_θ-λ points. The experiments were run at two velocities, 1.00 and 1.50 ms^{-1}, the corresponding aligned cases show that there has been no significant drop in the turbines torque performance due to the misalignment.

For comparison the steady state ±10˚ yaw angle cases performed in CFD and discussed in section 6.2.1 have been plotted as solid lines. The steady state CFD appears to have under-predicted performance across the entire range of TSRs.

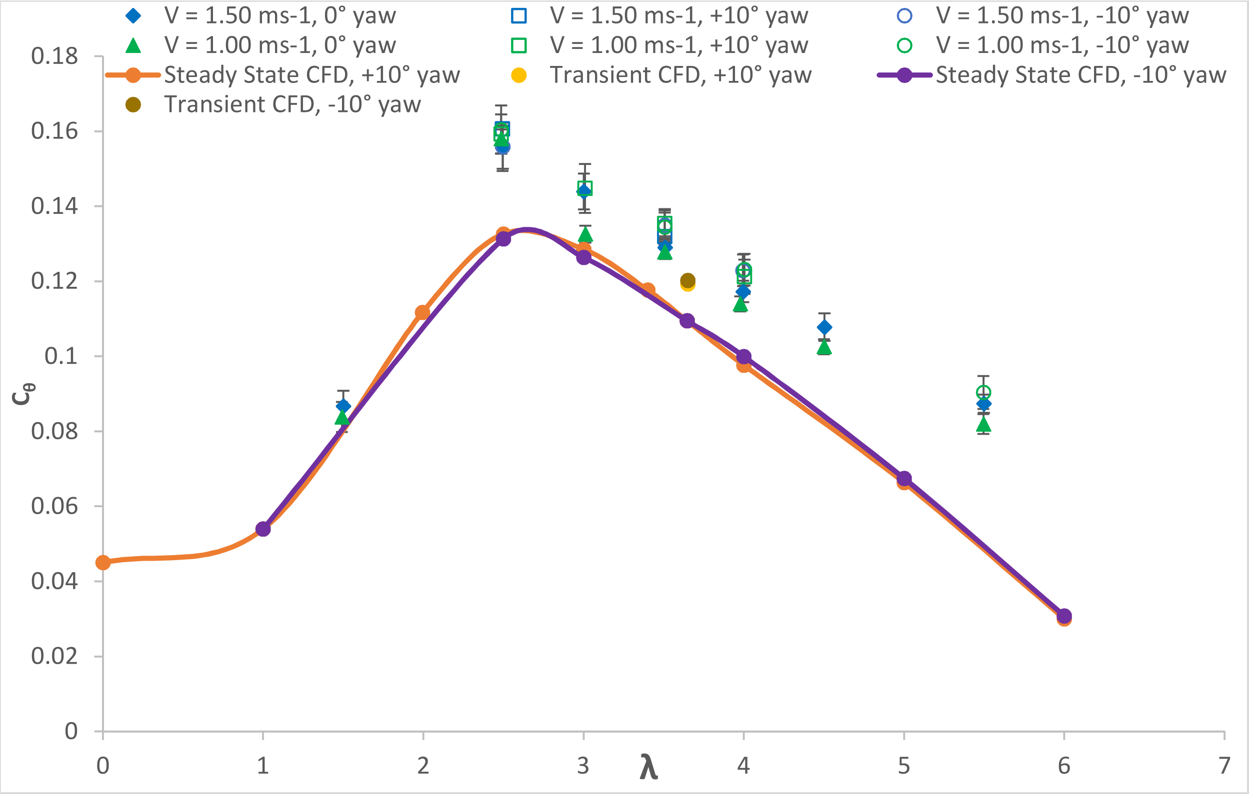

Figure 8.3 Coefficient of Torque with increasing TSR for 0° and ±10° yaw angle in comparison to steady state and transient CFD

The same experiments were conducted at ±20˚ yaw angles at CNR-INSEAN and the mean torque values used to plot Figure 8.4 as non-dimensional C_θ-λ points. The drop in torque performance between the aligned and ±20˚ misaligned cases is within the overlapping regions of the standard deviation. The -20˚ yaw angle at 1.00 ms^{-1} and 1.50 ms^{-1} shows a higher peak torque performance than their positive counterparts. In all cases, as λ increases the performance of the yaw cases appears to converge with the aligned cases. The +20˚ yaw angle at 1.50 ms^{-1} is an exception to this trend, it shows the lowest performance at peak torque and converges with the aligned data at a much higher TSR (λ = 5.5).

Again the ±20˚ misaligned cases from steady state and transient CFD (Section 6.2.1) have been plotted. The steady state CFD underperforms in comparison to the experimental data, however the transient CFD shows closer agreement, which is consistent with the other comparisons made in this section.

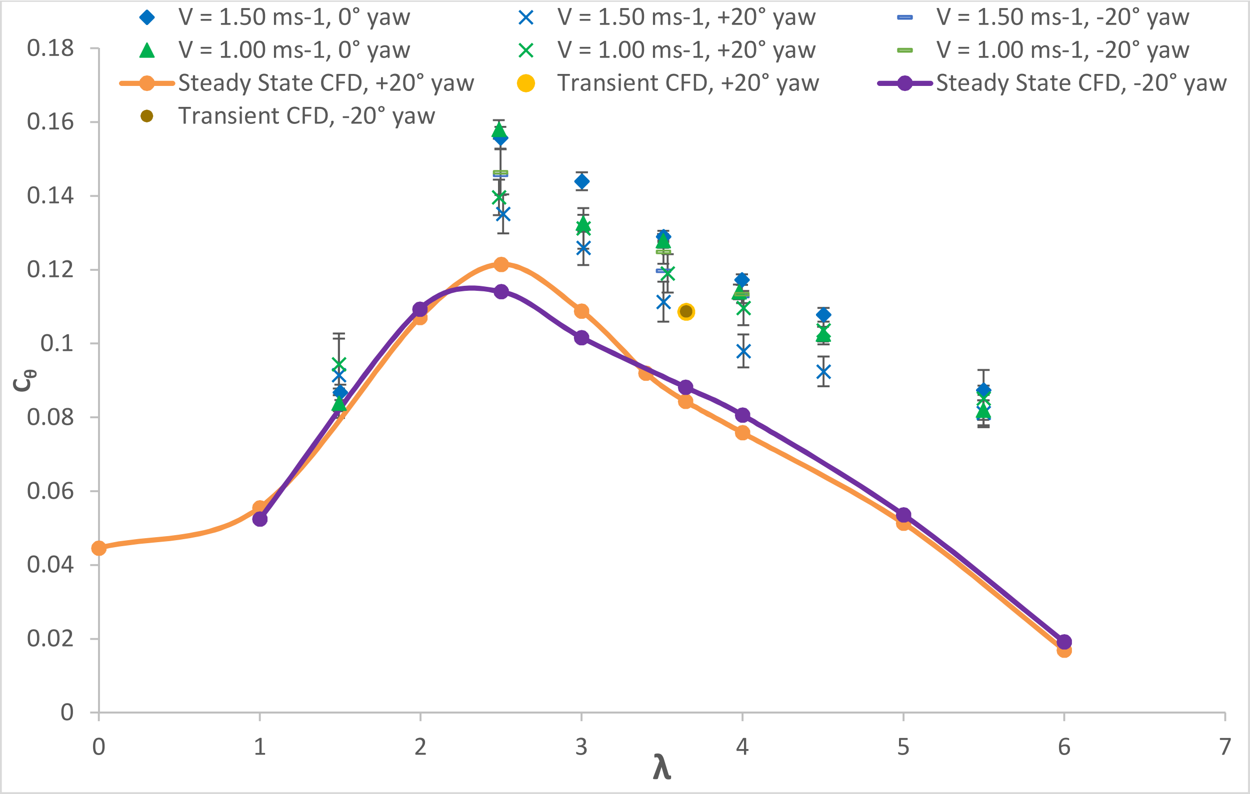

Figure 8.4 Coefficient of Torque with increasing TSR for 0° and ±20° yaw angle in comparison to steady state and transient CFD

The time averaged torque results have shown the trends seen in the CFD data are consistent with those recorded in the experimental campaign. The peak torque performance is approximately at a λ = 2.5 and for the aligned case the steady state CFD has shown close agreement in terms of magnitude at λ = 3.4. Table 8.1 shows the peak C_θ values from experimental and steady state CFD at λ = 2.5. The experiments show that at extreme yaw angles there is a drop in peak torque, however it is unclear that angles as low as ±10˚ have significant impact on performance at this scale experimental work. The full scale CFD, steady state results show a lower peak and more significant drop in performance as the yaw angle deviates from aligned.

Table 8.1 C_θ values for Experimental and CFD cases for all yaw angle cases at λ= 2.5

Yaw Angle (˚)	V = 1.00 ms^{-1}, Exp. C_θ	V = 1.50 ms^{-1}, Exp. C_θ	Steady State CFD - C_θ
-20	0.146	0.146	0.114
-10	0.160	0.156	0.131
0	0.158	0.156	0.118
10	0.159	0.161	0.133
20	0.140	0.135	0.121

In order to assist in distinguishing the trends, Figure 8.5 shows the performance of the CFD and experimental results with each case as a percentage change against their aligned result for λ = 3.65, peak power performance. The figure shows the C_θ unexpectedly increases above the aligned case for the ±10˚ yaw angles in the experimental data, yet drops for the steady-state and transient CFD. As the yaw angle increases to ±20˚ the C_θ performance decreases below levels of the aligned case, for the experimental data. At this yaw angle the 1.50 ms^{-1} experimental data points and the transient CFD data points are within 8.5% for the -20˚ yaw angle and 4.5% for the positive yaw angle, showing much closer agreement. These percentage changes will be the same for the turbines C_P performance also, therefore it will not be repeated in section 8.1.2. The steady state CFD consistently under predicts the performance with increasing yaw angle. As described in section 4.3.1 the steady-state models ignore higher-order temporal features of the RANS equations, simplifying the model and allowing convergence to be obtained quicker. However these temporal features are evidently significant in this case. For this reason, steady-state CFD must be used cautiously in predicting performance characteristics of misaligned flow scenarios.

In summary, the experimental torque data has shown the same trends as identified in the CFD, nonetheless two separate points of interest must be noted:

- The steady-state CFD results showed worse agreement with the experimental data as the yaw angle increased.
- Transient CFD results have been shown to have closer agreement with experimental data, than the steady state CFD results, independent of yaw angle.

The implications of these two points highlights the transient nature of flow misalignment and this must be considered carefully when the choice of numerical model simulation type is being made. Transient CFD models are more demanding, computationally if a commercial package is used consideration for licenses relating to parallel processing must be considered and the time to a full converged transient solution. Further data points on the C_θ-λ curve from the transient CFD analysis would further support this work.

The disparity between what was expected from theory, the CFD results and the experimental results at ±10° yaw angle is of particular note and further consideration of these findings should be made using other performance parameters.

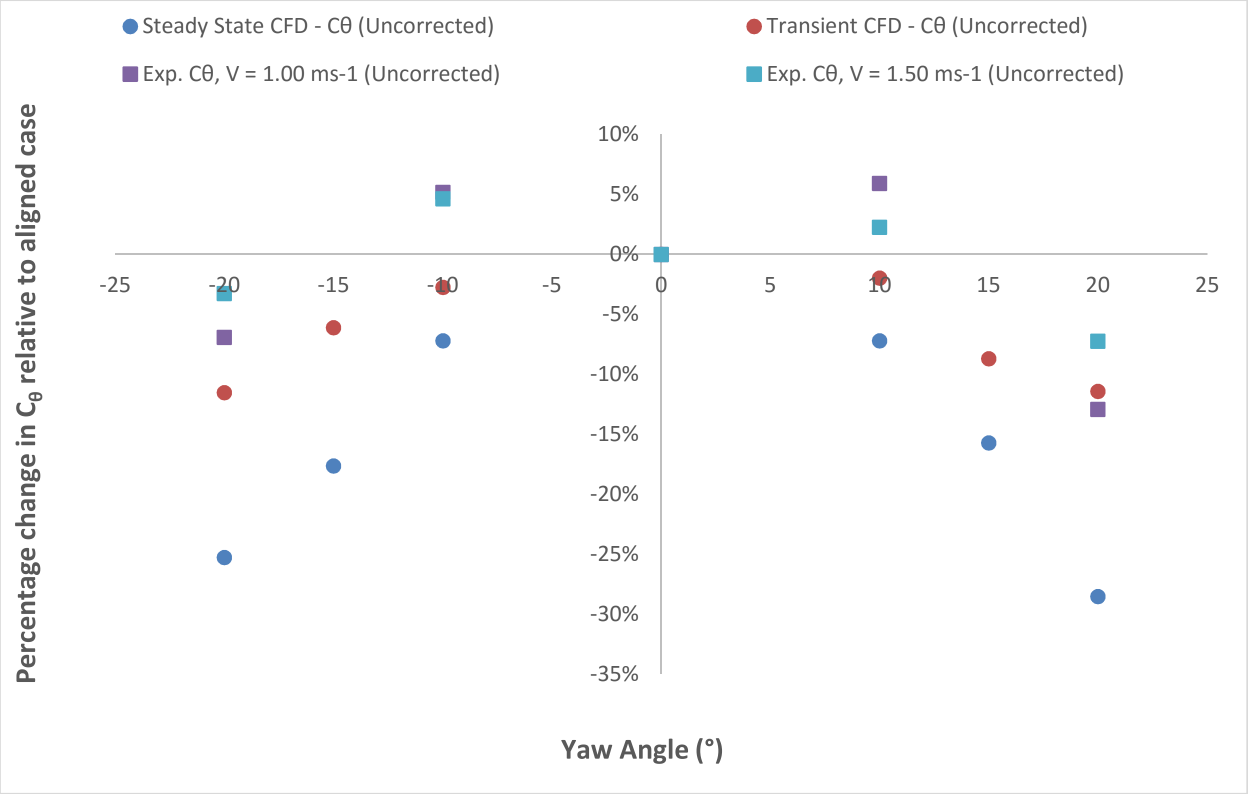

Figure 8.5 Percentage change in C_θ performance comparison at λ = 3.5 for increasing and decreasing yaw angle

8.1.2. Power

The mean power over the middle portion as described in Chapter 7 has been taken to provide each data point. Figure 8.6 shows the alternator's mean power for the aligned test cases, prior to the correction for frictional losses. Similarly with the torque data sets, the negative power in the 0.50 ms^{-1} and the highest rotational velocity cases for 0.75 ms^{-1} and 1.00 ms^{-1} cases, indicates the alternator is driving the rotor at these points and not being driven by the fluids motion on the rotor. For this reason these data points will be ignored. The 95% confidence intervals appear to increase with increasing rotational velocity.

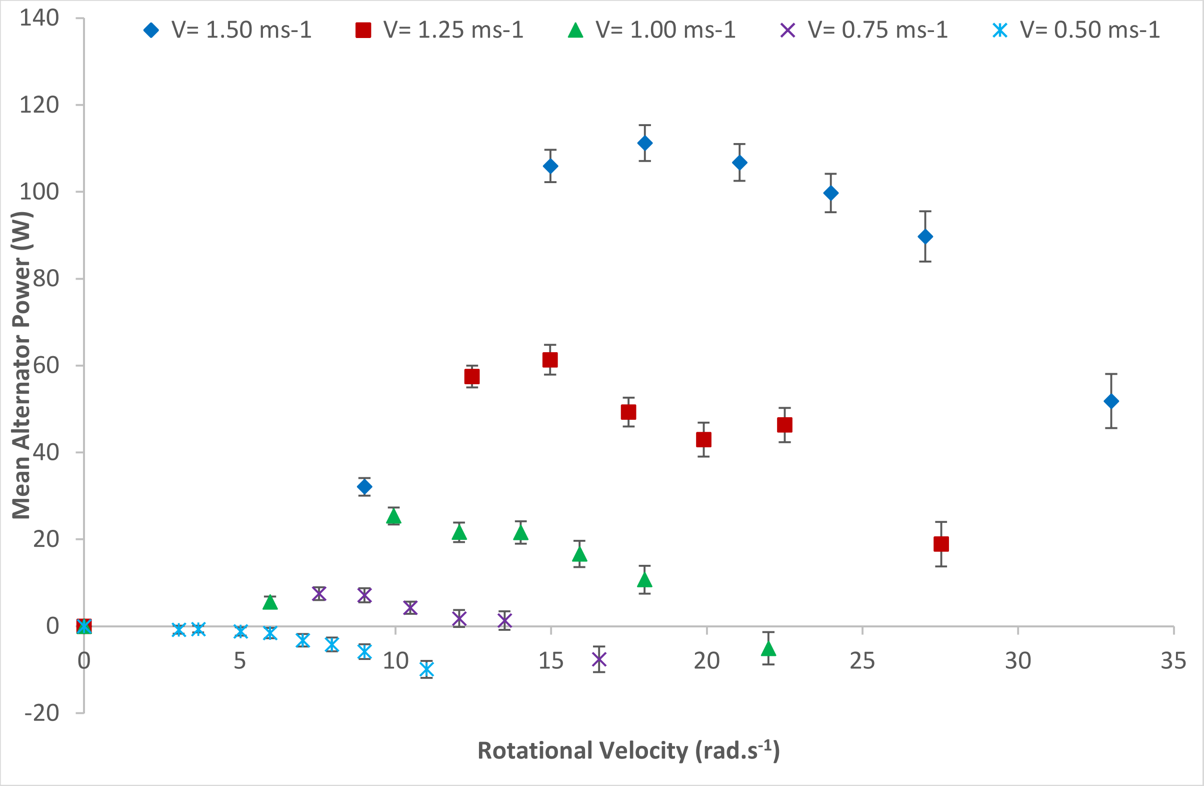

Figure 8.6 Mean and standard deviation of alternator power with increasing turbine rotational velocity for 0° yaw angle

Once the frictional losses are applied to the data sets and the mean power taken, it is used to calculate the C_P-λ curve for the turbine. Figure 8.7 shows the C_P-λ curves for the aligned cases in comparison to the steady-state and transient CFD data points. The experimental results in isolation first show that the data sets for the considered carriage velocities collapse onto one curve when considered non-dimensionally. There is some spread in the data sets with the 0.75 ms^{-1} case with a significant outlier at TSR = 4.5, this was also identified in the torque values. The 1.25 ms^{-1} case has two data points at TSR = 3.5 and 4 which appear to be lower than expected causing a dip in the curve, around the peak power. Ignoring outliers the peak $C_P = 0.45$ for $\lambda = 3.65$, for the V = 0.75 ms^{-1} carriage velocity.

When considering the experimental results relative to the CFD results, it can be seen clearly that the steady state and transient CFD lie within the boundaries of the experimental data points around the peak power. However there is some divergence between the experimental results and CFD as λ reaches the turbine's freewheeling point. The transient CFD results have a higher C_P than all but the V = 0.75 ms^{-1} at peak power, however it shows close agreement at the other points.

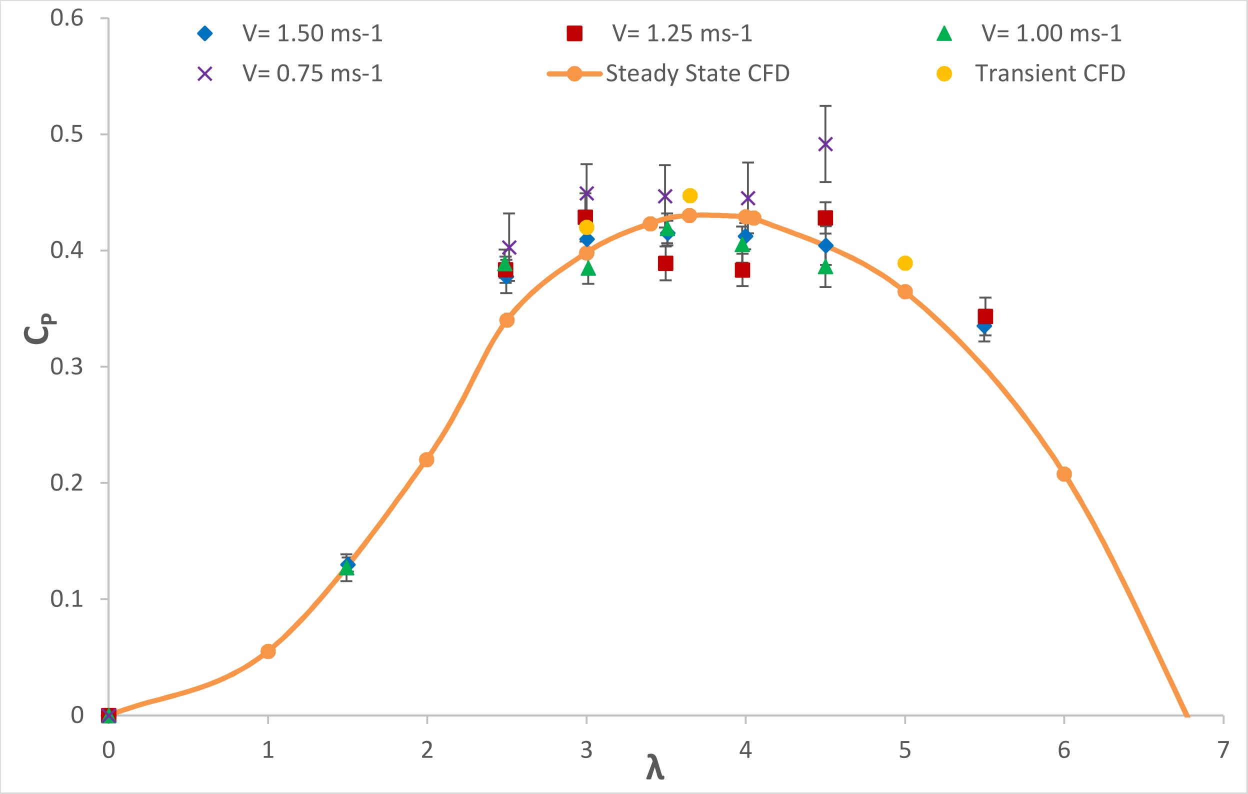

Figure 8.7 Coefficient of Power with increasing λ for 0° yaw angle in comparison to steady state and transient CFD

Consideration of the ±10˚ yaw angle experimental cases can be seen in Figure 8.8. In comparison to the aligned case the C_P has increased, however it shows the same trend as the aligned case, peaking around λ = 3.5. The 95% confidence intervals of the -10˚ yaw angle, for the V =1.50 ms^{-1} data point at λ = 2.5 shows an unusually high error band. It was later identified that the turbine start-up was included in the middle third of the data, resulting in a high standard deviation. This was caused by an increase in the fluctuations of the power signal and will be considered in the temporal results discussed in section 8.2.

The steady state CFD showed the same trend as the experimental data, the steady state however under predicted the power performance. The transient data point on the other hand agreed with the experimental data at the given λ points.

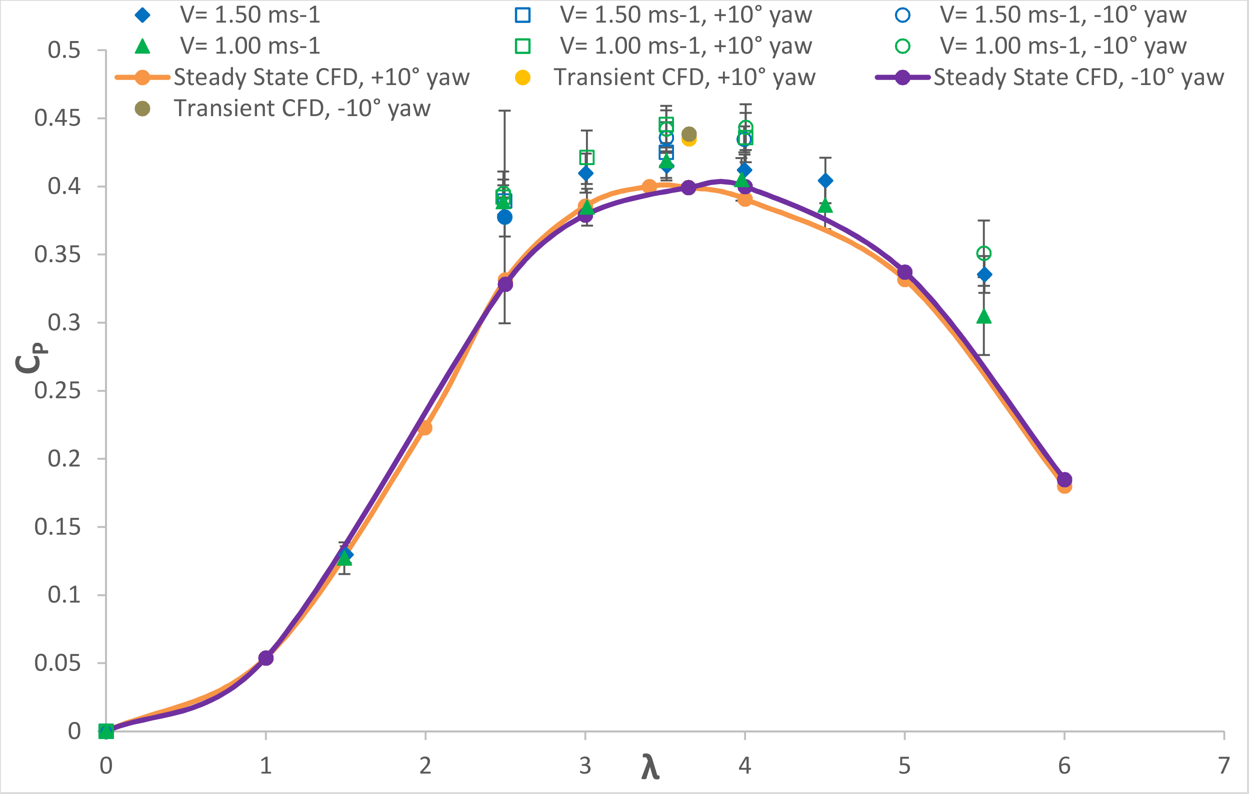

Figure 8.8 Coefficient of Power with increasing λ for 0° and ±10° yaw angle in comparison to steady state and transient CFD

When the yaw angle was increased to ±20˚ for the experimental testing the C_P responded by dropping, as can be seen in Figure 8.9. In this figure the ±20˚ yaw angles have a lower peak power performance than the aligned experiments. The +20˚ yaw angle at 1.50 ms^{-1} showed the worst performance as it peaked earlier than the aligned case at a λ = 3. The trend of the other misaligned cases was similar however and at higher λ values overlap with the aligned data points.

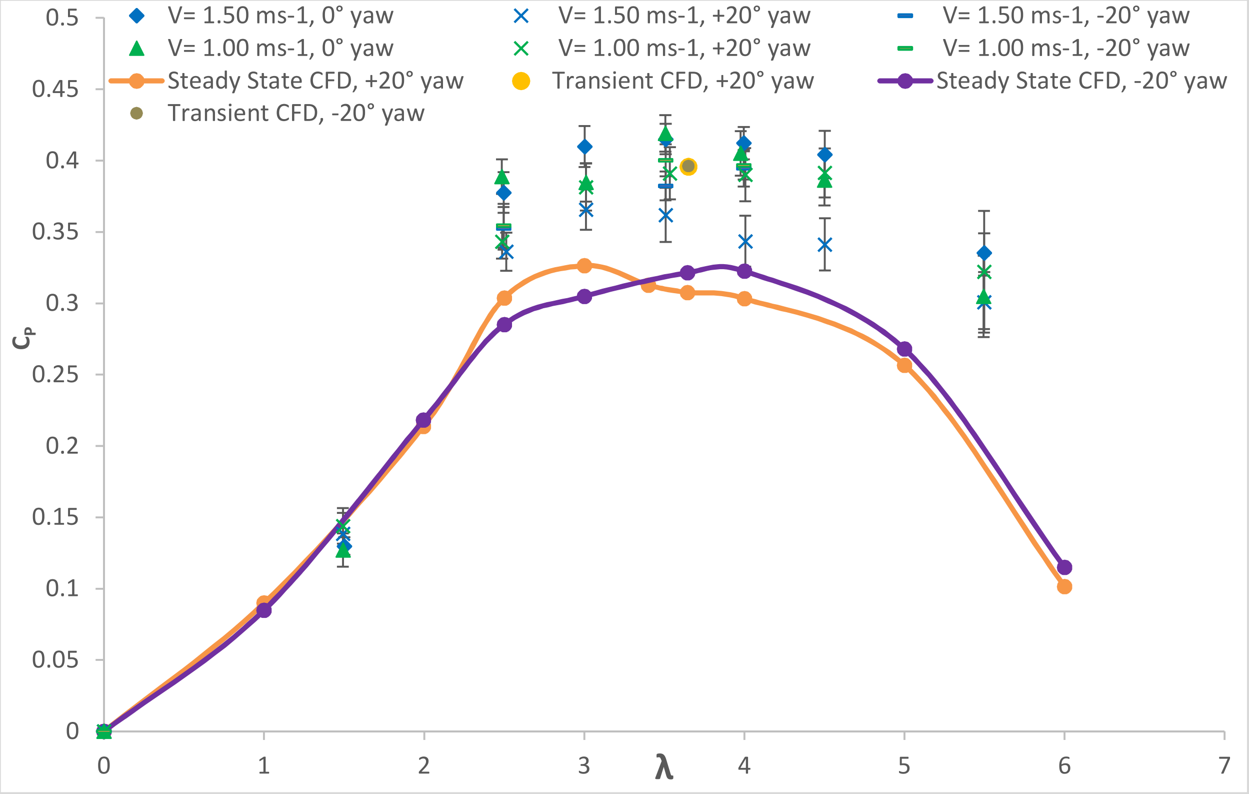

Figure 8.9 Coefficient of Power with increasing λ for 0° and ±20° yaw angle in comparison to steady state and transient CFD

8.1.3. Thrust

The thrust from blade 1 has been plotted against the rotational velocity of the turbine for increased carriage speeds in Figure 8.10. It can be seen that with the increased carriage speed the thrust on blade 1 also increased. It appears that the thrust at 0.50 ms^{-1} was close to zero during some runs, this would occur if the rotor was acting as a pump rather than a turbine (as identified in section 8.1.1), therefore applying a reverse thrust load on the blade. For this reason the 0.50 ms^{-1} will not be considered further. Outliers to the data trend have been identified for the 1 ms^{-1} data set. The first data point at a rotational velocity close to 6 rad.s^{-1} is far lower than expected. In analysing the data it appears the Arduino reset itself during the experiment, this resulted in a poor data point. For that reason it will not be considered as a part of the trend.

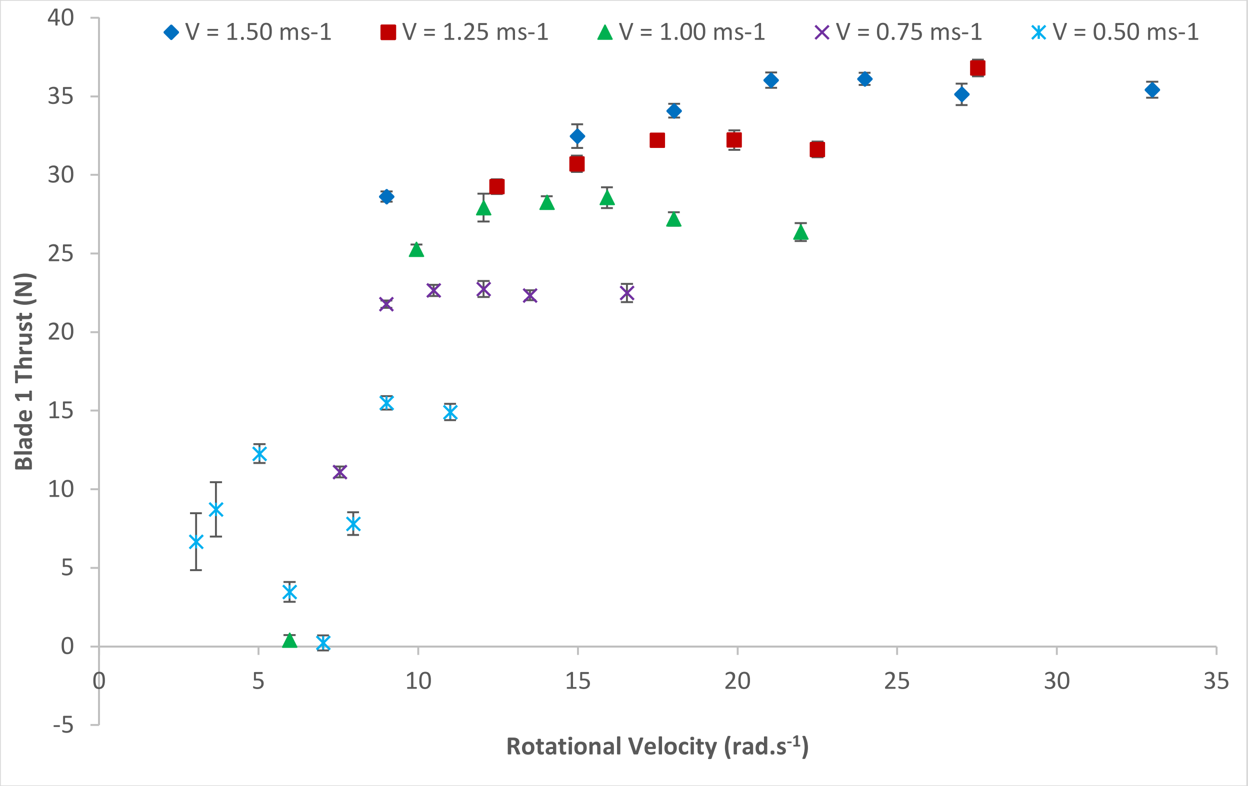

Figure 8.10 Mean and standard deviation of Blade1 Thrust with increasing turbine rotational velocity for 0° yaw angle

As described in Section 7.6 the C_T values for the turbine were calculated by multiplying the thrust for blade 1 by the number of blades, before applying to equation [**3.14**]. Once this was done the C_T-λ curve was created as seen in . The figure showed that whilst the confidence intervals for the data are tight, the data sets for each carriage velocity did not collapse onto one curve. This has shown the results are carriage velocity dependent, contradicting expected results. This was unexpected. It can be seen that the inverse order in magnitude of Figure 8.10 is occurring, with the higher carriage velocities having lower C_T values. This indicates that whilst the thrust can be seen to be increasing in Figure 8.10 it is not increasing at a squared rate. Further investigation into the reason for this discrepancy is required, however initial understanding suggests the instrumented blade flexures were not seeing a pure translational thrust force but a combination of thrust and bending moment. This issue with the blade thrust instrumentation has made the data unusable for characterising the blade performance. Therefore further analysis and discussion of these results will not be included in this thesis and will be left for further work.

8.1.4. Discussion

Section 8.1 has shown the torque, power and thrust performance characteristics of an experimental tidal stream turbine aligned to the flow and at yaw angles of ±10˚ and ±20˚. The data sets are time averaged and have been used in the validation of CFD models.

The experimental turbine has captured both the LHS and RHS of the performance curves, which is a real enhancement in comparison to previous work, one of the main objectives identified in Section 7.1 (Morris, 2014). The test facilities provided negligible turbulence in the flow and highly accurate carriage speeds; which minimised the uncertainty from these sources. The range of velocities operated at provided good validation of the rotors non-dimensional performance and has shown the impact of flow misalignment on these performance parameters. The inclusion of the 0.5 ms^{-1} carriage velocity has shown the frictional losses in the turbine were not overcome by the fluid and therefore this data set was unusable.

The non-dimensional performance characteristics for C_θ –λ and C_P –λ collapsed onto once curve for carriage velocities greater than V = 1.00 ms^{-1}. The aligned turbine case had a peak $C_\theta = 0.16$ at $\lambda = 2.5$, outperforming the CFD models and a peak $C_P = 0.45$ at $\lambda = 3.65$, which agreed with the transient CFD. The increase in all performance characteristics at ±10° yaw angle was unexpected and disagreed with both transient and steady-state CFD results for the same conditions. The possible reasons for this discrepancy remain unclear, however it may be a feature of the high twist angle (33°) experienced along the blade, causing the blade to operate at a more effective pitch angle for periods of the rotation. If this is the case, consideration of the temporal data will reveal azimuth angles of high performance and low performance corresponding to the passage of blades through this region. Additional insight into this possible explanation for this unexpected increase in performance may be seen in Section 8.2. Further work investigating this unexpected performance increase would be to consider experimental cases at yaw angles of ±5° and ±15° to see the sensitivity of the experimental set up and at which yaw angle the turbine begins to experience a negative drop in performance. The ±20° yaw angle cases performed as expected with percentage change in torque performance ranging from -2.4% to -13.7%, the power performance saw a similar change ranging from -4.5% to -12.8%. The coefficient of thrust had issues due to instrumentation not performing as expected, however the percentage change at ±20° yaw angle for V = 1.00 ms^{-1}, was between -4% and -5.8%. This shows the detrimental impact of misaligned flow on the performance of tidal stream turbines.

8.2. Temporal Results

As defined in the experimental methodologies (Section 7.6) the temporal results are formed from the middle third of the data sets. The results discussed in this section have come from data sets with the carriage speed V = 1.00 and 1.50 ms^{-1} and λ = 3.5. Included in each figure is the corresponding transient CFD data, which has been wrapped in order to conserve φ = 180° as BDC. The results are described and discussed figure by figure. The other transient results can be found in Appendix, Section E and are referred to as required.

8.2.1. Torque

The derivation of C_θ has been defined previously (Section 3.4) and was used to create the temporal torque performance curves from the experimental data. The blue points represent unfiltered data, whilst the orange points represent filtered data. The green points represent the transient CFD results.

Figure 8.11 shows the turbine's torque coefficient for the aligned case at peak power operation (λ = 3.5) in a 1.50 ms^{-1} flow. The unfiltered results show a clear periodic fluctuation occurring 10 times during each rotation, which is azimuth dependent. This is caused by the alternator's pole pairs of which there are 10 (Bosch-Rexroth, 2015). The filtered results show no clear fluctuation and in comparison to the CFD results, it does not appear that the blades stanchion interaction has been captured in the C_θ case. Relating this work to Section 5.2.3, the turbine's rotating plane is 4 stanchion diameters (D_{St} = 4) upstream of its stanchion, lying outside the range considered in CFD and therefore little interaction with the stanchion would be expected. The period used in the filter equated to half a rotation of the turbine at peak power for the fastest carriage speed, this may appear to be too coarse a filter to identify the temporal trends in the data sets. The difference in magnitude between the transient CFD and experimental results has been discussed in the previous Section 8.1.1. The transient CFD results show the blade-stanchion interaction occurring as each blade passes BDC as discussed in Section 6.2.1. However this was performed at a closer turbine-stanchion distance, D_{St} = 1.36.

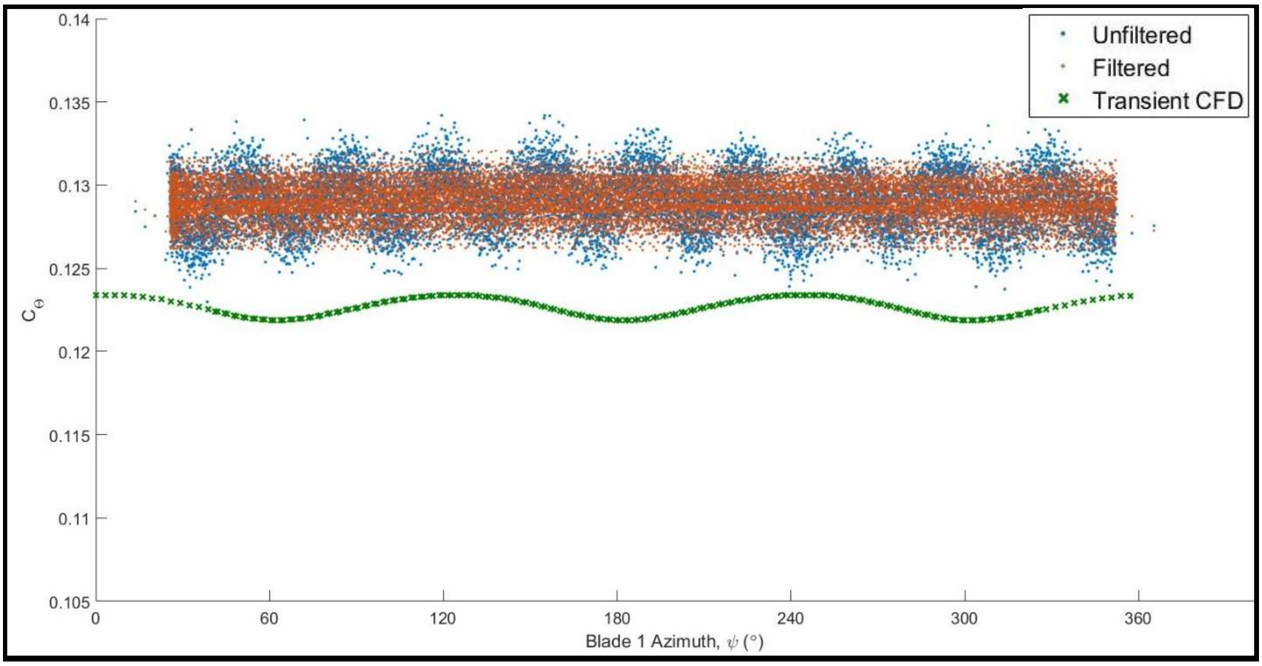

Figure 8.11 Filtered and unfiltered alternator C_θ - φ for aligned, 0° yaw angle at $V = 1.50$ ms^{-1} and $\lambda = 3.5$ with corresponding transient CFD results

As the time domain does not show clearly the trend in the results, the frequency domain must be considered to gain further insight into the results. To achieve this the Power Spectral Density (PSD) Periodogram was plotted for the mid-thirds of the torque signal as shown in Figure 8.12 and Figure 8.13 for $\lambda = 3.5$ and $V = 1.50$ and 1.00 ms^{-1} respectively. The figures include the aligned, ±10° and ±20° experimental results, showing the excitation frequencies of the transient data. This was done in accordance with the methodology in Section 7.6.1.

It can be seen from Figure 8.12 that the turbine's rotational frequency is detected as annotated on the figure at 3.35 Hz. Twice the rotational frequency was also seen, but this has not been annotated because its lower amplitude indicates it was a second harmonic. However the three times rotational frequency had a higher amplitude indicating that the torque signal is affected by the blades passing the stanchion at TDC. Whilst this is not identifiable from the time-domain it was found in the frequency domain, at 10.05 Hz. The next annotated excitation is at ten times the rotational frequency, at 33.50 Hz this is the alternators pole pairs and was clearly visible in the time domain as discussed earlier. These excitations were seen in the results for the turbine aligned to the flow and all the yaw angle cases in the frequency domain, for $\lambda = 3.5$ and $V = 1.50$ ms^{-1}. Due to the overlapping nature of these excitation frequencies differentiating the plotted lines in Figure 8.12 is unclear. The x-axis was limited to 35 Hz as no further excitation frequencies were visible at higher frequencies.

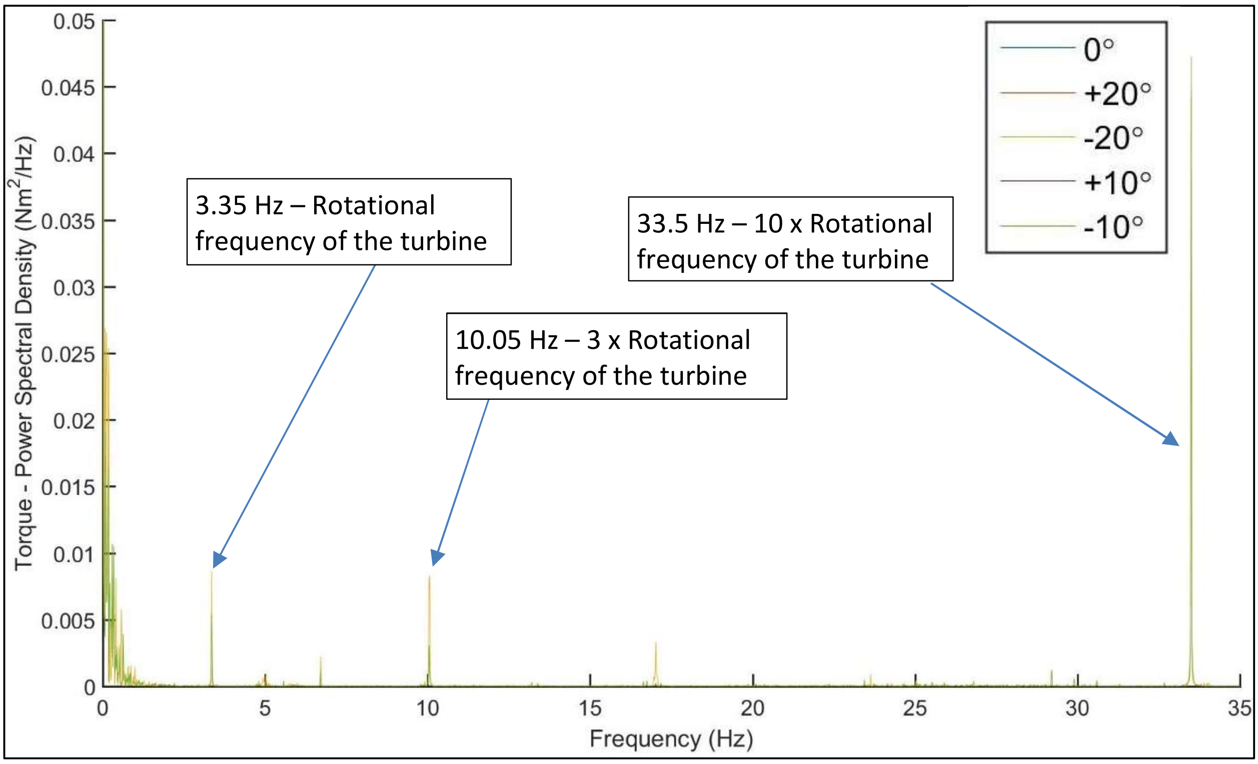

Figure 8.12 Periodogram of rotor torque signal for all cases at λ = 3.5 and V = 1.50 ms^{-1}

The same approach was made for plotting the Periodogram for all the cases at TSR = 3.5 and V = 1.00 ms^{-1}. Figure 8.13 shows a similar pattern in excitation frequencies as Figure 8.12, however differences are notable and of interest. The three time rotational frequency is identifiable at 6.70 Hz and shows the blades passing TDC, producing a change in the torque signal. The pole-pairs are again identifiable at 10 times the rotational frequency. There is an unexpected excitation frequency at 12 times the rotational frequency which was noted in these results. Further investigation into this found that this 12 times rotational frequency was strongly present in carriage speeds at V = 0.75 and 1.00 ms^{-1} (Appendix, Section E). It was faintly seen in the V = 1.25 ms^{-1} but is not seen in the V = 1.50 ms^{-1} periodogram. A probable source of this unexpected frequency response could have been due to stanchion vibration. Given the length of the stanchion, based on the clamping arrangement described in Section 7.2 and using the formula by Blevins (2001) for calculating the first mode frequency of a hollow tube (equations in Appendix D). As an estimate the stanchion has a first order vibrational frequency of 26 Hz. This is close to the frequency seen at V = 1.00 ms^{-1}. To avoid this in future work the stanchion should feature fairings along the downstream face, or increased stiffness so that the frequency is higher than the range considered for the turbine.

It was noted that Figure 8.13 had a shadowing frequency in close proximity to each of the excitation frequencies. This second peak is from the -20° yaw angle cases and is due to a slightly different carriage velocity being set.

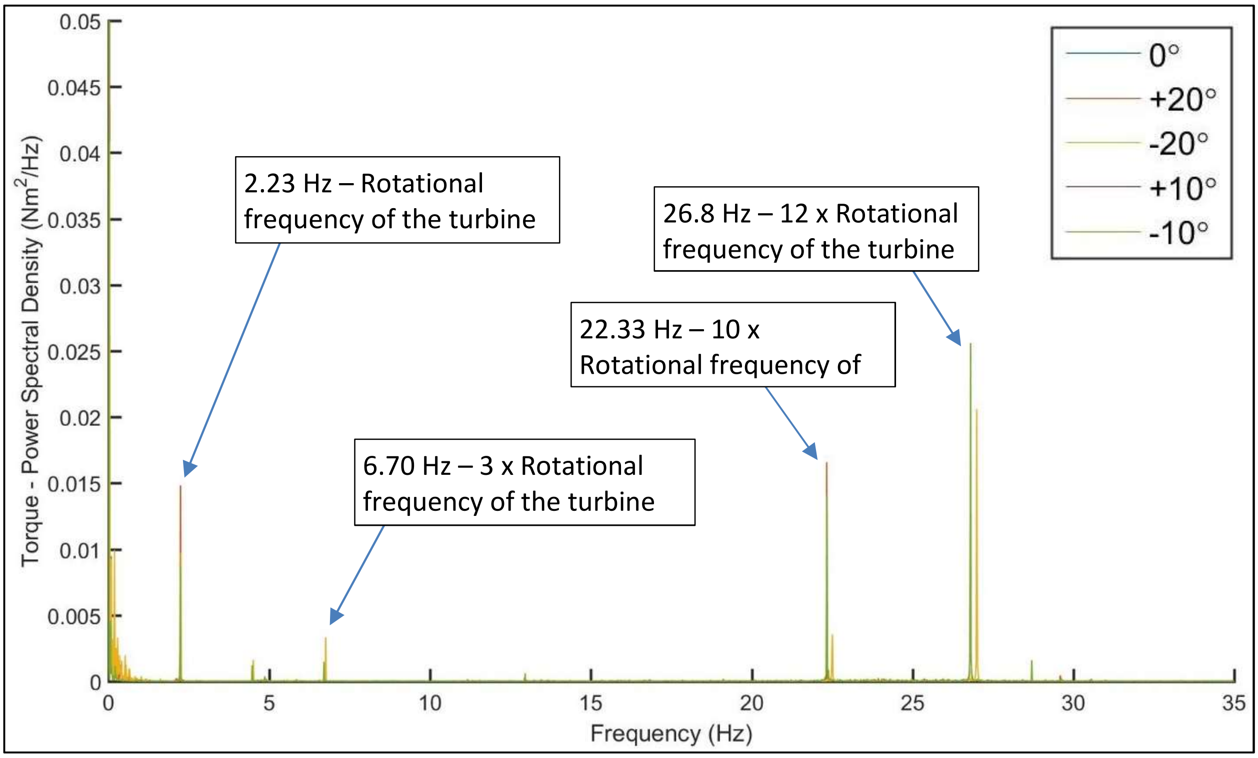

Figure 8.13 Periodogram of rotor torque signal for all cases at λ = 3.5 and V = 1.00 ms^{-1}

These results are significant, as they show that even in this experimental set-up, with the rotor 4 stanchion diameters upstream of the support stanchion, the interaction with the blades is identifiable in the torque signal. Whilst the magnitude was small relative to other signals identified in the frequency domain, and the trend in-distinguishable in the time-domain, the blade-stanchion interaction was evident.

The results were limited as the PSD in the frequency domain did not show shift in the location of the troughs, due to the various yaw angles. It is recommended that further work to investigate this ought to consider reducing the stanchion to rotor separation, making the interaction more distinguishable in the time-domain.

8.2.2. Power

The same experimental case as in Section 8.2.1 is used in Figure 8.14 to show the power performance within a rotational cycle of the turbine using the time domain. Figure 8.14 showed C_P-φ for aligned case at V = 1.50 ms^{-1} and λ = 3.5. It was seen that the unfiltered results showed a clear interaction with the pole-pairs causing 10 peaks and troughs with the rotation. The filtered results showed a slight rise of once per rotation. In comparison to the CFD results the spread in the results were lower, and this was discussed with respect to the differences in the mean values, in Section 8.1.2. Additionally the three peaks and troughs per rotation due to blade stanchion interaction did not appear to be visible in the time domain.

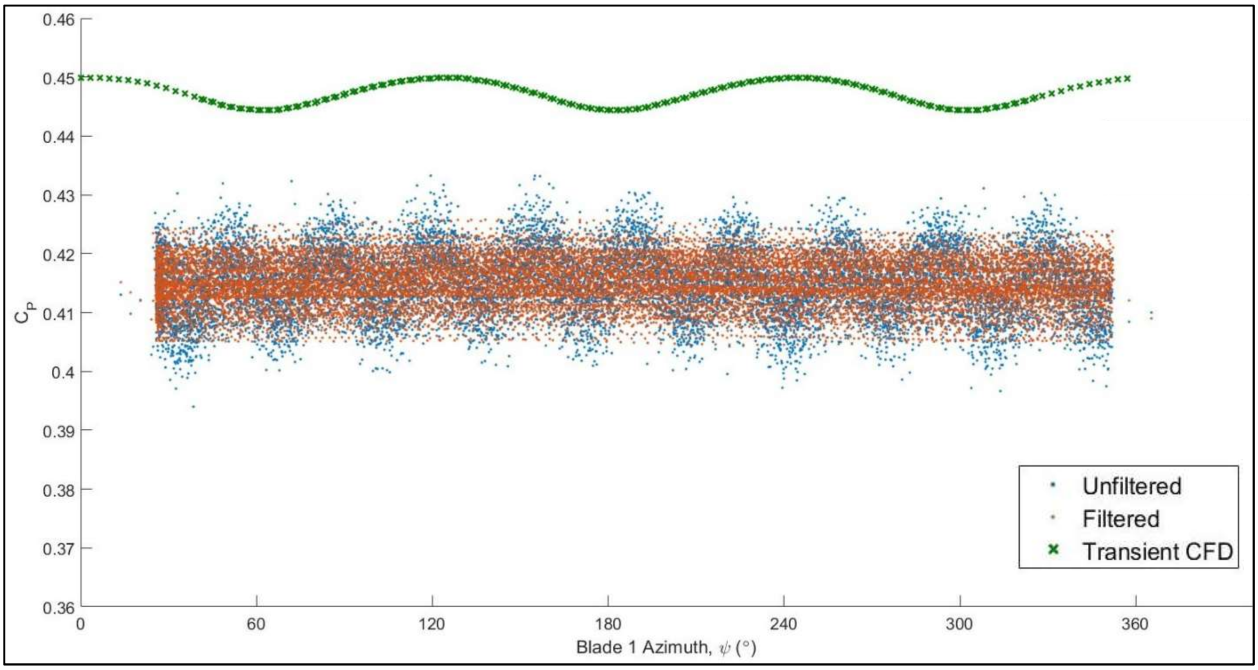

Figure 8.14 Filtered and unfiltered alternator C_P - φ for aligned, 0° yaw angle at V = 1.50 ms^{-1} and λ = 3.5 with corresponding Transient CFD results

In order to investigate these results and those at the ±10° and ±20° yaw angles the frequency domain was used. By transforming the signal as described in Section 7.6, the PSD periodogram of the mechanical power from the rotor was plotted for aligned and yaw angle cases, as seen in Figure 8.15 and Figure 8.16. In Figure 8.15 all the results can be seen to lie close to one another. As the rotor power is a function of its torque and rotational velocity it is clear the frequency responses were the same as in Figure 8.12 the only difference being in the magnitude of the responses.

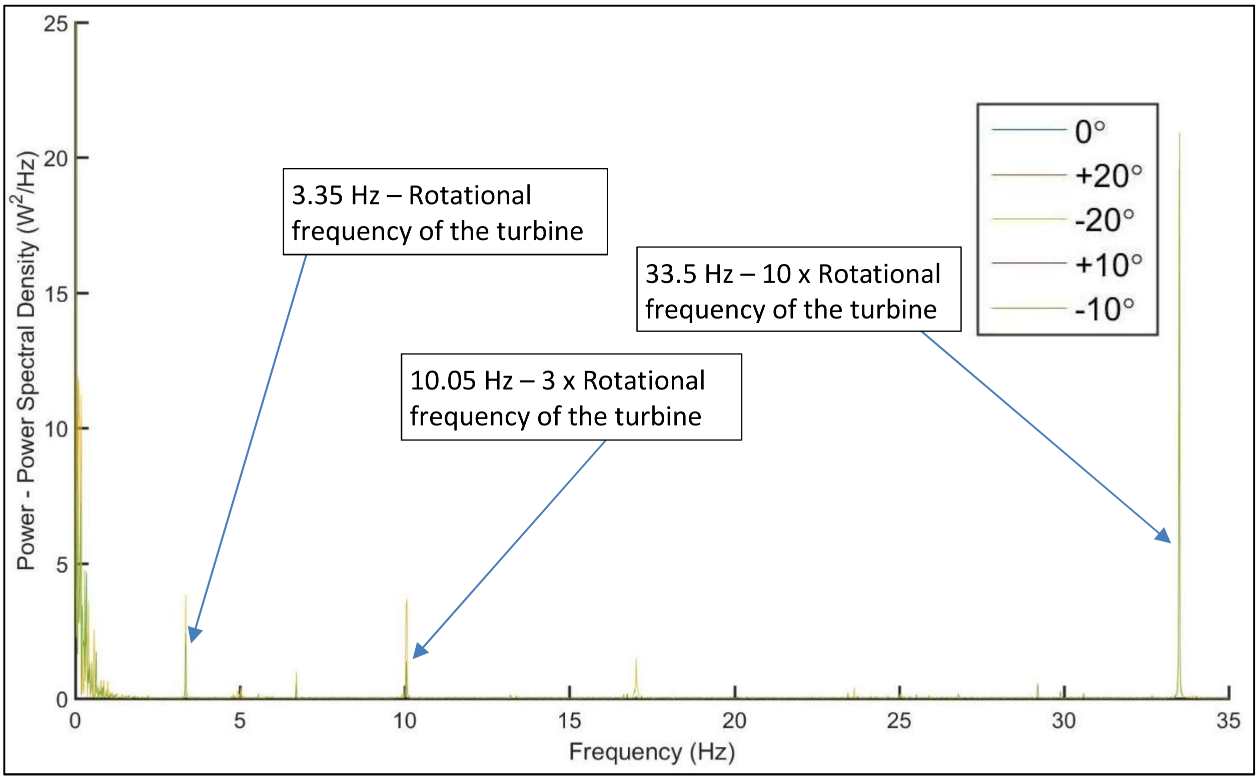

Figure 8.15 Periodogram of rotor power signal for all cases at λ = 3.5 and V = 1.50 ms^{-1}

For a λ = 3.5 at a velocity of V = 1.00 ms^{-1} the same frequency responses in the rotor torque signal (Figure 8.13) were revealed in the rotor power signal (Figure 8.16). The change in PSD between these figures was due to the significance of the rotational speed of the turbine. The stanchion vibrational frequency remained visible as would be expected. As was seen in Figure 8.13 the shadowing of the peaks was due to the -20° yaw angle case being run at a slightly different carriage velocity.

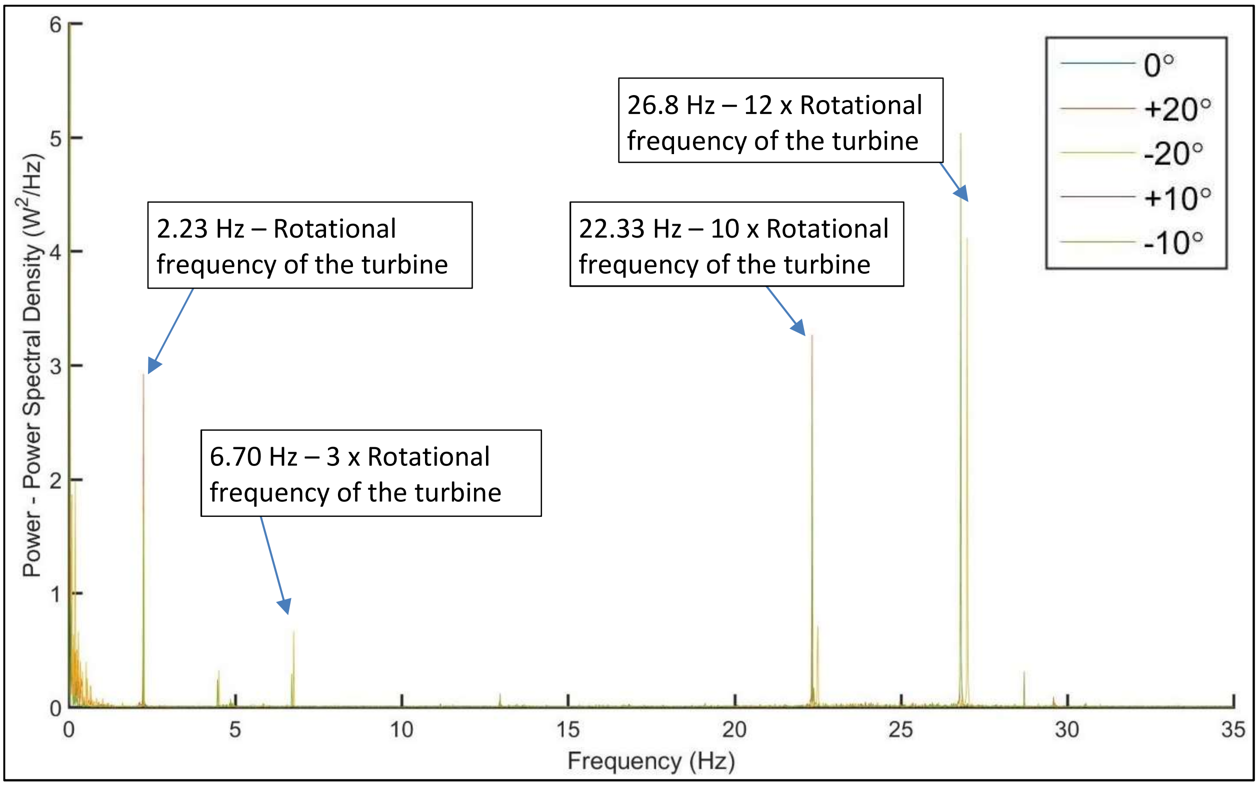

Figure 8.16 Periodogram of rotor power signal for all cases at $\lambda = 3.5$ and V = 1.00 ms^{-1}

Both the torque and power temporal results showed the experimental turbine provided insight into the turbine's performance during rotation, and not just mean values. The annotated frequencies picked up from the analysis of the results revealed that a clear stanchion interaction occurred with each of the blades. This was masked in the time domain which was dominated by the alternators pole pairs. A first order resonance frequency was detected at carriage speeds of 1.00 ms^{-1} or less. It is recommended this be avoided in further work, as also identified in Figure 8.13. Reducing the distance of the clamping arrangement to the turbine nacelle increases the frequency of this first mode to a higher frequency, moving it beyond the interested area. Alternatively the use of a profiled stanchion or fairings which can be adjusted to always be on the downstream face of the stanchion to prevent vortex shedding, may cause the harmonic vibration. The use of fairings is deemed to be more appropriate if experimenting at various yaw angles are be performed.

8.2.3. Thrust

The hub thrust instrument was seen to have issues in capturing the magnitude of the blades thrust and section 8.1.3 showed the inverse dependency between the carriage velocity and the coefficient thrust. Therefore the data will not be analysed as temporal results in this section. Further work is required to amend the identified issues with the instrument,

8.2.4. Discussion

The results in Section 8.2 showed the temporal performance of a tidal turbine, using both the time domain and frequency domain analysis. The torque and power signals from the turbine showed the rotor's sensitivity to stanchion interaction, alternator pole pairs and stanchion vibrational frequency. The stanchion interaction was significant as it confirmed the same interaction seen in CFD, but at a greater stanchion clearance distance. Further work to enhance this interaction may reveal more confidence in these results, and identify the trends seen in CFD for yaw angled cases.

The cause for the rise in performance at ±10° yaw angles was not clear from the temporal data and the sharp peak at the 3 x rotational frequency suggests it is not due to the blades passing through a region of higher performance. Further work as suggested in Section 8.1.4 may reveal the cause of this performance increase.

The issue with the blade thrust instrumentation prevented further analysis in the temporal results showing stanchion interaction, and further work into the mitigation or capture of the out-of-plane bending moment is required.

The benefits of performing this temporal analysis, highlights the complexity of obtaining detailed results at this 20th scale lab experiments. However it also showed it was feasible to analyse the performance during a rotation, and it is considered this may encourage further work in comparison with varying flow conditions, such as a shear profile or highly turbulent flows, using the same experimental apparatus.

8.3. Correcting Non-Dimensional Performance Characteristics for Flow Misalignment

Throughout Chapters 6 and 8 the performance characteristics were calculated using the swept area of the rotor and the inlet velocity of the CFD model as inputs for the performance characteristic equation [3.12] - [3.15]. This enabled the relative comparison of the impact of flow misalignment on the turbine performance. However as established in Section 3.6, corrections for geometrical and environmental scenarios need to be made to maintain the non-dimensional performance characteristics. Section 3.7 continued by proposing a correction method for flow misalignment, the correction maybe applied to the swept area, A or the velocity, V terms of the non-dimensional performance equations. As seen in Section 3.7 the area correction method provided the same nominal drop in performance for each of the characteristics and has been hypothesised as the correction method for misalignment. In this section both these correction methods were applied separately to the CFD and experimental results in order to determine if the non-dimensional performance for the aligned case were preserved in the flow misalignment cases. The aim was to demonstrate which method correctly accounts for misalignment.

8.3.1.Correcting for misalignment; Coefficient of Torque

For the coefficient of Torque (C_θ), as discussed in Section 3.7 the denominator of equation [**3.12**] must account for the misalignment, and this is done by inserting equation [**3.25**] into the denominator. Figure 8.17 showed the area corrected C_θ as a percentage change for each flow misalignment case when considered against the aligned case for steady state and transient CFD at $\lambda = 3.65$ and the experimental results at $V = 1.00 \text{ ms}^{-1}$ and $V = 1.50 \text{ ms}^{-1}$.

Figure 8.17 showed the steady state CFD, even with area correction has not accounted for the effect of the yaw angle. The figure also showed that the correction for the transient CFD cases match more closely to the aligned values than the steady state models. The area corrected experimental results have a significant gain in C_θ at ±10° yaw angle, this is not seen in the experimental results and has been discussed in Section 8.1.1. The experimental results both more closely match the percentage change in the transient CFD at ±20° yaw angle. Significantly, whilst this correction accounts for some of the performance differences due to misalignment it did not capture the complete cause for the change in performance.

Figure 8.17 Percentage change in Coefficient of Torque at increasing angles of misalignment for uncorrected and area corrected result

Figure 8.18 shows the percentage change of the velocity correction method in C_θ from the aligned case for increasing yaw angles from the steady state and transient CFD results presented in Chapter 6, and the experimental results from Chapter 8 also. Both V = 1.00 ms^{-1} and V = 1.50 ms^{-1} carriage velocities are presented using the velocity corrected method.

Figure 8.18 showed that again the steady state CFD results with velocity correction do not compare to the aligned case as would be expected. The velocity corrected CFD results, show a closeness to the aligned performance at all yaw angles. This indicates the velocity correction method ought to be the one used for correcting C_θ in misaligned flow. The experimental results when velocity corrected over predict the performance change at ±10° yaw angles for both carriage velocities. However at +20° yaw angles the V = 1.50 ms^{-1} carriage velocity has seen a small percentage drop relative to the aligned case. The 10% overcorrection seen in the V = 1.00 ms^{-1} data set indicates the rotor has a better torque performance with misalignment.

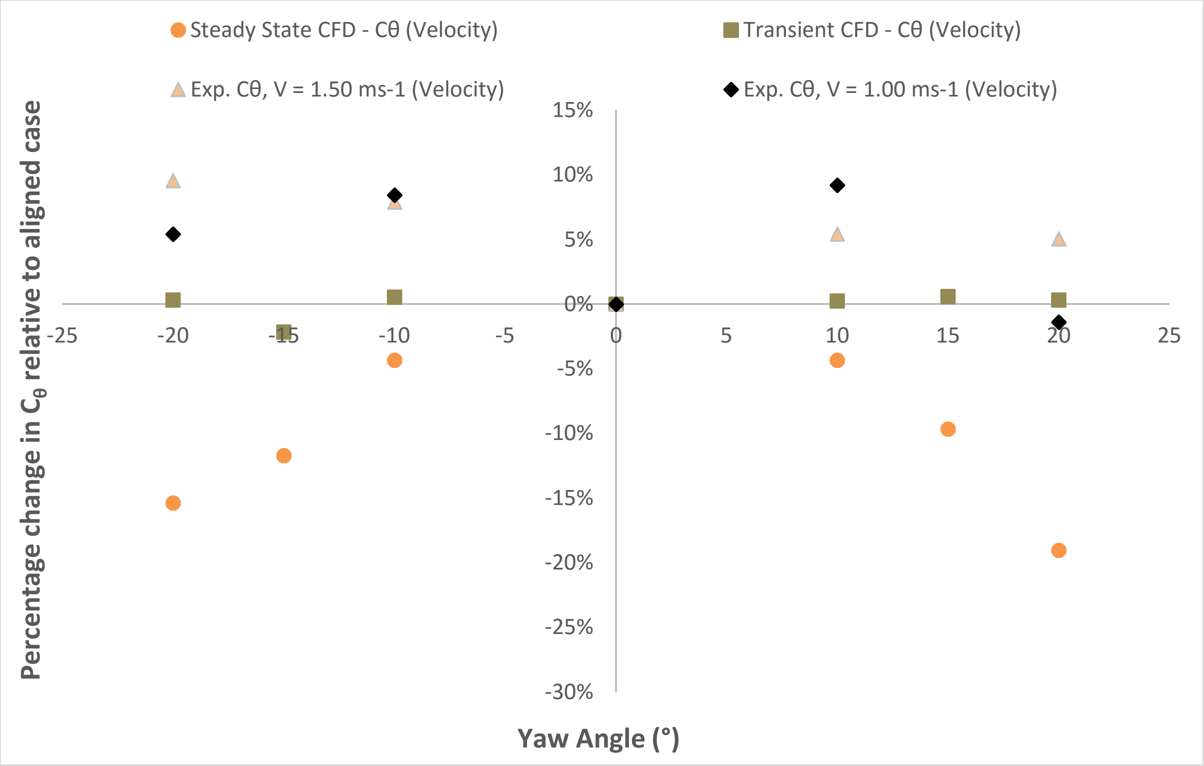

Figure 8.18 Percentage change in Coefficient of Torque at increasing angles of misalignment for uncorrected and velocity corrected result

8.3.2. Correcting for misalignment; Coefficient of Power

Figure 8.19 shows the percentage change in power performance (C_P) of the turbine at λ = 3.65 for the steady state and transient CFD numerical models using the area corrected method. The same method was applied to the V = 1.00 ms^{-1} and V= 1.50 ms^{-1} experimental results. The correction is performed by substituting equation [**3.25**] into equation [**3.13**] as discussed in section 3.7. The area corrected C_P percentage changes for steady state at increasing angles of flow misalignment significantly under predicts the turbine's power performance. The area corrected, transient CFD results show the closest to the aligned case for all angles of misalignment, with some over estimation at ±10° yaw angles. The area corrected experimental results area similarly to the area corrected transient CFD results. In comparison to the velocity corrected results, shown in Figure 8.20 and discussed below, the area corrected results give closest comparison to the aligned case and ought to be used for accounting for misalignment when considering a turbines C_P.

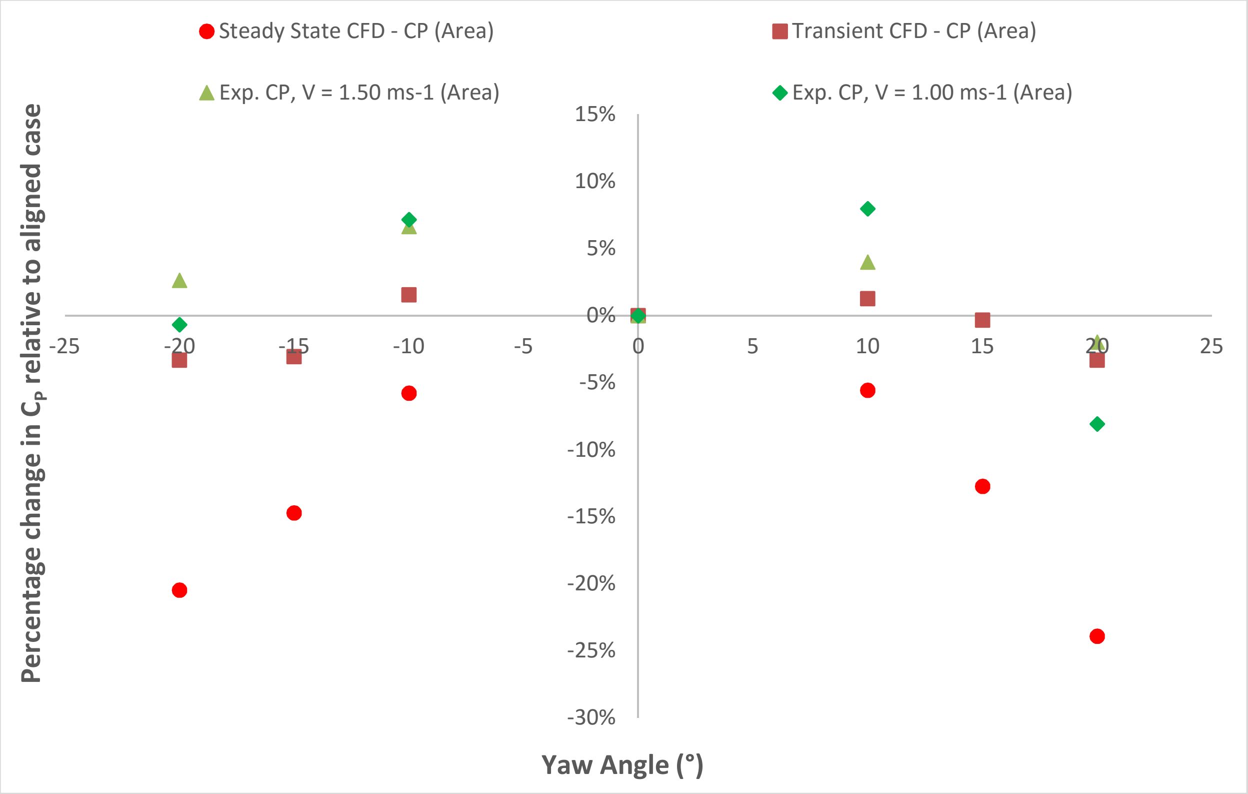

Figure 8.19 Percentage change in Coefficient of Power at increasing angles of misalignment for uncorrected and area corrected result

Figure 8.20 shows the percentage change in C_P from the aligned case for increasing yaw angles from the steady state and transient CFD results presented in Chapter 6 using the velocity correction method. The experimental results from Chapter 8 are also presented for V = 1.00 ms^{-1} and V = 1.50 ms^{-1} using the same velocity corrected method.

Figure 8.20 showed the steady state CFD results still underestimate the power performance of the turbine in yawed flow, however the velocity correction draws the results closer than the area correction discussed above did. The transient CFD results on the other hand, over predict the performance by up to 10% in misaligned flow, when velocity corrected. The velocity corrected experimental results and transient CFD results closely agree with one another. However the same over prediction seen in the transient results is seen in the experimental results when velocity corrected.

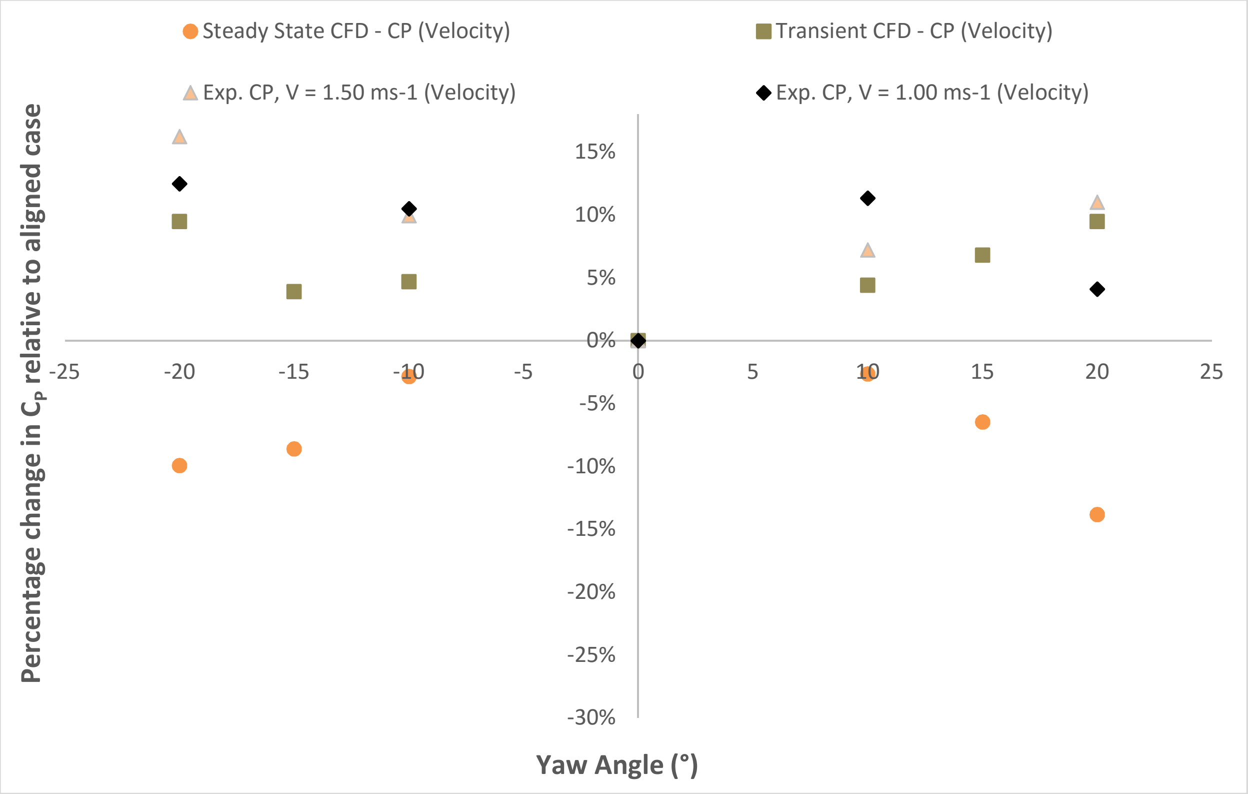

Figure 8.20 Percentage change in Coefficient of Power at increasing angles of misalignment for uncorrected and velocity corrected result

8.3.3. Discussion

Two methods of correcting for flow misalignment were proposed, the first method accounts for the reduction in projected area of a turbine as the yaw angle increases. The second method accounts for the component of the free stream velocity that is flowing perpendicular to the turbine. These methods were known as the area and velocity correction methods, respectively. It was expected that the velocity correction method would account for the changes in inflow angle due to accounting the squared and cubed terms in the non-dimensional performance equations. Both correction methods were plotted using CFD and experimental results in order to compare with respect to their percentage change in non-dimensional coefficients relative to their aligned cases. It was expected that the correct method would show the closest percentage change in results with misalignment to the aligned case.

The steady state CFD have been shown to over-predict the percentage change in each case due to its ineffectiveness in capturing the transient nature of misaligned flow through the turbine. The transient CFD results have shown that for the coefficient of torque the velocity correction method matched the aligned results to within 2%. The coefficient of power when area corrected for transient CFD results matched within 3%. It was expected one correction method would work for all the non-dimensional performance characteristics, as this has not occurred, it is clear further work must be made to establish which is the correct method, if either.

The experimental results were shown to agree with the transient CFD results to within a few percent, however this was inconsistent at ±10° specifically. The performance at this yaw angle has been shown to be an unexpected result in Section 8.1 and further work at similar yaw angles (±5° and ±15°) is proposed for experimental testing with this device to determine if this performance increase occurs.

8.4. Summary

The 1:20th scale (0.5 m diameter) turbine developed for numerical validation was tested in the 220 m towing tank at CNR-INSEAN in Italy. The Turbine was designed to operate at constant RPM's which when coupled with a fixed carriage speed provided the full range of Tip Speed Ratio desired. The turbines instrumentation included a rotational encoder providing both the rotational velocity of the turbine and azimuth position during rotation. The torque of the rotor came from the alternators torque generating current which was corrected for losses through the system to provide the rotor torque. The turbine's hub and nosecone featured strain gauge flexures designed to record the thrust force on one blade.

The turbine in aligned flow had a peak $C_\theta = 0.16$ at $\lambda = 2.5$ and peak $C_P = 0.45$ at $\lambda = 3.65$. The C_θ-λ and C_P-λ characteristics collapsed onto a single curve for carriage velocities greater than $V = 1.00$ ms^{-1}. This agreed with the critical Reynolds number identified in Section 3.8. The issues with magnitude of C_T at different carriage velocities drew attention to an issue with the blade thrust instrumentation. The instrument configuration does not prevent out-of-plane bending moments, which are not captured by the hub's instrumentation. This created a velocity dependency in the non-dimensional thrust characteristics. For the aligned case at $V = 1.00$ ms^{-1} the thrust of the turbine was $C_T = 0.87$ at $\lambda = 4$, however it is recognised the issue with all these results remains. The negative yaw angles show a lower torque and power performance drop at the furthest offset, agreeing with CFD outcomes discussed in Section 6.3.

Table 8.2 Maximum percentage change in non-dimensional performance from experimental results

λ = 3.5	**Yaw angle**				
	-20°	**-10°**	**0°**	**+10°**	**+20°**
C_θ - μ	-3.3%	5.2%	0.159	5.9%	-7.2%
C_P - μ	-6.7%	5.5%	0.419	6.3%	-13.6%
C_T – μ	-5.8%	-4.6%	0.865	9.6%	-4.0%

The time averaged yaw angle results showed an increase in C_θ and C_P performance by up to 6% for both at ±10°, in comparison to the aligned case. This was inexplicable, and contrary to expected performance from CFD and theory. Possible causes were suggested as the blade experiencing a rotational period of higher performance due to the change in pitch angle seen through rotation. However this was not identifiable from the temporal results and therefore further work is required.

The temporal results considered were able to identify stanchion interaction with the turbine in the frequency domain. Also identified was the pole pairs in the alternator and a stanchion vibration at certain carriage velocities. Whilst the limitations in the temporal results did not make it directly comparable to transient CFD, the work has shown further effort in this area may provide these temporal features seen in transient CFD analysis in experimental results.

It was shown that correcting for misalignment was not as simple as accounting for the change in the swept area of the turbine as proposed in the hypothesis in Section 3.7. The velocity correction method proved to account for misalignment for C_θ conditions and the area correction method was shown to agree most with aligned conditions for C_P results in misaligned flow. The analysis shows these correction methods could prove useful if testing of a full scale device requires accounting for flow misalignment.

9. Conclusions

The aims and objectives in this work were defined in the Introduction (Section 0.) The work of this thesis was undertaken with the purpose of fulfilling these aims and objectives. This Chapter will consider each objective in turn and summarise the outcomes. Recommendations to industry based upon the work are made and options for furthering the work are outlined with respect to each objective.

9.1. Directionality & Proximity

The first objective was to characterise the turbines performances at varying proximities upstream and downstream of the support structure, through the numerical modelling. This was achieved through four non-dimensional characteristics, the coefficient of torque, power, thrust and out-of-plane bending moment. The peak of these values came from steady state and transient CFD analysis giving $C_\theta = 0.12$, $C_P = 0.45$ and $C_T = 0.85$ and operated over the TSR range of 0-7. These characteristics compared well with those found in published literature for the same geometry.

The primary conclusion of the work revealed that performance of the rotor increased with greater clearance distance of the turbine rotating plane upstream from the stanchion. Whilst this result was expected, the best performance was found to be when the rotor was positioned at greater than 2 stanchion diameters upstream of the support stanchion. This position resulted in a 5.4% drop in C_θ and C_P and a 6.5% reduction in C_T performance at peak power ($\lambda = 3.65$) relative to the no stanchion case. The outcome of this work showed that the greater the clearance distance the better the performance of the rotor. However, the diminishing returns from this increase in clearance showed that for the upstream case a realistic clearance would likely be between 1.5 and 2 stanchion diameters clearance. It was noted from literature (Burton, et al., 2001) that the wind industry sees tower effects on rotor performance and loading at 1 - 1.5 stanchion diameters upstream.

Further investigation into the performance using the transient CFD models showed that consideration of the steady-state results alone do not provide the required information to make an informed decision. The transient results showed nearly 10x greater fluctuations in the torque and power signals during downstream operation. The thrust performance signal featured 40x greater fluctuations. These increases could lead to an accelerated fatigue life, increasing the risk of blade or bearing failure.

The recommendation to industry is therefore to seriously consider the stanchion interaction, because whilst the detrimental performance reduction maybe justifiable, there is a considerable increase in the fluctuating thrust loads on the blades. With regard to array spacing, the wake characteristics from the study found that stanchion proximity and directionality do not significantly affect the wake recovery rate, and so array spacing will not be adversely affected by this.

9.2. Flow Misalignment

The flow misalignment conditions considered include yaw angles of 0˚, ±10˚, ±15˚ and ±20˚. It was found that with greater yaw angles the turbine's non-dimensional performance characteristics dropped. The extreme misalignment angles ($\alpha = \pm 20°$) considered showed that both C_P and C_θ dropped by up to 11.5% whereas C_T only dropped by 6.5% relative to its aligned turbine case. The coefficient of the out-of-plane bending moment showed significant increases in magnitude from its aligned value of $C_M = 0.01$ to more than 200% higher at ±20° yaw angles.

It is recommended that whilst a yawing mechanism is considered by device developers, a passive mechanism has its advantages of being able to be used continually and negate these angles. However for an active yawing mechanism it is recommended that a flow misalignment threshold is considered, and if during the tidal cycle a device experiences extended periods of operation with flow misalignment then the active yawing of the turbine into the flow for this period is maybe justified in order to maintain performance, but more importantly to reduce the out-of-plane bending moments which significantly increase with flow misalignment.

From the work considered it is recommended that a bi-directional device developer without actively pitching blades to compensate for flow misalignment ought to consider sites with ebb-flood cycles that experience little asymmetry. From current projects 10° misalignment has been used as the threshold.

9.3. Experimental Testing

The 1:20th scale (0.5 m diameter) turbine developed for numerical validation was tested in the 220 m towing tank at CNR-INSEAN in Italy. The testing matrix facilitated a full set of non-dimensional curves (C_θ-λ, C_P-λ and C_T-λ) for the aligned turbine testing at 5 independent carriage velocities ($V = 0.5 - 1.5$ ms^{-1}). Then key points on the curves were tested at yaw angles ±10° and ±20°.

The towing tank testing showed that the time averaged non-dimensional characteristics for C_θ and C_P collapse onto one curve for velocities higher than V = 1.00 ms$^{-1,}$ that is the turbine is operating with Reynolds independence. In comparison to the steady state CFD results the C_θ and C_P lay within 15% and 3% at peak values, respectively. The transient CFD points did not reach the peak C_θ values, however at peak C_P was within 6%. The blade thrust instrumentation did not perform as expected causing issues in the blade 1 thrust results. This resulted in the non-dimensional performance characteristics not collapsing onto a single curve, and instead showing velocity dependency. The cause of this was found to be the instrumentation design, which did not mitigate out-of-plane bending moments, and was also not instrumented to account for them.

The time averaged yaw angle results showed an increase in C_θ and C_P performance by up to 6% for both at ±10°, in comparison to the aligned case. The torque performance characteristics dropped at ±20° yaw angles relative to the aligned turbine case, up to 7.2% in the +20° case and 3.3% in the -20° case. The power performance dropped similarly at ±20° yaw angles, up to 13.6% in the +20° case and 6.7% in the -20° case. The lesser performance drop for negative flow misalignment agreed with findings in the CFD study (Chapter 6). The transient CFD results closely matched the experimental results for the ±20° yaw angles. Transient CFD modelling provide vital insight into the physics of misaligned flow and stanchion interaction for tidal turbines, the temporal features are of vital importance to industry as commercial devices near realisation. The drawbacks remain in the computational expense required to deliver transient results. However with ever increasing computational power these drawbacks are being mitigated.

The temporal results found the stanchion interaction and other temporal features were masked in the time domain by the dominant effect of the alternator's pole-pair interaction. The results were therefore transformed into the frequency domain which revealed the stanchion interaction, pole-pair interaction from the alternator and in the case of the V = 1.00 ms^{-1} cases there was a stanchion vibration also found.

The recommendation to industry from the experimental testing, highlights the continued need of numerical model validation and shows that the experimental non-dimensional performance of tidal stream turbines at 1:20th scale agree reasonably well to full scale transient CFD results, when it is operating within the critical Reynolds number range. Steady state CFD models in aligned flow performed similarly to the experimental turbine. However Due to the recognised limitations of steady-state numerical modelling, it is recommended that developers adopt the common approach of steady-state modelling during the design stage where a number of geometrical concepts will be present. Then as the process draws toward a final design adopt transient modelling to gain further insight and final assessments for predicting performance.

9.4.Further Work

Further research opportunities were identified throughout this thesis. The validation between CFD and experimental results identified a closer agreement with transient CFD results for flow misalignment cases. The transient CFD analysis for flow misalignment was limited to one tip speed ratio ($\lambda = 3.65$). Further transient studies at key tip speed ratios such as $\lambda = 2.5$ and $\lambda = 5$ or $\lambda = 6$ would confirm that the transient performance agrees throughout the non-dimensional performance curves. Experimental work was conducted at ±10° and ±20° yaw angles, repeating this study at additional yaw angles such as ±5° and ±15° would provide further insight into the unexpected results at ±10°.

Further work must also be undertaken on the instrumented hub design, as the issue has been deemed to be both mechanically and electronically limited. Mechanically the slot in which the blade is secured does not move in pure translation with the onset of thrust on the blades. The inclusion of bending moments is likely to be present, and this requires eliminating or capturing with additional strain gauge flexures. The electronic limitations are a result of insufficient baud rate and bit size to store sufficient resolution in the nose cone Arduino. Increasing this capability will reduce the banding in the results and provide further insight into blade loading performance.

The work presented in this thesis is a contribution to a growing body of knowledge in the sector of tidal energy. As recognised at the start of this work, the need of renewable energy is great and tidal energy offers a significant and predictable supply globally. It is a pioneering technology that has the potential to deliver at the utility scale. In order for the technology to achieve this full potential the tidal energy community must continue to collaborate and strive to de-risk the sector through critical research and development.

References

Abbott, I. H. & Von Doenhoff, A. E., 1949. *Theory of Wing Sections.* New York: Dover Publications.

Ali, M. H., 2013. Experimental Comparison Study for Savonius Wind Turbine of Two & Three Blades At Low Wind Speed. *International Journal of Modern Engineering Research (IJMER),* 3(5), pp. 2978-2986.

Allmark, M. J., 2016. Condition Monitoring and Fault Diagnosis of Tidal Stream Turbines Subjected to Rotor Imbalance Faults. *Cardiff University.*

Allmark, M. J., 2016. *Perosnal Correspondance.* Cardiff: s.n.

Alstom Ocean Energy, 2013. *Press Centre.* [Online] Available at: http://www.alstom.com/press-centre/2013/7/alstoms-tidal-turbine-reaches-1mw-in-offshore-conditions/

Ansys, 2015. *Ansys CFX Help,* s.l.: s.n.

ASM International, 2008. Fatigue. In: *Elements of Metallurgy and Engineering Alloys.* Ohio: ASM International, pp. 243-264.

Bahaj, A. S., Molland, A. F., Chaplin, J. R. & Batten, W. M. J., 2007. Power and thrust measurements of marine current turbines under various hydrodynamic flow conditions in a cavitation tunnel and a towing tank. *Renewable Energy,* 32(3), pp. 407-426.

Bahaj, A. S. & Myers, L. E., 2013. Shaping array design of marine current energy converters through scaled experimental analysis. *Energy,* Volume 59, pp. 83-94.

Batten, W. M., Bahaj, A. S., Molland, A. F. & Chaplin, J. R., 2007. Experimentally validated numerical method for the hydrodynamic design of horizontal axis tidal turbines. *Ocean Engineering,* 34(7).

Black & Veatch, 2004. *UK, Europe and Global Tidal Stream Energy Resource Assessment,* London: Carbon Trust.

Black & Veatch, 2005. *Phase II - UK Tidal Stream Energy Resource Assessment,* London: Carbon Trust.

Blevins, R. D., 2001. *Formulas for Natural Frequency and Mode Shape.* s.l.:Krieger Publishing Company.

Blue Energy, 2016. *Vertical Axis Hydro Turbine.* [Online] Available at: http://www.bluenergy.com/technology_method_vaht.html

Bosch-Rexroth, 2015. *Rexroth IndraDyn T Synchronous Torque Motors.* [Online] Available at: ftp://ftp.boschrexroth.pl/brc/Motors/mbt.pdf

Bossanyi, E., 1997. *Bladed for windows theory manual.* Bristol: Garrad Hassan and Partners Limited.

Boyle, G. e., 2012. *Renewable Energy: Power for a Sustainable Future.* Oxford: Oxford University Press and Open University.

Burton, T., Sharpe, D., Jenkins, N. & Bossanyi, E., 2001. *Wind Energy Handbook.* Chichester: John Wiley & Sons Ltd.

Cape Sharp Tidal, 2015. *SUBSEA CABLE INSTALLATION AND DEPLOYMENT BARGE LAUNCHED.* [Online] Available at: http://capesharptidal.com/nov10/

Church, J. P. C. A. C. J. G. S. J. A. L. M. M. G. M. R., 2013. *Sea Level Change. In: Climate Change 2013: The Physical Science Basis. Contribution of Working Group I to the Fifth Assessment Report of the Intergovernmental Panel on Climate Change,* Cambridge and New York: Cambridge University Press.

CNR-INSEAN, 2002. *Marine Technology Research Institute INSEAN.* [Online] Available at: insean.cnr.it
[Accessed 16 10 2015].

Coleman, H. W. & Steele, W. G., 2009. Errors and uncertainty in a measured variable. In: *Experimentation, validation and uncertainty analysis for engineers.* New Jersey: John Wiley & Sons, pp. 29-60.

CorPower Ocean, 2012. *The CorPower Wave Energy Converter.* [Online] Available at: http://www.corpowerocean.com/corpower-technology/corpower-wave-energy-converter/
[Accessed 26 09 2016].

Day, A. et al., 2015. Hydrodynamic modelling of marine renewable energy devices: A state of the art review. *Ocean Engineering,* pp. 46-69.

DECC, 2012. *Electricity Generation Costs,* London: Department of Energy and Climate Change.

DECC, 2013. *UK Renewable Energy Roadmap Update,* London: Crown Copyright.

DECC, 2015. *Fuelling the Debate: Committee Success and Future Challenges,* London: s.n.

DECC, 2015. *Swansea Bay Tidal Lagoon: potential support for the project through the CFD mechanism,* London: Crown Copyright.

DECC, 2016. *Review of Tidal Lagoons.* [Online] Available at: https://www.gov.uk/government/news/review-of-tidal-lagoons

Doman, D. et al., 2015. Tow-tank Testing of a 1/20th Scale Horizontal Axis Tidal Turbine with Uncertainty Analysis. *International Journal of Marine Energy,* pp. 105-119.

DTI, 2005. *Dvelelopment, installation and testing of a large-scale tidal current turbine,* s.l.: Crown Copyright.

E.ON Energy, 2011. *Ofgem's five year strategy 2011 – 2016,* London: Ofgem.

Easton, M. C., Woolf, D. K. & Pans, S., 2010. *An operational hydrodynamic model of a key tidal-energy site: Inner Sound of Stroma, Pentland Firth (Scotland, UK).* Bilboa, Spain, s.n.

Edmunds, M. et al., 2014. Aspects of Tidal Stream Turbine Modelling in the Natural Environment Using a Coupled BEM-CFD Model. *International Journal of Marine Energy,* Volume 7, pp. 20-42.

Egarr, D. A., O'Doherty, T., Morris, S. & Ayre, R. G., 2004. *Feasibility study using Computational Fluid Dynamics for the use of a turbine for extracting energy from the tide.* Sydney, s.n.

Eling Experience, 2015. *The Eling Experience Project.* [Online] Available at: elingexperience.co.uk [Accessed 19 09 2016].

Energy Technologies Institute , 2015. *Tidal Energy: Insight into Tidal Stream Energy,* Loughborough: ETI.

ETSU, 1993. *Tidal Stream Energy Review,* London: s.n.

European Environment Agency, 2015. *Rising sea surface temperature: towards ice-free Arctic summers and a changing marine food chain.* [Online] Available at: http://www.eea.europa.eu/themes/coast_sea/sea-surface-temperature/rising-temp#full-eea-report

European Marine Energy Centre, 2016. *Tidal Developers.* [Online] Available at: http://www.emec.org.uk/marine-energy/tidal-developers/

European Wind Energy Associsation, 2014. *Wind energy's frequently asked questions.* [Online] Available at: http://www.ewea.org/wind-energy-basics/faq/ [Accessed 26 09 2016].

Fairley, I. et al., 2013. Evaluation of tidal stream resource in a potential array area via direct measurments. *Renewable Energy,* pp. 70-78.

Fewings, A. D. et al., 2014. *Application Performance on HPC Wales' Westmere and Sandy Bridge System,* s.l.: HPCW.

Frost, C. H. et al., 2015. The Effect of Tidal Flow Directionality on Tidal Turbine Performance Characteristics. *Renewable Energy,* Volume 78, pp. 609-620.

Galloway, P. W., Myers, L. E. & Bahaj, A. S., 2014. Quantifying wave and yaw effects on a scale tidal stream turbine. *Renewable Energy,* pp. 297-307.

Gaurier, B., Davies, P., Deuff, A. & Germain, G., 2013. Flume tank characterization of marine current turbine blade behaviour under current and wave loading. *Renewable Energy,* Volume 59, pp. 1-12.

Gaurier, B. et al., 2015. Tidal energy ''Round Robin'' tests comparisons between towing tank and circulating tank results. *Intnaional Journal of Marine Energy,* pp. 87-108.

Gaurier, B. et al., 2015. *Tidal energy "Round Robin" tests comparisons between towing tank and circulating tank results.* s.l.:International Journal of Marine Energy.

GOV.UK, September 2015. *UK energy statistics: statistical press release,* London: UK Gov.

Haddon, J., Smith, J., Krog, A. & Scandling, E., 2011. *First Installation at London Array.* [Online] Available at: http://www.londonarray.com/wp-content/uploads/First-foundation-installed-at-London-Array.pdf

Hansen, M., 2001. *Aerodynamics of Wind Turbines : Rotors, Loads and Structure.* London: James & James (Science Publishers) Ltd.

Harding, S. F. & Bryden, I. G., n.d. Directionality in prospective Northern UK tidal current energy deployment sites. *Renewable Energy,* pp. 474-477.

Harper, S., Pittam, G. & Harrison, J., 2015. *Tidal Turbine and Foundation Load Limiting Controller.* Nantes, France, s.n.

Hau, E., 2006. Wind Turbines: Fundamentals, Technologies, Application, Economics (2nd Edition). *Springer.*

Heidenhain, 2014. *EQN 425 Product Information,* s.l.: Heidenhain.

Hydrovolts Inc, 2012. *C-12 Canal Turbine.* [Online] Available at: http://hydrovolts.com/wp-content/uploads/2012/04/Hydrovolts_C-12-Canal-Turbine.pdf

IEA, 2016. *Energy Security.* [Online] Available at: http://www.iea.org/topics/energysecurity/ [Accessed December 2016].

IEC 62600-200, 2012. Power Performance Assessment of Electricity Producing Tidal Energy Converters. *International Elecrotechnical Commission.*

International Renewable energy Agency, 2014. *Tidal Energy: Technology Brief,* s.l.: IRENA.

ITTC, 2008. Uncertainty Analysis - Instrument Calibration. *Recommended Procedures and Guidlines.*

Iyer, A. S., Couch, S. J., Harrison, G. P. & Wallace, A. R., 2013. Variability and phasing ot tidal current energy around the UK. *Renewable Energy,* pp. 343-357.

Jannson, A., n.d. *KIC InnoEnergy.* [Online] Available at: http://www.kic-innoenergy.com/innovationproject/our-innovation-projects/deepgreen500/
[Accessed 23 May 2016].

Jeffcoate, P., Elsaesser, B., Whittaker, T. & Boake, C., 2014. *Testing Tidal Turbines - Part 1: Steady Towing Tests vs Tidal.* Glasgow, QUB.

Jeffcoate, P., 2014. *Betz Limit and Blade Element Momentum Theory Lecture,* Belfast: QUeens University Belfast.

Jeffcoate, P. et al., 2015. Field measurements of a full scale tidal turbine. *International Journal of Marine Energy,* Volume 12, pp. 3-20.

Jeffcoate, P., Whittaker, T. & Elsaesser, B., 2015. Field tests of multiple 1/10th scale tidal turbine devices in steady flows. *Renewable Energy.*

Journee, J. & Massie, W., 2001. *Offshore Hydrodynamics.* Delft : Delft University of Technology.

Kepler Energy - Press Release, 2016. *Kepler Energy - Press Release.* [Online] Available at: http://www.keplerenergy.co.uk/press-release.html

Lewis, M., Neill, S. P., Robins, P. E. & Hashemi, M. R., 2015. Resource assessment for future generations of tidal-stream energy arrays. *Energy,* pp. 403-415.

Lynn, P. A., 2014. *Electricity from wave and tide.* London: Wiley.

Malki, R. et al., 2013. A coupled blade element momentum – Computational fluid dynamics model for evaluating tidal stream turbine performance. *Applied Mathematical Modelling,* Volume 37, pp. 3006-3020.

Manwell, J., McGowan, J. & Rogers, A., 2009. *WInd energy explained: Theory design and application.* s.l.:John Wiley & Sons Ltd.

MaRINET FP7, n.d. *Transnational Access - Facilities Available.* [Online] Available at: fp7-marinet.eu/CNR-INSEAN-wave-tank.html
[Accessed 16 10 2015].

Mason-Jones, A., 2010. *PhD Thesis.* s.l., s.n.

Mason-Jones, A., O'Doherty, D. M., Morris, C. E. & O'Doherty, T., 2013. Influence of a Velocity Profile & Support Structure on Tidal Stream Turbine Performance.. *Renewable Energy,* Volume 52, pp. 23-30.

Mason-Jones, A. et al., 2012. Non-dimensional Scaling of Tidal Stream Turbines. *Energy,* Volume 44, pp. 820-829.

Matlab, 2015. *Matlab Help Documnetation.* s.l.:The MathWorks, Inc..

McAdams, R. A., 2012. Studies into the technical feasibility of the transverse horizontal axis water turbine. *PhD Thesis.*

McAdams, R. A., Houlsby, G. T. & Oldfield, M. L. G., 2013. Experimental measurments of the hydrodynamic performance and structural loading of the transverse horizontal axis water turbine: part 1. *Renewable Energy,* pp. 105-114.

Menter, F. R., 1994. Two-equation eddy-viscosity turbulence models for engineering applications. *AIAA-Journal,* pp. 1598-1605.

Minesto, 2016. *Deep Green Technology.* [Online]
Available at: http://minesto.com/deep-green/

Morris, C., 2014. *Influence of Solidity on the Performance, Swirl Characteristics, Wake Recovery and Blade Deflection of a Horizontal Axis Tidal Turbine.* Cardiff: Cardiff University.

Muljadi, E. & Butterfield, C. P., 2000. Pitch-Controlled Variable-Speed Wind Turbine Generation. *National Renewable Energy Laboratory, ,* NREL/CP-500-27143(1999 IEEE Industry Applications).

NASA, n.d. *Definition of Technology Readiness Levels.* [Online]
Available at: esto.nasa.gov/files/trl_definitions.pdf
[Accessed 16 10 2015].

Nautricity, 2013. *Proving CoRMaT.* [Online]
Available at: http://www.nautricity.com/cormat/cormat-reliability/

Nevalainen, T. M., Johnstone, C. M. & Grant, A. D., 2016. A sensitivity analysis on tidal stream turbine loads caused by operational, geometric design and inflow parameters. *International Journal of Marine Energy,* Volume 16, pp. 51-64.

New Energy Cooperation, 2011. *Chilla Canal, India - March.* [Online]
Available at: http://www.newenergycorp.ca/2011.html
[Accessed December 2016].

Nicholas-Lee, R. F. & Turnock, S. R., 2008. Tidal energy extraction: renewable, sustainable and predictable. *Science Progress,* 91(1), pp. 81-111.

Nuclear Energy Agency, 2014. *Nuclear Energy Agency Press Room.* [Online]
Available at: https://www.oecd-nea.org/news/press-kits/economics-FAQ.html
[Accessed 09 26 2016].

O'DOherty, T. et al., 2010. Considerations of a horizontal axis tidal turbine. *Proceedings of the Institution of Civil Engineers,* 163(3), p. 119–130 .

Offshore-Technology, 2012. *Healthy competition: demand grows for specialised offshore vessels.* [Online]
Available at: http://www.offshore-technology.com/features/featureoperation-maintenance-offshore-wind-oil-gas-hydrocarbons-installed-capacity-wind-farm-specialised-resources-ship-boat-vessel-installation/
[Accessed 25 May 2016].

OfGEM, 2014. *Written Evidence submitted by OfGEM,* London: (LGY0023).

Olczak, A., Stallard, T., Feng, T. & Stansby, P. K., 2016. Comparison of a RANS blade element model for tidal turbine arrays with laboratory scale measurements of wake velocity and rotor thrust. *Journal of Fluids and Structures ,* Volume 64, pp. 87-106.

Park, S. W., Park, S. & Rhee, S. H., 2013. *Performance Predictions of a Horizontal Axis Tidal Stream Turbine.* Tasmania, Third International Symposium on Marine Propulsors.

Ragheb, M. & Ragheb, A., 2011. *Wind Turbines Theory - The Betz Equation and Optimal Rotor Tip Speed Ratio,* s.l.: InTech.

RenewableUK, 2015. *Wind Energy in the UK,* London: RenewableUK.

Retiere, C., 1994. Tidal power and the aquatic environment of La Rance. *Biological Journal of the Linnean Society,* pp. 25-36.

S P Neill, M. R. H. M. J. L., 2016. Tidal energy leasing and tidal phasing. *Renewable Energy,* pp. 580-587.

Schottel, 2016. *Schottel Instream Turbine.* [Online]
Available at: http://www.schottel.de/schottel-hydro/sit-instream-turbine/

Shafiee, M. & Dinmohammadi, F., 1996. An FMEA-Based Risk Assessment Approach for Wind TurbineSystems. *Energies,* pp. 916-642.

Strathclyde University, 2013. *Tidal Stream Energy: Toards Reliability.* [Online]
Available at: http://www.esru.strath.ac.uk/EandE/Web_sites/12-13/Tidal_stream_energy/env2.html

SubSea World News, 2015. *Swansea Bay Tidal Lagoon Commercial Negotiations Start.* [Online]
Available at: http://subseaworldnews.com/2015/03/18/swansea-bay-tidal-lagoon-commercial-negotiations-start/
[Accessed December 2016].

Sustainable Marine Energy, 2016. *SME Technology.* [Online]
Available at: http://sustainablemarine.com/#technology

Tatum , S. et al., 2015. *Modelling Tidal Stream Turbines.* London, Conference Procedings at World Renewable Energy Consortium.

Tedds, S. et al., 2011. *Experimental Investigation of Horizontal Axis Tidal Stream Turbines.* Southampton, s.n.

Thomson, J., Polagye, B., Durgesh, V. & Richmond, M. C., 2012. Measurements of Turbulence at Two Tidal Energy Sites in Puget Sound, WA. *Journal of Ocean Engineering,* 37(3).

Tidal Energy Ltd, 2016. *Ramsey Sound.* [Online]
Available at: http://www.tidalenergyltd.com/?page_id=650

Tidal Lagoon Swansea Bay , 2015. [Online]
Available at: http://www.tidallagoonswanseabay.com/

UK Gov., 2008. *Climate Change Act,* s.l.: s.n.

UK Science and Technology Committee, 2015. *The Resilience of the Electricity System,* London: Parliamentary copyright 2015.

United Nations, 2012. *Cancun Agreements.* [Online]
Available at: http://unfccc.int/key_steps/cancun_agreements/items/6132.php

Univeristy of Strathclyde, 2012. *Kelvin Hydrodynamics Laboratory.* [Online]
Available at: https://www.strath.ac.uk/engineering/navalarchitectureoceanmarineengineering/ourfacilities/kelvinhydrodynamicslaboratory/
[Accessed 27 09 2016].

Versteeg, H. & Malalaserekera, W., 1995. *An Introduction to Computational Fluid Dynamics.* London: Longman Group Ltd.

Walker, S., 2014. Hydrodynamic interaction of a tidal stream turbine and support structure. *PhD Thesis.*

Walker, S. R., Howell, R. & Cappietti, L., 2015. Optimising the Design of a Tidal Stream Turbine Support Structure for Improved Turbine Performance. *11th European Wave and Tidal Energy Conference.*

Wello, 2012. *The Penguin Wave Energy Converter.* [Online]
Available at: http://www.wello.eu/en/penguin
[Accessed 26 09 2016].

Whelan, J., Graham, J. & Peiro, J., 2009. A free-surface and blockage correction for tidal turbines. *Journal of Fluid Mechanics,* pp. 281-291.

Whittaker, T. J. T. et al., 2002. *ISLAY LIMPET WAVE POWER PLANT,* QUB: Queens Univeristy Belfast.

Wilcox, D., 1986. *Multiscale model for turbulent flows,* s.l.: American Institute of Aeronautics and Astronautics.

Appendix

A. Wortmann FX63-137

The Wortmann FX63-137 blade profile used is shown in Figure 0.1 with nominal chord length and relative thickness.

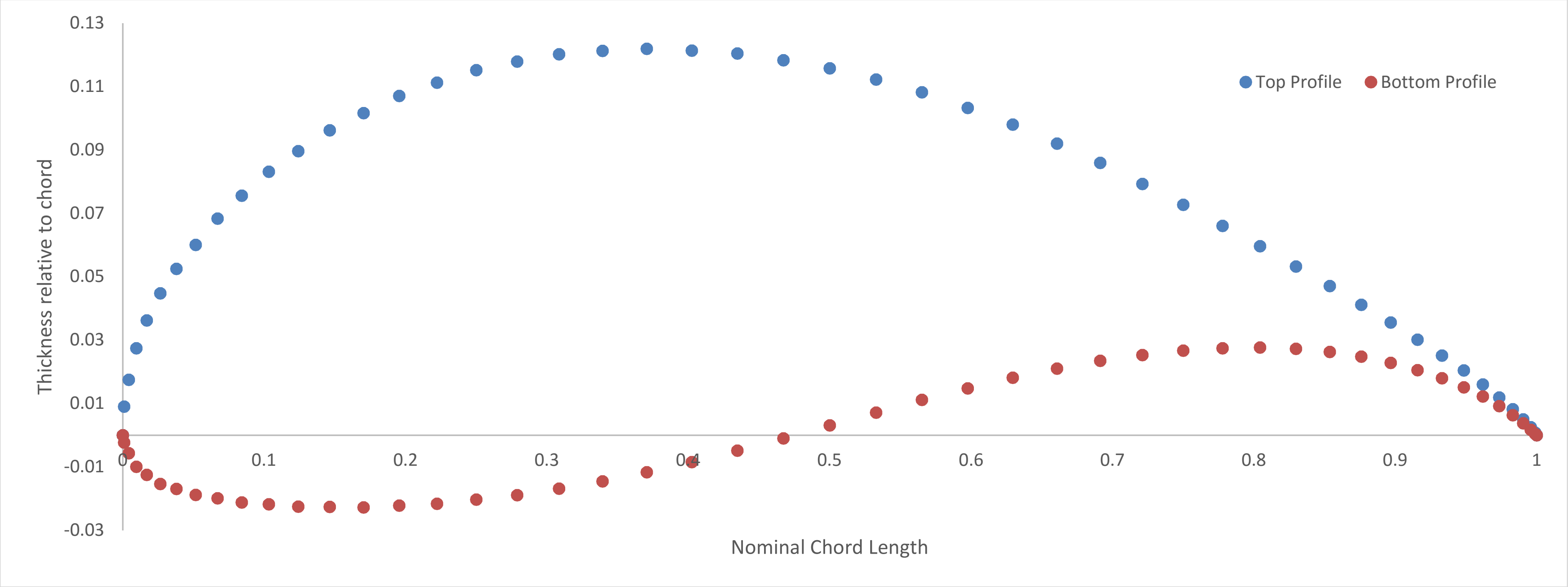

Figure 0.1 FX63-137 Blade Profile relative to Chord Length

Table 0.1 Reynolds Number Parameters at various r/R values

Turbine Scale	r/R	Turbine Diameter, D = 2R(m)	Chord Length, $C_{r/R}$ (m)	Velocity, V (ms^{-1})	Tangential Velocity at peak power, U_T (ms^{-1})	Resultant Velocity, $U_{r/R}$ (ms^{-1})	Resultant Direction, $\theta_{r/R}$ (°)	Blade Pitch angle, $\beta_{0.7}$ (°)	Angle of Attack, α (°)	Diameter-based Reynolds Number	Chord-based Reynolds Number
1:1	0.7	10	0.896	3.09	7.80	8.39	68.41	11.00	10.59	2.36E+07	5.74E+06
1:20		0.5	0.047	0.50	1.26	1.36	68.41	11.00	10.59	1.91E+05	4.88E+04
			0.047	0.75	1.90	2.04	68.41	11.00	10.59	2.86E+05	7.32E+04
			0.047	1.00	2.53	2.72	68.41	11.00	10.59	3.82E+05	9.76E+04
			0.047	1.25	3.16	3.40	68.41	11.00	10.59	4.77E+05	1.22E+05
			0.047	1.50	3.79	4.08	68.41	11.00	10.59	5.73E+05	1.46E+05
1:1	0.8	10	0.767	3.09	8.91	9.43	70.90	8.20	10.90	2.36E+07	5.52E+06
1:20		0.5	0.041	0.50	1.44	1.53	70.90	8.20	10.90	1.91E+05	4.78E+04
			0.041	0.75	2.17	2.29	70.90	8.20	10.90	2.86E+05	7.18E+04
			0.041	1.00	2.89	3.06	70.90	8.20	10.90	3.82E+05	9.57E+04
			0.041	1.25	3.61	3.82	70.90	8.20	10.90	4.77E+05	1.20E+05
			0.041	1.50	4.33	4.58	70.90	8.20	10.90	5.73E+05	1.44E+05
1:1	0.9	10	0.683	3.09	10.03	10.49	72.89	6.46	10.65	2.36E+07	5.47E+06
1:20		0.5	0.037	0.50	1.62	1.70	72.89	6.46	10.65	1.91E+05	4.80E+04
			0.037	0.75	2.44	2.55	72.89	6.46	10.65	2.86E+05	7.20E+04
			0.037	1.00	3.25	3.40	72.89	6.46	10.65	3.82E+05	9.61E+04
			0.037	1.25	4.06	4.25	72.89	6.46	10.65	4.77E+05	1.20E+05
			0.037	1.50	4.87	5.10	72.89	6.46	10.65	5.73E+05	1.44E+05

Profile Performance Characteristics

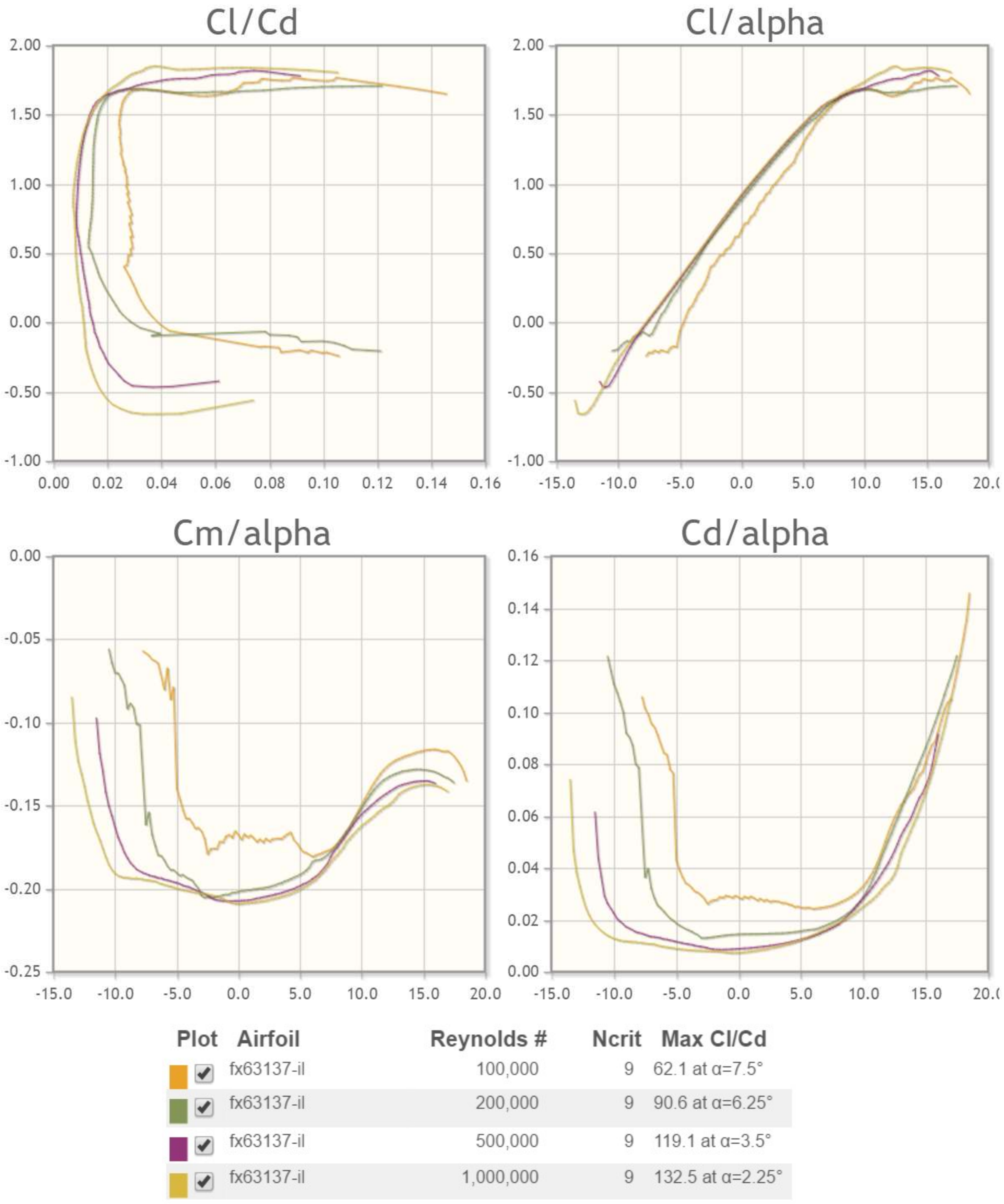

Plot		Airfoil	Reynolds #	Ncrit	Max Cl/Cd
🟧	☑	fx63137-il	100,000	9	62.1 at α=7.5°
🟩	☑	fx63137-il	200,000	9	90.6 at α=6.25°
🟪	☑	fx63137-il	500,000	9	119.1 at α=3.5°
🟨	☑	fx63137-il	1,000,000	9	132.5 at α=2.25°

Figure 0.2 FX63-137 performance characteristics from xfoil software

B. Thrust Gauge Calibration

Equipment

- Field Laptop with Labview
- Labview script for recording thrust measurements
- Instrumented Hub
- G-Clamps x2
- Metal bar, L = 230 mm D= 15 mm
- 10 kg of hanging weights (mix of sizes)
- Volt meter
- Weighing scales (up to 2 kg)

Set-up

1. Load laptop and labview program
2. Communicate with SG
3. Record SG measurements.
4. Clamp SG to the worktop (Figure…)
5. Record SG measurement
6. Weigh metal bar (0.3 kg)
7. Insert and secure metal bar (Figure…)
8. Adjust grub screw to appropriate sensitivity (point at which negative load applied still registers a voltage reading).
9. Record SG measurement (this will be required to yaw angle against the rest of the results/zero the data)

Methodology

1. Take zero reading
2. Apply 0.5 kg mass at set distance from root
3. Record SG measurements
4. Add 0.5 kg mass to hanger
5. Record SG measurements
6. Repeat steps 5 and 6 till maximum load of 8 kg reached
7. Unload 0.5 kg mass from hanger
8. Record SG measurements
9. Repeat steps 8 and 9 till unloaded
10. Repeat with next set distance from root along until the complete length has been done
11. Repeat full set x 3

Checking for drift:

Add mass to r/R = Centre of Pressure (from CFD)

Set recorder over lunch period (~ 1 hr) to detect drift/ settling issues.

C. Test Matrix

Table 0.2 CNR-INSEAN Test Schedule

Date:	05/06/2015	08/06/2015	09/06/2015	10/06/2015	11/06/2015	12/06/2015
Attendees:	Matthew Allmark	Carwyn Frost	Carwyn Frost	Carwyn Frost	Carwyn Frost	Carwyn Frost
	Carwyn Frost	Tim O'Doherty	Tim O'Doherty	Tim O'Doherty	Tim O'Doherty	Tim O'Doherty
	Kate Porter	Kate Porter	Kate Porter	Kate Porter	Kate Porter	Kate Porter
		Cameron Johnstone	Cameron Johnstone	Cameron Johnstone	Cameron Johnstone	
Carriage Instrumentation:	Non	Non	Pieto Static Tube	Pieto Static Tube, Wave Height	Pieto Static Tube, Wave Height	Non
8am-10am	Arrival and Introduction to INSEAN	Arrival and Introductions, Setup	Setup, V= 1 ms-1 V= 1.5 ms-1	Wave Probe Setup Test Setup V= 0.5 ms-1 Wave Form 1	V= 1 ms-1 +10°	V= 0.5 ms-1 V= 0.75 ms-1 V= 1.25 ms-1
10am-1pm	Unpacking and Commissioning	Low RPM Tests	V= 0.5 ms-1 V= 0.75 ms-1 V= 1.25 ms-1		V= 1.5 ms-1 +10° V= 1 ms-1 Wave Form 1	V= 1 ms-1 -10° V= 1 ms-1 12° Pitch
2pm-4pm	Dry/Wet Test	V= 1 ms-1 Tests	V= 1 ms-1 +20° V= 1.5 ms-1 +20°	V= 1 ms-1 Wave Form 1	V= 0.5 ms-1 Wave Form 1 V= 1 ms-1 Wave Form 2 V= 0.5 ms-1 Wave Form 2	V= 1.5 ms-1 12° Pitch
4pm-6pm	NA		V= 1 ms-1 -20° V= 1.5 ms-1 -20°	No Carriage Driver	V= 0.5 ms-1 Wave Form 3 V= 1 ms-1 Wave Form 3 V= 1 ms-1 Wave Form 1 - Torque Ctrl	Decommissioning and Packing
Note:	All tests were performed for a range of λ's, from 1.5 to 5.5			Summary:		
	Wave Form 1:	Height = 0.4 m	Time Period = 2 s	Total number of test run:		107
	Wave Form 2:	Height = 0.3 m	Time Period = 2 s	Total distance travelled:		15840
	Wave Form 3:	Height = 0.2 m	Time Period = 2 s	Total operating time of turbine:		34.5

Table 0.3 CNR-INSEAN Completed Test Matrix Part 1

Key		Case 1:	Aligned Turbine, Blades at 6° Pitch angle, No Waves				Case 2:	+20° Yawed Turbine, Blades at 6° Pitch angle, No Waves				Case 3:	-20° Yawed Turbine, Blades at 6° Pitch angle, No Waves		
🟩 **Completed**		Carriage Speed (m/s)					Carriage Speed (m/s)					Carriage Speed (m/s)			
🟥 **Not Completed**		0.5	0.75	1	1.25	1.5	0.5	0.75	1	1.25	1.5	0.5	0.75	1	1.25
TSR	1.5	🟩 28.65	🟥 42.97	🟩 57.30	🟥 71.62	🟩 85.94	🟥 28.65	🟥 42.97	🟩 57.30	🟥 71.62	🟥 85.94	🟥 28.65	🟥 42.97	🟩 57.30	🟥 71.62
	2.5	🟩 47.75	🟩 71.62	🟩 95.49	🟩 119.37	🟩 143.24	🟥 47.75	🟥 71.62	🟩 95.49	🟥 119.37	🟩 143.24	🟥 47.75	🟥 71.62	🟩 95.49	🟥 119.37
	3	🟩 57.30	🟩 85.94	🟩 114.59	🟩 143.24	🟩 171.89	🟥 57.30	🟥 85.94	🟩 114.59	🟥 143.24	🟥 171.89	🟥 57.30	🟥 85.94	🟩 114.59	🟥 143.24
	3.5	🟩 66.85	🟩 100.27	🟩 133.69	🟩 167.11	🟩 200.54	🟥 66.85	🟥 100.27	🟩 133.69	🟥 167.11	🟩 200.54	🟥 66.85	🟥 100.27	🟩 133.69	🟥 167.11
	4	🟩 76.39	🟩 114.59	🟩 152.79	🟩 190.99	🟩 229.18	🟥 76.39	🟥 114.59	🟩 152.79	🟥 190.99	🟩 229.18	🟥 76.39	🟥 114.59	🟩 152.79	🟥 190.99
	4.5	🟩 85.94	🟩 128.92	🟩 171.89	🟩 214.86	🟩 257.83	🟥 85.94	🟥 128.92	🟩 171.89	🟥 214.86	🟥 257.83	🟥 85.94	🟥 128.92	🟩 171.89	🟥 214.86
	5.5	🟩 105.04	🟩 157.56	🟩 210.08	🟩 262.61	🟩 315.13	🟥 105.04	🟥 157.56	🟩 210.08	🟥 262.61	🟥 315.13	🟥 105.04	🟥 157.56	🟩 210.08	🟥 262.61

Table 0.4 CNR-INSEAN Completed Test Matrix Part 2

Key		Case 4:	+10° Yawed Turbine, Blades at 6° Pitch, No Waves				Case 5:	-10° Yawed Turbine, Blades at 6° Pitch, No Waves				Case 6:	Aligned Turbine, Blade 1 at 12° Pitch, Blades 2 & 3 at 6° Pitch, No Waves		
🟩 **Completed**		Carriage Speed (m/s)					Carriage Speed (m/s)					Carriage Speed (m/s)			
🟥 **Not Completed**		0.5	0.75	1	1.25	1.5	0.5	0.75	1	1.25	1.5	0.5	0.75	1	1.25
TSR	1.5	🟥 28.65	🟥 42.97	🟩 57.30	🟥 71.62	🟥 85.94	🟥 28.65	🟥 42.97	🟩 57.30	🟥 71.62	🟥 85.94	🟥 28.65	🟥 42.97	🟩 57.30	🟥 71.62
	2.5	🟥 47.75	🟥 71.62	🟩 95.49	🟥 119.37	🟩 143.24	🟥 47.75	🟥 71.62	🟩 95.49	🟥 119.37	🟩 143.24	🟥 47.75	🟥 71.62	🟩 95.49	🟥 119.37
	3	🟥 57.30	🟥 85.94	🟩 114.59	🟥 143.24	🟥 171.89	🟥 57.30	🟥 85.94	🟩 114.59	🟥 143.24	🟥 171.89	🟥 57.30	🟥 85.94	🟩 114.59	🟥 143.24
	3.5	🟥 66.85	🟥 100.27	🟩 133.69	🟥 167.11	🟩 200.54	🟥 66.85	🟥 100.27	🟩 133.69	🟥 167.11	🟩 200.54	🟥 66.85	🟥 100.27	🟩 133.69	🟥 167.11
	4	🟥 76.39	🟥 114.59	🟩 152.79	🟥 190.99	🟩 229.18	🟥 76.39	🟥 114.59	🟩 152.79	🟥 190.99	🟩 229.18	🟥 76.39	🟥 114.59	🟩 152.79	🟥 190.99
	4.5	🟥 85.94	🟥 128.92	🟩 171.89	🟥 214.86	🟥 257.83	🟥 85.94	🟥 128.92	🟩 171.89	🟥 214.86	🟥 257.83	🟥 85.94	🟥 128.92	🟩 171.89	🟥 214.86
	5.5	🟥 105.04	🟥 157.56	🟩 210.08	🟥 262.61	🟥 315.13	🟥 105.04	🟥 157.56	🟩 210.08	🟥 262.61	🟥 315.13	🟥 105.04	🟥 157.56	🟩 210.08	🟥 262.61

Table 0.5 CNR-INSEAN Completed Test Matrix Part 3

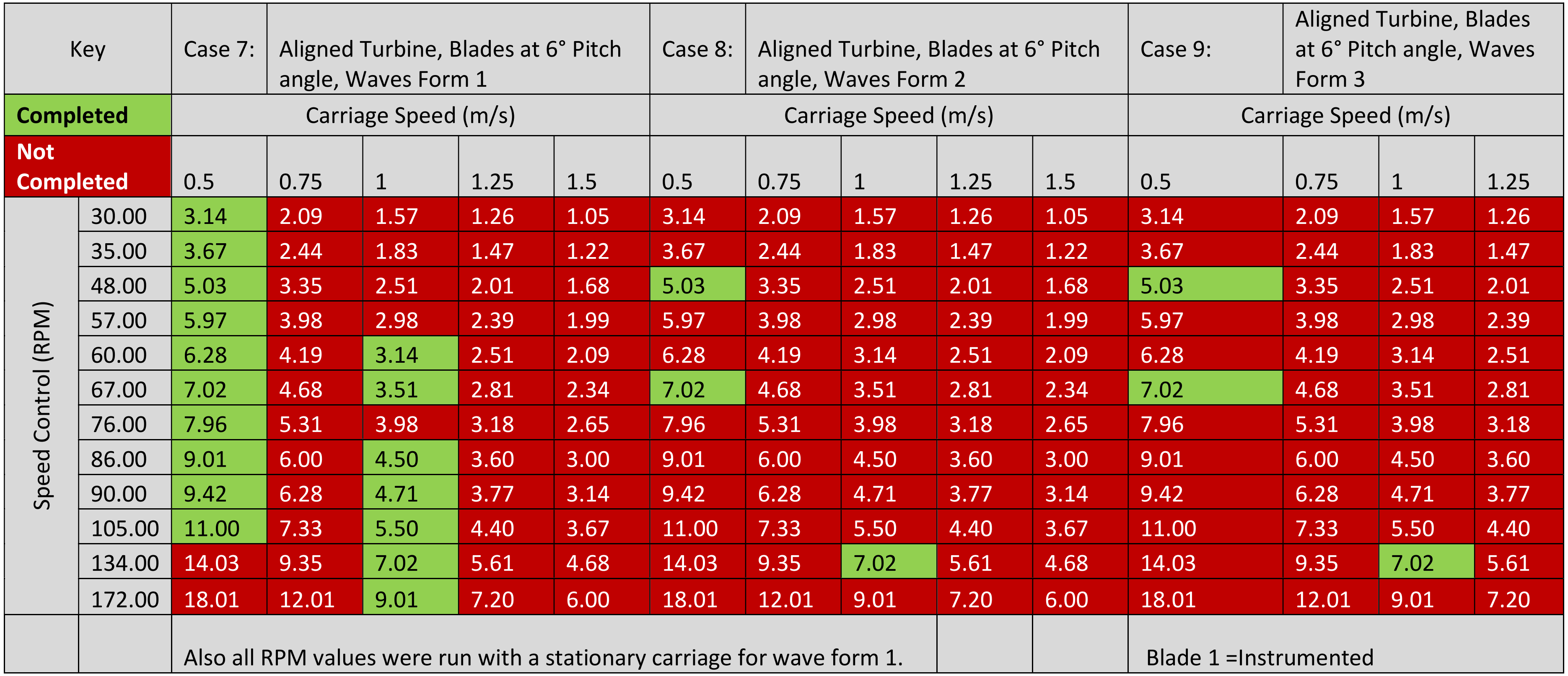

Key		Case 7:	Aligned Turbine, Blades at 6° Pitch angle, Waves Form 1				Case 8:	Aligned Turbine, Blades at 6° Pitch angle, Waves Form 2				Case 9:	Aligned Turbine, Blades at 6° Pitch angle, Waves Form 3		
Completed		Carriage Speed (m/s)					Carriage Speed (m/s)					Carriage Speed (m/s)			
Not Completed		0.5	0.75	1	1.25	1.5	0.5	0.75	1	1.25	1.5	0.5	0.75	1	1.25
Speed Control (RPM)	30.00	3.14	2.09	1.57	1.26	1.05	3.14	2.09	1.57	1.26	1.05	3.14	2.09	1.57	1.26
	35.00	3.67	2.44	1.83	1.47	1.22	3.67	2.44	1.83	1.47	1.22	3.67	2.44	1.83	1.47
	48.00	5.03	3.35	2.51	2.01	1.68	5.03	3.35	2.51	2.01	1.68	5.03	3.35	2.51	2.01
	57.00	5.97	3.98	2.98	2.39	1.99	5.97	3.98	2.98	2.39	1.99	5.97	3.98	2.98	2.39
	60.00	6.28	4.19	3.14	2.51	2.09	6.28	4.19	3.14	2.51	2.09	6.28	4.19	3.14	2.51
	67.00	7.02	4.68	3.51	2.81	2.34	7.02	4.68	3.51	2.81	2.34	7.02	4.68	3.51	2.81
	76.00	7.96	5.31	3.98	3.18	2.65	7.96	5.31	3.98	3.18	2.65	7.96	5.31	3.98	3.18
	86.00	9.01	6.00	4.50	3.60	3.00	9.01	6.00	4.50	3.60	3.00	9.01	6.00	4.50	3.60
	90.00	9.42	6.28	4.71	3.77	3.14	9.42	6.28	4.71	3.77	3.14	9.42	6.28	4.71	3.77
	105.00	11.00	7.33	5.50	4.40	3.67	11.00	7.33	5.50	4.40	3.67	11.00	7.33	5.50	4.40
	134.00	14.03	9.35	7.02	5.61	4.68	14.03	9.35	7.02	5.61	4.68	14.03	9.35	7.02	5.61
	172.00	18.01	12.01	9.01	7.20	6.00	18.01	12.01	9.01	7.20	6.00	18.01	12.01	9.01	7.20
		Also all RPM values were run with a stationary carriage for wave form 1.										Blade 1 =Instrumented			

D. Matlab Scripts

Experimental Data Processing '*Run*' post processing scripts

```
clear all
CarriageVelocity=input('Carriage Velocity (m/s)...');
TimeStep=0.004; %input('Time Step Size...');
pathname3= ('C:\Users\Carwyn\Documents\Matlab\Cardiff\PhD\Rome\');
cd(pathname3)

Rome_MultiFile_Preprocess

% Save Data
savefile=sprintf('RomeData_Raw_Vel_%.2f.mat',CarriageVelocity);
save(savefile);

%% Load Data
filename=sprintf('RomeData_Raw_Vel_%.2f.mat',CarriageVelocity);
load (filename);
cd(pathname3)

Z_Thrust_Adjustment

% Save Data
savefile=sprintf('RomeData_Z-Th_Vel_%.2f.mat',CarriageVelocity);
save(savefile);

%% Load Data
loadfile=sprintf('RomeData_Z-Th_Vel_%.2f.mat',CarriageVelocity);
load(loadfile);
cd(pathname3)

Calibration_Means_SDs

% Save Data
savefile=sprintf('RomeResults_ReCal_0.043_Vel_%.2f.mat',CarriageVelocity)
;
save(savefile);

%% Load Data
loadfile=sprintf('RomeResults_ReCal_0.043_Vel_%.2f.mat',CarriageVelocity)
;
load(loadfile);
cd(pathname3)

Exp_to_CSV

Trans_Vs_Azimuth

Spectral_Analysis
```

Rome_MultiFile_Preprocess Script (adapted from Allmark, 2016)

```
%% Data from test files....

[filename, pathname, filterindex] = uigetfile('*.txt', 'Pick Data
from test files....','MultiSelect','on');
cd (pathname);

%Input Variables
MotorData1Cali=72;
MotorData1Offset=0;
MotorData2Cali=0.31;
MotorData2Offset=-1.2;
% CarriageVelocity=input('Carriage Velocity (m/s)...');
FlumeData.NonDim.Cp2(1)=0;
FlumeData.NonDim.Cp1(1)=0;
FlumeData.NonDim.CpError1(1)=0;
FlumeData.NonDim.CpError2(1)=0;
FlumeData.NonDim.M_TSR_P(1)=0; %M_TSR_P is for the Power Non-
Dimensional Terms as Zero-Zero Value is included
FlumeData.Means.M_Hub_Power(1)=0;

%Non-Dimensional Variables
W_Density=998.2;
Turbine_Rad=0.25;


for i=1:size(filename,2)
%% Data analysis for single file.
    %% Import Data
    data=importdata(filename{i});
    rpmbef=data.data(:,15);
    rpmbef(rpmbef(2:size(rpmbef,1))==0)=[];
    RPMINDEX=size(rpmbef,1);

RPM=floor(mean(rpmbef(round(1*RPMINDEX/4):round(3*RPMINDEX/4))));
    if RPM<=0
        RPM=0;
    end
    RPM_Log(i)=RPM;

%% Organise and clean up data....

FlumeData.(sprintf('RPM_%d',RPM)).RawData.FluidVel_X=CarriageVeloc
ity;

FlumeData.(sprintf('RPM_%d',RPM)).Stats.M_FluidVel_X=CarriageVeloc
ity;

FlumeData.(sprintf('RPM_%d',RPM)).RawData.FluidVel_Y=data.data(:,2
);

FlumeData.(sprintf('RPM_%d',RPM)).RawData.FluidVel_Z=data.data(:,3
);
```

```
FlumeData.(sprintf('RPM_%d',RPM)).RawData.StanchionThrust=data.dat
a(:,4);

FlumeData.(sprintf('RPM_%d',RPM)).RawData.WaveProbe=data.data(:,5)
;

FlumeData.(sprintf('RPM_%d',RPM)).RawData.MotorData1=data.data(:,6
);

FlumeData.(sprintf('RPM_%d',RPM)).RawData.MotorData2=data.data(:,7
);


FlumeData.(sprintf('RPM_%d',RPM)).RawData.PLC_Time=data.data(:,8);

FlumeData.(sprintf('RPM_%d',RPM)).RawData.PLC_MotorPosition=data.d
ata(:,9);

FlumeData.(sprintf('RPM_%d',RPM)).RawData.PLC_MotorVelocity=data.d
ata(:,15).*0.10472; %Convert to Rads-1

FlumeData.(sprintf('RPM_%d',RPM)).RawData.PLC_MotorTorque=data.dat
a(:,10);

FlumeData.(sprintf('RPM_%d',RPM)).RawData.PLC_MotorPower=data.data
(:,11);

FlumeData.(sprintf('RPM_%d',RPM)).RawData.PLC_MotorVoltage=data.da
ta(:,12);

FlumeData.(sprintf('RPM_%d',RPM)).RawData.PLC_MotorTGC=data.data(:
,13);

FlumeData.(sprintf('RPM_%d',RPM)).RawData.PLC_MotorTemp=data.data(
:,14);


FlumeData.(sprintf('RPM_%d',RPM)).RawData.Hub_AccX=data.data(:,16)
;

FlumeData.(sprintf('RPM_%d',RPM)).RawData.Hub_AccZ=data.data(:,17)
;

FlumeData.(sprintf('RPM_%d',RPM)).RawData.Hub_AccY=data.data(:,18)
;

FlumeData.(sprintf('RPM_%d',RPM)).RawData.Hub_Twist=data.data(:,20
);

FlumeData.(sprintf('RPM_%d',RPM)).RawData.Hub_Thrust=data.data(:,1
9);

%% Organise and clean up data for export...
```

```
%Clean up flume and hub data

hubsize(i)=size(FlumeData.(sprintf('RPM_%d',RPM)).RawData.Hub_Thru
st,1);

analogsize(i)=size(FlumeData.(sprintf('RPM_%d',RPM)).RawData.Motor
Data2,1);

    if analogsize(i)>=hubsize(i)
%
FlumeData.(sprintf('RPM_%d',RPM)).RawData.FluidVel_X(hubsize+1:ana
logsize)=[];
%
FlumeData.(sprintf('RPM_%d',RPM)).RawData.FluidVel_Y(hubsize+1:ana
logsize)=[];
%
FlumeData.(sprintf('RPM_%d',RPM)).RawData.FluidVel_Z(hubsize+1:ana
logsize)=[];
%
FlumeData.(sprintf('RPM_%d',RPM)).RawData.StanchionThrust(hubsize+
1:analogsize)=[];

FlumeData.(sprintf('RPM_%d',RPM)).RawData.WaveProbe(hubsize(i)+1:a
nalogsize(i))=[];

FlumeData.(sprintf('RPM_%d',RPM)).RawData.MotorData1(hubsize(i)+1:
analogsize(i))=[];

FlumeData.(sprintf('RPM_%d',RPM)).RawData.MotorData2(hubsize(i)+1:
analogsize(i))=[];
        % Create time variable for analog measurements...

EndTime=size(FlumeData.(sprintf('RPM_%d',RPM)).RawData.MotorData1,
1)*TimeStep;

FlumeData.(sprintf('RPM_%d',RPM)).RawData.AnalogTime=linspace(0,En
dTime,size(FlumeData.(sprintf('RPM_%d',RPM)).RawData.MotorData1,1)
)';

    else


FlumeData.(sprintf('RPM_%d',RPM)).RawData.Hub_AccX(analogsize(i)+1
:hubsize(i))=[];

FlumeData.(sprintf('RPM_%d',RPM)).RawData.Hub_AccZ(analogsize(i)+1
:hubsize(i))=[];

FlumeData.(sprintf('RPM_%d',RPM)).RawData.Hub_AccY(analogsize(i)+1
:hubsize(i))=[];

FlumeData.(sprintf('RPM_%d',RPM)).RawData.Hub_Twist(analogsize(i)+
1:hubsize(i))=[];
```

```
FlumeData.(sprintf('RPM_%d',RPM)).RawData.Hub_Thrust(analogsize(i)
+1:hubsize(i))=[];
        % Create time variable for analog measurements...

EndTime=size(FlumeData.(sprintf('RPM_%d',RPM)).RawData.Hub_AccX,1)
*TimeStep;

FlumeData.(sprintf('RPM_%d',RPM)).RawData.AnalogTime=linspace(0,En
dTime,size(FlumeData.(sprintf('RPM_%d',RPM)).RawData.Hub_AccX,1))'
;

    end

%% Clean Up Motor Data
    PLC_Time=data.data(:,8); %For Indexing
    FlumeData.(sprintf('RPM_%d',RPM)).RawData.PLC_Time(1)=[];

FlumeData.(sprintf('RPM_%d',RPM)).RawData.PLC_MotorPosition(1)=[];

FlumeData.(sprintf('RPM_%d',RPM)).RawData.PLC_MotorVelocity(1)=[];

FlumeData.(sprintf('RPM_%d',RPM)).RawData.PLC_MotorTorque(1)=[];

FlumeData.(sprintf('RPM_%d',RPM)).RawData.PLC_MotorPower(1)=[];

FlumeData.(sprintf('RPM_%d',RPM)).RawData.PLC_MotorVoltage(1)=[];
    FlumeData.(sprintf('RPM_%d',RPM)).RawData.PLC_MotorTGC(1)=[];
    FlumeData.(sprintf('RPM_%d',RPM)).RawData.PLC_MotorTemp(1)=[];

FlumeData.(sprintf('RPM_%d',RPM)).RawData.PLC_MotorPosition(PLC_Ti
me(2:size(PLC_Time,1))==0)=[];

FlumeData.(sprintf('RPM_%d',RPM)).RawData.PLC_MotorVelocity(PLC_Ti
me(2:size(PLC_Time,1))==0)=[];

FlumeData.(sprintf('RPM_%d',RPM)).RawData.PLC_MotorTorque(PLC_Time
(2:size(PLC_Time,1))==0)=[];

FlumeData.(sprintf('RPM_%d',RPM)).RawData.PLC_MotorPower(PLC_Time(
2:size(PLC_Time,1))==0)=[];

FlumeData.(sprintf('RPM_%d',RPM)).RawData.PLC_MotorVoltage(PLC_Tim
e(2:size(PLC_Time,1))==0)=[];

FlumeData.(sprintf('RPM_%d',RPM)).RawData.PLC_MotorTGC(PLC_Time(2:
size(PLC_Time,1))==0)=[];

FlumeData.(sprintf('RPM_%d',RPM)).RawData.PLC_MotorTemp(PLC_Time(2
:size(PLC_Time,1))==0)=[];

FlumeData.(sprintf('RPM_%d',RPM)).RawData.PLC_Time(PLC_Time(2:size
(PLC_Time,1))==0)=[];

end
```

Thrust_Adjustment Script

```
cd(pathname);

%Function Objective: Find mean Start Thrust (ie thrust before
carriage is
%moving)

%Compare Zero thrust from start and end of test with zero data.
%Uses lowest value from the test, in all cases.

%% Load Data
[filename2, pathname2, ~] = uigetfile('*.txt', 'Pick Data from
zero files....','MultiSelect','on');
cd(pathname2);

%% ZeroThrust Values
ZeroFiles=size(filename2,2);
for h=1:ZeroFiles
    data2=importdata(filename2{:,h});
    RPM=RPM_Log(h);
    ZeroData.(sprintf('RPM_%d',RPM)).Thrust_Raw=data2.data(:,19);
    TZRSize=size(ZeroData.(sprintf('RPM_%d',RPM)).Thrust_Raw,1);


ZeroData.M_ZeroThrust(h)=mean(ZeroData.(sprintf('RPM_%d',RPM)).Thr
ust_Raw(round(1*TZRSize/3):round(2*TZRSize/3),1));
end

h=size(RPM_Log,2);

%% Compare first and last 200 with zero thrust
for i=1:h

    RPM=RPM_Log(i);

hub_not_zero=find(FlumeData.(sprintf('RPM_%d',RPM)).RawData.Hub_Th
rust>0);
    dY_Size=size(hub_not_zero);


dX=FlumeData.(sprintf('RPM_%d',RPM)).RawData.AnalogTime(1:dY_Size,
:);

dY=FlumeData.(sprintf('RPM_%d',RPM)).RawData.Hub_Thrust(1:dY_Size,
:);

    n=251; %equivalent to 1 second of data
%     if dY>n
        M_StartThrust(i)=mean(dY(1:n,1));
        M_EndThrust(i)=mean(dY(end-n:end,1));

        if M_StartThrust(i)<=M_EndThrust(i)
```

```
FlumeData.Means.In_Test_Zero_Thrust(i)=M_StartThrust(i);
        else
            FlumeData.Means.In_Test_Zero_Thrust(i)=M_EndThrust(i);
    end
end
```

Exp_to_CSV Script

```
%% Transpose Data

FlumeResults.M_TSR_P=transpose(FlumeResults.M_TSR_P);
FlumeResults.M_PLC_MotorVelocity_P=transpose(FlumeResults.M_PLC_Mo
torVelocity_P);
FlumeResults.M_Power=transpose(FlumeResults.M_Power);
FlumeResults.SD_Power=transpose(FlumeResults.SD_Power);
FlumeResults.M_PLC_MotorPower=transpose(FlumeResults.M_PLC_MotorPo
wer);
FlumeResults.SD_PLC_MotorPower=transpose(FlumeResults.SD_PLC_Motor
Power);
FlumeResults.M_CP=transpose(FlumeResults.M_CP);
FlumeResults.SD_CP=transpose(FlumeResults.SD_CP);
FlumeResults.M_CP1=transpose(FlumeResults.M_CP1);
FlumeResults.SD_CP1=transpose(FlumeResults.SD_CP1);
FlumeResults.M_CP2=transpose(FlumeResults.M_CP2);
FlumeResults.SD_CP2=transpose(FlumeResults.SD_CP2);

FlumeResults.M_TSR=transpose(FlumeResults.M_TSR);
FlumeResults.M_PLC_MotorVelocity=transpose(FlumeResults.M_PLC_Moto
rVelocity);
FlumeResults.M_Torque=transpose(FlumeResults.M_Torque);
FlumeResults.SD_Torque=transpose(FlumeResults.SD_Torque);
FlumeResults.M_PLC_MotorTorque=transpose(
FlumeResults.M_PLC_MotorTorque);
FlumeResults.SD_PLC_MotorTorque=transpose(
FlumeResults.SD_PLC_MotorTorque);
FlumeResults.M_CQ=transpose(FlumeResults.M_CQ);
FlumeResults.SD_CQ=transpose(FlumeResults.SD_CQ);
FlumeResults.M_CQ1=transpose(FlumeResults.M_CQ1);
FlumeResults.SD_CQ1=transpose(FlumeResults.SD_CQ1);
FlumeResults.M_CQ2=transpose(FlumeResults.M_CQ2);
FlumeResults.SD_CQ2=transpose(FlumeResults.SD_CQ2);
FlumeResults.M_Hub_Thrust=transpose(FlumeResults.M_Hub_Thrust);
FlumeResults.SD_Hub_Thrust=transpose(FlumeResults.SD_Hub_Thrust);
FlumeResults.M_CT=transpose(FlumeResults.M_CT);
FlumeResults.SD_CT=transpose(FlumeResults.SD_CT);
FlumeResults.DrivenOrDriving=transpose(FlumeResults.DrivenOrDrivin
g);
%% Data for exporting to .csv

exp2=horzcat(FlumeResults.M_TSR_P,
FlumeResults.M_PLC_MotorVelocity_P, FlumeResults.M_Power,
FlumeResults.SD_Power, FlumeResults.M_PLC_MotorPower,
FlumeResults.SD_PLC_MotorPower, FlumeResults.M_CP,
FlumeResults.SD_CP, FlumeResults.M_CP1, FlumeResults.SD_CP1,
FlumeResults.M_CP2, FlumeResults.SD_CP2);
headers1={'TSR', 'Rotational Velocity (rad/s)', 'Power(W)',
'SD_Power', 'PLC_MotorPower', 'SD_PLC_MotorPower', 'CP', 'SD_CP',
'CP1', 'SD_CP1', 'CP2', 'SD_CP2'};
csvwrite_with_headers('Dec_Cal_CP_TSR.csv', exp2, headers1);

exp3=horzcat(FlumeResults.M_TSR, FlumeResults.M_PLC_MotorVelocity,
FlumeResults.M_Torque, FlumeResults.SD_Torque,
```

```
FlumeResults.M_PLC_MotorTorque, FlumeResults.SD_PLC_MotorTorque,
FlumeResults.M_CQ, FlumeResults.SD_CQ, FlumeResults.M_CQ1,
FlumeResults.SD_CQ1, FlumeResults.M_CQ2, FlumeResults.SD_CQ2,
FlumeResults.M_Hub_Thrust, FlumeResults.SD_Hub_Thrust,
FlumeResults.M_CT, FlumeResults.SD_CT);
headers2={'TSR', 'Rotational Velocity (rad/s)', 'Torque (Nm)',
'SD_Torque', 'PLC_Torque', 'SD_PLC_Torque', 'C_Q', 'SD_CQ',
'C_Q1', 'SD_CQ1', 'C_Q2', 'SD_CQ2', 'Blade Thrust (N)', 'SD_BT',
'C_T', 'SD_CT'};
csvwrite_with_headers('Dec_Cal_0.043_CT_CQ_TSR.csv', exp3,
headers2);
```

Calibration_Means_SDs Script

```
cd(pathname);

%% Calibration calculations...
for i=1:h

    RPM=RPM_Log(i);


MDINDEX=size(FlumeData.(sprintf('RPM_%d',RPM)).RawData.MotorData2,
1);

MPINDEX=size(FlumeData.(sprintf('RPM_%d',RPM)).RawData.PLC_MotorVe
locity,1);

%Hub data to voltage...

FlumeData.(sprintf('RPM_%d',RPM)).RawData.Hub_AccZ=(FlumeData.(spr
intf('RPM_%d',RPM)).RawData.Hub_AccZ./1023).*5;

FlumeData.(sprintf('RPM_%d',RPM)).RawData.Hub_AccX=(FlumeData.(spr
intf('RPM_%d',RPM)).RawData.Hub_AccX./1023).*5;

FlumeData.(sprintf('RPM_%d',RPM)).RawData.Hub_Thrust_Volt=((FlumeD
ata.(sprintf('RPM_%d',RPM)).RawData.Hub_Thrust-
FlumeData.Means.In_Test_Zero_Thrust(i)).*5/1023);

FlumeData.(sprintf('RPM_%d',RPM)).RawData.Hub_AccY=(FlumeData.(spr
intf('RPM_%d',RPM)).RawData.Hub_AccY./1023).*5;

% Thrust Calibration...

FlumeData.(sprintf('RPM_%d',RPM)).RawData.Hub_Thrust=(FlumeData.(s
printf('RPM_%d',RPM)).RawData.Hub_Thrust_Volt)/0.043;

% Motor Data Calibration.....

FlumeData.(sprintf('RPM_%d',RPM)).RawData.MotorData1_Cali=(FlumeDa
ta.(sprintf('RPM_%d',RPM)).RawData.MotorData1*MotorData1Cali)+Moto
rData1Offset;

FlumeData.(sprintf('RPM_%d',RPM)).RawData.MotorData2_Cali=(FlumeDa
ta.(sprintf('RPM_%d',RPM)).RawData.MotorData2*MotorData2Cali)+Moto
rData2Offset;


%% Calculate mean and non-dimensional values...

ZerosStart=find(FlumeData.(sprintf('RPM_%d',RPM)).RawData.PLC_Moto
rPower==0,1);

MPINDEX=size(FlumeData.(sprintf('RPM_%d',RPM)).RawData.PLC_MotorPo
wer,1);
```

```
MDINDEX=size(FlumeData.(sprintf('RPM_%d',RPM)).RawData.MotorData2,
1);

    %% Transient Data Rotational Position

FlumeData.(sprintf('RPM_%d',RPM)).TransientData.Rot_Pos=FlumeData.
(sprintf('RPM_%d',RPM)).RawData.MotorData1_Cali;

FlumeData.(sprintf('RPM_%d',RPM)).TransientData.Rot_Pos_Mid_Third=
FlumeData.(sprintf('RPM_%d',RPM)).TransientData.Rot_Pos(round(1*MD
INDEX/4):round(3*MDINDEX/4),1);

    %% Transient Torque and Thrust

FlumeData.(sprintf('RPM_%d',RPM)).TransientData.Torque=(((FlumeDat
a.(sprintf('RPM_%d',RPM)).RawData.MotorData2_Cali*6.66)-(8e-
06*(RPM^2)+0.0056*(RPM)+0.6811))*-1);

FlumeData.(sprintf('RPM_%d',RPM)).TransientData.Hub_Thrust=FlumeDa
ta.(sprintf('RPM_%d',RPM)).RawData.Hub_Thrust;


FlumeData.(sprintf('RPM_%d',RPM)).TransientData.Torque_Mid_Third=F
lumeData.(sprintf('RPM_%d',RPM)).TransientData.Torque(round(1*MDIN
DEX/4):round(3*MDINDEX/4),1);

FlumeData.(sprintf('RPM_%d',RPM)).TransientData.Hub_Thrust_Mid_Thi
rd=FlumeData.(sprintf('RPM_%d',RPM)).TransientData.Hub_Thrust(roun
d(1*MDINDEX/4):round(3*MDINDEX/4),1);


FlumeData.(sprintf('RPM_%d',RPM)).TransientData.Ct_full=(FlumeData
.(sprintf('RPM_%d',RPM)).RawData.Hub_Thrust)/(0.5*W_Density*Turbin
e_Rad^2*pi*FlumeData.(sprintf('RPM_%d',RPM)).Stats.M_FluidVel_X^2)
;


FlumeData.(sprintf('RPM_%d',RPM)).TransientData.Cq=FlumeData.(spri
ntf('RPM_%d',RPM)).TransientData.Torque_Mid_Third/(0.5*W_Density*T
urbine_Rad^3*pi*FlumeData.(sprintf('RPM_%d',RPM)).Stats.M_FluidVel
_X^2);

FlumeData.(sprintf('RPM_%d',RPM)).TransientData.Ct=(FlumeData.(spr
intf('RPM_%d',RPM)).TransientData.Hub_Thrust_Mid_Third*3)/(0.5*W_D
ensity*Turbine_Rad^2*pi*FlumeData.(sprintf('RPM_%d',RPM)).Stats.M_
FluidVel_X^2);

FlumeData.(sprintf('RPM_%d',RPM)).TransientData.CtBlade=FlumeData.
(sprintf('RPM_%d',RPM)).TransientData.Hub_Thrust_Mid_Third/(0.5*W_
Density*Turbine_Rad^2*pi*FlumeData.(sprintf('RPM_%d',RPM)).Stats.M
_FluidVel_X^2);

%% Means & SDs PLC, Torque and Thrust
```

```
    [MD1_mu,
MD1_s]=normfit(FlumeData.(sprintf('RPM_%d',RPM)).RawData.MotorData
1_Cali(round(1*MDINDEX/4):round(3*MDINDEX/4),1));
    [MD2_mu,
MD2_s]=normfit(FlumeData.(sprintf('RPM_%d',RPM)).RawData.MotorData
2_Cali(round(1*MDINDEX/4):round(3*MDINDEX/4),1));
    [Om_mu,
Om_s]=normfit(FlumeData.(sprintf('RPM_%d',RPM)).RawData.PLC_MotorV
elocity(round(1*MPINDEX/4):round(3*MPINDEX/4),1));
    [PLC_MT_mu,
PLC_MT_s]=normfit(FlumeData.(sprintf('RPM_%d',RPM)).RawData.PLC_Mo
torTorque(round(1*MPINDEX/4):round(3*MPINDEX/4),1));
    [PLC_MP_mu,
PLC_MP_s]=normfit(FlumeData.(sprintf('RPM_%d',RPM)).RawData.PLC_Mo
torPower(round(1*MPINDEX/4):round(3*MPINDEX/4),1));
    [PLC_MV_mu,
PLC_MV_s]=normfit(FlumeData.(sprintf('RPM_%d',RPM)).RawData.PLC_Mo
torVoltage(round(1*MPINDEX/4):round(3*MPINDEX/4),1));
    [PLC_MTGC_mu,
PLC_MTGC_s]=normfit(FlumeData.(sprintf('RPM_%d',RPM)).RawData.PLC_
MotorTGC(round(1*MPINDEX/4):round(3*MPINDEX/4),1));
    [TD_Q_mu,
TD_Q_s]=normfit(FlumeData.(sprintf('RPM_%d',RPM)).TransientData.To
rque_Mid_Third);
    [TD_HT_mu,
TD_HT_s]=normfit(FlumeData.(sprintf('RPM_%d',RPM)).TransientData.H
ub_Thrust_Mid_Third);
    [TD_CQ_mu,
TD_CQ_s]=normfit(FlumeData.(sprintf('RPM_%d',RPM)).TransientData.C
q);
    [TD_CT_mu,
TD_CT_s]=normfit(FlumeData.(sprintf('RPM_%d',RPM)).TransientData.C
t);
    [TD_CTB_mu,
TD_CTB_s]=normfit(FlumeData.(sprintf('RPM_%d',RPM)).TransientData.
CtBlade);

    FlumeResults.M_PLC_MotorVelocity(i)=Om_mu;
    FlumeResults.M_PLC_MotorVelocity_P(i+1)=Om_mu;
    FlumeResults.M_PLC_MotorTorque(i)=PLC_MT_mu*-1;
    FlumeResults.M_PLC_MotorPower(i+1)=PLC_MP_mu*-1;

    FlumeResults.M_Hub_Thrust(i)=TD_HT_mu;
    FlumeResults.M_Torque(i)=TD_Q_mu;

    if MD2_mu<0
        FlumeResults.DrivenOrDriving(i)=1; %This means the motor
is being driven by the rotor
    else
        FlumeResults.DrivenOrDriving(i)=0; %this means the motor
is driving the rotor
    end

    FlumeResults.SD_Hub_Thrust(i)=TD_HT_s*1.96;
    FlumeResults.SD_Torque(i)=TD_Q_s*1.96;
```

```
    FlumeResults.SD_PLC_MotorTorque(i)=PLC_MT_s*1.96;
    FlumeResults.SD_PLC_MotorPower(i+1)=PLC_MP_s*1.96;

    FlumeResults.SD_CQ(i)=TD_CQ_s*1.96;
    FlumeResults.SD_CQ1(i)=PLC_MTGC_s*1.96;
    FlumeResults.SD_CQ2(i)=PLC_MT_s*1.96;
    FlumeResults.SD_CT(i)=TD_CT_s*1.96;

    %% Transient Power

FlumeData.(sprintf('RPM_%d',RPM)).TransientData.Power=((FlumeData.
(sprintf('RPM_%d',RPM)).RawData.MotorData2_Cali*6.66*Om_mu)-
(0.0002*(RPM^2)+0.1289*(RPM)-1.5592))*-1;

FlumeData.(sprintf('RPM_%d',RPM)).TransientData.Power_Mid_Third=Fl
umeData.(sprintf('RPM_%d',RPM)).TransientData.Power(round(1*MDINDE
X/4):round(3*MDINDEX/4),1);

FlumeData.(sprintf('RPM_%d',RPM)).TransientData.Cp=FlumeData.(spri
ntf('RPM_%d',RPM)).TransientData.Power_Mid_Third/(0.5*W_Density*Tu
rbine_Rad^2*pi*FlumeData.(sprintf('RPM_%d',RPM)).Stats.M_FluidVel_
X^3);

%% Means and SDs Power
    [TD_P_mu,
TD_P_s]=normfit(FlumeData.(sprintf('RPM_%d',RPM)).TransientData.Po
wer_Mid_Third);
    [TD_CP_mu,
TD_CP_s]=normfit(FlumeData.(sprintf('RPM_%d',RPM)).TransientData.C
p);

    FlumeResults.M_Power(i+1)=TD_P_mu;

    FlumeResults.SD_Power(i+1)=TD_P_s*1.96;
    FlumeResults.SD_CP(i+1)=TD_CP_s*1.96;
    FlumeResults.SD_CP1(i+1)=PLC_MTGC_s*1.96;

FlumeResults.SD_CP2(i+1)=std(FlumeData.(sprintf('RPM_%d',RPM)).Tra
nsientData.Cp)*1.96;

%% Non-Dimensional Values

FlumeResults.M_TSR_P(i+1)=(Turbine_Rad*Om_mu)/CarriageVelocity;
    FlumeResults.M_TSR(i)=(Turbine_Rad*Om_mu)/CarriageVelocity;

    FlumeResults.M_CQ(i)=TD_CQ_mu;
    FlumeResults.M_CQ1(i)=(((PLC_MTGC_mu*6.66)-(8e-
06*(RPM^2)+0.0056*(RPM)+0.6811))*-
1)/(0.5*W_Density*Turbine_Rad^3*pi*CarriageVelocity^2);
    FlumeResults.M_CQ2(i)=(((PLC_MT_mu)-(8e-
06*(RPM^2)+0.0056*(RPM)+0.6811))*-
1)/(0.5*W_Density*Turbine_Rad^3*pi*CarriageVelocity^2);

    FlumeResults.M_CP(i+1)=TD_CP_mu;
```

```
    FlumeResults.M_CP1(i+1)=(((PLC_MTGC_mu*6.66*Om_mu)-
(0.0002*(RPM^2)+0.1289*(RPM)-1.5592))*-
1)/(0.5*W_Density*Turbine_Rad^2*pi*CarriageVelocity^3);
    FlumeResults.M_CP2(i+1)=(((PLC_MP_mu)-
(0.0002*(RPM^2)+0.1289*(RPM)-1.5592))*-
1)/(0.5*W_Density*Turbine_Rad^2*pi*CarriageVelocity^3);

    FlumeResults.M_CT(i)=TD_CT_mu;

FlumeResults.M_CTblade(i)=(TD_HT_mu)/(0.5*W_Density*Turbine_Rad^2*
pi*CarriageVelocity^2);

%% Filtered Results

WindowSize=0.124/TimeStep;
b=(1/WindowSize)*ones(1,WindowSize);
a=1;

FlumeData.(sprintf('RPM_%d',RPM)).TransientData.Filtered.Rot_Vel_M
id_Third=filtfilt(b,a,FlumeData.(sprintf('RPM_%d',RPM)).RawData.PL
C_MotorVelocity(round(1*MPINDEX/4):round(3*MPINDEX/4),1));
FlumeData.(sprintf('RPM_%d',RPM)).TransientData.Filtered.Torque_Mi
d_Third=filtfilt(b,a,FlumeData.(sprintf('RPM_%d',RPM)).TransientDa
ta.Torque_Mid_Third);
FlumeData.(sprintf('RPM_%d',RPM)).TransientData.Filtered.Cq=filtfi
lt(b,a,FlumeData.(sprintf('RPM_%d',RPM)).TransientData.Cq);
FlumeData.(sprintf('RPM_%d',RPM)).TransientData.Filtered.Power_Mid
_Third=filtfilt(b,a,FlumeData.(sprintf('RPM_%d',RPM)).TransientDat
a.Power_Mid_Third);
FlumeData.(sprintf('RPM_%d',RPM)).TransientData.Filtered.Cp=filtfi
lt(b,a,FlumeData.(sprintf('RPM_%d',RPM)).TransientData.Cp);
FlumeData.(sprintf('RPM_%d',RPM)).TransientData.Filtered.Hub_Thrus
t_Mid_Third=filtfilt(b,a,FlumeData.(sprintf('RPM_%d',RPM)).Transie
ntData.Hub_Thrust_Mid_Third);
FlumeData.(sprintf('RPM_%d',RPM)).TransientData.Filtered.Ct=filtfi
lt(b,a,FlumeData.(sprintf('RPM_%d',RPM)).TransientData.Ct);
FlumeData.(sprintf('RPM_%d',RPM)).TransientData.Filtered.CtBlade=f
iltfilt(b,a,FlumeData.(sprintf('RPM_%d',RPM)).TransientData.CtBlad
e);

%% Uncertainty in CT

Mu_Thrust=0.2334; %calcualted in thesis

Temp_data=[5 10 15 20];
specif_vol=[0.10001 0.10003 0.10010 0.10018].*10^-2;
rho_data=1./specif_vol;
mu_data=[1501 1300 1136 1002].*10^-6;
Temp=18;    % Change according to the day's temp.
%Linearly interpolate for meu
Mu_Rho=interp1(Temp_data,mu_data,Temp);
%Linearly interpolate for rho
Rho=interp1(Temp_data,rho_data,Temp);
%
```

```
Mu_A=(2*0.001); % +sqrt(0.005^2+0.15^2); this part only applies
for yaw angle cases.

Mu_Vel=0.005;

FlumeResults.Mu_CT(i)= sqrt((Mu_Thrust/FlumeResults.M_CT(i))^2-
(Mu_Rho/W_Density)^2-(Mu_A/(pi*Turbine_Rad^2))^2-
((2*Mu_Vel)/CarriageVelocity)^2)*FlumeResults.M_CQ(i)^2;
end
```

Trans_Vs_Azimuth Script

```
for i=1:size(RPM_Log,2)
    RPM=RPM_Log(i);

figure;
plot(FlumeData.(sprintf('RPM_%d',RPM)).TransientData.Rot_Pos_Mid_T
hird,FlumeData.(sprintf('RPM_%d',RPM)).TransientData.Cq,'.')
hold on
plot(FlumeData.(sprintf('RPM_%d',RPM)).TransientData.Rot_Pos_Mid_T
hird,FlumeData.(sprintf('RPM_%d',RPM)).TransientData.Filtered.Cq,'
.')
hold off
title(sprintf('RPM_%d',RPM))
ylabel('C_\Theta','fontsize',16);
xlabel('Blade 1 Azimuth, \psi (\circ)','fontsize',16);
ax=gca;
set(ax,'XTick',[0:60:360]);
set(ax,'fontsize',16);
set(ax,'box','off');
legend ('Unfiltered', 'Filtered');


figure;
plot(FlumeData.(sprintf('RPM_%d',RPM)).TransientData.Rot_Pos_Mid_T
hird,FlumeData.(sprintf('RPM_%d',RPM)).TransientData.Cp,'.')
hold on
plot(FlumeData.(sprintf('RPM_%d',RPM)).TransientData.Rot_Pos_Mid_T
hird,FlumeData.(sprintf('RPM_%d',RPM)).TransientData.Filtered.Cp,'
.')
hold off
title(sprintf('RPM_%d',RPM))
ylabel('C_P','fontsize',16);
xlabel('Blade 1 Azimuth, \psi (\circ)','fontsize',16);
ax=gca;
set(ax,'XTick',[0:60:360]);
set(ax,'fontsize',16);
set(ax,'box','off');
legend ('Unfiltered', 'Filtered');

figure;
plot(FlumeData.(sprintf('RPM_%d',RPM)).TransientData.Rot_Pos_Mid_T
hird,FlumeData.(sprintf('RPM_%d',RPM)).TransientData.Ct,'.')
```

```
hold on
plot(FlumeData.(sprintf('RPM_%d',RPM)).TransientData.Rot_Pos_Mid_T
hird,FlumeData.(sprintf('RPM_%d',RPM)).TransientData.Filtered.Ct,'
.')
hold off
title(sprintf('RPM_%d',RPM))
ylabel('C_T','fontsize',16);
xlabel('Blade 1 Azimuth, \psi (\circ)','fontsize',16);
ax=gca;
set(ax,'XTick',[0:60:360]);
set(ax,'fontsize',16);
set(ax,'box','off');
legend ('Unfiltered', 'Filtered');
end
```

Spectral_Analysis Script

```
%% Selecting Data Set to interrogate

for i=1:size(RPM_Log,2)
    RPM=RPM_Log(i);


MDINDEX=size(FlumeData.(sprintf('RPM_%d',RPM)).RawData.MotorData2,
1);

MPINDEX=size(FlumeData.(sprintf('RPM_%d',RPM)).RawData.PLC_MotorVe
locity,1);


DataSet.(sprintf('RPM_%d',RPM))(:,1)=FlumeData.(sprintf('RPM_%d',R
PM)).TransientData.Hub_Thrust_Mid_Third;

DataSet.(sprintf('RPM_%d',RPM))(:,2)=FlumeData.(sprintf('RPM_%d',R
PM)).TransientData.Filtered.Hub_Thrust_Mid_Third;

%% Input Variables For Non-Filtered Results

dt=TimeStep;                                 %TimeStepSize
fs=1/dt;                                     %SampleFrequency
x=DataSet.(sprintf('RPM_%d',RPM))(:,1);      %ThrustDataSet
m=length(x);                                 %WindowLength
n=m;                                         %TransformLength
t=(0:m-1)/fs;                                %TimeRange
y=fft(x,n);                                  %DFT
f=(0:n-1)*(fs/n);                            %FrequencyRange
NyquistRange=fs/2;

%% Performing FFT of Thrust Data

power=(abs(y).^2)/n;

y0=fftshift(y);
```

```
f0=(-n/2:n/2-1)*(fs/n);
power0 = y0.*conj(y0)/n;

[pxx,f,pxxc] =
periodogram(x,rectwin(length(x)),length(x),fs,'ConfidenceLevel',
0.95);


%% Plot Periodgram

figure;
hold on

plot(f(:,1),pxx(:,1))

xlim([0 10])
xlabel('Frequency (Hz)')
ylim([0 10])
ylabel('Thrust, Power Spectral Analysis')
title(sprintf('{\bf 0-Centered Periodogram of Thrust} RPM
%d',RPM))

end
```

Blevins first mode of vibration in a hollow stanchion (adapted from Blevins, 2001)

```
%% Blevins formula for calulating the first mode
%  of vibration in a hollow tube:

% f=[A/(2*pi*L^2)]*sqrt(E*I/m)

% where:
% A = 9.87 for firsty mode
% L = Tube Length (m)
% E = Youngs Modulus (Pa)
% I = Area moment of Inertia (m^4)
% m = mass per unit length (m/kg)
% OD = Outside Diameter (m)
% ID = Inside Diameter (m)
% Rho = Density of material (kg/m^3)

A=9.87;
L=2.5;
E=2E11;
OD=0.070;
ID=0.050;
Rho=7500;
I=(pi/64)*(OD^4-ID^4);
m=pi*OD*((OD-ID)/2)*7500;

f=[A/(2*pi*L^2)]*sqrt(E*I/m)
```

```
%% Vortex Shedding Frequency

U=[0.75,1.00,1.25,1.75];
D=0.07;
Ki=1.002E-3;

Re=(U*D)/Ki

St=[0.115,0.145,0.155,0.185];

Fs=(St.*U)/D
```

E. Experimental Results

Aligned Temporal Results

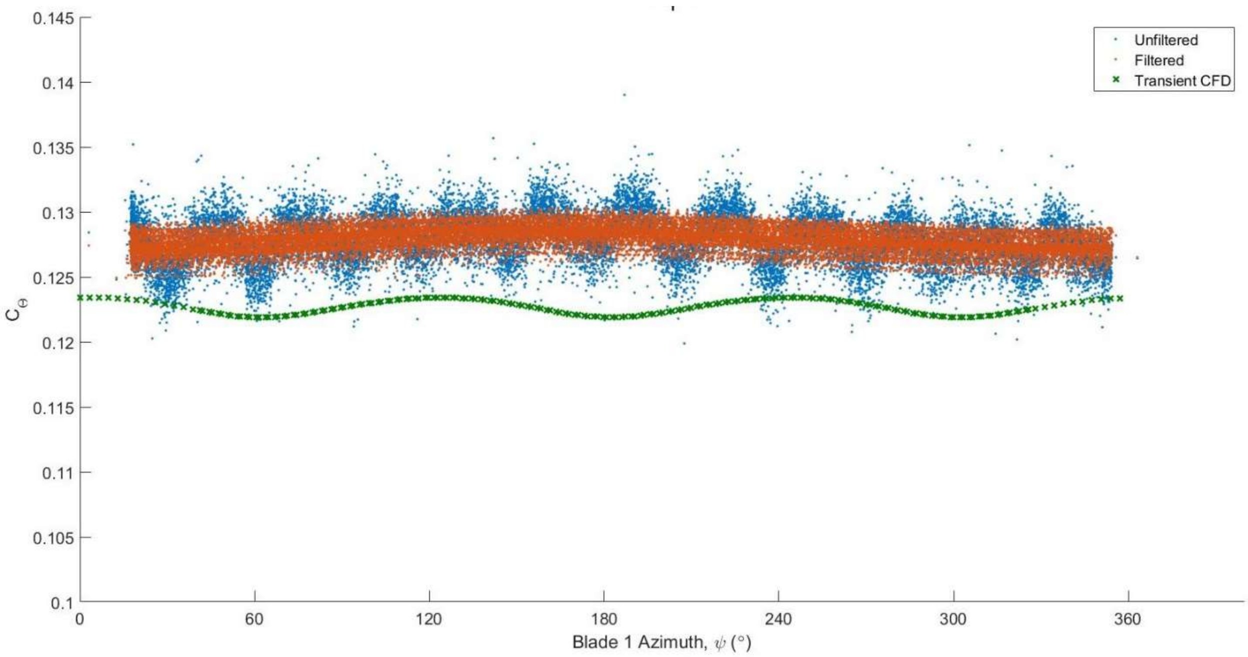

Figure 0.3 Filtered and unfiltered alternator C_θ - φ for aligned, 0° yaw angle at V = 1.00 ms^{-1} and λ= 3.5 with corresponding transient CFD results

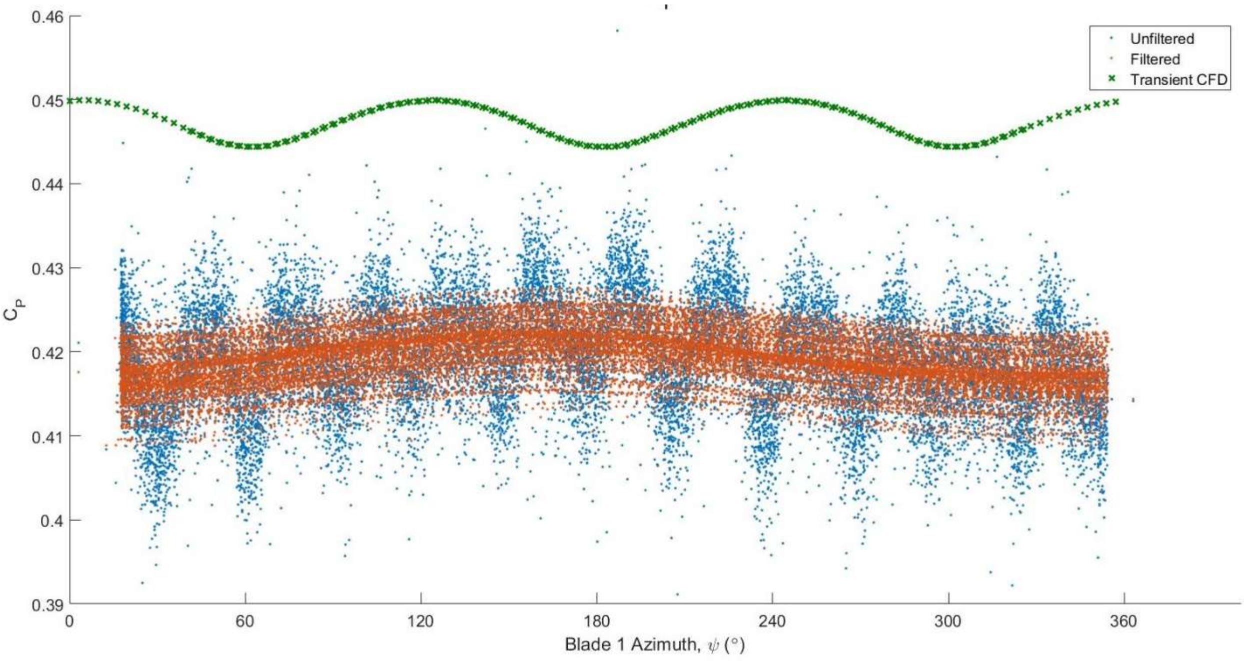

Figure 0.4 Filtered and unfiltered alternator C_P - φ for aligned, 0° yaw angle at V = 1.00 ms^{-1} and λ= 3.5 with corresponding transient CFD results

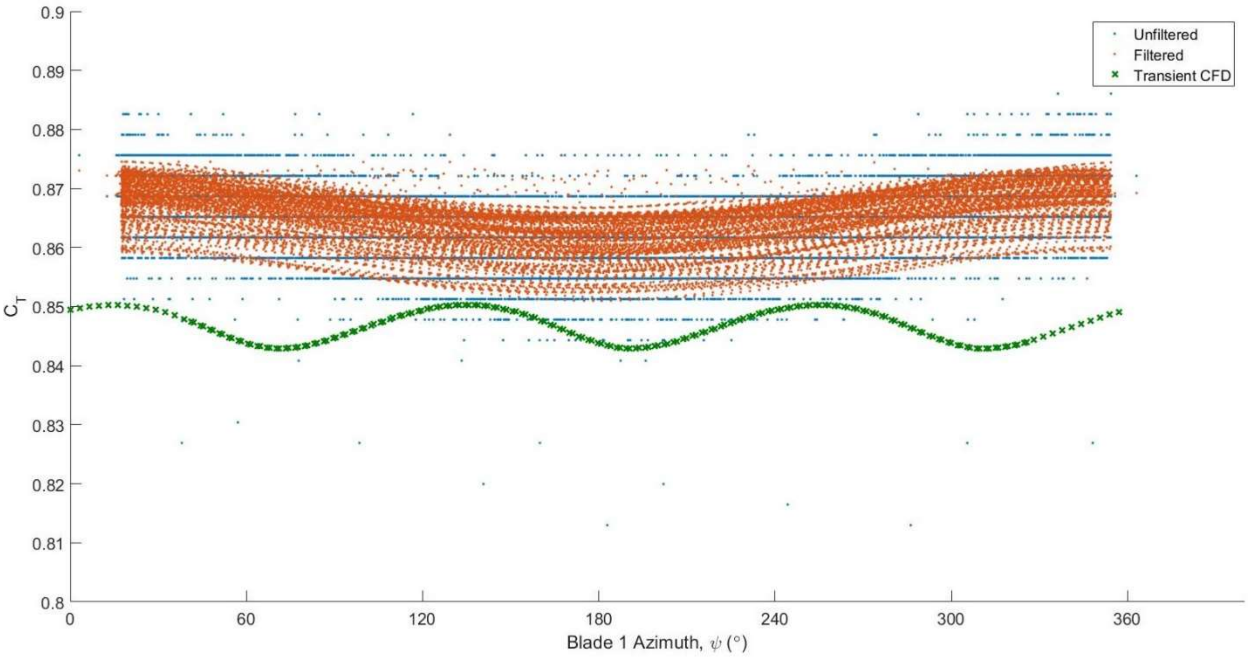

Figure 0.5 Filtered and unfiltered alternator C_T - φ for aligned, 0° yaw angle at V = 1.00 ms^{-1} and λ= 3.5 with corresponding transient CFD results

±10° Temporal Results

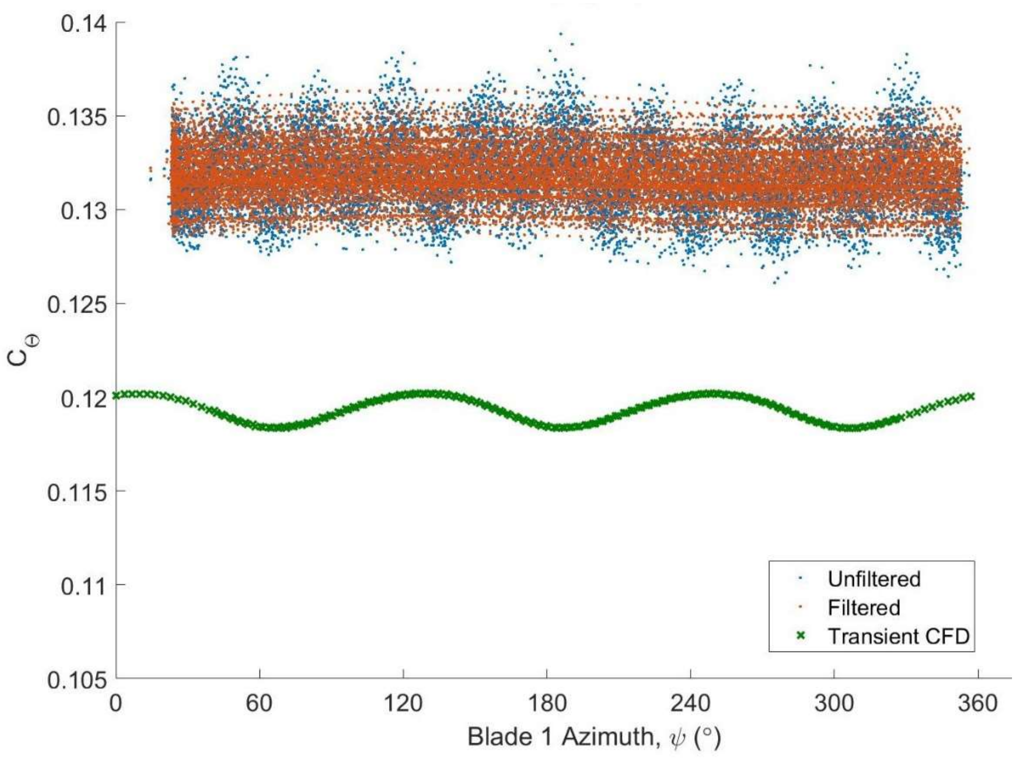

Figure 0.6 Filtered and unfiltered alternator C_θ - φ for +10° yaw angle at V = 1.50 ms^{-1} and λ= 3.5 with corresponding transient CFD results

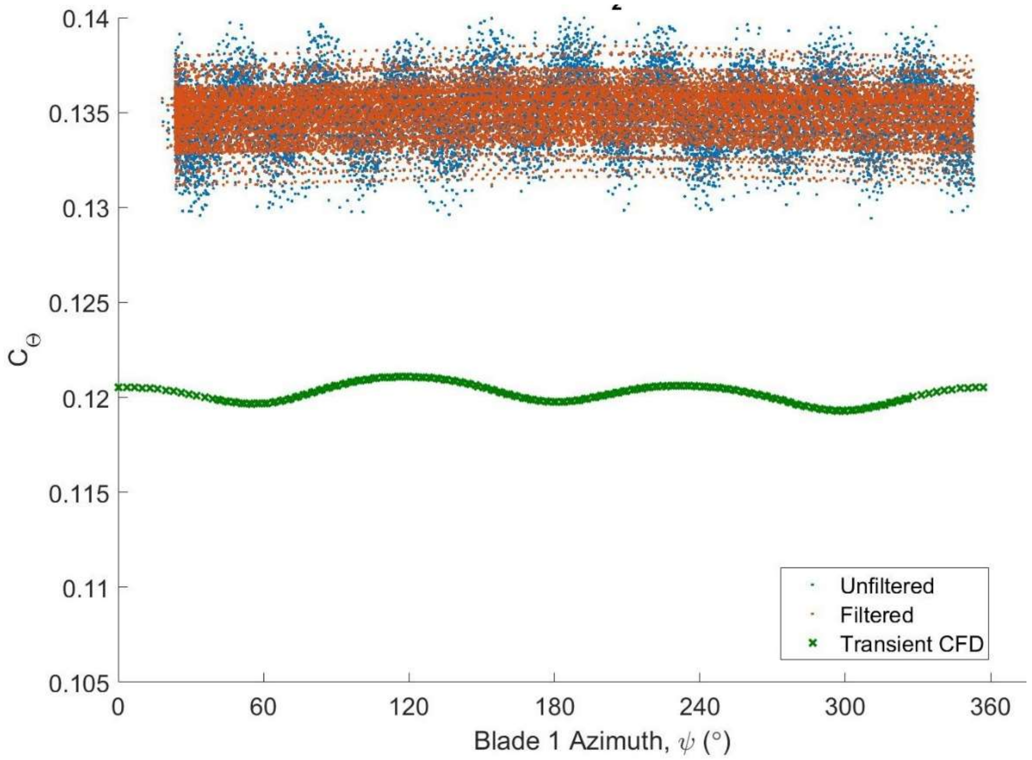

Figure 0.7 Filtered and unfiltered alternator C_θ - φ for -10° yaw angle at V = 1.50 ms^{-1} and λ= 3.5 with corresponding transient CFD results

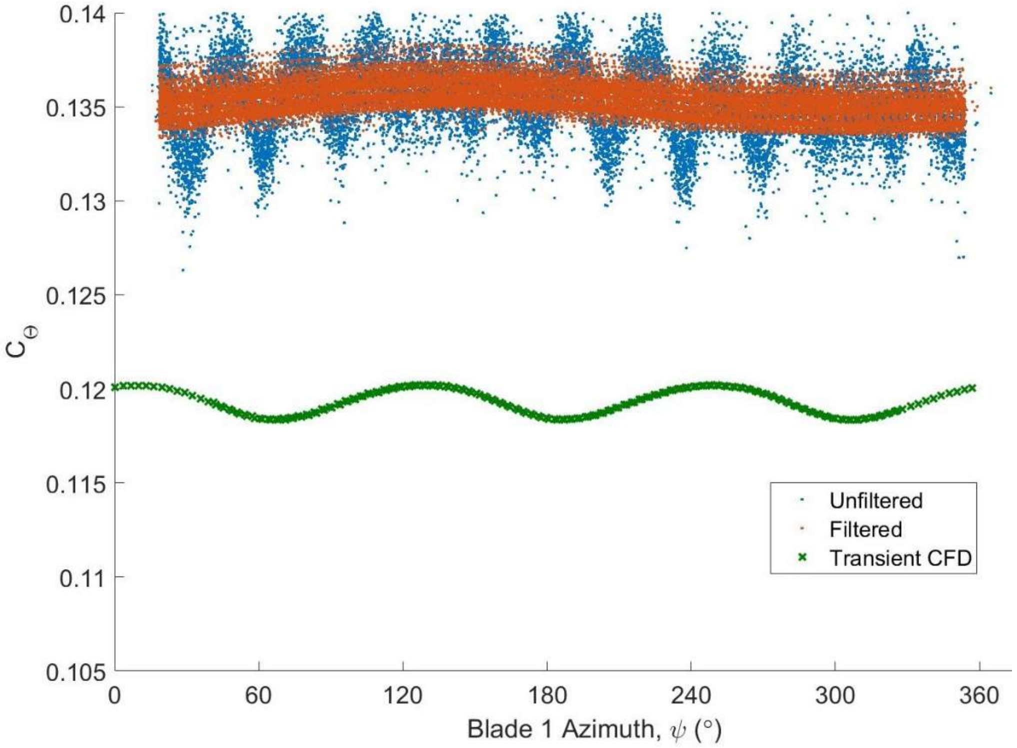

Figure 0.8 Filtered and unfiltered alternator C_θ - φ for +10° yaw angle at V = 1.00 ms^{-1} and λ= 3.5 with corresponding transient CFD results

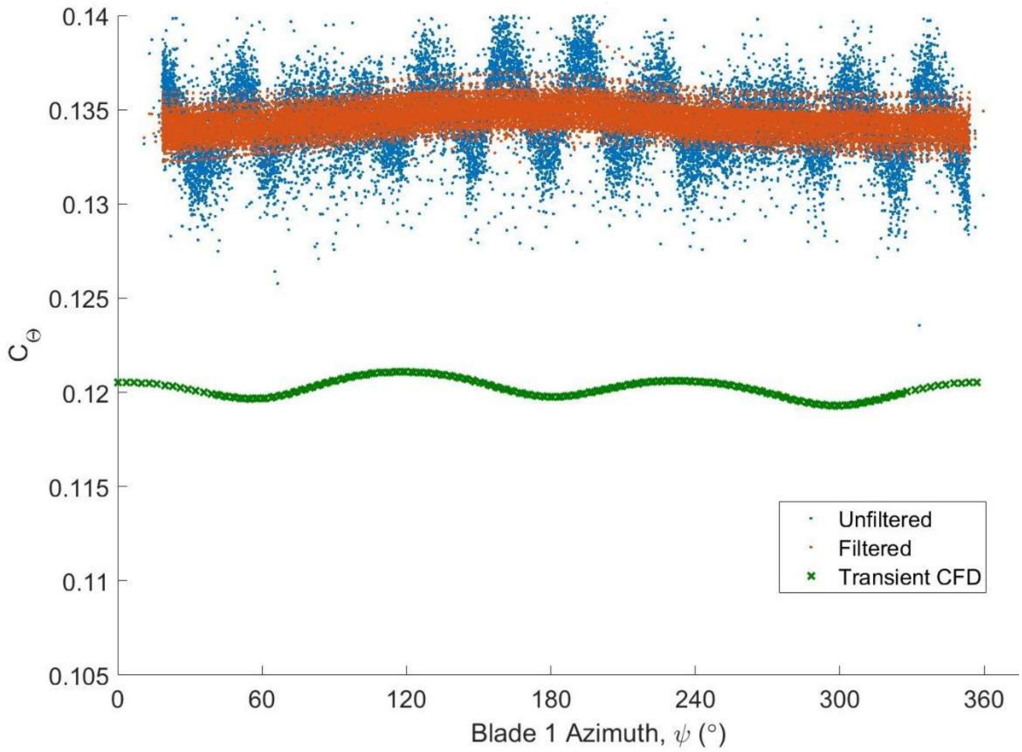

Figure 0.9 Filtered and unfiltered alternator C_θ - φ for -10° yaw angle at V = 1.00 ms^{-1} and λ= 3.5 with corresponding transient CFD results

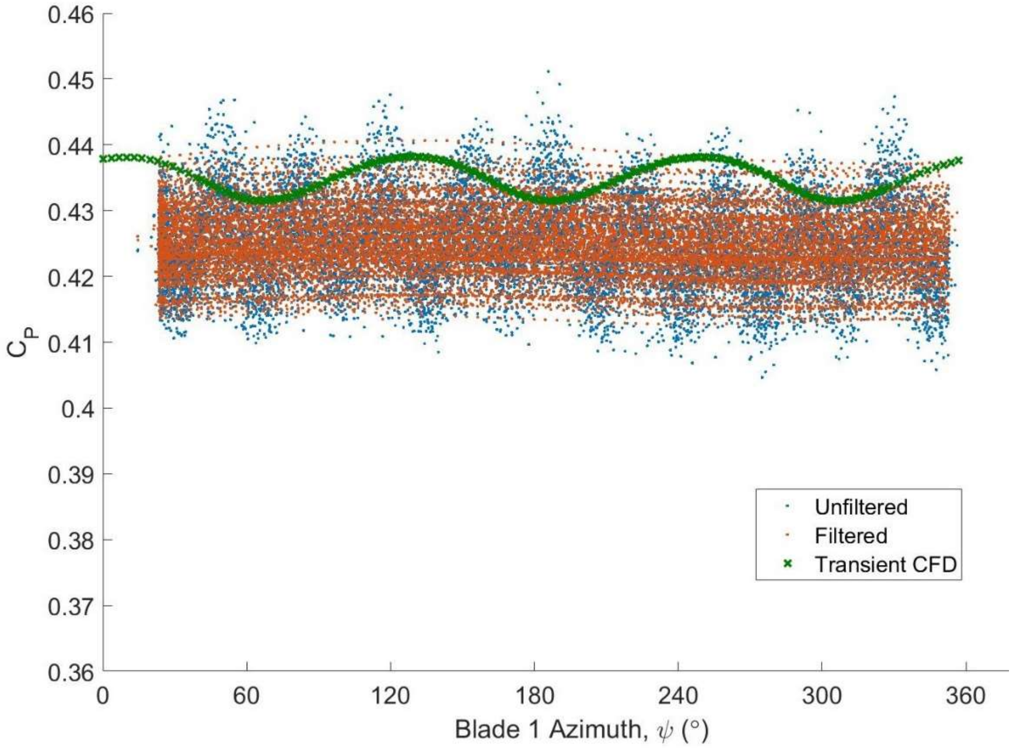

Figure 0.10 Filtered and unfiltered alternator C_P - φ for +10° yaw angle at V = 1.50 ms^{-1} and λ= 3.5 with corresponding transient CFD results

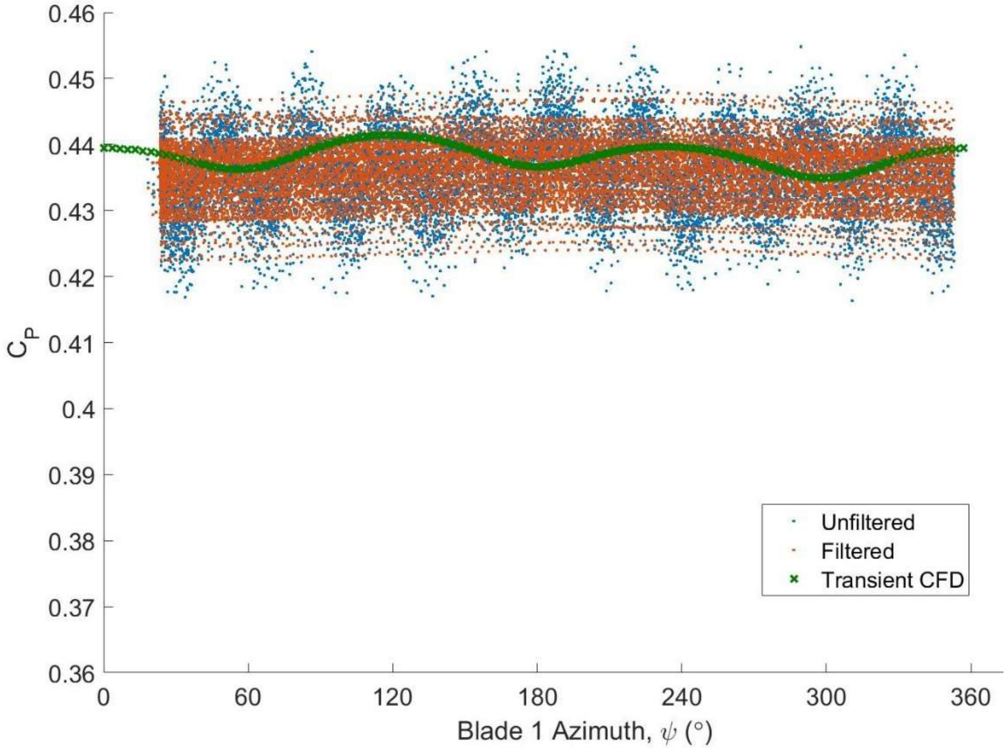

Figure 0.11 Filtered and unfiltered alternator C_P - φ for -10° yaw angle at V = 1.50 ms^{-1} and λ= 3.5 with corresponding transient CFD results

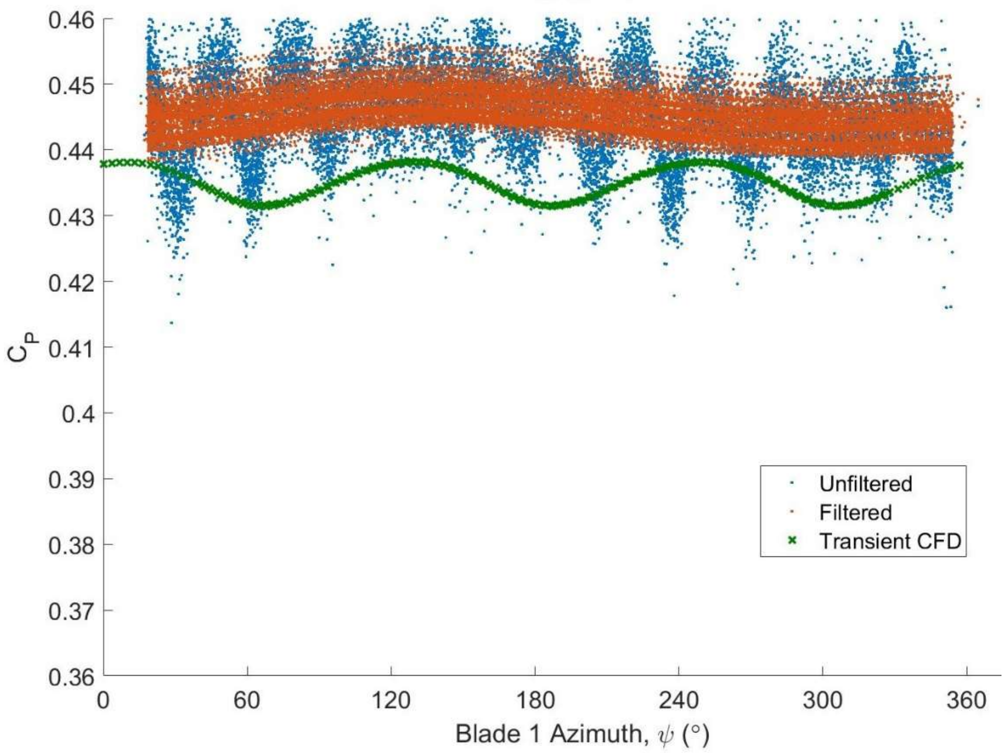

Figure 0.12 Filtered and unfiltered alternator C_P – φ for +10° yaw angle at V = 1.00 ms^{-1} and λ= 3.5 with corresponding transient CFD results

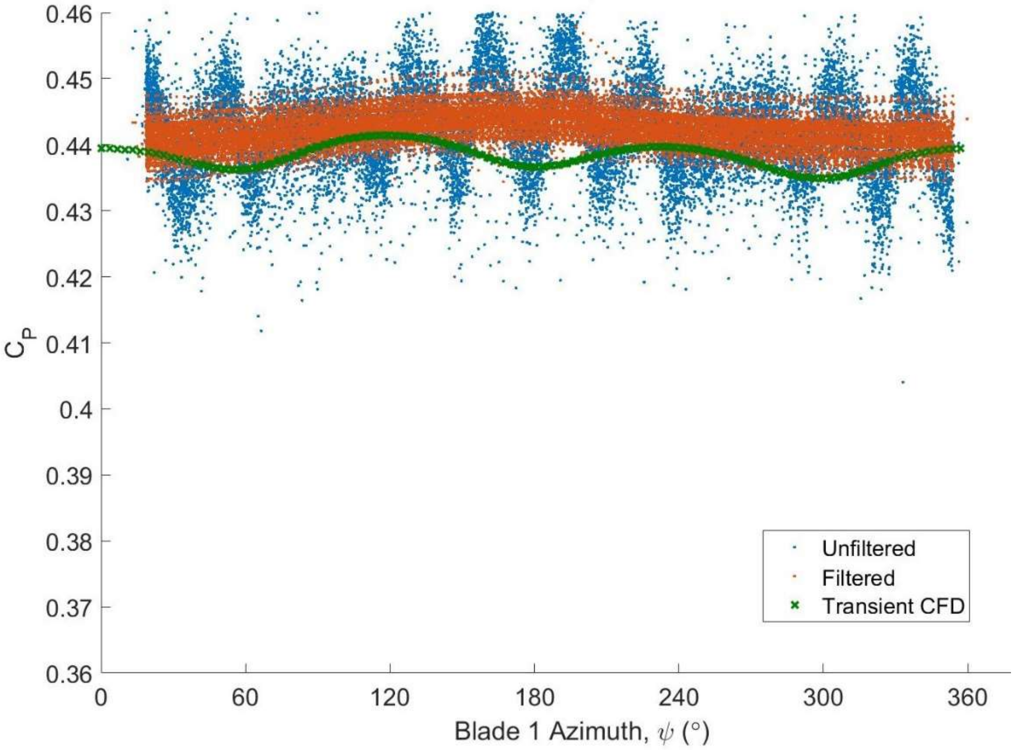

Figure 0.13 Filtered and unfiltered alternator C_P - φ for -10° yaw angle at V = 1.00 ms^{-1} and λ= 3.5 with corresponding transient CFD results

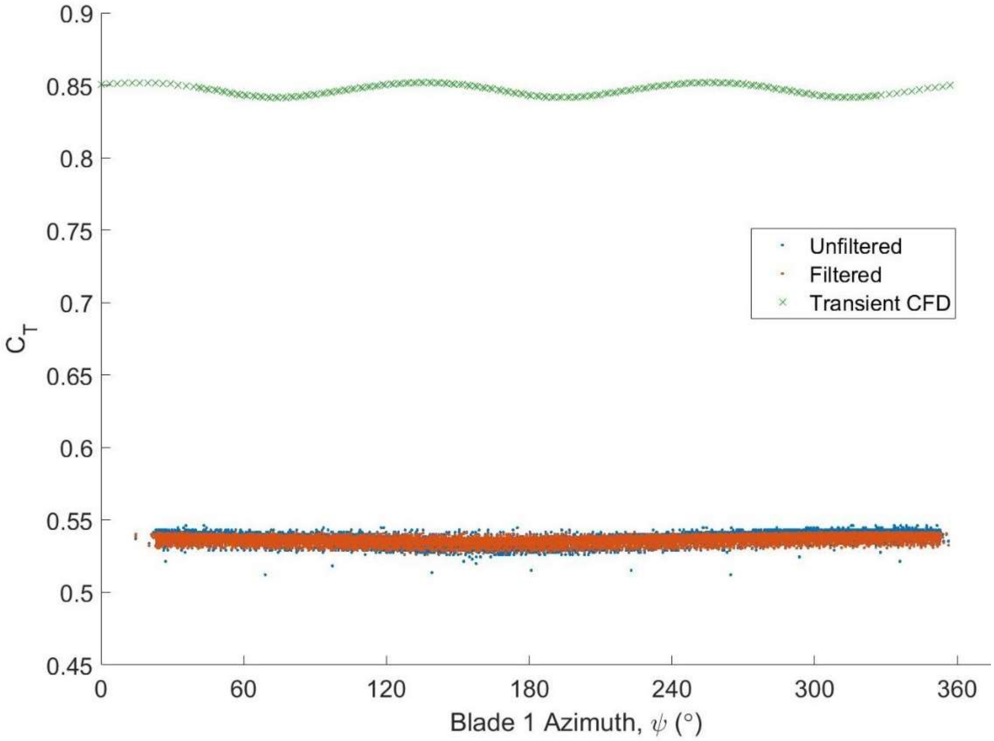

Figure 0.14 Filtered and unfiltered alternator C_T - φ for +10° yaw angle at V = 1.50 ms^{-1} and λ= 3.5 with corresponding transient CFD results

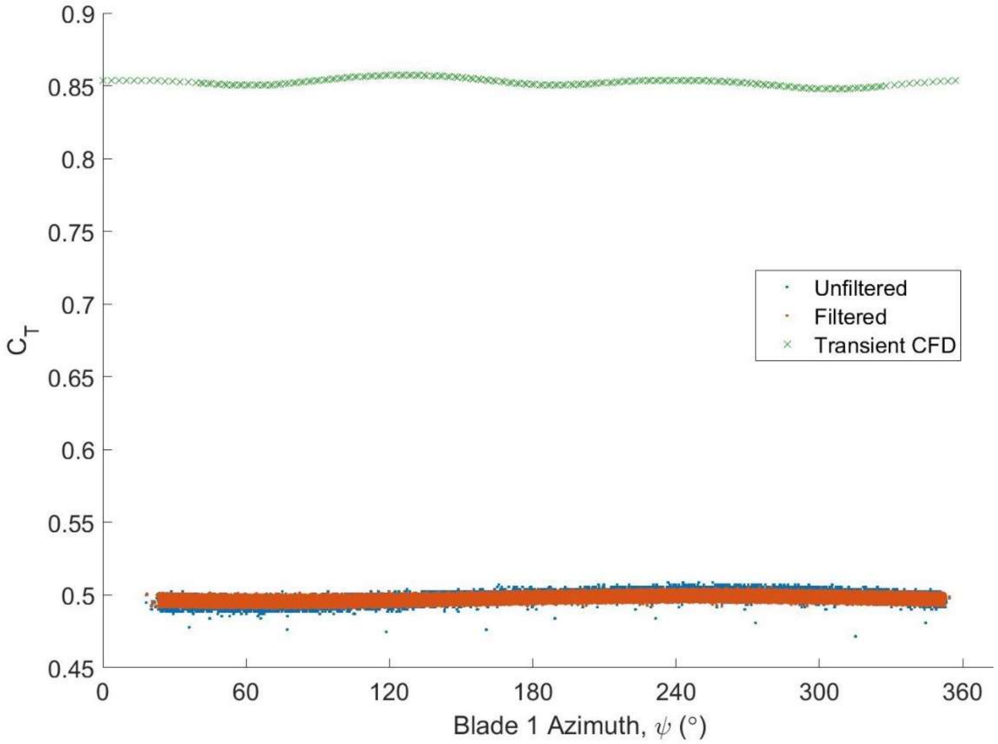

Figure 0.15 Filtered and unfiltered alternator C_T - φ for -10° yaw angle at V = 1.50 ms^{-1} and λ= 3.5 with corresponding transient CFD results

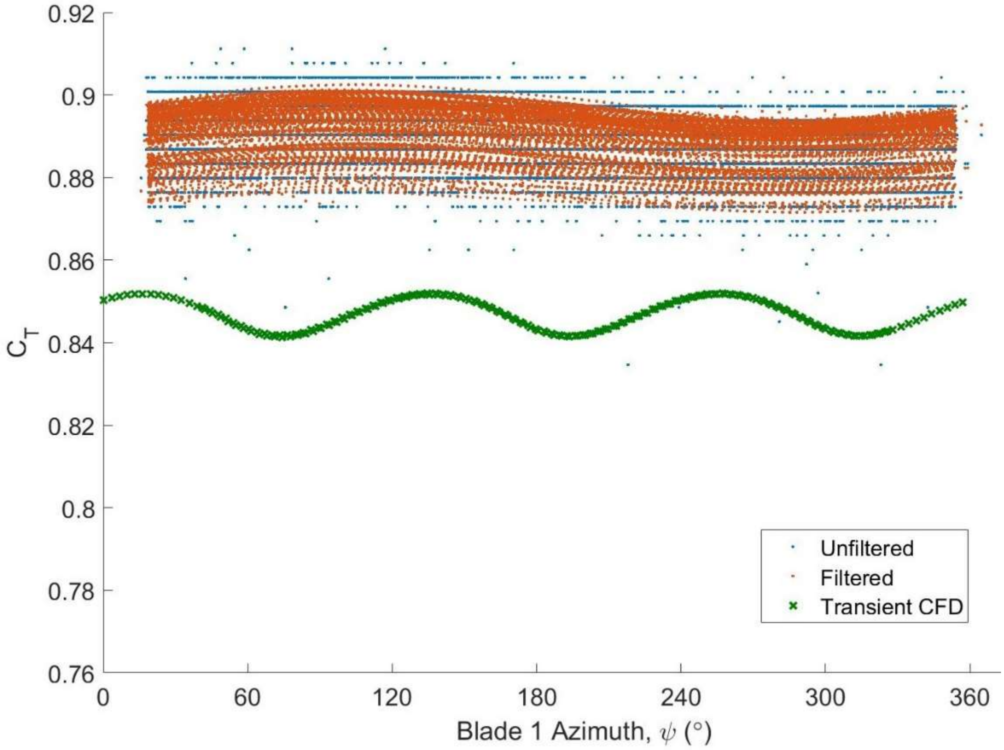

Figure 0.16 Filtered and unfiltered alternator C_T - φ for +10° yaw angle at V = 1.00 ms^{-1} and λ= 3.5 with corresponding transient CFD results

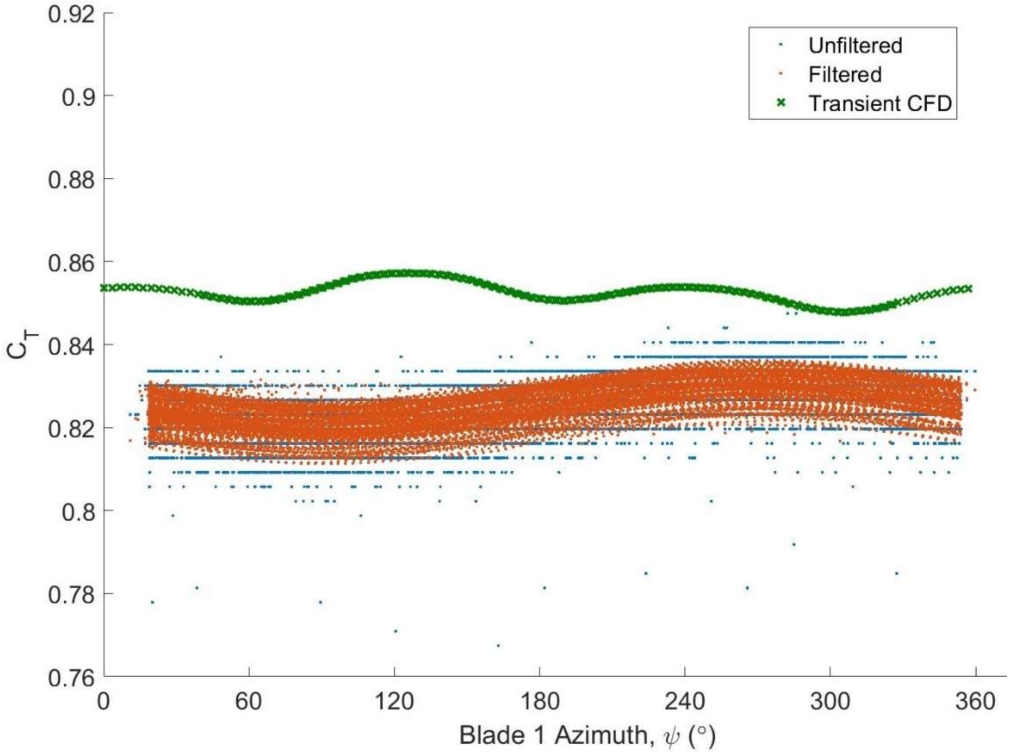

Figure 0.17 Filtered and unfiltered alternator C_T - φ for -10° yaw angle at V = 1.00 ms^{-1} and λ= 3.5 with corresponding transient CFD results

±20° Temporal Results

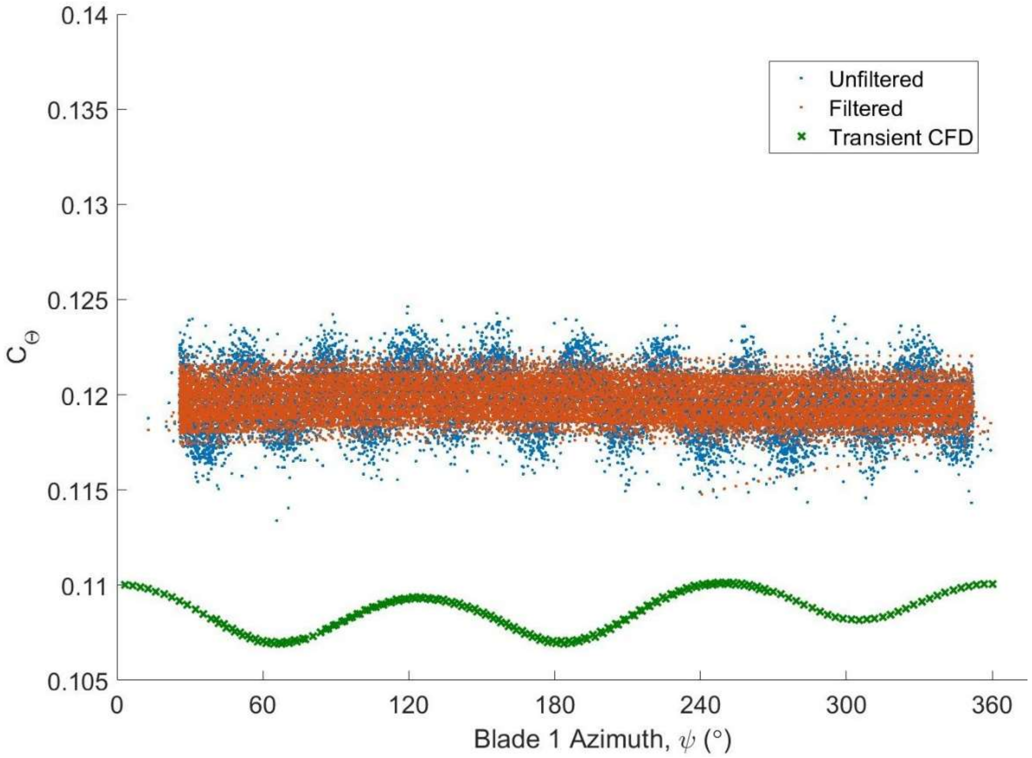

Figure 0.18 Filtered and unfiltered alternator C_θ - φ for +20° yaw angle at V = 1.50 ms^{-1} and λ= 3.5 with corresponding transient CFD results

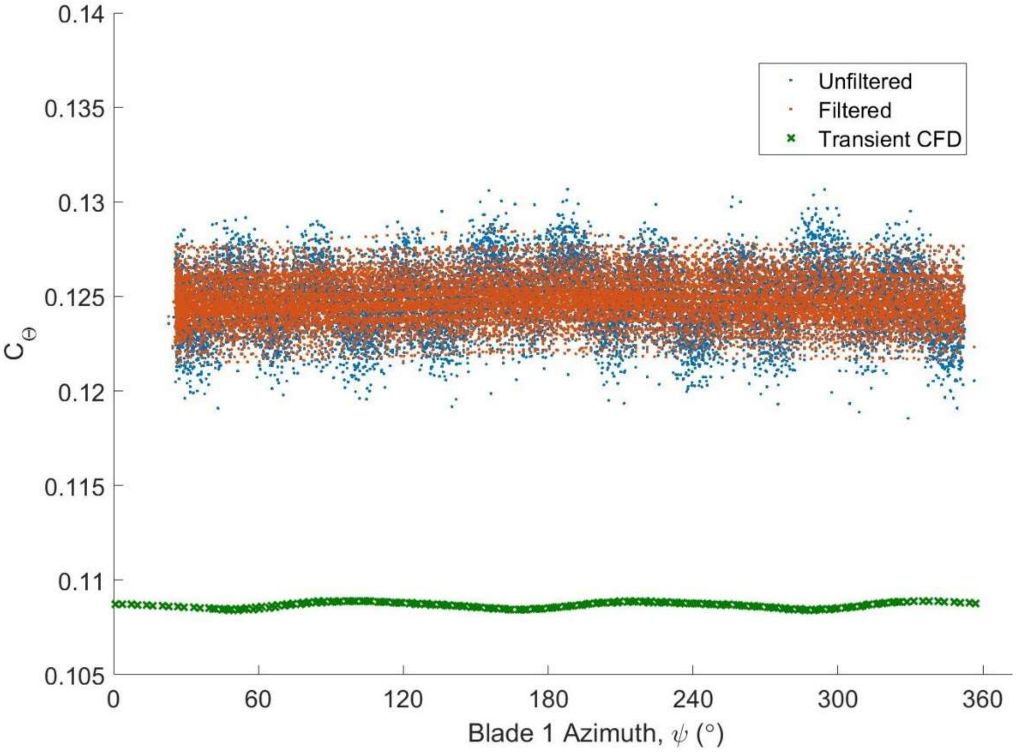

Figure 0.19 Filtered and unfiltered alternator C_θ - φ for -20° yaw angle at V = 1.50 ms^{-1} and λ= 3.5 with corresponding transient CFD results

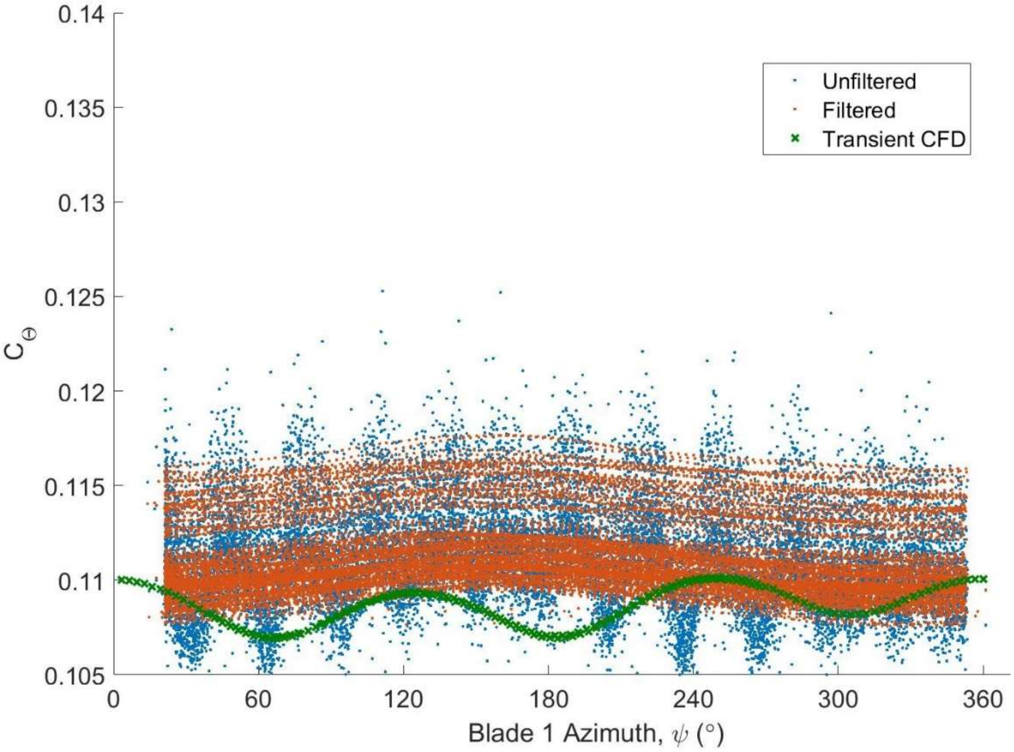

Figure 0.20 Filtered and unfiltered alternator C_θ - φ for +20° yaw angle at V = 1.00 ms^{-1} and λ= 3.5 with corresponding transient CFD results

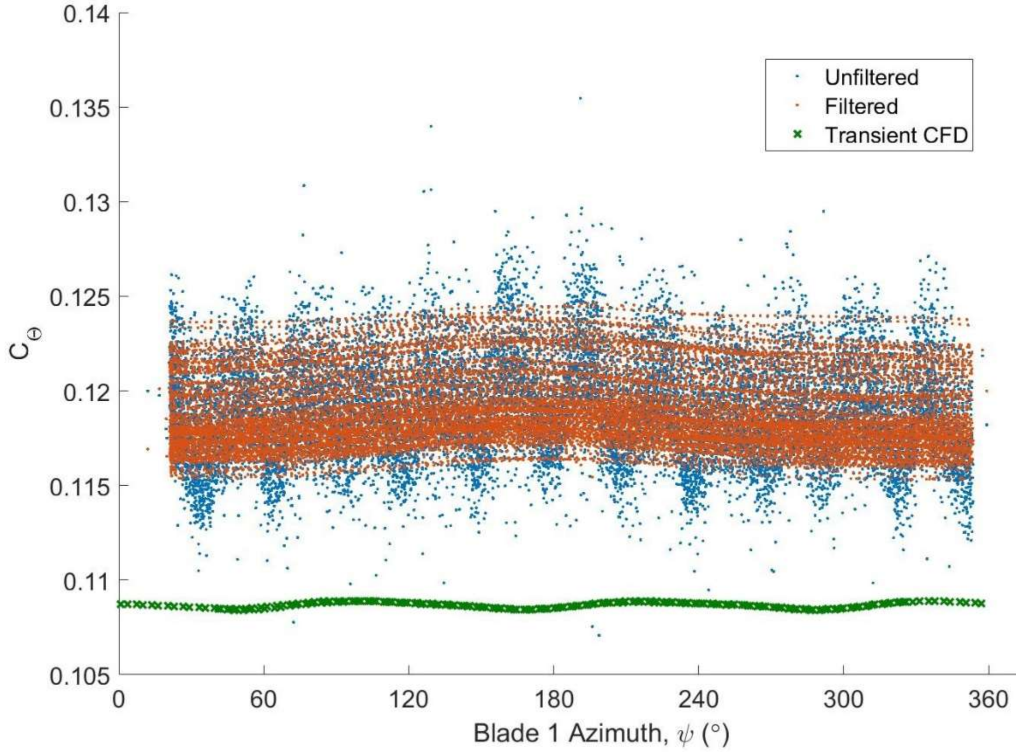

Figure 0.21 Filtered and unfiltered alternator C_θ - φ for -20° yaw angle at V = 1.00 ms^{-1} and λ= 3.5 with corresponding transient CFD results

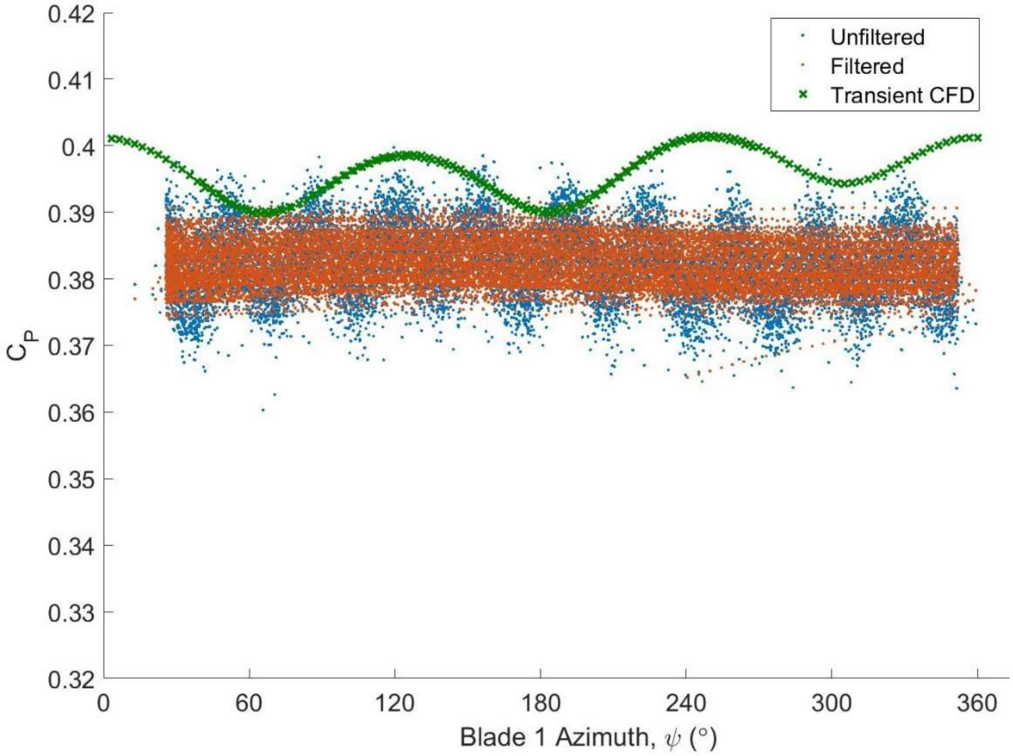

Figure 0.22 Filtered and unfiltered alternator C_P - φ for +20° yaw angle at V = 1.50 ms^{-1} and λ= 3.5 with corresponding transient CFD results

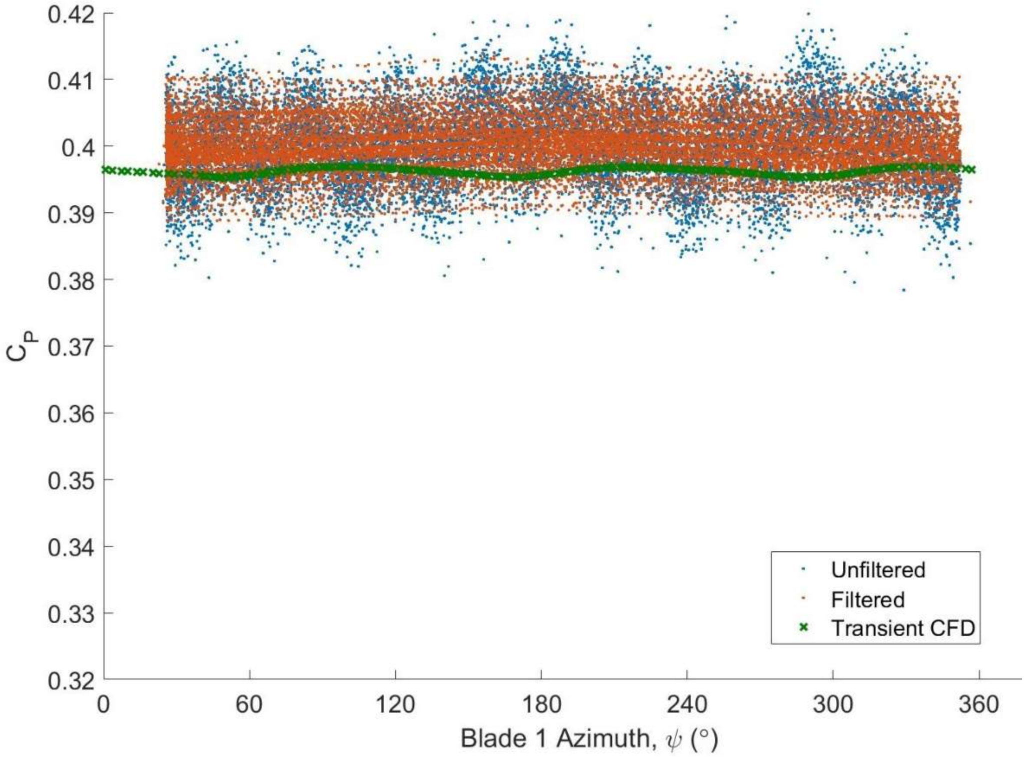

Figure 0.23 Filtered and unfiltered alternator C_P - φ for -20° yaw angle at V = 1.50 ms^{-1} and λ= 3.5 with corresponding transient CFD results

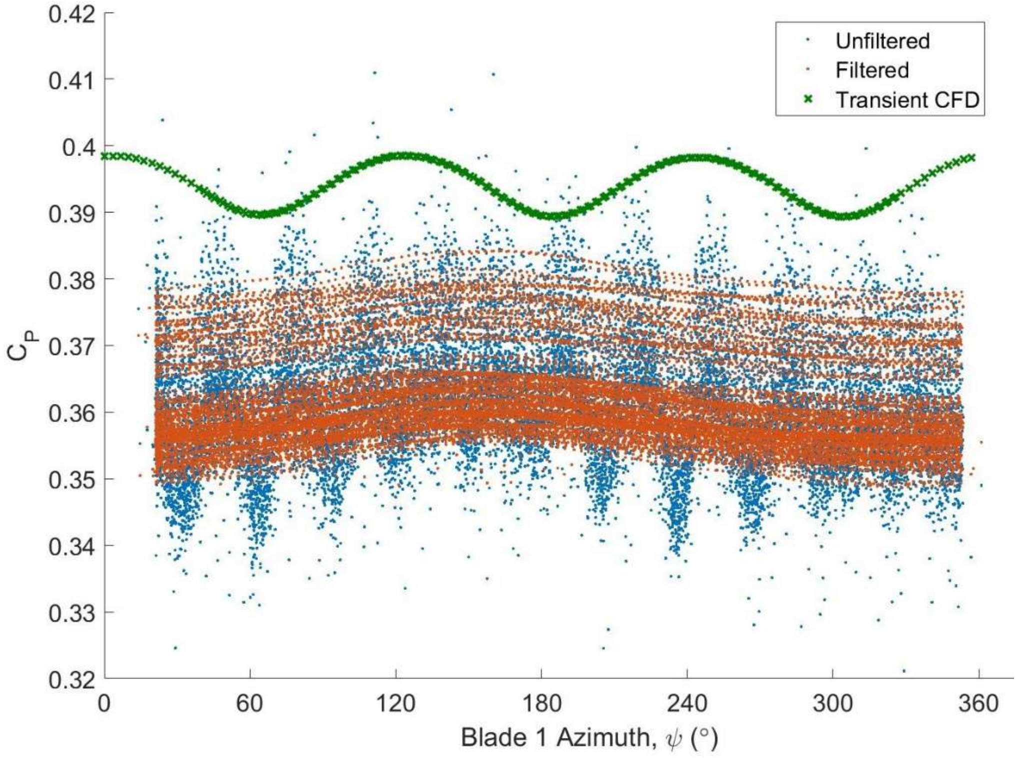

Figure 0.24 Filtered and unfiltered alternator C_P - φ for +20° yaw angle at V = 1.00 ms^{-1} and λ= 3.5 with corresponding transient CFD results

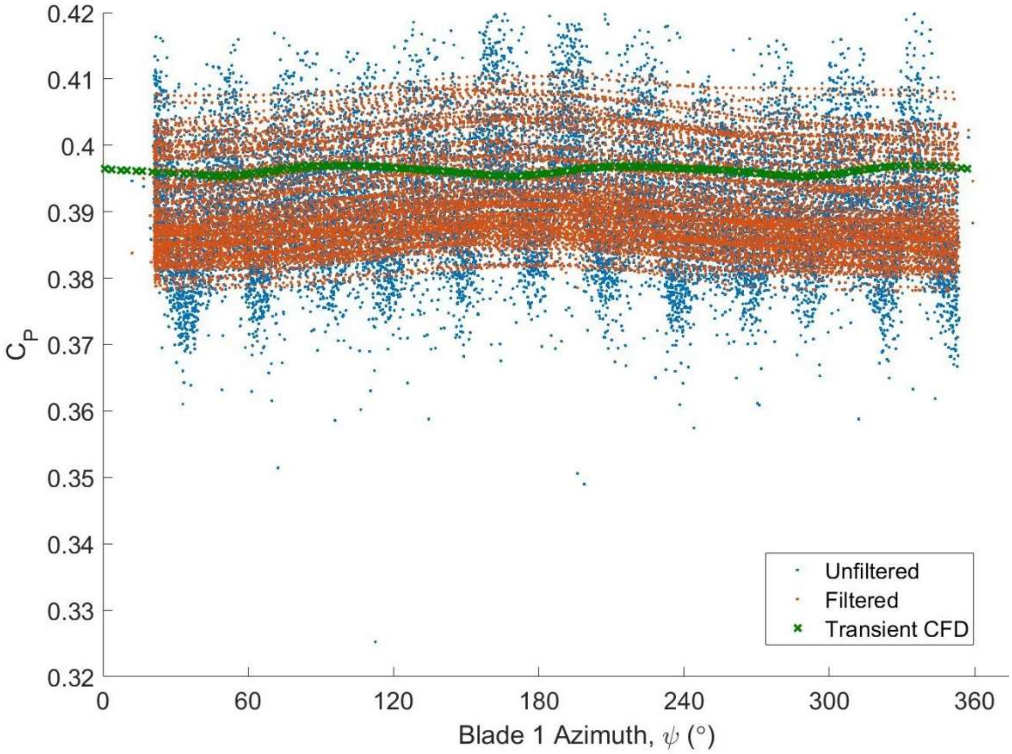

Figure 0.25 Filtered and unfiltered alternator C_P - φ for -20° yaw angle at V = 1.00 ms^{-1} and λ= 3.5 with corresponding transient CFD results

Spectral Analysis

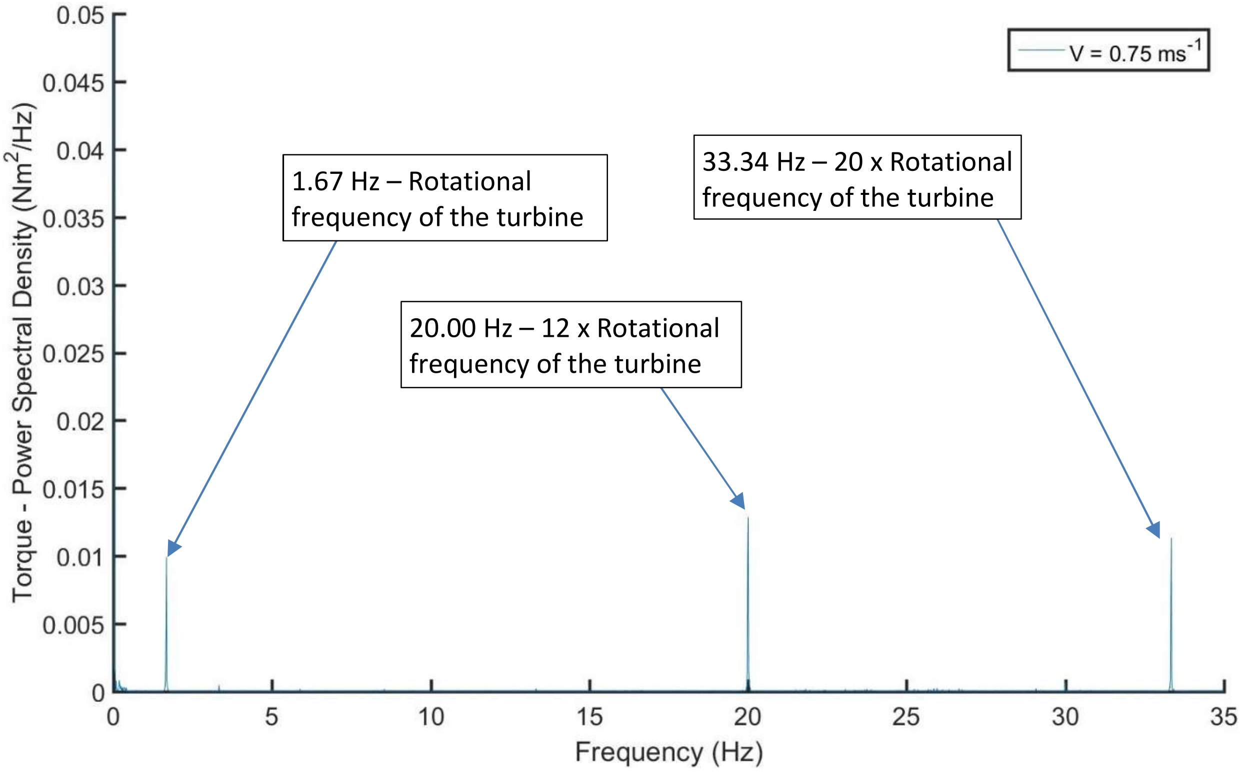

Figure 0.26 Periodogram of rotor torque signal for aligned, 0° yaw angle at λ = 3.5 and V = 0.75 ms^{-1}

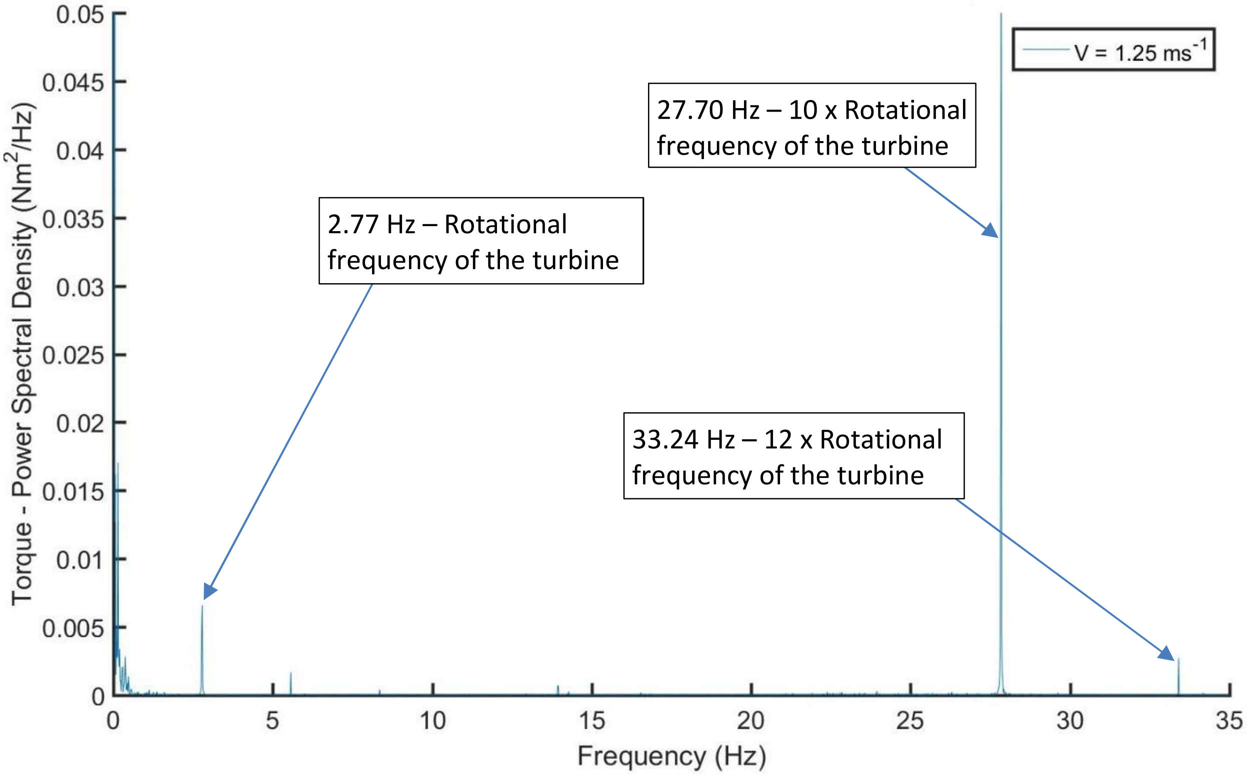

Figure 0.27 Periodogram of rotor torque signal for aligned, 0° yaw angle at λ = 3.5 and V = 1.25 ms^{-1}

F. Publications related to this thesis

Book Contributions

S Tatum, C Frost, D O'Doherty, A Mason-Jones and T O'Doherty, Modelling Tidal Stream Turbines, *Renewable Energy in the Service of Mankind, Vol 1* Part IV, Chapter 32, Pg 351 – 364, DOI 10.1007/978-3-319-17777-9, ISBN 978-3-319-17776-2 (eBook: ISBN 978-3-319-17777-9), Publishers: Springer (2015).

Refereed Journals

C H. Frost, P S. Evans, M Harrold, A Mason-Jones, T O'Doherty, D M. O'Doherty. The Impact of Axial Flow Misalignment on Tidal Turbines. Submitted 2016. Energy

S Tatum, M Allmark, C Frost, D O'Doherty, A Mason-Jones, T O'Doherty. CFD modelling of a tidal stream turbine subjected to profiled flow and surface gravity waves, International Journal of Marine Energy, DOI 10.1016/j.ijome.2016.04.003 (2016).

S C Tatum, C H Frost, M Allmark, D M O'Doherty, A Mason-Jones P W Prickett, R I Grosvenor, C B Byrne, T O'Doherty. Wave –Current Interaction Effects on Tidal Stream Turbine Performance and Loading Characteristics. *International Journal of Marine Energy*, DOI 10.1016/j.ijome.2015.09.002 (2015).

C H Frost, C E Morris, A Mason-Jones, D M O'Doherty, T O'Doherty. Effects of tidal directionality on tidal turbine characteristics. Renewable Energy, DOI 10.1016/j.renene.2015.01.053 (2015).

Refereed Conferences

S Ordonez-Sanchez, K Porter, C Frost, M Allmark, C Johnstone, T O'Doherty. Effects of Wave-Current Interactions on the Performance of Tidal Stream Turbines, 3rd AWTEC, Singapore (2016).

C H Frost, P S Evans, C Morris, A Mason-Jones, D M O'Doherty, T O'Doherty. Flow Misalignment and Tidal Stream Turbines, 11th EWTEC, Nantes, ISSN 2309-1983 (2015).

S Tatum, M Allmark, C H Frost, D M O'Doherty, A Mason-Jones, T O'Doherty. CFD modelling of a tidal stream turbine subjected to profiled flow and surface gravity waves, 11th EWTEC, Nantes, ISSN 2309-1983 (2015).

C H Frost, P S Evans, C E Morris, A Mason-Jones, T O'Doherty, D M O'Doherty. The Effect of Axial Flow Misalignment on Tidal Turbine Performance. 1st Intl Conf. on Renewable Energies Offshore, Lisbon, Portugal (2014).

S Tatum, C H Frost, D O'Doherty, A Mason-Jones, T O'Doherty. Modelling tidal stream turbines. World Renewable Energy Conference, Kingston, UK (2014).